



HAL
open science

Electromagnetic design of a disc rotor electric machine as integrated motor-generator for hybrid vehicles

Mickaël Kremer

► **To cite this version:**

Mickaël Kremer. Electromagnetic design of a disc rotor electric machine as integrated motor-generator for hybrid vehicles. Other. Université de Haute Alsace - Mulhouse, 2016. English. NNT : 2016MULH8792 . tel-01558838

HAL Id: tel-01558838

<https://theses.hal.science/tel-01558838>

Submitted on 10 Jul 2017

HAL is a multi-disciplinary open access archive for the deposit and dissemination of scientific research documents, whether they are published or not. The documents may come from teaching and research institutions in France or abroad, or from public or private research centers.

L'archive ouverte pluridisciplinaire **HAL**, est destinée au dépôt et à la diffusion de documents scientifiques de niveau recherche, publiés ou non, émanant des établissements d'enseignement et de recherche français ou étrangers, des laboratoires publics ou privés.

Année : 2016

N° d'ordre :

UNIVERSITÉ DE HAUTE-ALSACE
ÉCOLE DOCTORALE DE MATHÉMATIQUES,
SCIENCES DE L'INFORMATION ET DE L'INGÉNIEUR
LABORATOIRE MIPS

THÈSE

présentée par

MICKAËL KREMER

pour l'obtention du grade de

Docteur de l'Université de Haute-Alsace

Discipline : Électronique, Électrotechnique et Automatique

Electromagnetic design of a disc rotor electric machine as integrated motor-generator for hybrid vehicles

Arrêté ministériel du 24 août 2006

Soutenue publiquement le 12 mai 2016 devant le jury composé de :

Pr.	Joël Fontaine	INSA, Strasbourg	Président
Pr.	Mohamed Gabsi	ENS, Cachan	Rapporteur
Pr.	Éric Semail	ENSAM, Lille	Rapporteur
Dr.	Juliette Soulard	KTH, Stockholm	Éxaminatrice
Dr.	Martin Braun	Robert Bosch GmbH, Stuttgart	Co-encadrant
Dr.	Damien Flieller	INSA, Strasbourg	Co-encadrant
Dr.	Guy Sturtzer	INSA, Strasbourg	Co-encadrant
Pr.	Jean Mercklé	UHA, Mulhouse	Directeur

À mes grands-pères,

Remerciements

Une thèse est tout sauf un travail solitaire. Au cours des trois dernières années et au cours de mes études j'ai eu l'honneur et la chance de faire de magnifiques rencontres et de recevoir de nombreux soutiens. C'est avec joie que je leur consacre ces quelques lignes afin leur exprimer toute ma gratitude.

En premier lieu, je tiens à remercier chaleureusement mon directeur de thèse, Monsieur Jean Mercklé d'avoir accepté de diriger mes recherches, ainsi que pour son implication et les nombreux conseils qu'il m'a donnés tout au long de mes recherches.

J'adresse également toute ma gratitude à Monsieur Damien Flieller pour l'encadrement de mes recherches et les nombreuses heures qu'il a consacrées à la correction de ce travail. Les conseils de Damien m'ont permis de surpasser les difficultés et ont indéniablement enrichi cette thèse. Je remercie également Monsieur Guy Sturtzer pour son co-encadrement et son soutien.

Mein ganz herzlicher Dank gilt Herr Martin Braun für die Themastellung dieser Doktorarbeit, seine hilfreiche Betreuung und seine Unterstützung. Unsere regelmäßige und interessante Diskussionen haben meine Arbeit sehr gut unterstützt.

J'exprime toute ma reconnaissance envers Monsieur Joël Fontaine, Monsieur Mohamed Gabsi, Monsieur Éric Semail et Madame Juliette Soulard de me faire l'honneur d'évaluer mon travail et de l'intérêt qu'ils portent à mes recherches.

J'adresse ensuite mes remerciements les plus chaleureux à mes parents et à ma sœur dont l'amour, les conseils et l'inconditionnel et indispensable soutien moral et matériel m'ont permis de m'épanouir dans toutes les étapes de ma vie et de réussir mes études. Cette thèse c'est aussi la vôtre.

Je souhaite ensuite remercier ma famille qui m'a toujours soutenu et encouragé. Je remercie tous ceux qui ont pu venir assister à ma soutenance et j'adresse une pensée émue à celles et ceux qui ne sont pas là aujourd'hui pour partager ce moment avec moi.

Je remercie également mes amis que j'ai eu la chance et le plaisir de rencontrer tout au long de mes études. J'espère que de nombreux souvenirs viendront s'ajouter à ceux que nous avons déjà vécus.

Zum Schluss möchte ich meine Arbeitskollegen für ihre Unterstützung im Lauf dieser Promotion und für die freundschaftliche Arbeitsatmosphäre herzlich danken.

Contents

Contents	i
Abbreviations	vii
Symbols	ix
Introduction	1
1 State of the art: disc rotor electric machines	7
Introduction	8
1.1 Disc rotor axial-flux machines	9
1.1.1 Permanent-magnet axial-flux machines	10
1.1.1.1 Single air gap axial-flux machines	10
1.1.1.2 Internal stator axial-flux machines	11
1.1.1.3 Internal rotor axial-flux machines	17
1.1.1.4 Multidisc axial-flux machines	20
1.1.2 Other axial-flux machines technologies	21
1.1.3 Applications of axial-flux machines	21
1.1.3.1 Automotive applications	22
1.1.3.2 Other applications fields	23
1.2 Other disc rotor electric machines	24
1.2.1 Transverse-flux machines	24
1.2.2 Combination of axial-flux and other technologies	25
Conclusion	26
2 Electromagnetic design	27
Introduction	28
2.1 Requirements	28
2.2 Constraints on electric parameters	32
2.2.1 Induced voltage	32
2.2.2 Power factor and short circuit current	33
2.3 Selection of a topology	35
2.3.1 Selection of suitable technologies for automotive applications	35
2.3.1.1 Transverse-flux machines	35
2.3.1.2 Axial-flux machines	38
2.3.2 Comparison of suitable topologies	39

2.3.2.1	Evaluation of selected topologies	39
2.3.2.2	Discussion and selection of suitable topology	41
2.4	Design	43
2.4.1	Winding technology	44
2.4.2	Electric connection	45
2.4.3	Teeth alignment	46
2.4.4	Permanent-magnets	49
2.4.5	Magnetic material	50
2.4.5.1	Soft magnetic composite	50
2.4.5.2	Steel lamination	52
2.4.5.3	Selection of the magnetic material	52
Conclusion	54
3	Selection of the number of slots per pole per phase	55
Introduction	56
3.1	Possible numbers of slots per pole per phase	57
3.2	Concentrated winding with NSPP=0.5	59
3.2.1	Presentation	59
3.2.2	Axial forces	60
3.3	Integer numbers of slots per pole per phase	61
3.3.1	Presentation	61
3.3.2	Unbalanced induced voltages	62
3.3.3	Axial forces on magnets	65
3.4	Fractional number of slots per pole per phase	67
3.4.1	Fractional NSPP with concentrated windings	67
3.4.2	Fractional NSPP with distributed windings	67
3.4.3	Fractional distributed winding with NSPP=1.5	71
3.5	Comparison between the numbers of slots per pole per phase	72
3.5.1	Magneto-motive force	72
3.5.2	FEM simulations	74
3.5.3	Selection of the optimum NSPP	77
Conclusion	78
4	Analytic model for losses in axial-flux machines	79
Introduction	80
4.1	Joule losses in the electric conductors	80
4.1.1	Generalities over conductor losses	80
4.1.2	Alternating current losses	81
4.1.2.1	Skin effect in electrical machines	81
4.1.2.2	Analytic model	82
4.1.3	Optimized hairpin winding for axial-flux machines	87
4.1.3.1	Concept and FEM calculations	87
4.1.3.2	Analytic model	90
4.2	Iron losses in the stator soft magnetic material	93
4.2.1	Hysteresis losses	93
4.2.2	Eddy current losses	94
4.2.3	Excess losses and global expression	94

4.3	Eddy current losses in the rotor permanent-magnets	96
4.3.1	Generalities over magnet eddy current losses	96
4.3.2	Analytic model for magnet losses	98
4.3.2.1	Influence of the coil current on magnet losses	98
4.3.2.2	Influence of the temperature	102
	Conclusion	105
5	Dimensioning	107
	Introduction	108
5.1	Manual dimensioning	109
5.1.1	Design	109
5.1.1.1	Publications	109
5.1.1.2	Designing of the machine	110
5.1.1.3	Final design (AFM ₆₀)	112
5.1.2	Validation of the design definition	116
5.1.2.1	Teeth alignment	117
5.1.2.2	Winding construction	118
5.1.2.3	Electric connection	119
5.1.2.4	Number of slots per pole per phase	121
5.2	Multi-objective optimization	124
5.2.1	Presentation	124
5.2.1.1	Software toolchain	124
5.2.1.2	Parameters and objectives	128
5.2.2	Sensitivity analysis	129
5.2.2.1	Presentation and motivation	129
5.2.2.2	Results	130
5.2.2.3	Conclusion	134
5.2.3	Optimization	135
5.2.3.1	Selection of optimized design	135
5.2.3.2	Torque and power characteristics	138
5.2.3.3	Comparison with the manually designed machine	140
	Conclusion	143
6	Comparison with a radial-flux machine	145
	Introduction	146
6.1	Comparison with same specification	147
6.1.1	RFM design RFM ₃₀₀	147
6.1.2	Design comparison	149
6.1.3	Torque and power characteristics	149
6.1.4	Losses and efficiency	150
6.1.5	Torque ripple	153
6.2	Comparison with same dimensions	154
6.2.1	RFM design RFM ₂₈₂	154
6.2.2	Design comparison	156
6.2.3	Torque and power characteristics	156
6.2.4	Losses and efficiency	157
6.2.5	Torque ripple	160

Conclusion	161
7 Prototypes and tests	163
Introduction	164
7.1 First prototype: AFM _{P1}	164
7.1.1 Description	164
7.1.2 Measurements	165
7.1.2.1 Induced voltage and short circuit current	165
7.1.2.2 Torque current characteristic	167
7.1.2.3 Torque speed characteristic	169
7.2 Second prototype: AFM _{P2}	171
7.2.1 Description	171
7.2.2 Measurements	172
7.2.2.1 Induced voltage and no load losses	172
7.2.2.2 Short circuit current and short circuit losses	175
7.2.2.3 Torque current characteristic	177
7.2.2.4 Losses performance map	178
Conclusion	179
Conclusion	181
Appendices	183
A Permanent-Magnet Synchronous Machines (PMSM)	184
A.1 Equivalent circuit	184
A.2 dq transformation	185
A.3 Torque expression	186
A.4 Characteristic and evolution of the current	187
A.5 Effects of a phase shift in the induced voltages	191
B Torque generation in axial-flux machines	194
B.1 Analytic calculation	194
B.2 Determination of the optimum diameter ratio	197
C Material database	200
C.1 Permanent-magnets	200
C.2 Soft magnetic composite	202
C.3 Electric properties of copper	203
D Multi-objective optimization	204
D.1 Example of multi-objective optimization	204
D.2 Multi-objective optimization algorithms	205
E Manually designed machine (AFM ₆₀)	207
E.1 Losses and efficiency	207
E.2 Axial forces	209
E.3 Torque ripple	211
E.4 Short circuit current	212
E.5 Demagnetization safety	213
F Multi-objective optimized machine (AFM _{MOO})	216
F.1 Winding technology	216

F.2	Losses and efficiency	218
F.3	Axial forces and torque ripple	222
F.4	Short circuit current	225
F.5	Demagnetization safety	226
List of Figures		229
List of Tables		235
Bibliography		237

Abbreviations

AFM	Axial-Flux Machine
AFIR	Axial-Flux Internal Rotor
AFIS	Axial-Flux Internal Stator
EV	Electric Vehicle
FEM	Finite Element Method
HEV	Hybrid Electric Vehicle
IMG	Integrated Motor-Generator
MHEV	Mild Hybrid Electric Vehicle
MOO	Multi-Objective Optimization
MTPA	Maximum Torque Per Ampere
NdFeB	Neodym iron Boron (permanent-magnet)
NEDC	New European Drive Cycle
NSPP	Number of Slots per Pole per Phase
PHEV	Plug-in Hybrid Electric Vehicle
PMSM	Permanent-Magnet Synchronous Machines
REX	Range EXtender vehicle
RFM	Radial-Flux Machine
SMC	Soft Magnetic Composite
SMG	Separated Motor-Generator
TFM	Transverse-Flux Machine
THD	Total Harmonic Distortion
TORUS	TORoidally wound internal Stator
YASA	Yokeless And Segmented Armature

AFM₁	AFM: first design
AFM₆₀	AFM: manually designed
AFM_{MOO}	AFM: multi-objective optimization
AFM_{P1}	AFM: first prototype
AFM_{P2}	AFM: second prototype
IMG300	Radial flux reference Bosch IMG (VW Touareg)
RFM₃₀₀	Scaled IMG300 radial flux machine ($D_{out} = 300mm$)
RFM₂₈₂	Scaled IMG300 radial flux machine ($D_{out} = 282mm$)

Symbols

B_r	Permanent-magnet remanence	T
D_{in}	Machine inside diameter	mm
D_{out}	Machine outside diameter	mm
f	Frequency	Hz
H_{cj}	Permanent-magnet coercivity	A.m ⁻¹
H_{k95}	Maximum reversible magnetic field strength	A.m ⁻¹
h_c	Conductor height	mm
h_s	Slot height	mm
I	Phase current	Arms
I_{sc}	Short circuit current	Arms
k_{cu}	Copper fill factor	%
k_d	Distribution factor	
k_E	Armature constant	V.s
k_p	Pitch factor	
k_r	Skin effect coefficient	$k_r(f) = \frac{R(f)}{R_{dc}}$
k_ω	Winding factor	$k_\omega = k_p \cdot k_d$
k_{wr}	Inverter ratio	$k_{wr} = 0.37$
L	Inductance	H
L_d	Inductance on the direct axis	H
L_q	Inductance on the quadratic axis	H
l_{fe}	Iron length	mm
l_{tot}	Total length	mm
l_{wdg}	Conductor length	mm
N	winding number	
N_h	Electric conductor per slot arranged above each other	

Symbols

n	Rotational speed (rotation per minute)	rpm
n_p	Pole pairs number	
n_{phase}	Number of phases	
n_{slots}	Number of slots	
$NSPP$	Number of Slots per Pole per Phase	$NSPP = \frac{n_{slots}}{n_{phase} \cdot 2n_p}$
P	Power	W
P_{cu}	Conductor losses	W
P_F	Power factor	
P_{fe}	Electromagnetic losses in soft magnetic material	W
P_{feh}	Hysteresis losses (soft magnetic material)	W
P_{fej}	Eddy current losses (soft magnetic material)	W
P_{fee}	Excess losses (soft magnetic material)	W
P_{mag}	Eddy current losses (magnets)	W
p_{wdg}	Number of parallel conductors	
R	Phase resistance	Ω
R_{dc}	Phase resistance for a DC current	Ω
$R(f)$	Phase resistance at the frequency f	Ω
s_{wdg}	Section of the conductor	mm ²
T	Mechanical torque	Nm
T_{em}	Electromagnetic torque	Nm
w_c	Conductor width	mm
w_s	Slot width	mm
η	Efficiency	%
μ	Magnetic permeability	$\mu = \mu_r \mu_0 \text{ H.m}^{-1}$
μ_0	Vacuum permeability	$\mu_0 = 4\pi \cdot 10^{-7} \text{ H.m}^{-1}$
μ_r	Relative magnetic permeability	
ρ	Electric resistivity	$\Omega.m$
σ	Electric conductivity	$\Omega^{-1}.m^{-1}$
ω	Angular frequency	rad.s ⁻¹
ω_e	Electric angular frequency	rad.s ⁻¹

Introduction

Global warming, the exhaustion of fossil energies and the air pollution in mega cities are great challenges for the 21st century. A revolution of the energy consumption in the automotive industry will be necessary to achieve these objectives. The development of the electromobility is a major priority. Electric and hybrid vehicles are classified in four main categories:

- Mild Hybrid Electric Vehicles (MHEV): these vehicles have the smallest electric power. The electric drive train is designed to recover energy when the car brakes and assist the combustion engine during the acceleration. The storage capacity of the battery is limited to minimize the cost. The electric drive train of these vehicles reduces their consumption, especially in cities, but is too small to enable a pure electric drive.
- Plug-in Hybrid Electric Vehicles (PHEV): these vehicles have a stronger electric drive train. The storage capacity of the battery and the power are increased to enable pure electric drive over a limited distance (30 to 80 km). The battery can be loaded with the electric network. The combustion engine remains necessary for long range travels.
- Range Extender vehicles (REX): these vehicles have the specificity that the electric machine is the only one which generates the traction torque. The combustion engine is only used in combination with a smaller electric machine to load the battery and extend the range.
- Electric Vehicles (EV)

The distribution of these categories depending on the electric range and the drive train power is displayed in figure 1:

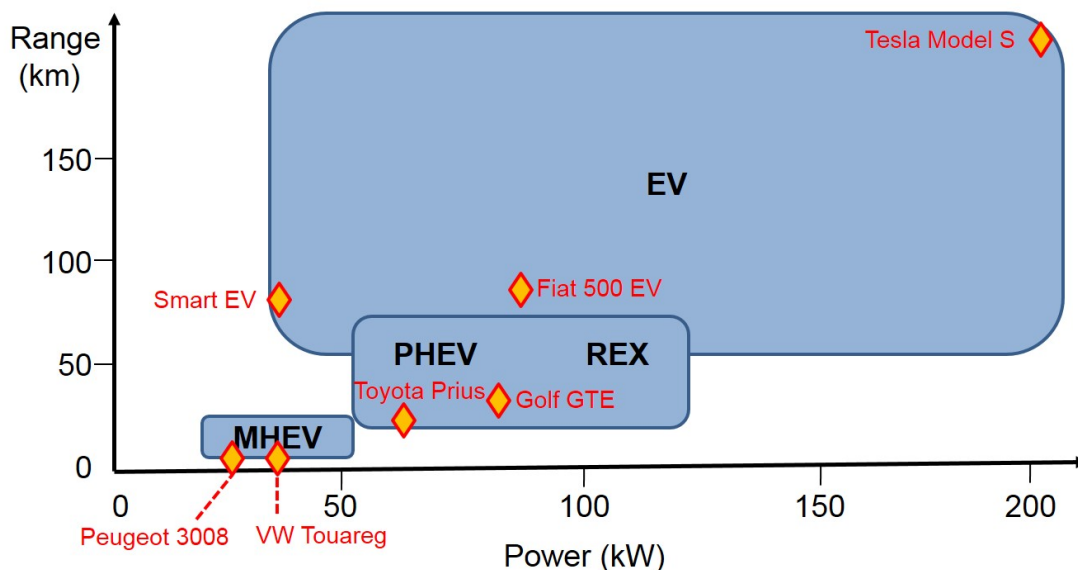


FIGURE 1: Hybrid and electric vehicles categories

For the moment the electromobility is a niche business due to insufficient technology and high cost, especially for the battery. Besides batteries, improving electric machines is necessary. These machines for automotive applications are divided in two categories:

- Integrated Motor-Generator (IMG): these electric machines are especially adapted for hybrid vehicles. The electric motor is integrated on the drive shaft between the combustion engine and the gearbox. The rotational speed of the motor is fixed by the combustion engine. These machines are characterized by a large diameter and a short axial length. The electric machine is used to increase or decrease the torque produced by the combustion engine, start it or getting back energy by braking the car. The magnetic circuit is in the shape of a ring limited by an inside diameter D_{in} , an outside diameter D_{out} and an axial length.
- Separated Motor-Generator (SMG): these electric machines are adapted for hybrid and electric vehicles. The electric motor is built as standalone component in the car. It can transmit torque to one or both drive shaft through a speed reducer. These machines are longer but with a smaller diameter than IMGs. Their rotational speed is higher.

This PhD focuses on integrated motor-generators. These machines require a high torque density and make the use of rare earth permanent-magnets necessary. Rare earth magnets are expensive and their price can vary in a very short time, like in 2010-2011 when it

had been multiplied by 10 within a few months [1]. Radial-flux machines with cylindrical rotors are the most common topology for automotive applications.

Disc rotor electric machines are an alternative to radial-flux machines. The short axial length and large diameter of disc rotor electric machines could make them suitable to an application as integrated motor-generator in hybrid cars. Disc rotor electric machines can be built as transverse-flux machine presented by the patents [2, 3] in 2006 or as axial-flux machine. The main objective of this PhD is to evaluate this suitability and propose the design of a disc rotor machine as integrated motor-generator. Following objectives will be prioritized for the dimensioning:

- Minimization of the weight of rare earth permanent-magnets
- Minimization of the axial length of the machine
- Minimization of the cost
- Maximization of the motor efficiency to maximize the range of the vehicle

This PhD has been done as part of a cooperation between Bosch, the INSA Strasbourg and the Université de Haute Alsace to estimate the feasibility of a disc rotor electric machine as integrated motor-generator. The project involved approximately 15 persons. The chronology of the PhD is presented in the context of the electromobility. At the begin of the PhD, the Transverse-Flux Machine (TFM) was the preferred solution. The first simulations and the publication of the iFlux report [4] have shown that the Axial-Flux Machine (AFM) had more potential for an IMG application. During the PhD, 2 AFM prototypes have been built in 2014 and 2015.

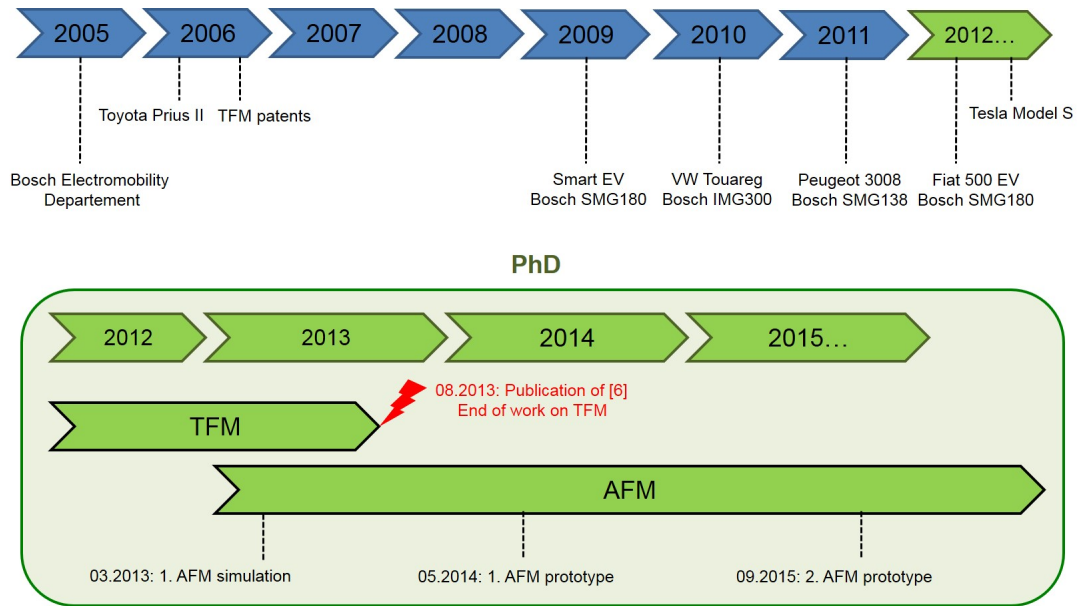


FIGURE 2: Chronology of the PhD

Chapter 1 presents the state of the art of disc rotor machines. The different families of axial-flux machines and other disc rotor topologies are presented. Current and future applications of disc rotor machines in the automotive and other application fields are shown.

Chapter 2 presents the requirements of the electric machine. In this chapter, the electromagnetic design of the machine is defined. At first, the suitability of the topologies presented in the state of the art for an automotive application is evaluated. The internal rotor axial-flux machine is selected. In a second step, the magnetic design is specified in details. For example, the shape of the magnets and the stator teeth are defined.

Chapter 3 presents the choice of the optimum number of slots per pole per phase. This number defines the relation between the number of stator slots and the number of poles. The advantages and disadvantages of each combination are presented.

Chapter 4 presents a study of the main losses sources in axial-flux machines. Winding losses, iron losses and eddy current in permanent-magnets are studied. Analytic models are proposed to interpolate the winding and the magnet losses in every operating points without or with a limited number of FEM calculations. These models enable a fast estimation of the losses.

Chapter 5 presents the dimensioning of the machine. At first, the machine is manually designed. The design selection performed in the chapter 2 and 3 is validated. In a second step, a multi-objective optimization is performed to improve the performances of the machine. Both machines are characterized and compared.

Chapter 6 presents a comparison between the axial-flux machine and a radial-flux machine (IMG300). In this study the performances and the dimensions of both machines are investigated to highlight the advantages and disadvantages of both topologies.

Chapter 7 presents the results of the experiments. Two prototypes have been built for the project. The measurements are compared with the calculated performances.

Chapter 1

State of the art: disc rotor electric machines

Contents

Introduction	8
1.1 Disc rotor axial-flux machines	9
1.1.1 Permanent-magnet axial-flux machines	10
1.1.1.1 Single air gap axial-flux machines	10
1.1.1.2 Internal stator axial-flux machines	11
1.1.1.3 Internal rotor axial-flux machines	17
1.1.1.4 Multidisc axial-flux machines	20
1.1.2 Other axial-flux machines technologies	21
1.1.3 Applications of axial-flux machines	21
1.1.3.1 Automotive applications	22
1.1.3.2 Other applications fields	23
1.2 Other disc rotor electric machines	24
1.2.1 Transverse-flux machines	24
1.2.2 Combination of axial-flux and other technologies	25
Conclusion	26

Introduction

Since the beginning of the 19th century and the discovery of magnetism, the development of new technologies for electric machines has been continuously improving. DC, synchronous and induction motors have successively been invented. The geometry of the magnetic circuit has also been continuously improved. Radial-flux machines with both cylindrical inside rotor and outside stator are most common electric motors. Today, the application field of disc rotor electric machines stays restricted even if some of the first electric machines built by Faraday and Jacobi in the 1830s or the Barlow's wheel designed in 1822 were disc rotor axial-flux machines [5, 6]. Disc rotor electric machines can be classified in following categories:

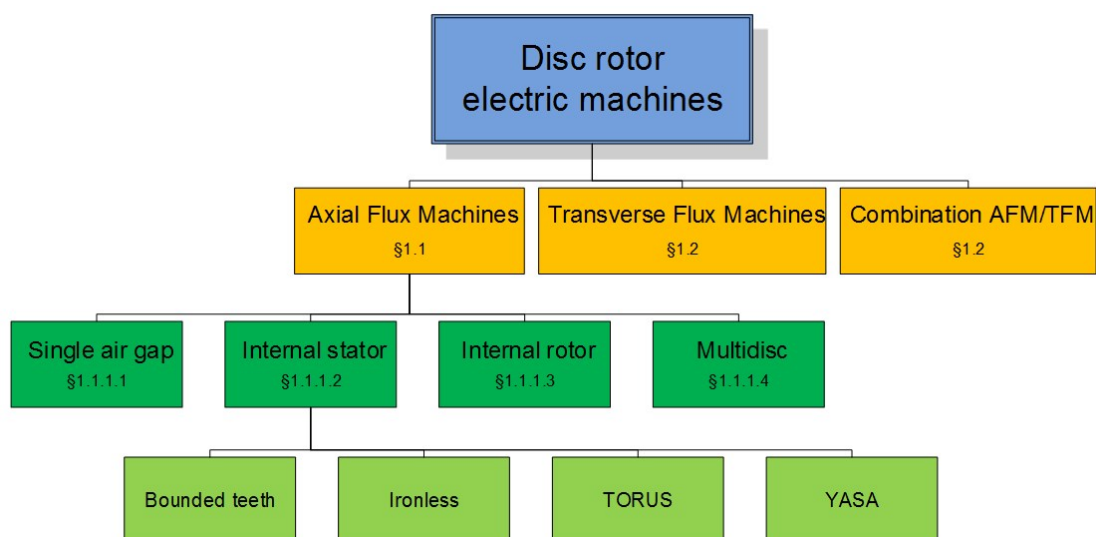


FIGURE 1.1: Classification of disc rotor electric machines

In this PhD, following frame is used for cylindrical coordinates:

- r : radial direction (perpendicular to the rotation axis)
- θ : angle (around the rotation axis)
- z : axial direction (parallel to the rotation axis)

The cut plane drawn in figure 1.2 will be used for every 2D cuts.

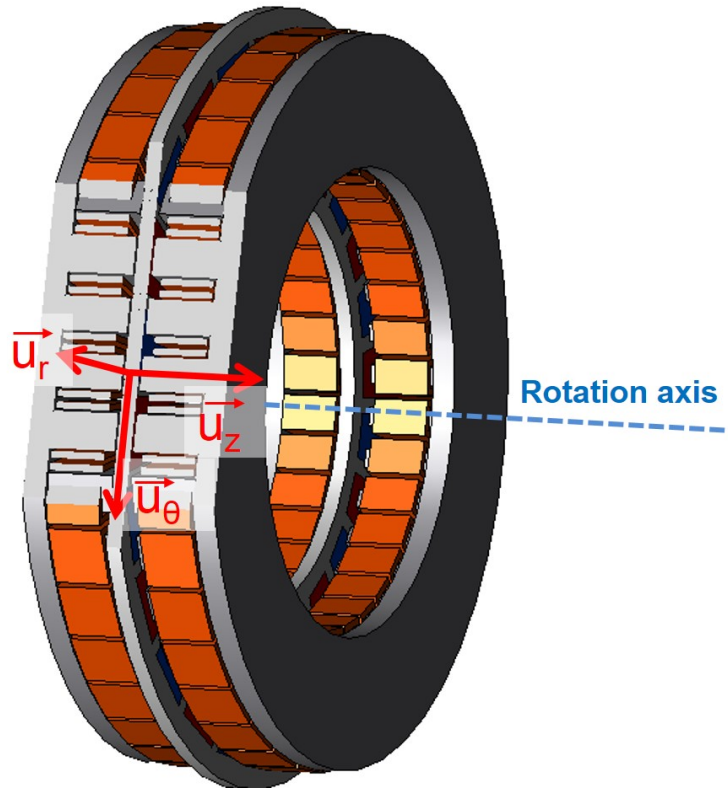


FIGURE 1.2: Cylindrical coordinates frame

1.1 Disc rotor axial-flux machines

Axial-Flux Machines (AFM) are disc rotor electric machines, where the magnetic flux in the air gap flows parallel to the rotation axis. The majority of axial-flux machines are permanent-magnet machines [5]. For this reason this section is mainly focused on this technology. Other technologies like current excited machines, DC machines, induction machines or switch reluctance axial-flux machines are presented in 1.1.2.

Disc rotor machines and especially axial-flux machines offer a multitude of possible configurations and the possibility to build them with one or several air gaps. There are four main configurations of axial-flux machines:

- AFM with one air gap built of one stator and one rotor
- AFM with two air gaps:
 - internal stator AFM (one stator and two rotors)
 - internal rotor AFM (two stators and one rotors)
- AFM with three or more air gaps

This is an advantage over radial-flux machines (RFM) which are often limited to one air gap. RFM with several air gaps showing electromagnetic advantages are possible in the literature [7–11] but are always characterized by a very complex mechanical construction.

1.1.1 Permanent-magnet axial-flux machines

1.1.1.1 Single air gap axial-flux machines

1.1.1.1.1 Presentation and magnetic circuit

The single air gap is the simplest configuration of AFM. These machines are composed of one rotor and one stator like state of the art RFM. Figure 1.3 shows the magnetic circuit at no load of a single air gap AFM.

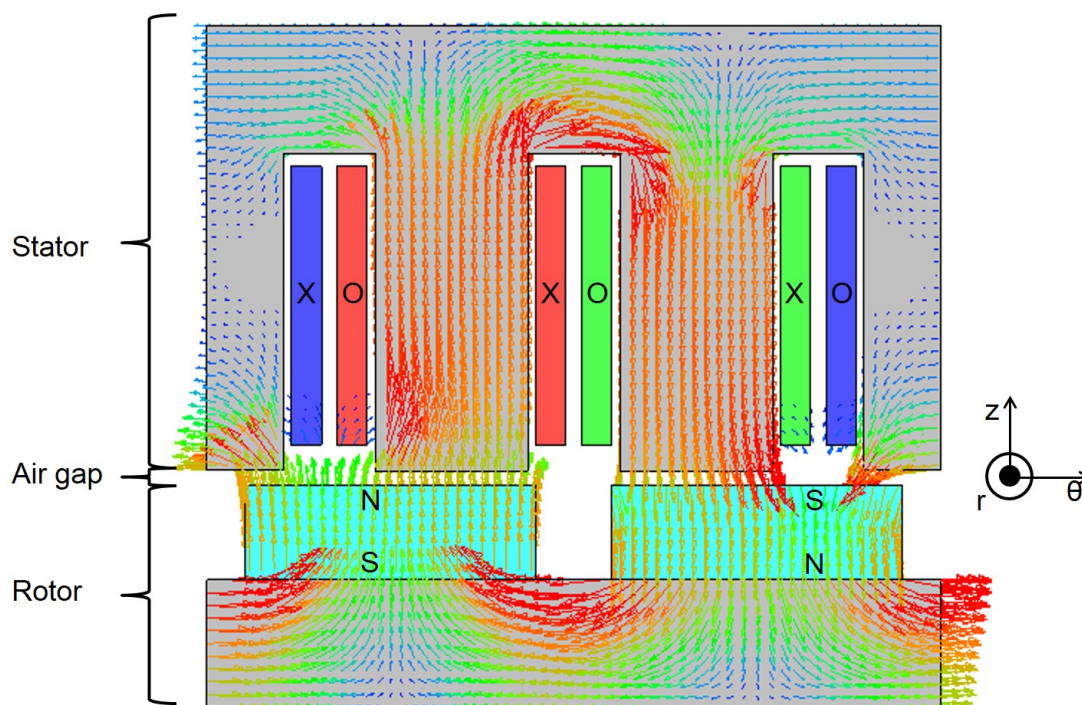


FIGURE 1.3: Magnetic circuit a single air gap AFM ($I = 0$)

Magnets are alternately axially magnetized in the rotor. Magnetic flux lines flow parallel to the rotation axis in the air gap and in the stator teeth. Single air gap AFMs are characterized by two magnetic back irons where the magnetic flux flows tangentially: one in the rotor behind the magnets and one in the stator. This magnetic circuit is also similar to the magnetic circuit of a RFM with an inversion of radial and axial direction.

One of the most interesting characteristic of single air gap AFM is the axial force between the stator and the rotor [12, 13]. In RFM there is no resulting radial force between the

rotor and the stator due to the compensation of all local radial forces. In case of an AFM, all local axial forces between magnets and the stator are added. For large machines, the resulting axial force can reach thousands of Newton[13] and could lead to mechanical difficulties, especially for the bearing [14].

1.1.1.1.2 Examples of single air gap axial-flux machines

The axial force between the stator and the rotor can be used during the construction of the machine to place the rotor with high precision. The patent [13] presents a method to determine the length of the air gap by measuring this force. Its dependence in function of the air gap is very sensitive and can easily be calculated. So the measurement of this force enables an accurate determination of the air gap length. The patent [15] shows a special configuration of the magnets where each magnetic pole is built with a plurality of magnets. [16] presents first design method to start the dimensioning of this type of machine.

1.1.1.2 Internal stator axial-flux machines

1.1.1.2.1 Presentation and magnetic circuit

1.1.1.2.1.1 Internal stator AFM with stator back iron

An Internal Stator Axial-Flux (AFIS) machine is composed of one stator and two rotors. Its magnetic circuit at no load is shown in figure 1.4.

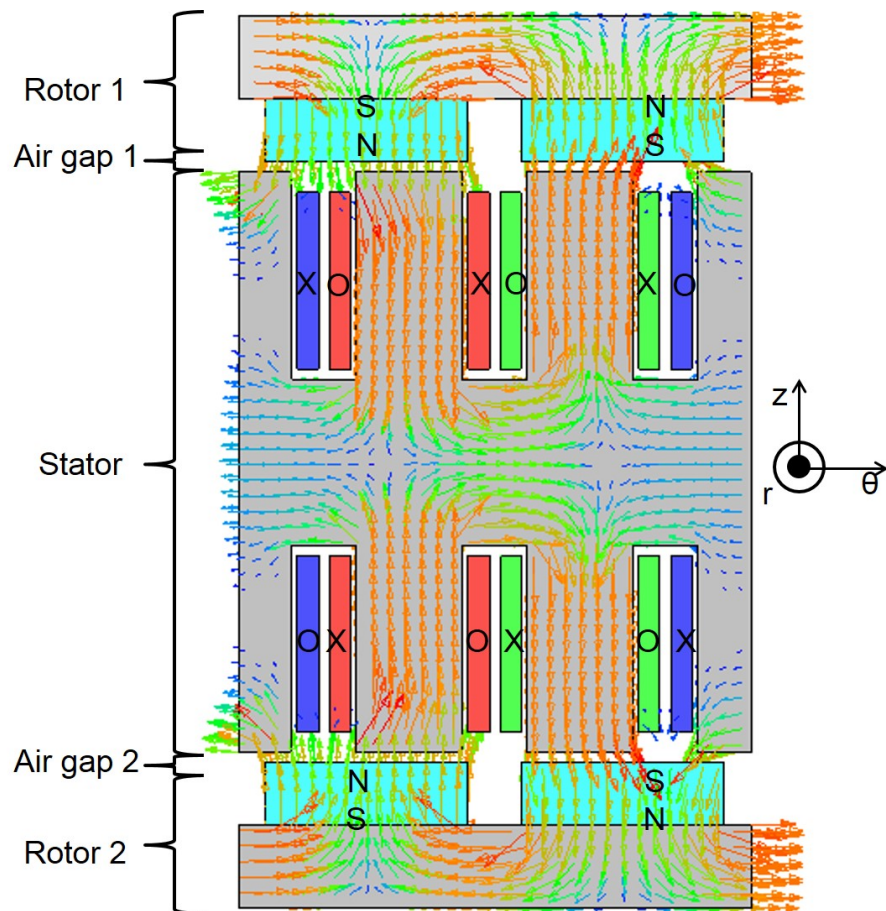


FIGURE 1.4: Magnetic circuit a double air gap internal stator AFM ($I = 0$)

Magnetic flux lines flow from one rotor to the stator and flows back to the same rotor. A magnetic back iron is necessary in each rotor. In this configuration, another magnetic core is necessary in the stator. Stator windings can be wound around the stator teeth or around the magnetic core. This last type of AFIS machine is called TORUS (Toroidally wound internal stator) and is presented in figure 1.5.

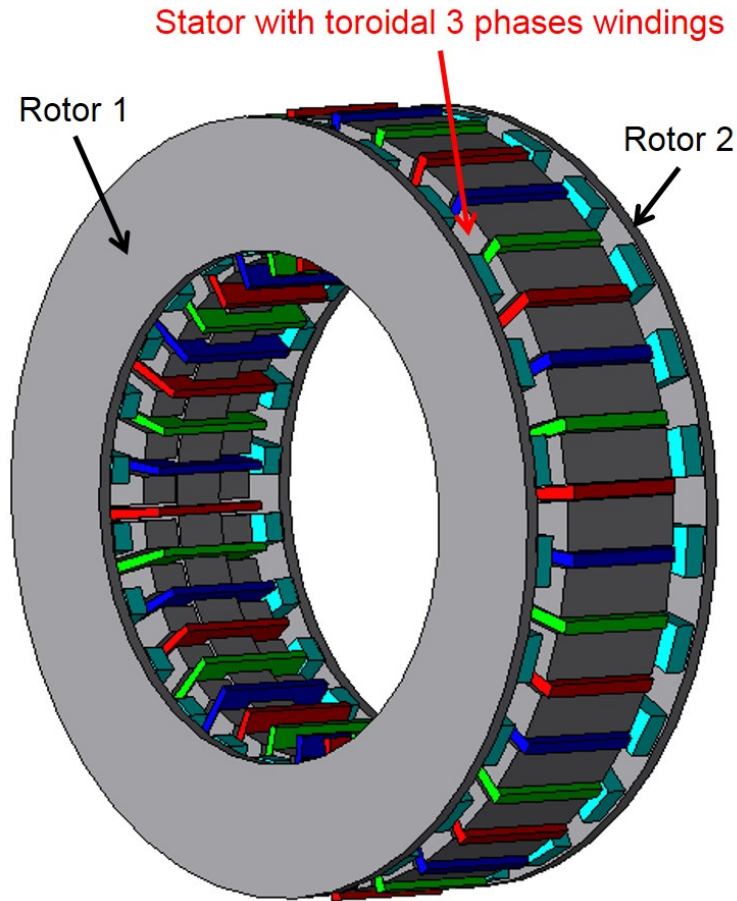


FIGURE 1.5: TORUS axial-flux machine

This TORUS topology is state of the art in the literature. Slotted or non-slotted topologies are possible and compared in [17, 18]. The slotted topology shows a higher torque density and efficiency than the non-slotted topology. Due to the teeth in the stator, the slotted topology presents a cogging torque and a higher torque ripple than the non-slotted topology. The skewing of the magnets could reduce it. In [19] a 70Nm/30kW TORUS machine is designed and studied. The patent [20] shows an example of TORUS machine where the stator is composed of a plurality of parts fixed together. In [21] iron segments are inserted on the teeth of a TORUS machine to modulate the magnetic flux in the air gap.

1.1.1.2.1.2 Internal stator AFM without stator back iron

The stator magnetic back iron is not essential for AFIS machines and can be removed with an adaptation of the magnetic circuit. Figure 1.6 shows the magnetic circuit at no load of this type of machine.

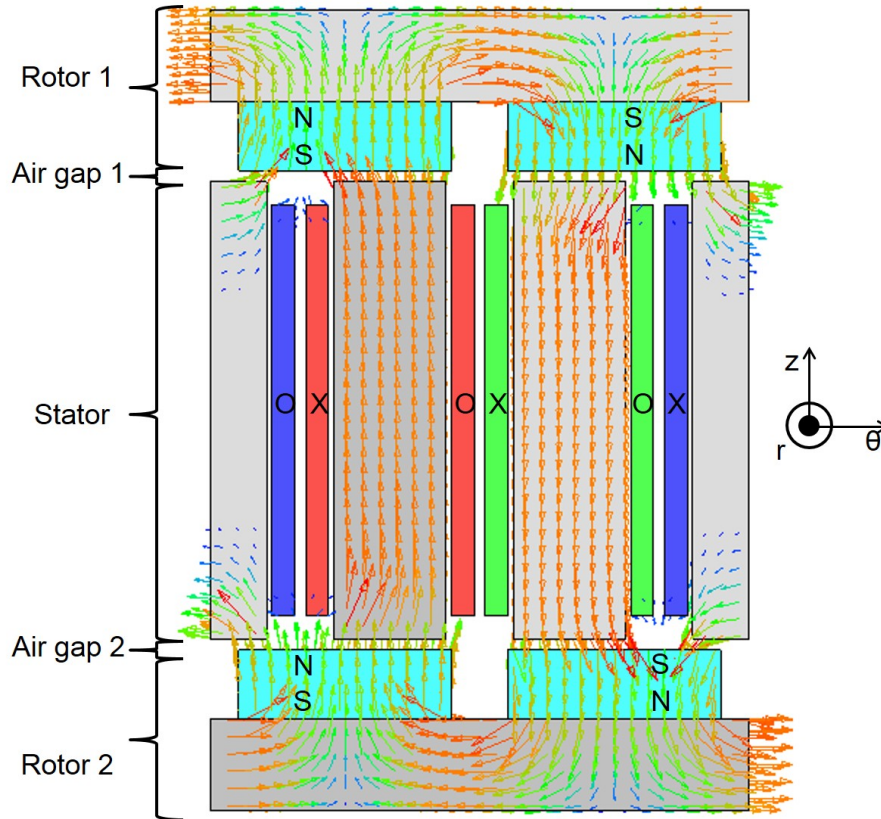


FIGURE 1.6: Magnetic circuit an AFIS machine without back iron ($I = 0$)

In that case, magnetic flux lines flow only axially in the stator teeth. Each field line flows in both rotors. The stator can thus be built with independent teeth without any magnetic core between them. This configuration reduces the axial length of AFIS and the iron losses of the machine. However, if the stator is only composed of independent teeth, it is harder to fix them to each other, making the mechanical construction of the stator harder. A solution by fixing each tooth on an inside shaft is proposed in [22].

The YASA (Yokeless And Segmented Armature) topology is one the most common topology of AFIS machine without magnetic back iron in the stator. The stator of the machine is built with independent teeth. Teeth are built with stator shoes which overlap the radial coil end winding to increase the torque density and reduce copper losses.

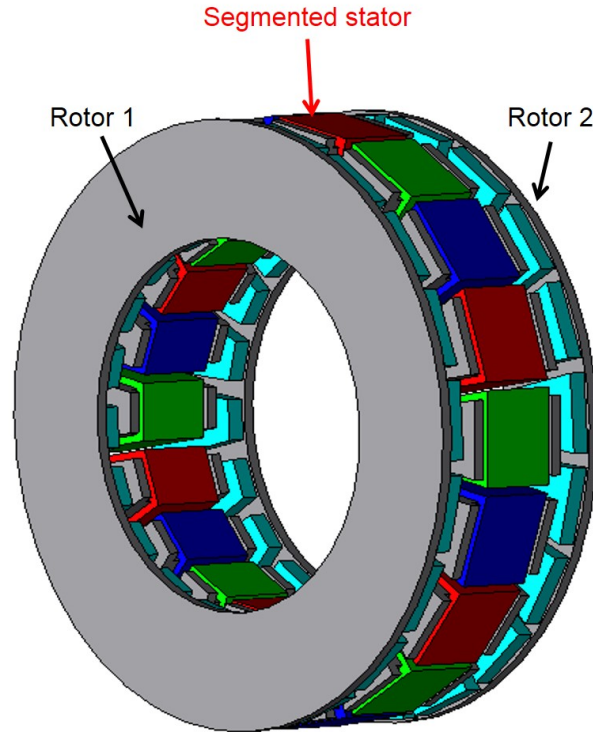


FIGURE 1.7: YASA axial-flux machine

The YASA topology has been studied in [14, 23]. The axial coil end winding can be hidden by the stator shoes to reduce the radial space loss due to coil end winding. Reduced coil end winding and the absence of magnetic back iron in the stator increase the efficiency of the machine. The YASA topology offers higher torque density and shorter axial length than other AFIS [23]. In [24] a 10 poles/12 teeth YASA machine for automotive in wheel application is designed. Contrary to [14] the stator is built with radially laminated steel and not in soft magnetic composite. Magnetic materials for AFM are compared in section 2.4.5.

1.1.1.2.1.3 Ironless internal stator AFM

AFIS machines offer also the possibility to build ironless machines. In this case, the stator is only composed of copper windings (figure 1.8). The electromagnetic torque is produced by the Lorentz force. These machines have no iron and less no load losses. The absence of cogging torque and a shorter axial length are other advantages. However due to the large magnetic air gap between the two rotors the air gap magnetic flux density is low. For this reason these machines are often limited to low power applications, like reader heads in hard disk drives. An ironless AFIS machine has been designed in [25]. To save axial space and reduce the magnetic loss, a special arrangement of the coils has been developed for this application. The copper fill factor of the machine is above 90%.

This good result enables the reduction of the axial length of the winding and also the magnetic air gap between the two rotors. But the isolation between the electric phases is complex and has currently not been adapted to high voltage applications. The small magnetic flux density and the high copper losses, due to induced currents in the winding, reduce the efficiency of the machine. Another ironless AFIS machine is presented in [26]. The stator is not composed of windings but a printed circuit board. A sophisticated arrangement of the phases on both sides of the PCB ensure the isolation and a short axial length. Another coreless AFIS machine is shown in [27].

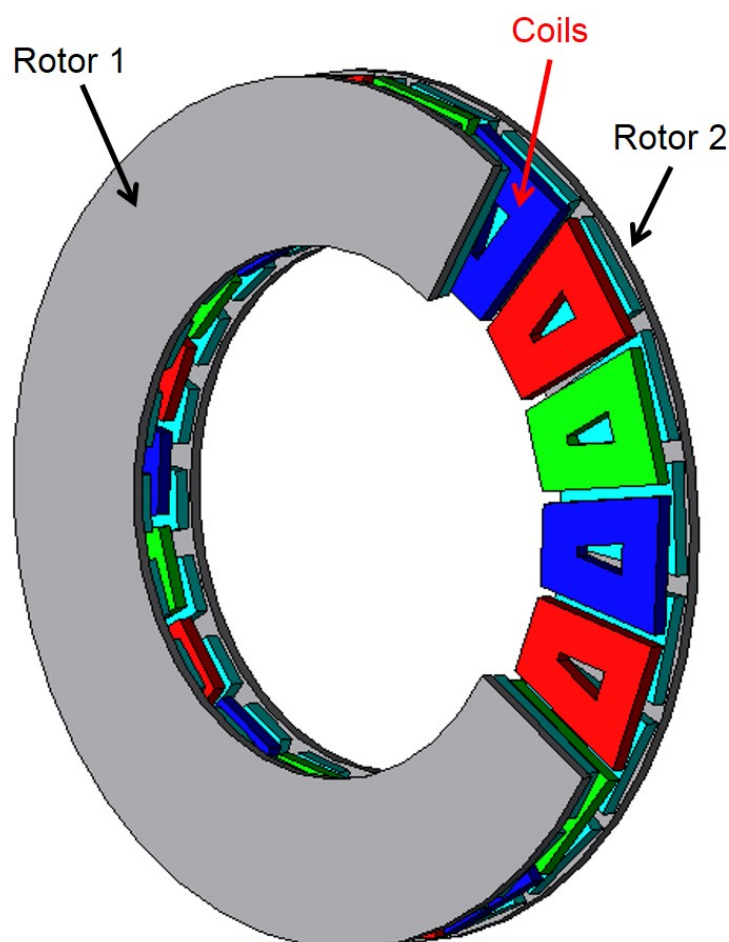


FIGURE 1.8: Ironless AFIS machine

Regarding to the single air gap machine, the problematic of axial forces in the AFIS machine is different. The stator is sandwiched between two rotors. If the machine is symmetrically built, it should not be submitted to any resulting axial force but each rotor is submitted to an axial attracting force. This force pulls the magnets which have to be fixed. In [28] magnets are fixed with a hook in the rotor and the cutting of two edges of the magnets. A global axial force acts on the rotor resulting in a bending constraint on them. Another way to fix the magnets with retention means on the rotor

is presented in [29]. In this patent, the magnets are inserted into pockets and held therein.

1.1.1.2.2 Examples of ironless internal stator AFM

YASA motors already sells a broad range of YASA machines. From 250 Nm to 900 Nm these machines are well suited for different applications including electric traction [30]. Thanks to the YASA topology, these machines enable high torque and power in small space and with light weight. For example YASA 750 achieves a torque density of 24Nm/kg. Due to efficient oil cooling, the maximum continuous power of the machine is over 75kW [31].

The machine presented in [32] shows a special configuration of a TORUS machine capable of field control. In this machine, permanent-magnets are arranged in two radial rows. On one rotor, the outside row is alternately composed of north pole magnets and iron teeth. The inside row is composed of south pole magnets and iron teeth. Magnetic polarity are inverted in the second rotor. The stator is composed of two parts radially separated by a DC field winding. This winding helps to reduce or increase the magnetic flux outgoing from the magnets thanks to the rotor magnetic teeth. Field weakening or improved torque are possible with this configuration. This machine appears as a hybrid between a permanent-magnet machine and a current-excited machine.

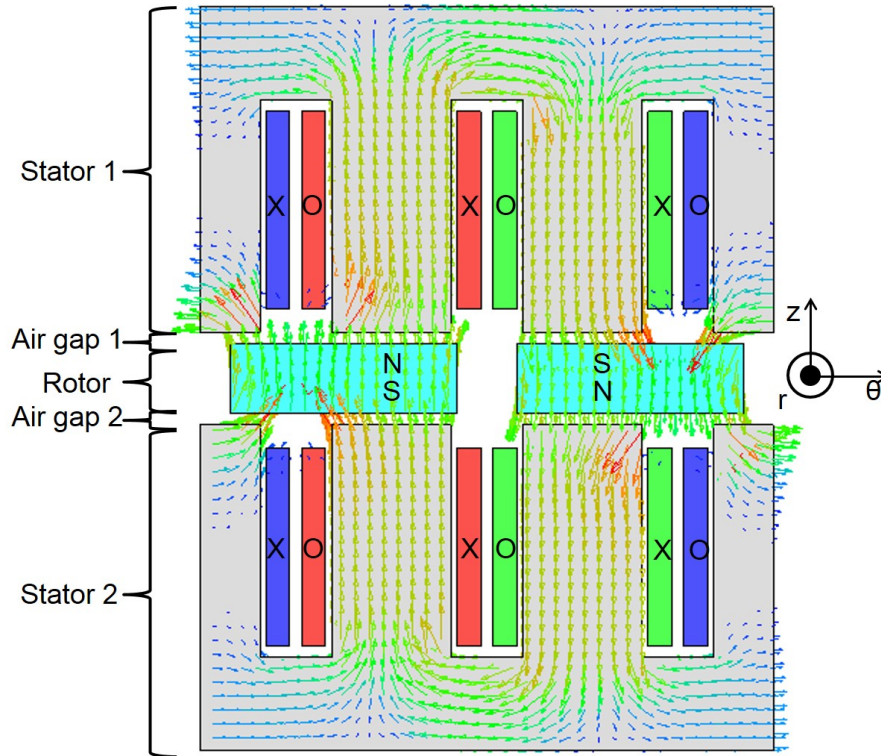
[33] presents an AFIS machine with variable air gap. In this machine, the air gap decreases in the radial direction. It reduces saturation effects in the stator and avoid radial components of the magnetic flux in them. In case of a radially segmented stator built in steel sheet, this flux generates high eddy current losses. The efficiency of the machine can be improved by increasing the maximum torque and reducing the stator losses.

Other niche application fields are possible for AFIS machines. [34] presents an AFIS micromotor with the particularity that only one rotor is implemented with magnets. The second rotor is only used as magnetic back iron. In [35] superconducting field coils are used for the stator windings.

1.1.1.3 Internal rotor axial-flux machines

1.1.1.3.1 Presentation and magnetic circuit

The Axial-Flux Internal Rotor (AFIR) machine is composed of one rotor sandwiched between two stators. The magnetic circuit at no load of this topology is shown in figure 1.9.

FIGURE 1.9: Magnetic circuit a double air gap internal rotor AFM ($I = 0$)

The magnetic flux lines flow axially through the rotor and the stator teeth and tangentially between the teeth in the stator back iron. Both stators of the AFIR machine need a magnetic back iron, but the rotor is built up without. Some AFIR machines like [36] use a magnetic material in the rotor, but the majority of AFIR are built without it to save axial length and reduce rotor losses. The rotor of the AFIR machine does not need any magnetic property and could, for example, be built in reinforced plastic to save rotor losses and weight [12, 37].

Regarding axial forces, the problematic is reversed. In case of a proper construction, the rotor is not submitted to any axial force. An axial force on the rotor can occur if it is not precisely centered between the stators. An axial force already occurs on both stators. This force has to be taken into account for the mechanical construction of the machine but is easier to handle compared to the axial force on the rotors of the AFIS or single air gap machine [12].

The AFIR machine gives already the possibility to shift the teeth of both stators (figure 1.10). This shifting can be useful to reduce the cogging torque of the machine or the no load losses in the permanent-magnets by reducing the magnetic flux density variation in them. In the case of shifted teeth, the magnets can be submitted to an axial alternating force. The problematic of axial forces on magnets is shown in [38] and a solution by

adjusting the shape of the magnets is proposed. Depending on the configuration of the stator, it could appear a resulting axial force on the rotor.

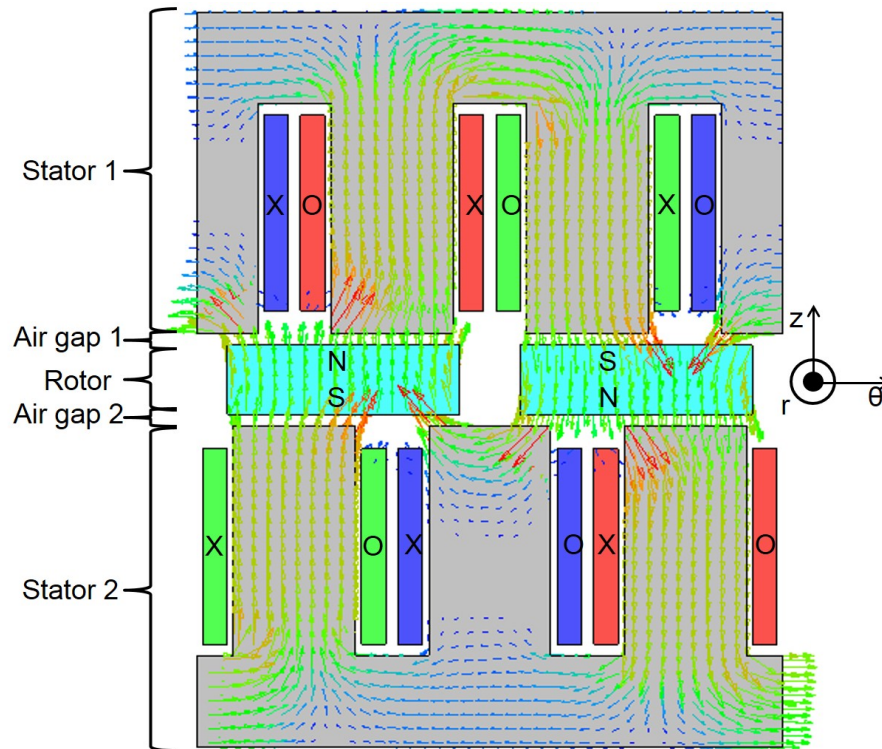


FIGURE 1.10: Magnetic circuit a double air gap internal rotor AFM (shifted teeth, $I = 0$)

In [39], a machine with two different air gap lengths has been designed. Thanks to electric switches, it is possible to enable or stop the current supply of one stator. At small rotational speeds, the maximum torque is achieved by supplying both stator windings. At high rotational speeds, the back-emf of the machine is reduced to avoid the necessity of field weakening (see appendix A). This patent shows another degree of freedom for the AFIR machine: the electric connection of the both stators is arbitrary. They can be connected in series or in parallel. The parallel connection enables an easier construction of both stator which can be identical. The current flowing in each stator is only the half of the global phase current, so the winding section can be proportionally reduced. The series connection ensure that both current flowing in each stator are identical and avoid the risk of circular currents.

1.1.1.3.2 Examples of internal rotor axial-flux machines

In the literature, some examples of AFIR machines can be found with unusual configurations. In [36] a special configuration of the rotor is proposed. Magnets are axially split and magnetically linked with an internal rotor core. In this configuration magnets are

submitted to axial forces. Two cover plates are disposed in front of each air gap to fix them. They need to be built of a non electric conducting material to avoid eddy current losses.

In [40] magnets are tangentially magnetized. Additional magnets are positioned on the outside and inside radius and radially magnetized to increase the exciting magnetic flux of the rotor. Another configuration is shown in [41]. Magnets are here disposed in two rows of magnets in a similar configuration as in [32].

In [42] an alternative construction of the winding is proposed. Both stator windings are built as one part surrounding the rotor. The stators can then be fixed on these windings. [43] proposes a method to ensure the axial position of the disc rotor with high precision.

1.1.1.4 Multidisc axial-flux machines

Multidisc axial-flux machines are machines with three or more air gaps. These machines can be divided in two families:

- Multidisc machines with one magnetic circuit
- Axial stacked up of several machines

Multidisc machines with one magnetic circuits are machines which are particularly designed as a single machine. [41] shows a triple-rotor double-stator machine. This topology is a summary of other configurations. Both outside rotors are submitted to an axial force like in the AFIS machine. The central rotor is similar to the rotor of a AFIR machine. Multidisc machines are suitable for ironless machines. Thanks to a higher number of rotor discs, and also of magnets in the magnetic circuit, the distance between two rotors can be reduced and the air gap magnetic flux density is increased [25]. In case of multiphase high-voltages applications, each phase can be separated in its own stator to increase the reliability regarding phase isolation.

The second family of multidisc rotors are machines which are built from several AFIS or AFIR machines. In that case, single machines are stacked up to increase the torque and maximum power of the machine if the available space or mechanical constraints do not allow to built them as a single machine with a larger diameter [5, 14]. Radial-flux machines are continuously scalable by increasing the axial length. In the case of AFM, this scalability is only discrete [12].

1.1.2 Other axial-flux machines technologies

AFM are not limited to permanent-magnet machines. In 1.1.1.2 and 1.1.1.3 the electric excited permanent-magnet machine presented in [32] has been mentioned. In [44] an example of switch reluctance AFIR machine is shown. The rotor is built with a magnetic conducting material. Both stators are carrying teeth which are tangentially shifted. This machine is a six phases machine and needs a specific converter. Some other examples can be found in [45–49]. [48] has the particularity to be a three-disc machine. In [49] a TORUS topology is proposed. To reduce the torque ripple the teeth of both rotors are shifted. This solution enables a reduction of the ripple over 50% with a torque reduction lower than 4%. But this shift in stator teeth results in unbalanced axial forces on the rotors and a resulting axial force on the stator which have to be mechanically handled.

Axial-flux induction machines are also possible. Theory and sizing equations have been studied in [50]. In [51] a 45 kW single air gap machine has been designed. The use of an aluminum cage reduces the costs of this machine but increases the rotor losses compared to a copper cage. Like for radial-flux machines, this machine is quite sensitive to the air gap. Increasing it reduces the harmonics of the air gap flux density. This is helpful to reduce the rotor losses and iron losses at high rotational speed. But at low rotational speed, the efficiency is better with a small air gap due to smaller winding losses. A method to build the rotor of a single air gap machine is proposed in [52]. A combination of SMC in the stator and steel lamination is used in [53]. The Australian company Evans Electric has developed induction axial-flux machines for electric car as in wheel motors. This motors delivers 625 Nm and a peak power of 75 kW in a AFIR configuration. This machine has the particularity that the stators cover only a part of the machine and not the complete disc. This enables a better air cooling of the machine but reduces the performance. This concept has been patented in [54] and reported in [55].

DC axial-flux machines are possible but more rare. Some examples can be found in [56] or [57].

1.1.3 Applications of axial-flux machines

Axial-flux machines are used in some specific applications. Without being exhaustive, this section will list some of them with focus on automotive applications.

1.1.3.1 Automotive applications

The research on integration of AFM in automotive is intensive. The state of the art has shown a large number of publications and patents on this topic. But today, there is no product on the market with an AFM for automotive applications.

Thanks to a high torque density and a good efficiency, the YASA topology is a good candidate for automotive applications. In [14], an axial-flux machine with YASA topology is designed in cooperation with Volvo Technology. This machine is suited for an application in an hybrid car to reduce the fuel consumption and increase the reliability of the car, especially by cold temperatures. The machine in [23] has been designed as part of the project LIFEcar which was aimed to produce the first hydrogen sport car. The Drayson B12/69 EV is a Le Mans prototype, designed to be the fastest electric racing car in the world. With a total power above 640 kW, the top speed of the car is above 320 km.h⁻¹ and it can reach 100 km.h⁻¹ in 3 seconds. The car integrates four YASA machines independently controlled by four inverters. The battery has a capacity of 30 kWh [58].

Volvo is not the only car manufacturer working on axial-flux machines. Nissan has developed a high torque AFIS machine for hybrid cars. This machine achieves more than 500 Nm in an outside diameter of 280 mm and an axial length of 82 mm. Thanks to a 9-phase configuration, the peak power is above 135 kW with a battery voltage of 300 V. With a peak efficiency above 96 % and a combination of water and oil cooling, the continuous power of the machine is 100 kW [28]. In 2014, Renault has developed the EOLAB prototype. This plug-in hybrid demonstrator has been presented at the Paris Motor Show and integrates nearly 100 technological innovations. As part of them, a permanent-magnet AFM developing 200 Nm and 50 kW is integrated to the traction shaft. This enables the prototype to achieve a very low fuel consumption (1 L/100km in the NEDC cycle) [59]. Renault has already patented a gearbox combined with an AFM in [60]. General Motors has published patents over AFM for hybrid applications as in-wheel motor [61]. Another axial-flux machine as in-wheel motor are also presented in [24].

A car demonstrator using an EVO electric AFM as range extender combined to a 2-cylinder combustion engine has been built by Mahle [12]. Other AFM constructors like YASA[62], Ashwood[63, 64], Axiflux[65] or Evans[55] are involved in the automotive market.

Small axial-flux machines could be used for electric scooters like in [66]. The short axial length and large diameter of an AFM is here an advantage. Other possible applications of AFM for automotive can be found in the patents [57, 67–69].

1.1.3.2 Other applications fields

The automotive market is not the only area for axial-flux machines. Other application fields are already supplied with AFM. In the 1990s, the Finnish lift supplier Kone started to build lifts with axial-flux machines. Thanks to the axial-flux design, the weight of the machine has been reduced and the Kone ecodisc enables the construction of a lift without machine room as well as a huge reduction of the construction cost and energy need [70]. The Kone ecodisc is a permanent-magnet single air gap machine. Light weight, high torque for huge diameter and short axial length make AFM well suited for wind generators. Application for low power wind generators are presented in [71, 72]. [73, 74] present a 7-phase design of an AFM for wind generators and an adapted controlling strategy. Additionally patents for low and high power wind generators can be found [75, 76].

1.2 Other disc rotor electric machines

1.2.1 Transverse-flux machines

Alongside axial-flux machines, disc rotor electric machines can be built as Transverse-Flux Machines (TFM). Disc rotor TFM are presented in [2, 3]. Their construction is similar to AFIR machines including one rotor sandwiched between two stators. But, contrary to radial or axial-flux machines, the stator winding is composed of one (or several) ring coil(s) wound around the rotational axis. The stator core is composed of two rows of teeth radially and alternately disposed over and under the ring coil and connected with a back iron. In figure 1.11 a single-phase stator of a disc rotor TFM is represented. In this example, the coil is built as a copper pipe. A cooling liquid can flow through the pipe and directly cool the machine inside of the winding. This direct cooling solution minimizes the thermal resistance between the losses generation in the conductor and the cooling liquid. This leads to an optimized cooling.

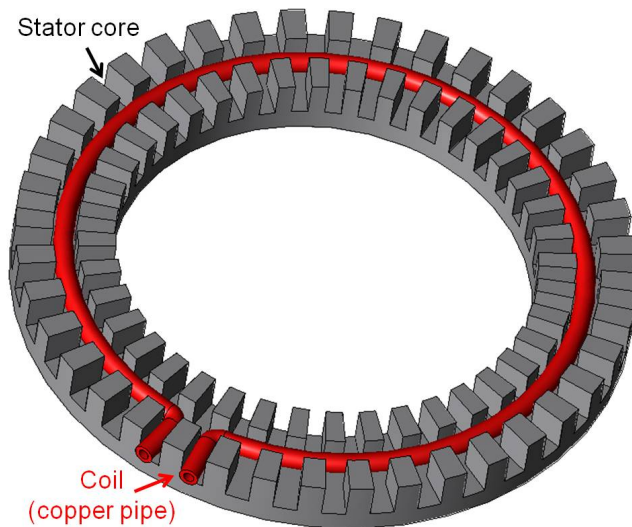


FIGURE 1.11: Stator for disc rotor transverse-flux machine

The rotor of a disc rotor TFM is similar to the rotor of an AFIS machine. The main difference, is that magnets are not magnetized in the axial direction, but tangentially [2]. In this configuration, the number of magnets should be as high as possible to increase the magnetic flux. The consequence of this high number of magnets is a high number of poles and a higher electric frequency.

Another characteristic of TFM, is that the magnetic flux of a multiphase TFM is not turning synchronously with the rotor like in AFM or RFM, but pulsating due to the magnetic isolation between the phases. In the case of a cylindrical TFM, independent magnetic circuits for each phase can be built in length [77], but for disc rotor machines

the mechanical construction with several rotors is more complex. In [78] a two-phase construction is proposed. The machine is tangentially divided in four parts. Each phase occupies two opposed segments. Due to the coil end winding, there is a loss of space between two neighboring phases. Another way to build multiphase TFM is to divide the machine in the radial direction. A first phase is built on the outside radius and the second one is built on an inside radius [4]. This construction is not symmetric and could lead to unbalanced induced voltages. A higher torque ripple can also occur. In each of these examples, the complexity of the building of multiphase disc rotors TFM has led to designs with only two electric phases which are not compatible with classical three-phase inverters.

To improve the torque of the machine or reduce the use of permanent-magnets, magnetic flux conductors can be disposed between the magnets [4, 79]. Thanks to this construction, the magnetic field density in the air gap is increased. But this makes the construction of the rotor very complex: mechanical tolerances are added. It leads to problems to insert the last part (remaining air gap or insufficient available space) or irregularity in the space between two magnets. Furthermore, electromagnetic losses (hysteresis and eddy current) are generated in the flux conductors and the mechanical stability is worse.

1.2.2 Combination of axial-flux and other technologies

To increase the performance of an electric machine, it can be useful to combine several technologies. In the literature some examples of machines combining axial-flux and another technologies can be found. For example, in [80] machines combining axial-flux AFIR or AFIS machines with radial-flux inside and outside rotors are presented. In the patent [81] a single air gap disc rotor machine is presented. In this machine, the winding is composed of a ring coil like in disc rotor TFM and two rows of teeth over and under the coil. These teeth are overlapping the coil to increase the magnetic field density. In that way, the magnetic field flows axially through the air gap. The patent [82] presents an alternative disc rotor AFM. The rotor is similar to an AFIR machine, but there is only one stator. The stator is built with a plurality of arcs placed around the rotor in the radial direction. Windings are wound around these arcs. The magnetic flux flows axially in the air gap, and uses the arc as back iron. [83] proposes another AFM where the magnetic flux flows axially in the air gap and uses a radial back iron. But in this machine, the stator is built in one part and supports ring coils. In [22] an AFIS machine with a similar topology to YASA is proposed. In addition to the magnets disposed on both rotors and generating an axial magnetic flux, two other rows of magnets are radially disposed on the rotor shaft.

Conclusion

In this chapter, the state of the art of disc-rotor electric machines has been presented. Axial-flux machines, especially permanent-magnet machines are the most common disc rotor electric machines. The following topologies have been presented:

- Single air gap axial-flux machines
- Internal stator axial-flux machines
- Internal rotor axial-flux machines
- Multidisc axial-flux machines
- Disc rotor transverse-flux machines
- Combination of several technologies

For each of these topologies, the advantages, disadvantages and applications have been presented. In the next chapter, these topologies are compared and the best suited for an integrated motor generator is selected.

Chapter 2

Electromagnetic design

Contents

Introduction	28
2.1 Requirements	28
2.2 Constraints on electric parameters	32
2.2.1 Induced voltage	32
2.2.2 Power factor and short circuit current	33
2.3 Selection of a topology	35
2.3.1 Selection of suitable technologies for automotive applications	35
2.3.1.1 Transverse-flux machines	35
2.3.1.2 Axial-flux machines	38
2.3.2 Comparison of suitable topologies	39
2.3.2.1 Evaluation of selected topologies	39
2.3.2.2 Discussion and selection of suitable topology	41
2.4 Design	43
2.4.1 Winding technology	44
2.4.2 Electric connection	45
2.4.3 Teeth alignment	46
2.4.4 Permanent-magnets	49
2.4.5 Magnetic material	50
2.4.5.1 Soft magnetic composite	50
2.4.5.2 Steel lamination	52
2.4.5.3 Selection of the magnetic material	52
Conclusion	54

Introduction

In this chapter, the electromagnetic design is defined. At first, the requirements and the objectives of the work are presented. Secondly, the constraints on the electric parameters are highlighted. In a third step the topologies of disc rotor electric machines presented in the previous chapter are compared and the internal rotor axial-flux machine is selected. Finally, the most important parameters of the electromagnetic designed are defined.

2.1 Requirements

The requirements on the axial-flux machine have been obtained from realistic specifications or characteristic of PHEV (Plug-in Hybrid Electric Vehicle). Table 2.1 presents main performance and available space specifications. Torque and power values are mechanical data.

Parameter	Description	Specification
D_{out}	Max. outside diameter	282 mm
D_{in}	Min. inside diameter	182 mm
L_{max}	Max. axial length	80 mm
U_{bat}	Battery voltage	300 Vdc
I_{max}	Max. phase current (10 s)	420 Arms
I_{cont}	Max. phase current (continuous)	235 Arms
I_{scmax}	Max. short circuit current	350 Arms
T_{peak}	Peak torque (10s)	330 Nm
P_{peak}	Peak power (10s)	80 kW
T_{cont}	Continuous torque	170 Nm
P_{cont}	Continuous power	60 kW
n_{max}	Max. rotational speed	7000 rpm

TABLE 2.1: Specifications

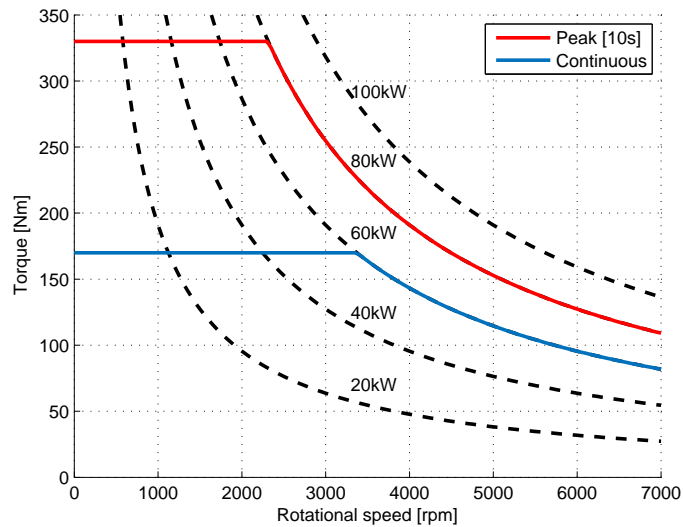


FIGURE 2.1: Peak and continuous performances specifications

The required peak and continuous torque characteristics are represented in figure 2.1. The thermal performances of the designed machine will not be evaluated in this PhD. It will only be checked, that the required continuous performances are achievable with the maximum continuous current. Losses, especially critical rotor losses, will be minimized during the dimensioning in order to enable high continuous performances. Beside these objectives some other points have to be taken into account:

- Demagnetization safety: NdFeB magnets are very sensitive to the temperature. At high temperature, the coercivity of these magnets decreases making a demagnetization possible. Furthermore, in case of default, PMSM machines are often short circuited. By short circuiting a PMSM, a high transient current occurs. This current can be much higher than the maximum phase current of the machine and threaten the magnets of demagnetization, especially if they are hot. For this application, it has been specified, that the magnet should not be demagnetized at a temperature of 150 °C and for a maximum current of $2\sqrt{2}I_{sc}$ [84], where I_{sc} is the RMS value of the short circuit current at 150 °C.
- Torque ripple: the torque ripple (especially the cogging torque) must be minimized. A too high torque ripple can present a mechanical risk and reduce the lifetime of the traction shaft and generate noise.
- The inverter constant k_{wr} : the inverter constant k_{wr} is the ratio between the RMS value of the maximum phase voltage and the battery voltage. In case of a sinusoidal output voltage: $k_{wr} \leq \frac{1}{\sqrt{6}} \approx 0.41$. Some particular controlling strategies can increase this value by injecting a third harmonic component in the output

voltage [85]. In practice, a safety margin needs to be applied and this value can not be achieved. In this work, an inverter ratio of $k_{wr}=0.37$ is assumed, so the maximum phase voltage is $V_{max} = k_{wr} \cdot U_{bat} = 111V_{rms}$.

- Maximum induced voltage: the maximum induced voltage is another important parameter of an electric machine. A too high induced voltage can create safety problems and forbid no load operation at high rotational speed. But a minimum voltage constant is necessary to achieve the required torque (see 2.2.1). To minimize the induced voltage while achieving the required peak torque, the machine has to be designed to reduce saturation effects.
- Efficiency: the efficiency of the machine should of course be maximized. In the practice, it is not possible to increase the efficiency in every operating point. The distribution of the operating points of the machine over its lifetime is represented in figure 2.2.

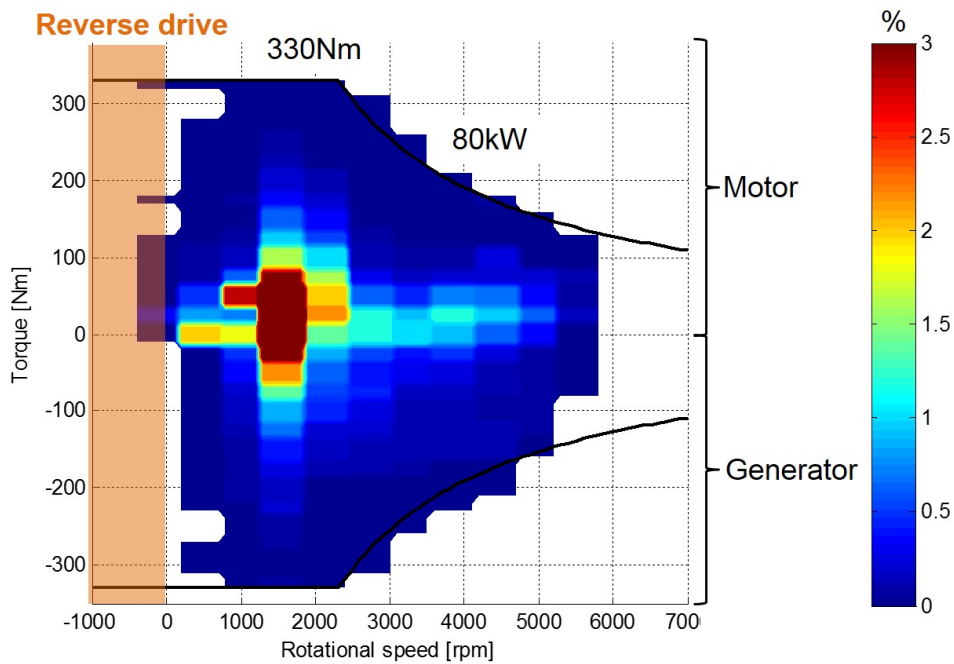


FIGURE 2.2: Distribution of the operating points an electrical machine for PHEV application [%]

This distribution has been obtained via the analysis of driving cycles. Red and orange operating points are more often driven than blue one. Positive torques correspond to motor operating points. Negative rotational speeds are reverse drive operating points. Figure 2.3 shows the distribution of the operating points depending on the rotational speed. The electric machine is mainly (80%) driven under 2500 rpm and very rarely

over 5000 rpm. For this reason, the efficiency of the machine should be optimized for low speed operating points.

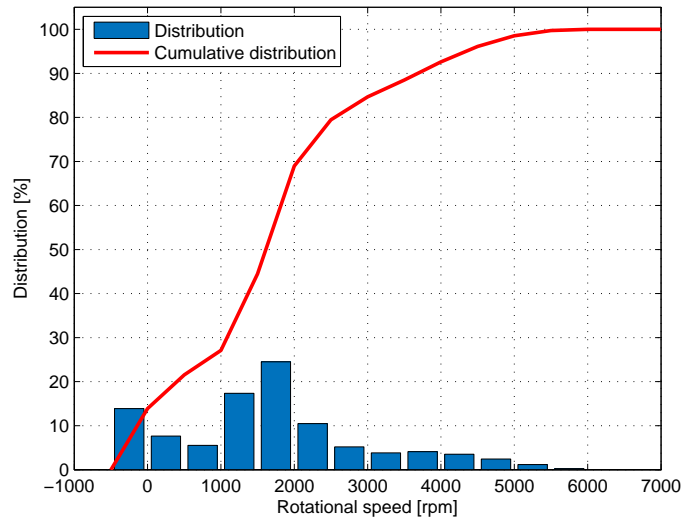


FIGURE 2.3: Distribution of the rotational speed of an electrical machine for PHEV application [%]

In this driving cycle the machine is more used in the motor operating points than in the generator operating points. This is a particularity of PHEV vehicles which are assumed to be used in pure electric drive. The average consumed power by the car is 2.19 kW.

2.2 Constraints on electric parameters

The equivalent circuit of a PMSM (Permanent-Magnet Synchronous Machine) is presented in appendix A. The induced voltage and the inductance have an influence on the maximum torque and the maximum output power of the machine. To achieve the specifications, these parameters are not free and need to meet specific values.

2.2.1 Induced voltage

The RMS value of the fundamental of induced voltage E_{1rms} of an electric machine is defined as (see appendix A) :

$$\begin{aligned} E_{1rms} &= k_E \omega_e \\ &= \frac{\Psi_{PM}}{\sqrt{2}} \omega_e \end{aligned} \tag{2.1}$$

where k_E is the armature constant of the machine in V.s, $\omega_e = n_p \omega_m$ is the electric pulsation in rad.s^{-1} , n the rotational speed in rpm, n_p the number of pole pairs and Ψ_{PM} the amplitude of the fundamental of magnetic flux generated by the magnets. The electromagnetic torque T_{em} of a PMSM without saliency can be calculated with equation 2.2.

$$\begin{aligned} T_{em} &= \sqrt{\frac{3}{2}} n_p \Psi_{PM} I_q \\ &= n_p k_E \sqrt{3} I_q \end{aligned} \tag{2.2}$$

The mechanical torque T delivered by the machine is always smaller than the electromagnetic torque defined in 2.2 due to the electromagnetic losses (iron and magnet losses) which have to be subtracted. For a machine without saliency the torque is maximized if I_q is maximized: $I_q = \sqrt{3} I_{max}$ where I_{max} is the RMS value of the maximum allowed phase current. Considering a perfect machine, it is possible to evaluate the minimum armature voltage necessary to achieve the required torque $T_{peak_{spec}}$ with the maximum phase current:

$$\begin{aligned}
T_{peak_{spec}} &\leq 3n_p k_E I_{max} \\
k_E n_p &\geq \frac{T_{peak_{spec}}}{3I_{max}} \\
k_E n_p &\geq \frac{330}{3 \cdot 420} \\
k_E n_p &\geq 0.262 V.s \\
E_{rms} &\geq 0.262 \cdot \frac{\pi}{30} n \\
E_{rms} &\geq 192 V_{rms@7000rpm}
\end{aligned} \tag{2.3}$$

Due to the saturation in the magnetic material at high phase current and the electromagnetic losses, this minimum value is not sufficient to achieve the required maximum torque. To reduce this oversizing, the saturation and the magnetic losses have to be minimized.

2.2.2 Power factor and short circuit current

The peak power of a PMSM supplied by an inverter strongly depends on its power factor and its short circuit current. The mechanical power P_m delivered by the machine is:

$$\begin{aligned}
P_m &= \eta P_{el} \\
&= \eta S_{el} P_F
\end{aligned} \tag{2.4}$$

Where P_{el} and S_{el} are the electric real and apparent power delivered by the inverter, η is the efficiency of the machine and P_F is its power factor. The electric power is limited by the maximum phase current I_{max} , the inverter ratio k_{wr} and the battery voltage U_{bat} :

$$\begin{aligned}
P_m &\leq 3\eta I_{max} k_{wr} U_{bat} P_F \\
P_F \cdot \eta &\geq \frac{P_m}{3I_{max} k_{wr} U_{bat}} \\
&\geq \frac{80000}{3 \cdot 420 \cdot 0.37 \cdot 300} \\
&\geq 0.572
\end{aligned} \tag{2.5}$$

To achieve the specified maximum power, the power factor needs to be greater than 0.57 considering a perfect machine ($\eta = 1$). With an efficiency of 90%, the power factor needs

to be greater than 0.64. 57.2% is already the minimum required efficiency to achieve the peak power is the power factor is equal to 1. At high rotational speed, the phase current decreases and approaches the short circuit current I_{sc} (see appendix A). At this operating point, the power factor is close to 1. Equation 2.5 becomes:

$$\begin{aligned} P_m &\leq 3\eta I_{sc} k_{wr} U_{bat} \\ I_{sc} \cdot \eta &\geq \frac{P_m}{3k_{wr} U_{bat}} \\ &\geq \frac{80000}{3 \cdot 0.37 \cdot 300} \\ &\geq 240.2 \end{aligned} \tag{2.6}$$

In the case of a perfect machine ($\eta = 1$), the short circuit current needs to be greater than 240.2 Arms. With an efficiency of 90%, the short circuit current needs to be greater than 266.9 Arms. If the short circuit current is too high, the inductance is very small and the machine needs more field-weakening increasing copper losses and worsen the efficiency at high rotational speed. An optimum design meets the minimum required short circuit current. In this application, the short circuit current is greater than the maximum allowed continuous current, so the short circuit safety can only be ensured with a thermal oversizing.

2.3 Selection of a topology

2.3.1 Selection of suitable technologies for automotive applications

2.3.1.1 Transverse-flux machines

The transverse-flux machine (TFM) has been presented in 1.2.1. This machine has 2 electric phases and is not compatible with standard inverters. In the first months of the PhD alternative designs have been published:

- Alternative teeth geometries to improve the magnetic properties [86]
- Overlapping of the teeth over the conductor to increase the torque density [87]
- Three-phase TFM with a concentrically distribution of the phases [88]

Figure 2.4 presents a three-phase TFM where the electric phases are placed concentrically based on the design presented in [88].

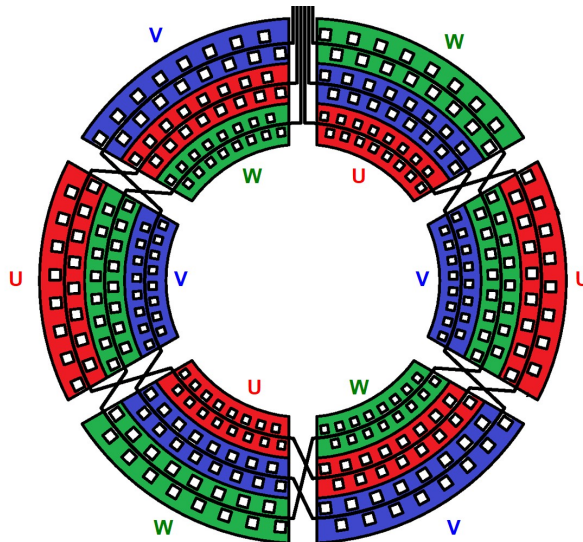


FIGURE 2.4: Three-phases concentric transverse-flux machine (1 stator)

Figure 2.5 focuses on one pole pair and shows the magnetic flux at no load ($I = 0$) with tangentially magnetized magnets.

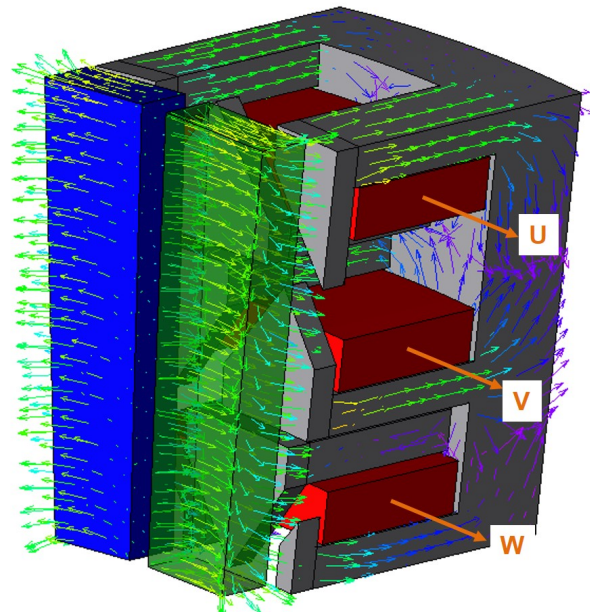


FIGURE 2.5: Three-phase concentric transverse-flux machine (1 pole pair at no load)

Several alternative designs are presented in figure 2.6. In these alternative designs, the magnets can be built with a rectangular shape (a) or with 3 small magnets (b and c). The stator teeth can be independent for each phase (a and b) or be shared between two phases (c):

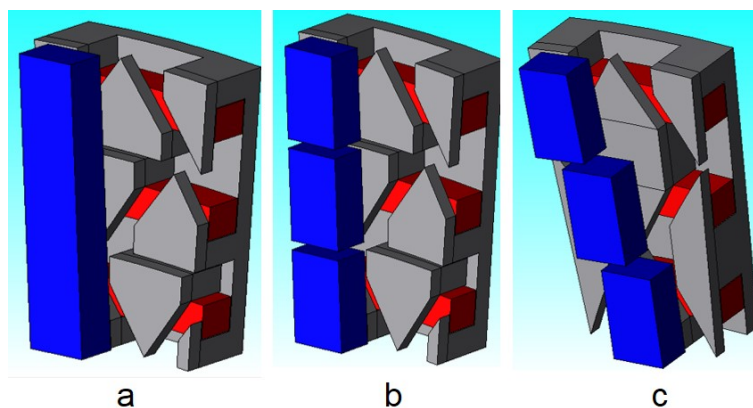


FIGURE 2.6: Alternative TFM designs

These designs have been simulated with FEM calculations. For each of these concepts, the transverse-flux machine shows a poor torque and power density. At maximum phase current, the saturation in the magnetic material limits the peak torque. Figure 2.7 shows that the magnetic flux density reaches more than 2 Tesla in the stator teeth.

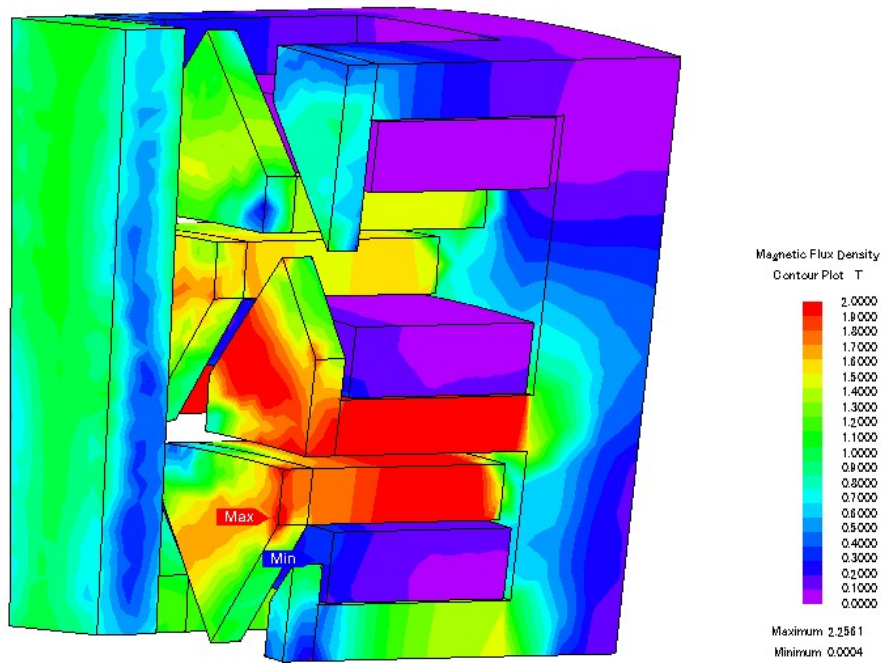


FIGURE 2.7: Magnetic saturation in the transverse-flux machine

For this machine, the peak torque was limited to 180 Nm. Furthermore the TFM has a poor power factor (smaller than 0.3 for high torque operating point). This poor power factor limits the peak power of the machine which is well short of the requirement:

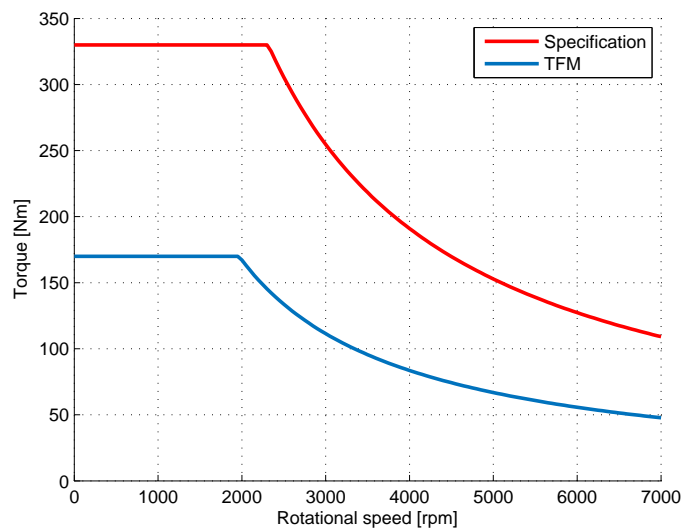


FIGURE 2.8: TFM performances compared to the specification

In [4] the possible application of a disc rotor transverse-flux machine for hybrid vehicles has been studied. Due to its complexity and high construction cost, this machine has

been excluded for a possible automotive application. Furthermore, the two-phase design and the high pole number are not compatible with state of the art automotive inverters.

For these reasons, the transverse-flux concept will not be further investigated and the PhD focuses on axial-flux machines.

2.3.1.2 Axial-flux machines

Single air gap axial-flux machines have the advantage to enable a short axial length. But the high axial force between the stator and the rotor is a difficulty in the mechanical construction. Furthermore, the air gap surface is half as high as in double air gap machines. To achieve the same torque, the magnetic field density has to be strongly increased. This could lead to a higher saturation of the magnetic material limiting the maximum torque. That is why the torque density of single air gap AFM is smaller than double air gap topologies [14]. For these reasons, this topology is rejected.

AFIS ironless machines offer the possibility to build light machines by saving iron. But, the torque density and the efficiency of these machines are poor. This technology is not suitable for a high torque density applications and will not be more investigated.

Multidisc machines are interesting to increase the performance of an electric machine by stacking up several machines in the length. This offers a possibility to scale the machine if the available space requires long axial length and small diameters. In the case of an integrated motor-generator, the axial length should be minimized. That's why multidisc designs are not convenient for this application.

The mechanical construction of machines combining AFM and other technologies is complex. Designs with radial and axial air gaps presented in [80] use a plurality of permanent-magnets with different sizes. Due to the combination of several technologies, the axial length of these machines is increased. The complex mechanical construction, high quantity and costs of permanent-magnets and long axial length make these topologies not suitable.

2.3.2 Comparison of suitable topologies

After this first selection, following topologies will be studied and compared:

- AFIS with bounded teeth (figure 1.4)
- TORUS machine (figure 1.5)
- YASA: Yokeless machine with independent teeth (figure 1.7)
- AFIR machine (figure 1.9)

2.3.2.1 Evaluation of selected topologies

The selected topologies will be compared regarding following objectives:

- Magnet mass and cost
- Axial length
- Torque density
- Mechanical construction
- Continuous torque and power

The electromagnetic, mechanical and thermal advantages and disadvantages of each design are presented in table 2.2.

	YASA	TORUS	AFIS	AFIR
Stator back iron	No stator back iron needed.	Back iron needed for magnetic circuit. Additional losses and saturation are possible. Increased axial length.	Back iron needed for mechanical resistance. Additional losses limited. Increased axial length.	Back iron needed for magnetic circuit. Additional losses and saturation are possible. Increased axial length.
Rotor back iron	Back iron needed for magnetic circuit. Additional losses and saturation are possible. Increased axial length.			No rotor back iron needed.
Winding construction	Concentrated winding around each tooth. Connection each other can cost space.	Winding around stator core can be difficult. Connections can cost space.	Windings can be axially inserted over the teeth.	Windings can be axially inserted over the teeth. Parallel or serial connection.

	YASA	TORUS	AFIS	AFIR
Coil end winding	Coil end winding partially behind stator teeth.	Short coil end winding.	Coil ends can significantly reduce the radial available space and the torque density in case of distributed winding.	
Magnets	High number of magnets. Eventually higher construction cost due to thinner magnets.			Less and thicker magnets than AFIS.
Axial force (rotor)	High force on magnets and on each rotor. Magnet fixation can be difficult. Bending force on rotor.			No resulting force (if rotor properly centered). Force on magnets possible.
Axial force (stator)	Small or no axial force on stator if properly centered.			High force on stator.
Stator fixation	Radial fixation of stator can lead to mechanical difficulties and reduction of available space for cooling or electric connection. YASA: Difficulties by fixing teeth together.			Radial or axial possible. Less conflict with cooling or electric connection.
Stator (SMC)	Pressing of small teeth state of the art.	Stator can be pressed as one or several parts.		
Stator (steel lamination)	Difficult due to independent teeth.	Possible, no additional difficulty due to topology.		
Stator cooling	Only radial heat transfer (reduced with large coil end).			Axial and radial heat transfer.
Rotor cooling	Convection in the air gap and on axial outside faces of the rotor, conduction to rotor shaft if rotor thermal conducting.			Limited convection in air gap. Conduction to rotor shaft if metallic rotor.
Rotor losses	Eddy current in magnets. Additional iron losses in rotor back iron.			Eddy current in magnets and in the rotor (if electric conductive material).

TABLE 2.2: Evaluation table of selected topologies

2.3.2.2 Discussion and selection of suitable topology

The advantages and disadvantages shown in table 2.2 can be summarized in figure 2.9.

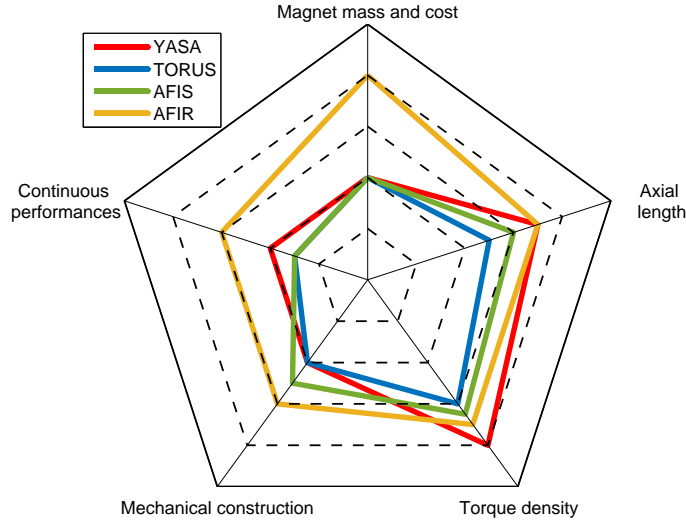


FIGURE 2.9: Spider plot comparison of the selected topologies

The YASA machine offers the best torque density thanks to small coil end windings and the absence of magnetic back iron at the stator. But, like other internal stator machines, magnet costs are higher and the cooling is harder compared to the internal rotor machine. Independent stator teeth make its construction harder. The TORUS machine does not present any advantage compared to the YASA machine. Coil end windings, even if they are small, and the necessary large stator back iron reduce the torque density. Compared to YASA the construction of the stator is easier, but the construction of the windings is harder. The AFIS machine with bounded teeth is easier to build compared to YASA and TORUS but large coil end windings and the small stator back iron reduce the torque density and increase the axial length.

In this comparison, the AFIR topology appears as the best solution and is selected for this specific application. The AFIR topology offers better cooling capability to increase the continuous power of the machine and is the only one without axial force acting on the rotor. Furthermore, it appears as the best choice to minimize the permanent-magnet cost. But the AFIR machines show some disadvantages which have to be minimized during the sizing:

- Rotor losses: despite the absence of magnetic back iron, eddy current losses are generated in the permanent-magnets. The cooling of the rotor is hard, so these

losses have to be minimized to avoid any overheating of the magnets and eventual demagnetization.

- Coil end winding: the coil ends reduce the available radial space, so the active area of the machine and its maximum torque. The winding topology has to be appropriately chosen in order to preserve the torque density.
- Axial force on the stator: even if this force is easier to handle than an equivalent force on the rotor, it has to be taken into account and eventually minimized.

2.4 Design

In this section, several concepts are compared to clarify the design of the magnetic circuit:

- The winding technology
- The electric connection
- The teeth alignment
- The permanent-magnets
- The stator magnetic material

To make a comparison between both concepts and choose the best one, an AFIR machine with a concentrated winding has been designed. This machine has a number of slots per pole per phase: $NSPP=0.5$ (see 3.2).

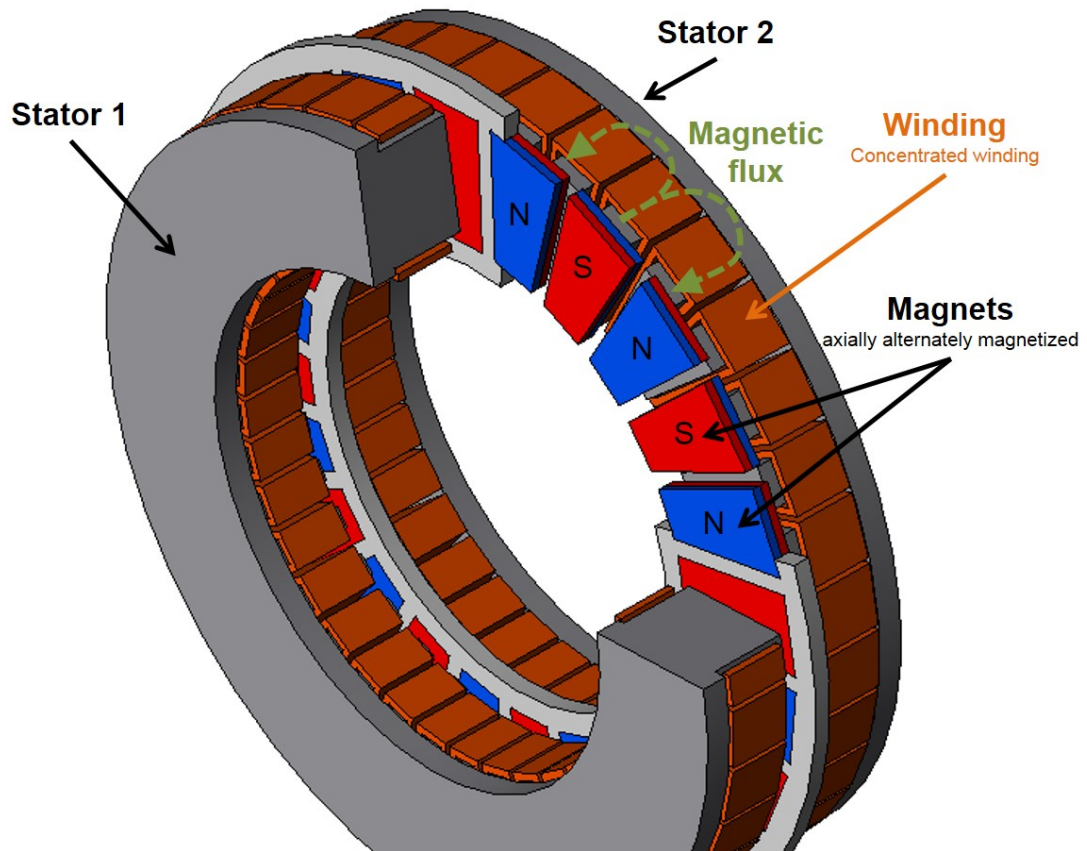


FIGURE 2.10: Single rotor double stator AFM with a concentrated winding

2.4.1 Winding technology

Conductors in electric machines, especially for automotive applications, are mainly built with following winding technologies:

- Pull-in winding: electric conductors are made of a great number of thin circular wires connected in parallel. In this configuration, conductors are wound outside of the machine and inserted in the slots. Small circular wires avoid skin effect and AC losses but limit the copper fill factor increasing the DC resistance. The high number of turns per winding enables a good modularity for the design of the machine. If the conductors are not properly positioned in the slot, the parallel connection causes the appearance of circulating currents between parallel wires increasing the conductor losses.
- Hairpin winding: electric conductors are built with large rectangular bars connected in series. For radial-flux machines, the conductors are preformed in a hairpin shape and inserted in the axial direction inside the stator slots. After this operation, the conductors are bent and connected together by welding.

The copper fill factor is higher. Large bars already allow a better thermal conductance of the losses. The serial connection of the bars avoids circular currents. The number of turns is smaller than a pull-in winding machine, so it is hard to modify the winding to fit it to another specification. Due to the large size of the conductors, hairpin windings are more sensitive to skin effect than pull in windings (see 4.1.2). For a given machine, the DC resistance is better with hairpin winding thanks to the better copper fill factor but the resistance is often worse at maximum rotational speed. An example of hairpin winding for automotive application is the Denso machine built in the Toyota Yaris [89].

For this application, this hair pin winding is selected for following reasons:

- Better copper fill factor and lower copper losses at small rotational speed. This maximizes the efficiency for the most often driven important operating points (the electric machine is mainly (80%) driven under 2500 rpm, see figure 2.3).
- Better thermal conductance of the copper losses to the soft magnetic material which enables a better cooling and a higher continuous power.

2.4.2 Electric connection

Internal rotor axial-flux machines have two stators and offer a degree of freedom in the electric connection. The stators can be connected in parallel (a and c) or in series (b and d). Furthermore, like in every three-phase electric machine, a star (a and b) or a delta (c and d) connection is possible. It results in four possible electric connections. The first stator is displayed in red, the second one is displayed in blue.

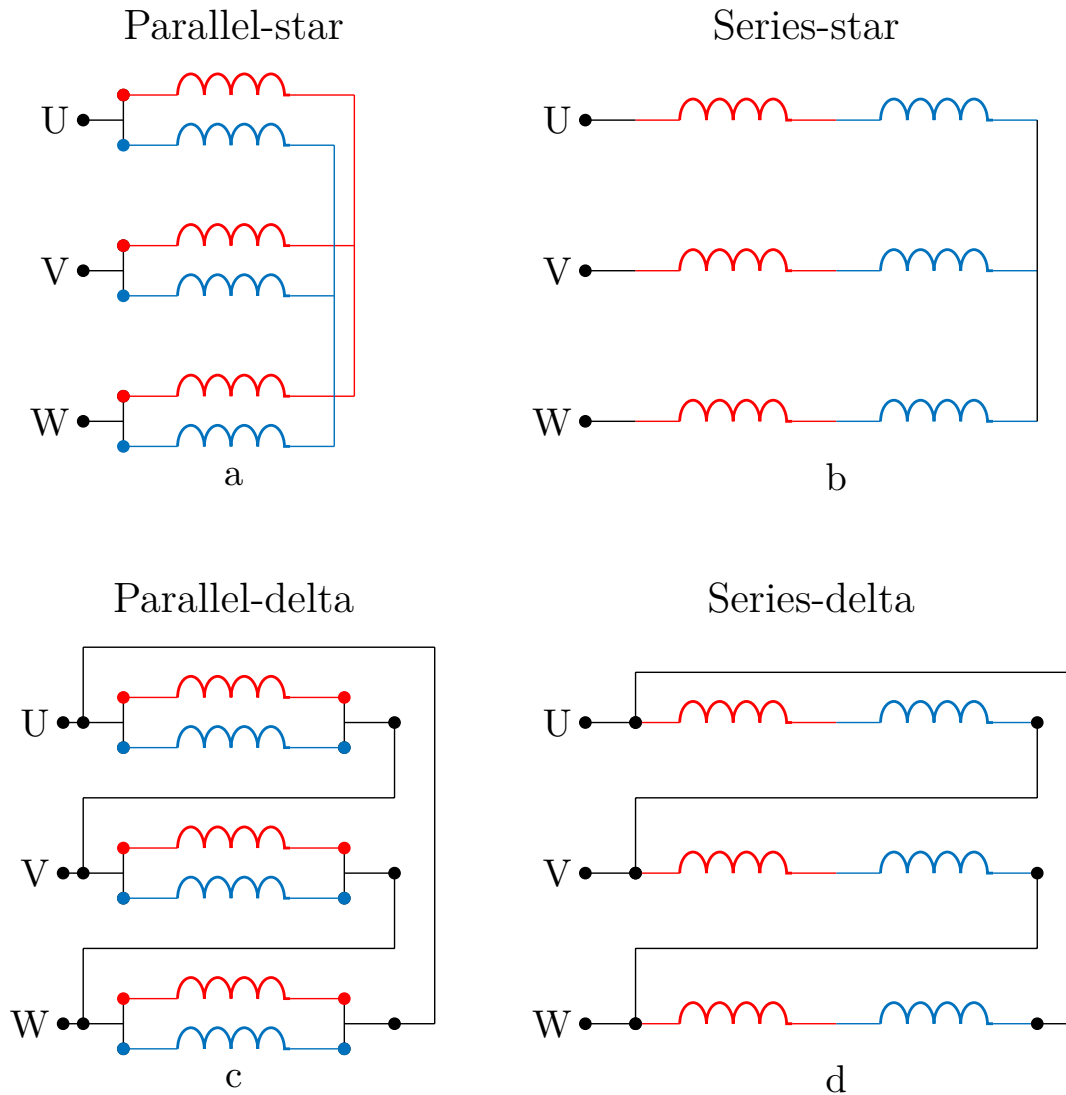


FIGURE 2.11: Star and delta electric connections a double stator AFM

Advantages and disadvantages of star and delta connections are well known. In the delta connection (c and d), the current flowing in the phase is $\sqrt{3}$ smaller than in the wire. To obtain the same performances, the number of turns has to be multiplied by $\sqrt{3}$ and the section divided by $\sqrt{3}$ to maintain the same current density and copper

fill factor. For pull in windings (see 2.4.1), the number of turns is large, so it is quite easy to approximate to an integer by multiplying or dividing by $\sqrt{3}$ and obtain similar performances. For hairpin windings, the number of turns is small (typically under 4), so multiplying or dividing by $\sqrt{3}$ could lead to a non integer number. In that case, the approximation to the next integer number strongly modifies the performances of the machine (current density, peak torque and power). One of the main disadvantage of the delta connection is the circular current flowing in the conductors. The 3rd, 6th, 9th, ... harmonics in the electromotive force of a three-phase winding are pulsating synchronously. In a delta-connected machine, these harmonics induce a circular current increasing the copper losses of the machine [90]. In a star-connected machines, the sum of the phase currents is fixed to zero, so there is no induced circular current. For this reason a star connection is selected.

With a parallel connection, the current is divided between both stators. To maintain the same electric loading, the number of turns needs to be doubled. So the number of welding spots is already doubled too. As the section of the conductors is divided by 2, the skin effect is smaller with the parallel connection. Furthermore with the parallel connection both stator are identical, so the mechanical construction is easier. In the case of mechanical asymmetries (non central rotor or error in the angular position of the stators), the induced voltages in both stators are different and a circular current is generated (see appendix A.5). With a serial connection, this circular current can be avoided. **To make the construction easier and minimize the skin effect the parallel-star connection (a) is selected.**

2.4.3 Teeth alignment

The construction of an AFIR machine offers the possibility to align or to shift the teeth of the both stators by a half step. The magnetic circuits of both these designs are presented in figures 1.9 and 1.10. The winding distributions are indicated in figures 2.12 and 2.13.

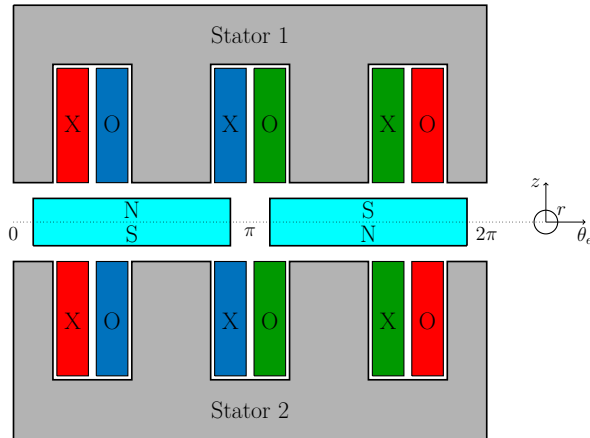


FIGURE 2.12: Winding distribution with aligned teeth

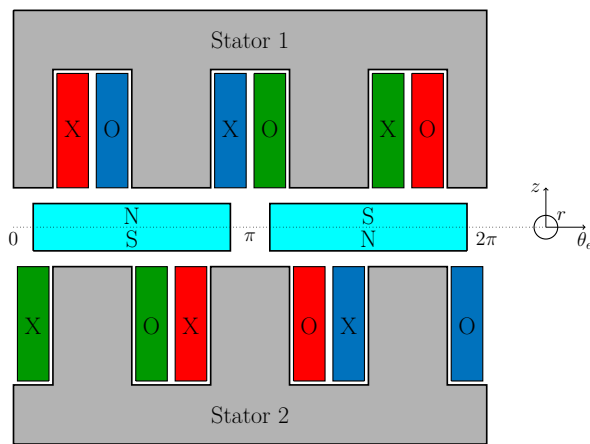


FIGURE 2.13: Winding distribution with unaligned teeth

The machine has been calculated in the three extreme operating points OP1, OP2 and OP3 defined in appendix A.4.

- OP1: no load ($I = 0$, α undefined, $n = n_{max}=7000$ rpm)
- OP2: full load ($I = I_{max}$, $\alpha = 90^\circ$, $n=2000$ rpm)
- OP3: short circuit ($I = I_{sc}$, $\alpha = 180^\circ$, $n = n_{max}=7000$ rpm)

Results of the FEM calculations are presented in table 2.3.

	Description	Aligned teeth	Shifted teeth	Evolution
OP1	Induced voltage	234 Vrms	226 Vrms	-3%
	Cogging torque (peak-peak)	36 Nm	38 Nm	+6%
	Magnet losses	4695 W	1536 W	-67%
	Axial force (per magnet)	0 N	16 N	
OP2	Maximum torque	295 Nm	296 Nm	+0.3%
	Torque ripple (peak-peak)	44 Nm	44 Nm	0%
	Magnet losses	1380 W	254 W	-82%
	Axial force (per magnet)	0 N	38 N	
OP3	Short circuit current	230 Arms	226 Arms	-2%
	Magnet losses	1375 W	571 W	-58%
	Axial force (per magnet)	0 N	38 N	

TABLE 2.3: Comparison between aligned and shifted teeth

These results show that eddy current losses in the magnets are strongly reduced with shifted teeth. Depending on the operating point, the reduction varies between -58% and -82%. The induced voltage, the maximum torque and the torque ripple are not impacted in this example. Shifted teeth have the disadvantage, that magnets are submitted to an axial force at every operating points. The attracting axial force F_z acting between a magnet and a stator is defined as:

$$F_z = \iint_S \frac{B_z^2}{2\mu_0} dS \quad (2.7)$$

Where S is the surface of the magnet in front of the stator and B_z the axial component of the magnetic field density. The axial force acting on the left magnet is:

$$\begin{aligned} \vec{F}_{z_{magleft}} &= \vec{F}_{z_{magleft \leftrightarrow stat1}} + \vec{F}_{z_{magleft \leftrightarrow stat2}} \\ &= \iint_{S_{North}} \frac{B_z(r, \theta_e, z_{mag})^2}{2\mu_0} dS \vec{z} - \iint_{S_{South}} \frac{B_z(r, \theta_e, -z_{mag})^2}{2\mu_0} dS \vec{z} \\ &= \iint_S \frac{B_z(r, \theta_e, z_{mag})^2 - B_z(r, \theta_e, -z_{mag})^2}{2\mu_0} dS \vec{z} \end{aligned} \quad (2.8)$$

Where r is the radius, θ_e is the electric angle, z is the axial position and r_i and r_o are the inside and outside radius of the magnetic circuit. In case of shifted teeth, the magnetic fields in both air gaps are unbalanced: $|B_z(r, \theta_e, -z)| \neq |B_z(r, \theta_e, z)|$, so magnets are, depending on the position of the rotor, alternately attracted by both stators. With aligned

teeth, the magnetic flux in both air gaps is opposed : $|B_z(r, \theta_e, -z)| = |B_z(r, \theta_e, z)|$, so there is no axial force on the magnet if the machine is perfectly balanced. Due to mechanical tolerances (axial position of the rotor, differences in the stator geometries, ...), the magnetic flux is perfectly equal in both air gaps and small axial forces on the magnets, even with aligned teeth, can not be avoided. **To minimize the magnets losses, the shifted teeth topology is selected for the rest of the work.** During the designing, the axial force on magnets has to be taken into account and minimized to ensure their fixation on the rotor. Furthermore, to save the rotor bearing, resulting axial force on the rotor should be avoided.

2.4.4 Permanent-magnets

Rare earth NdFeB permanent-magnets are characterized by their remanence B_r and their coercivity H_{cj} and are classified in grades depending on these characteristics (see appendix C.1). Magnets with the highest remanence have the smallest coercivity and are easy to demagnetize at high temperature [91]. The coercivity of a magnet can be improved by increasing its Dysprosium content which strongly increase its price. Grades SH, UH and EH are the main grades for automotive applications. The magnetic properties of these grades depending on the temperature are displayed in table 2.4.

Temperature [°C]	Br [T]			Hcj [kA.m ⁻¹]			Hk95 [kA.m ⁻¹]		
	SH	UH	EH	SH	UH	EH	SH	UH	EH
-20	1.36	1.29	1.23	-1900	-2413	-2993	-1805	-2293	-2843
20	1.31	1.25	1.20	-1594	-1995	-2377	-1515	-1895	-2258
90	1.22	1.18	1.14	-954	-1280	-1509	-906	-1216	-1433
150	1.11	1.08	1.05	-475	-747	-946	-451	-709	-899

TABLE 2.4: Magnetic properties of different magnet grades

Beside the material, the shape of the magnet is relevant for its cost. In the literature, examples with different magnet shapes can be found. Trapezoidal magnets are very common for AFM [5, 12, 14, 28, 92]. This shape is particularly optimized to increase the maximum torque of the machine and enables an optimum constant section of the bridge between two magnets. Other shapes have been proposed in [93–95] to minimize the cogging torque of the machine. Rectangular magnets are cheaper than other shapes. **The reduction of the magnet cost is a priority of this work, so a rectangular magnet shape is selected.**

In [92, 96], a segmentation of the magnets is proposed to reduce the eddy current losses. High number of segmentations in the circumferential and radial direction strongly decreases the losses (-80%) but increases the costs (especially if different geometries are used) and makes the fixation of the magnets harder.

2.4.5 Magnetic material

2.4.5.1 Soft magnetic composite

2.4.5.1.1 Generalities

Soft Magnetic Composite (SMC) is often used for axial-flux machines contrary to radial-flux machine. SMC is a powder composed of small (20 to 200 μm) isolated iron particles [97]. The isolation between SMC's particles allows some differences in the magnetic properties of the material compared to laminated steel. This isolation builds small magnetic air gaps reducing the magnetic flux density. For this reason SMC offers often a slightly worse magnetic curve than laminated steel. This curve can be improved by increasing the compacting pressure of the SMC [4, 98]. On the contrary, this isolation is an advantage to reduce eddy current losses. Thanks to this isotropic construction and contrary to steel lamination, SMC are capable to carry the magnetic flux in three dimensions. This is the reason, why this material is well suited for axial and transverse-flux machines [99].

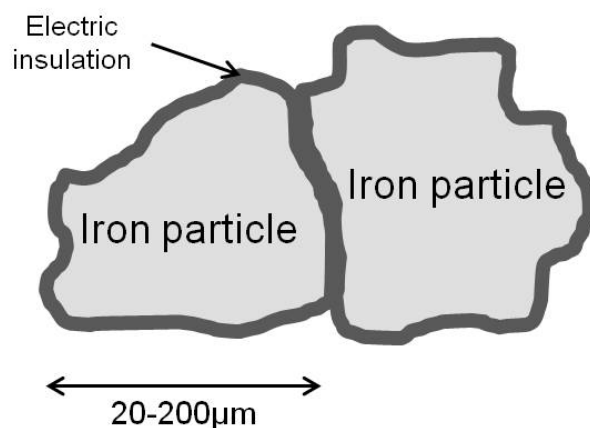


FIGURE 2.14: Schematic representation of a SMC powder

For applications in AFM, SMC needs to be pressed in a specific shape depending on the magnetic circuit. In case of an AFIS machine where the stator is composed of independent teeth (YASA topology), the fabrication of each single tooth is quite easy. For AFIS machines with magnetic core like the TORUS topology, or an AFIR machine,

the fabrication of the stator as one part of compacted SMC could be impossible for large machines due the limitation of the compacting pressure for large parts. A solution is to segment the stator in several parts [100, 101]. In that case, the gap between two parts should be minimized thanks to a proper mechanical construction to avoid any performance loss.

2.4.5.1.2 Constraints on geometry

The production of the stator by pressing soft magnetic composite necessitates some geometry conditions. These constraints are explained in [102] or have been discussed with experts and SMC manufacturers. The basic geometry of one stator segment is displayed in figure 2.15.

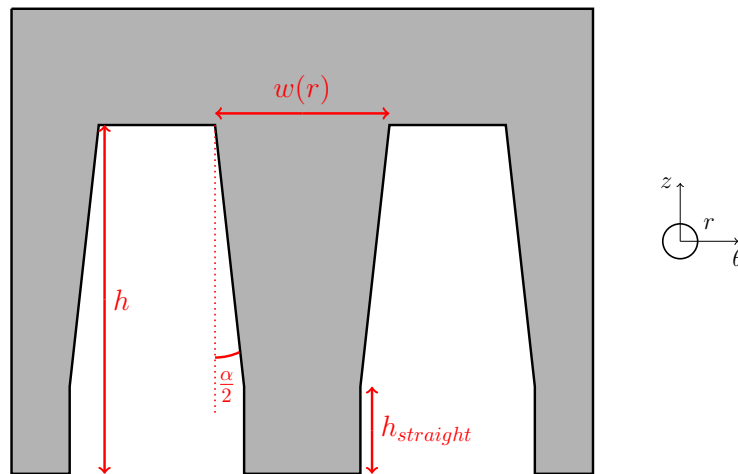


FIGURE 2.15: Detailed geometry of a SMC tooth

As displayed in figure 2.15, the tooth can only be pressed in a trapezoidal shape. For this work the angle has been fixed to $\alpha = 3^\circ$ (1.5° each side). Furthermore, to improve the performance of the machine, it is not necessary to chamfer the tooth over its whole height. A straight part $h_{straight} \approx 6mm$ can be designed at the top of the tooth. The width of the tooth ($w(r)$) depends on the radius and is minimized at the inside radius of the tooth (r_i). To ensure the mechanical resistance of the component, it is not possible to press high and thin teeth. A maximum ratio between the height and the width of the tooth has to be respected. [102] proposes 6 for materials with high mechanical resistance like metals. For SMC this ratio is limited to : $\frac{h}{w(r_i)} \leq 4$. This limitation of the height/width ratio leads to an indirect limitation of the number of teeth depending on their height, the slot width and the diameter of the machine.

2.4.5.2 Steel lamination

The construction of an axial-flux machine with laminated steel is different to a radial-flux machine. For a radial-flux machine, identical steel lamination are axially stacked up over all its length. In RFM, the magnetic flux does not flow in the axial direction (only radially and tangentially), thus this stacking is effective to reduce eddy current losses. For AFM, the magnetic flux flows mainly axially and tangentially, so the stator core built with steel lamination needs to be segmented in the radial direction. Furthermore the high mechanical strength from steel enables the construction of stators with small teeth [12].

Contrary to isotropic SMC, radial components of the magnetic flux are problematic in steel lamination machines due to the induction of eddy currents. This radial magnetic flux should be negligible, but in case of saturation in the magnetic core, this flux increases and induces high eddy currents losses. This problematic has been studied in [33]. A variable air gap in the radial direction minimized the saturation of the magnetic material and the iron losses.

Steel lamination seems particularly adapted for AFIS machines with magnetic back iron like the TORUS topology or AFIR machines. In these configurations, a stator can be built with one long wounded steel lamination [103, 104]. Other construction process with a plurality of parts are possible like in [105]. But steel lamination is not limited to configuration with massive stators. In [106] a yokeless machine (YASA topology) is studied. In case of a trapezoid lamination stacking, each steel lamination is different to its neighbor. This solution is complex and expensive, that is why three lamination stackings are proposed and studied in the paper (rectangular, T-shape and overlap).

2.4.5.3 Selection of the magnetic material

For this work, soft magnetic composite is selected as magnetic material:

- The manufacturing by pressing soft magnetic material is easier than steel lamination. SMC has a very interesting potential to enable the production of an AFM in series with limited production costs.
- SMC has lower losses at high frequency. This minimizes the stator losses at high rotational speed and improve the continuous power.
- SMC is isotropic and enables the circulation of the magnetic flux in every direction. Contrary to steel lamination, in case of saturation, there are no additional losses due to unwanted radial components of the magnetic flux [33].

The SMC Somaloy 5P700HR has been selected for the PhD. Its magnetic properties are presented in appendix C.2.

Conclusion

In this chapter, the requirements and the design of the machine have been defined. A peak torque of 330 Nm and a peak power of 80 kW are required. It has been proved, that the electric parameters like the induced voltage, the power factor and the short circuit current of the machine are not free and need to meet minimum values to achieve the requirements. In a second step the design of the machine has been defined:

- Topology: internal rotor axial-flux machine
- Hairpin winding
- Permanent-magnets: NdFeB rectangular permanent-magnets
- Soft magnetic material: soft magnetic composite Somaloy 5P700HR with a compressible geometry
- Design: shifted teeth and parallel star electric connection

Chapter 3

Selection of the number of slots per pole per phase

Contents

Introduction	56
3.1 Possible numbers of slots per pole per phase	57
3.2 Concentrated winding with NSPP=0.5	59
3.2.1 Presentation	59
3.2.2 Axial forces	60
3.3 Integer numbers of slots per pole per phase	61
3.3.1 Presentation	61
3.3.2 Unbalanced induced voltages	62
3.3.3 Axial forces on magnets	65
3.4 Fractional number of slots per pole per phase	67
3.4.1 Fractional NSPP with concentrated windings	67
3.4.2 Fractional NSPP with distributed windings	67
3.4.3 Fractional distributed winding with NSPP=1.5	71
3.5 Comparison between the numbers of slots per pole per phase	72
3.5.1 Magneto-motive force	72
3.5.2 FEM simulations	74
3.5.3 Selection of the optimum NSPP	77
Conclusion	78

Introduction

The Number of Slots per Pole per Phase (NSPP) defines the relation between the number of slots (n_{slots}), the number of poles ($2n_p$) and the number of phases (n_{phase}). In this chapter, the number of phases is fixed to 3, so the number of slots needs to be a multiple of 3. The NSPP can be calculated with following equation:

$$NSPP = \frac{n_{slots}}{3 \cdot 2n_p} = \frac{n_{slots}}{6n_p} \quad (3.1)$$

For example, the machine presented in figure 2.10 has 36 teeth and 12 pole pairs, so NSPP=0.5. The NSPP is a particularly important parameter of an electric machine. It has a direct influence on several important parameters like:

- The magnetic coupling between the magnets and stators which influences the torque density and the necessary magnet quantity
- The spectrum of the Magneto Motive Force (MMF) which influences the inductance and the iron and magnet losses
- The winding construction and the size of the coil ends
- The torque ripple and the axial forces

Furthermore, the period of the magnetic field and the construction of the winding depends on the NSPP. This period is the smallest number of pole pairs containing a multiple of 3 number of slots. For example, NSPP=0.5 contains 3 slots per pole pair, so the machine is periodic with a period of one pole pair. NSPP=0.75 contains 4.5 slots per pole pair, 2 pole pairs are necessary to obtain a number of slots which is a multiple of 3 (9 slots). The period is 2 pole pairs and this machine can not be built with uneven number of pole pairs.

The objective of this chapter is to determine the optimum NSPP for this application.

3.1 Possible numbers of slots per pole per phase

The possible combinations of number of slots, number pole pairs and the corresponding NSPP are shown in table 3.1.

Number of slots n_{slots}	Pole pairs (n_p)									
	6	7	8	9	10	11	12	13	14	15
9	0.25	0.21	0.19	0.17	0.15	0.14	0.13	0.12	0.11	0.10
12	X	0.29	0.25	0.22	0.20	0.18	0.17	0.15	0.14	0.13
15	0.42	0.36	0.31	0.28	0.25	0.23	0.21	0.19	0.18	0.17
18	0.50	0.43	0.38	X	0.30	0.27	0.25	0.23	0.21	0.20
21	0.58	0.50	0.44	0.39	0.35	0.32	0.29	0.27	0.25	0.23
24	X	0.57	0.50	0.44	0.40	0.36	X	0.31	0.29	0.27
27	0.75	0.64	0.56	0.50	0.45	0.41	0.38	0.35	0.32	0.30
30	0.83	0.71	0.63	0.56	0.50	0.45	0.42	0.38	0.36	X
33	0.92	0.79	0.69	0.61	0.55	0.50	0.46	0.42	0.39	0.37
36	1.00	0.86	0.75	X	0.60	0.55	0.50	0.46	0.43	0.40
39	1.08	0.93	0.81	0.72	0.65	0.59	0.54	0.50	0.46	0.43
42	1.17	1.00	0.88	0.78	0.70	0.64	0.58	0.54	0.50	0.47
45	1.25	1.07	0.94	0.83	0.75	0.68	0.63	0.58	0.54	0.50
48	X	1.14	1.00	0.89	0.80	0.73	X	0.62	0.57	0.53
51	1.42	1.21	1.06	0.94	0.85	0.77	0.71	0.65	0.61	0.57
54	1.50	1.29	1.13	1.00	0.90	0.82	0.75	0.69	0.64	0.60
57	1.58	1.36	1.19	1.06	0.95	0.86	0.79	0.73	0.68	0.63
60	X	1.43	1.25	1.11	1.00	0.91	0.83	0.77	0.71	X
63	1.75	1.50	1.31	1.17	1.05	0.95	0.88	0.81	0.75	0.70
66	1.83	1.57	1.38	1.22	1.10	1.00	0.92	0.85	0.79	0.73
69	1.92	1.64	1.44	1.28	1.15	1.05	0.96	0.88	0.82	0.77
72	2.00	1.71	1.50	X	1.20	1.09	1.00	0.92	0.86	0.80
75	2.08	1.79	1.56	1.39	1.25	1.14	1.04	0.96	0.89	0.83
78	2.17	1.86	1.63	1.44	1.30	1.18	1.08	1.00	0.93	0.87
81	2.25	1.93	1.69	1.50	1.35	1.23	1.13	1.04	0.96	0.90
84	X	2.00	1.75	1.56	1.40	1.27	1.17	1.08	1.00	0.93
87	2.42	2.07	1.81	1.61	1.45	1.32	1.21	1.12	1.04	0.97
90	2.50	2.14	1.88	X	1.50	1.36	1.25	1.15	1.07	1.00
93	2.58	2.21	1.94	1.72	1.55	1.41	1.29	1.19	1.11	1.03
96	X	2.29	2.00	1.78	1.60	1.45	X	1.23	1.14	1.07

X Non integer NSPP where the number of slots is a multiple of the number of magnets.
For these NSPP, it is not possible to generate a torque for every rotor position.

FIGURE 3.1: Advantageous numbers of slots per pole per phase

This table is limited to $6 \leq n_p \leq 15$ to avoid designs with too small number of pole pairs ($n_p < 6$, large coils ends) or with too high pole-pair numbers ($n_p > 15$) to avoid too high electric frequencies. The number of slots n_{slots} is limited to 96 to avoid designs with too thin teeth (see 2.4.5.1.2). Following NSPP are marked:

- Yellow: fractional concentrated winding (NSPP < 0.5) with $n_{slots} = 2n_p \pm 1$ or $n_{slots} = 2n_p \pm 2$
- Orange: concentrated winding with NSPP=0.5
- Violet: fractional NSPP with a period of 2 pole pairs (NSPP=0.75, 1.25, ...)
- Green: integer NSPP
- Blue: distributed winding with NSPP=1.5

The choice of the optimum NSPP depends on the requirements. The advantages and disadvantages of each of these NSPP are discussed in this chapter:

- Concentrated winding with NSPP=0.5
- Integer numbers of slots per pole per phase
- Fractional NSPP with concentrated winding
- Fractional NSPP with distributed windings
- Distributed winding with NSPP=1.5

3.2 Concentrated winding with NSPP=0.5

3.2.1 Presentation

Concentrated winding is used for small $\text{NSPP} \leq 0.5$. In this type of winding, copper coils are wound around one tooth and connected together in series or in parallel. The concentrated winding has the advantage to minimize the size of the coil ends. This makes this type of winding particularly interesting for radial-flux machines in automotive applications where the axial length needs to be minimized. Furthermore, short coil ends reduce the copper losses and improve the efficiency.

The most common concentrated winding is the winding with $\text{NSPP}=0.5$. In that case, there are 3 slots for 2 magnets, so one half slot per pole per phase. This NSPP is the smallest one which enables a period of the winding of one pole pair and is often used for integrated motor-generators [107, 108]. The construction of the winding with unaligned teeth has been displayed in figure 2.13 and is reminded in figure 3.2.

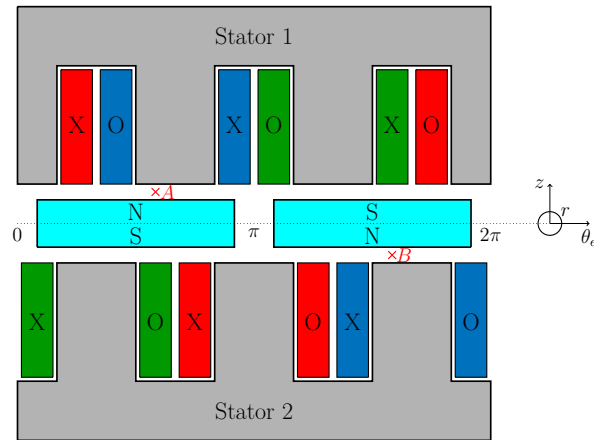


FIGURE 3.2: Winding distribution with unaligned teeth (NSPP=0.5)

The winding with $\text{NSPP}=0.5$ covers only 120 electric degrees, so the distribution factor of this winding is smaller than 1. The distribution factor k_d is equal to the winding factor $k_\omega = k_p \cdot k_d$, as the pitch factor k_p is 1:

$$\begin{aligned}
 k_\omega &= k_p \cdot k_d \\
 &= 1 \cdot \sin\left(\frac{120^\circ}{2}\right) \\
 &= 0.866
 \end{aligned} \tag{3.2}$$

3.2.2 Axial forces

In 2.4.3, the axial force acting on the magnet in case of shifted teeth has been highlighted. For NSPP=0.5, the magnetic field in the air gap between the first magnet and the first stator is opposed with the magnetic field in the air gap between the second magnet and the second stator: $B_z(A) = -B_z(B)$ (see figure 3.2), so:

$$B_z(r, \theta_e, z) = -B_z(r, \theta_e + \pi, -z) \quad (3.3)$$

This property of the magnetic field has the consequence that the attracting force between the left magnet and the stator 1 ($\vec{F}z_{mag_{left} \leftrightarrow stat1}$) and the right magnet and the stator 2 ($\vec{F}z_{mag_{right} \leftrightarrow stat2}$) are opposed (see equation 2.7), it results:

$$\begin{aligned} \vec{F}z_{mag_{left} \leftrightarrow stat1} &= -\vec{F}z_{mag_{right} \leftrightarrow stat2} \\ \vec{F}z_{mag_{left} \leftrightarrow stat2} &= -\vec{F}z_{mag_{right} \leftrightarrow stat1} \end{aligned} \quad (3.4)$$

The force acting on the right magnet is:

$$\begin{aligned} \vec{F}z_{mag_{right}} &= \vec{F}z_{mag_{right} \leftrightarrow stat1} + \vec{F}z_{mag_{right} \leftrightarrow stat2} \\ &= -\vec{F}z_{mag_{left} \leftrightarrow stat2} - \vec{F}z_{mag_{left} \leftrightarrow stat1} \\ &= -\vec{F}z_{mag_{left}} \end{aligned} \quad (3.5)$$

The axial forces acting on both magnets are opposed, so there is no resulting axial force acting on the rotor.

3.3 Integer numbers of slots per pole per phase

3.3.1 Presentation

Distributed windings are used for $\text{NSPP} > 0.5$. In this windings, the coils are wound over several teeth. The most common distributed windings are integer NSPP ($\text{NSPP}=1, 2, 3, \dots$). Increasing the NSPP has the main advantages to reduce the harmonics in the air gap and the rotor losses. This is particularly relevant for induction machines which are often built with high $\text{NSPP} > 3$. A higher NSPP has the disadvantage to require long coil ends which reduces the active area of the machine and its torque density as well as increases copper losses. Furthermore a high NSPP leads to designs with high number of teeth which can be hard to manufacture (see 2.4.5.1.2). Compared to concentrated winding with $\text{NSPP}=0.5$, distributed windings have a better magnetic coupling. The slot width is reduced, so the magnetic flux does not need to flow crooked through the air gap and does not loose so much flux density.

The winding distribution for a distributed winding with $\text{NSPP}=1$ and unaligned teeth is shown in figure 3.3. With $\text{NSPP}=1$, each conductor is wound around three teeth. This winding is the simplest distributed winding and is very common. The coil ends are limited and smaller than with greater NSPP. In this case, the rotor turns from the left to the right.

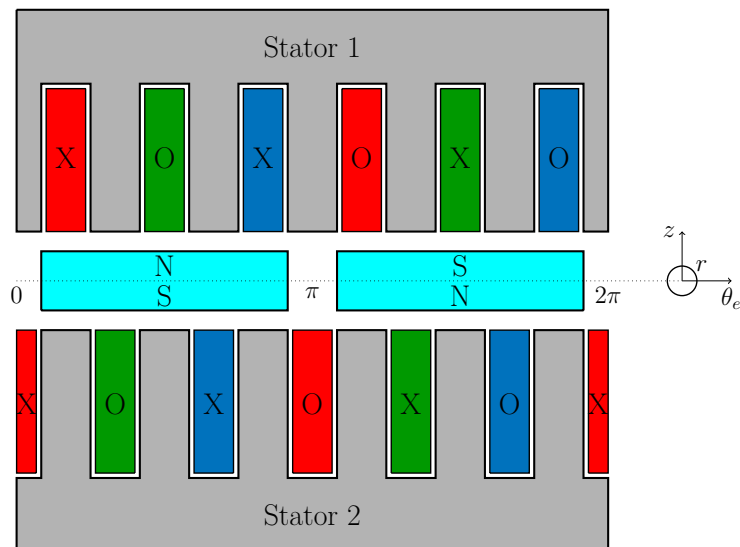


FIGURE 3.3: Winding distribution ($\text{NSPP}=1$)

3.3.2 Unbalanced induced voltages

In figure 3.3 the windings of the both stators are shifted due to the mechanical shifting. The induced voltages of both stators are phase shifted. The phasor diagram (figure 3.4) confirms this observation. The induced voltages of the first phase is shifted of 30 electrical degrees. With NSPP=2, this phase shifting is reduced to 15°. **Due to these unbalanced induced voltages, the parallel connection of both stators is dangerous. A circular current is generated. It increases the copper losses and reduces the electromagnetic torque.** This torque reduction is calculated in appendix A.5. As the winding covers the complete pole, the distribution factor k_{d0} is equal to 1, so the winding factor k_{ω_0} is :

$$\begin{aligned}
 k_{\omega_0} &= k_{p_0} \cdot k_{d_0} \\
 &= \frac{2\cos 15^\circ}{2} \cdot 1 \\
 &= 0.966
 \end{aligned}
 \tag{3.6}$$

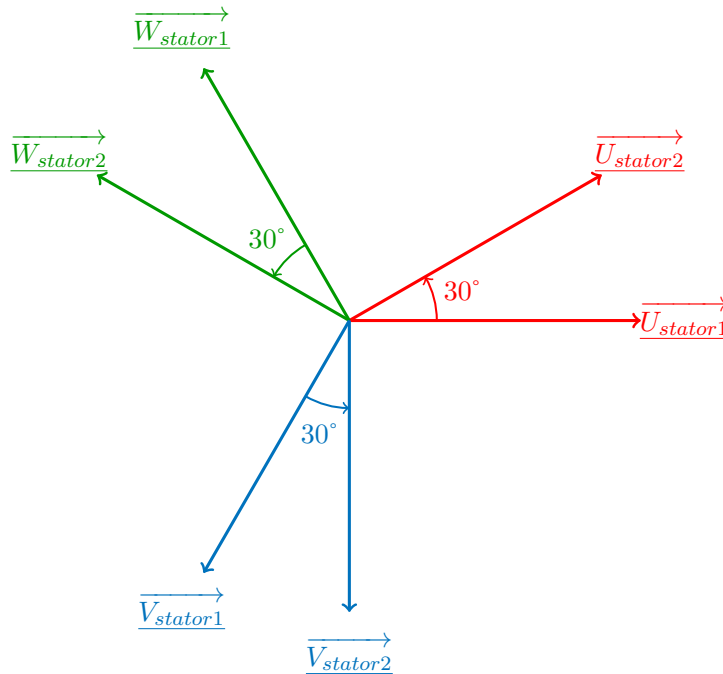


FIGURE 3.4: Complex phase diagram (NSPP=1)

A solution to reduce this problem is to make a short-pitching of the winding. In this case, it is proposed to shift a part of the turns (N_2 turns) to the neighbor coil. The

number of non-shifted turns is noted N_1 . The total number of turns is $N = N_1 + N_2$. An example with $N = 4$, $N_1 = 3$ and $N_2 = 1$ is proposed in figure 3.5.

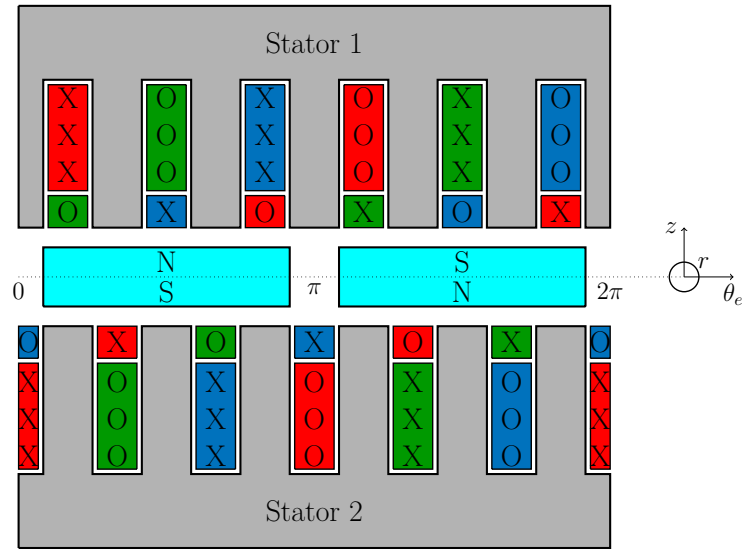


FIGURE 3.5: Winding distribution with short-pitch (NSPP=1)

The phase voltage of one stator is the sum of the voltages in the non-shifted coils (U_{11}) and in the shifted coils (U_{12}): $U_{stator1} = U_1 = U_{11} + U_{12}$. The phase diagram is displayed in figure 3.6.

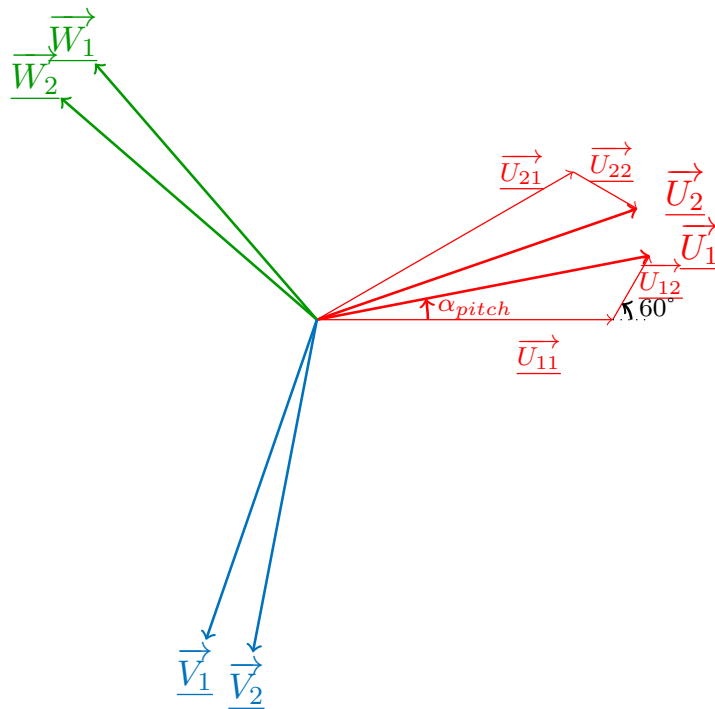


FIGURE 3.6: Phase diagram with short-pitch (NSPP=1)

The short-pitching reduces the phase shifting between both stators by shifting the induced voltages of each stator by an angle α_{pitch} . It reduces slightly the amplitude of the induced voltage. The value of this angle and the reduction of the amplitude are dependent on the relation between N_2 and N . By fixing $\alpha_{pitch} = 15^\circ$, the fundamental of both induced voltages are in phase. Thanks to the phasor diagram, α_{pitch} can be calculated with equation 3.7.

$$\begin{aligned}\tan \alpha_{pitch} &= \frac{N_2 \sin 60^\circ}{N_1 + N_2 \cos 60^\circ} \\ \alpha_{pitch} &= \arctan \left(\frac{\sqrt{3} \frac{N_2}{N_1}}{2 + \frac{N_2}{N_1}} \right) \\ &= \arctan \left(\frac{\sqrt{3} \frac{N_2}{N}}{2 - \frac{N_2}{N}} \right)\end{aligned}\quad (3.7)$$

The pitch factor per stator $k_{p_{stator}}$ is the relation between the amplitude of the induced voltage per stator with short-pitching and the amplitude of the induced voltage per stator without short-pitching (where all coils are in phase). It can be obtained with equation 3.8.

$$\begin{aligned}k_{p_{stator}} &= \frac{\sqrt{(N_1 + N_2 \cos 60^\circ)^2 + (N_2 \sin 60^\circ)^2}}{N_1 + N_2} \\ k_{p_{stator}} &= \frac{\sqrt{(N - N_2 + \frac{1}{2}N_2)^2 + (\frac{\sqrt{3}}{2}N_2)^2}}{N} \\ k_{p_{stator}} &= \sqrt{1 - \frac{N_2}{N} + \left(\frac{N_2}{N}\right)^2}\end{aligned}\quad (3.8)$$

The winding factor $k_{\omega_{shortpitch}}$ of the machine is:

$$\begin{aligned}k_{\omega_{shortpitch}} &= k_p \cdot k_d \\ &= k_{p_{stator}} \cdot \cos \left(\frac{30 - 2\alpha_{pitch}}{2} \right) \cdot 1 \\ &= \sqrt{1 - \frac{N_2}{N} + \left(\frac{N_2}{N}\right)^2} \cos(15 - \alpha_{pitch})\end{aligned}\quad (3.9)$$

The evolution of α_{pitch} and $k_{\omega_{shortpitch}}$ depending on $\frac{N_2}{N}$ are shown in figure 3.7. $\alpha_{pitch}=15^\circ$ is obtained for $N_2 = 0.268N$. In this configuration, the winding factor is reduced by 7.2%. N_1 and N_2 need to be integers. Taking $N_2 = 0.25N$ appears as a good compromise. In

that case, $\alpha_{pitch} = 13.9^\circ$, so it remains a phase shift of 2.2° between the induced voltages of both stators. The winding factor is approximately reduced by 6.7%.

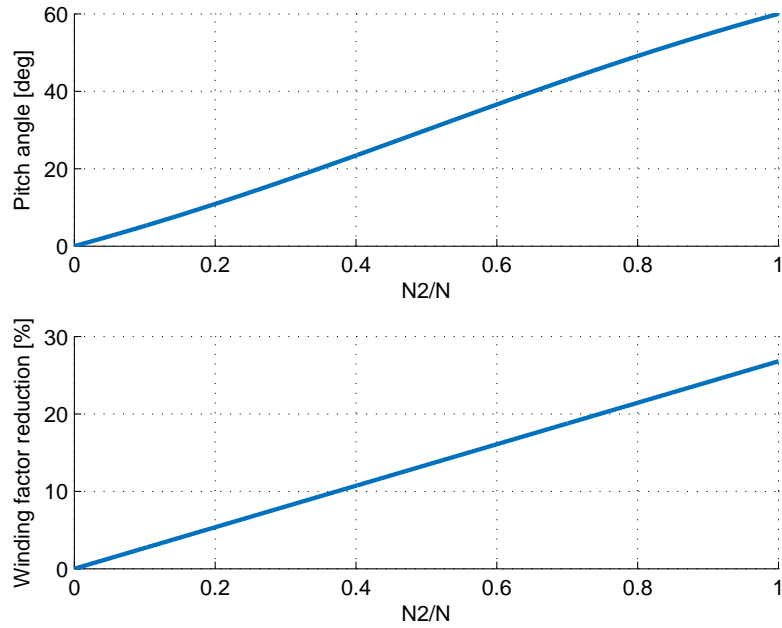


FIGURE 3.7: Pitch angle and winding factor reduction depending on $\frac{N_2}{N}$

3.3.3 Axial forces on magnets

The winding distribution for NSPP=1 with short pitch is reminded in figure 3.8.

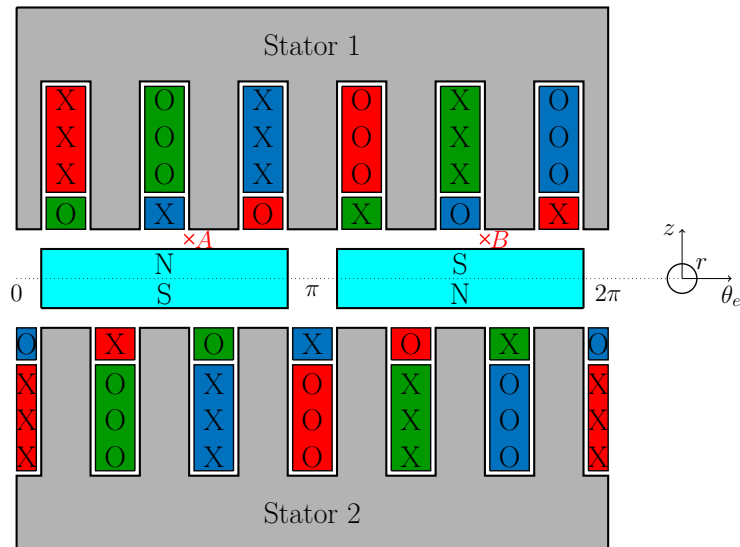


FIGURE 3.8: Winding distribution with short-pitch (NSPP=1)

For NSPP=1,2,... there is an integer number of stator slots per phase, so the magnetic field in each air gap is anti-periodic with a period π : $B_z(A) = -B_z(B)$, so:

$$B_z(r, \theta_e, z) = -B_z(r, \theta_e + \pi, z) \quad (3.10)$$

This property of the magnetic field has the consequences that the attracting force between the left magnet and the stator 1 ($\vec{F}z_{mag_{left} \leftrightarrow stat1}$) and the right magnet and the stator 1 ($\vec{F}z_{mag_{right} \leftrightarrow stat1}$) are equal (see equation 2.7), it results:

$$\begin{aligned} \vec{F}z_{mag_{left} \leftrightarrow stat1} &= \vec{F}z_{mag_{right} \leftrightarrow stat1} \\ \vec{F}z_{mag_{left} \leftrightarrow stat2} &= \vec{F}z_{mag_{right} \leftrightarrow stat2} \end{aligned} \quad (3.11)$$

The force acting on the right magnet is:

$$\begin{aligned} \vec{F}z_{mag_{right}} &= \vec{F}z_{mag_{right} \leftrightarrow stat1} + \vec{F}z_{mag_{right} \leftrightarrow stat2} \\ &= \vec{F}z_{mag_{left} \leftrightarrow stat1} + \vec{F}z_{mag_{left} \leftrightarrow stat2} \\ &= \vec{F}z_{mag_{left}} \end{aligned} \quad (3.12)$$

For integer NSPP, the axial force acting on both magnets are identical. There is a pulsating resulting axial force acting on the whole rotor. The frequency f of this pulsation is:

$$f = n_{slots} \frac{n}{60} \quad (3.13)$$

Where n_{slots} is the total number of teeth and n is the rotational speed in rpm. For example, a machine with NSPP=1 and 10 pole pairs ($n_p = 10$) has 60 teeth per stator, so the frequency of this force in Hz is equal to the rotational speed in rpm and reaches several kHz in the typical operating points of the machine. Its amplitude can reach several hundreds of N. This pulsating axial force needs to be withstood by the bearing of the rotor. High frequency pulsating forces are particularly critical for bearings and lead to a reduction of their lifetime.

3.4 Fractional number of slots per pole per phase

3.4.1 Fractional NSPP with concentrated windings

NSPP < 0.5 are fractional NSPP with concentrated windings. It is only possible to build them over a period of several pole pairs. For example, there are 3 teeth for 4 magnets with NSPP=0.25 proposed in [109]. Fractional concentrated windings have the advantage to offer a good magnetic coupling and high torque density [92]. The optimum magnetic coupling would be obtained with NSPP=0.33 where the number of teeth is equal to the number of magnets. But in this configuration, it is not possible to build multiphase machines and generate torque in every rotor position. NSPP with $n_{slots} = 2n_p \pm 1$ or $n_{slots} = 2n_p \pm 2$ have the best winding factor and offers the highest torque density[110]. In [14] NSPP=0.4 (12 slots for 10 magnets) is chosen. In [92], NSPP=0.375 (9 slots for 8 magnets) is proposed.

Fractional concentrated windings often offer a reduced torque ripple[110]. The cogging torque is small thanks to the particular combination of magnets and stators slots. Under load, the torque ripple is already small thanks to the low harmonic content of the induced voltage [111]. The main disadvantage of fractional concentrated windings machines is the high harmonic content of the spectrum of the magnetic field produced by the stator. The harmonics in the magnetic field increase the rotor losses [112]. In [111] two machines with NSPP=1 and NSPP=0.4 are compared. The machine with a fractional NSPP has at least twice as much losses in the magnets and in the rotor core than the machine with NSPP=1 under every load condition. The high harmonic content also strongly increases the inductance of the machine [92]. In [111] the reactive power is doubled. This high inductance and reactive power lead to a reduction of the power factor and the short circuit current of the machine. Finally, the peak power is reduced (see 2.2.2). High inductance and high rotor losses make fractional concentrated windings not well adapted for applications requiring high continuous and peak power like integrated motor-generators.

3.4.2 Fractional NSPP with distributed windings

Fractional distributed windings are also possible. Numbers of slots per pole per phase NSPP=0.75, 1.25, 1.75, . . . are respectively built with 9, 15 or 21 slots for 4 magnets and can only be built with a period of 2 pole pairs. Only designs with an even pole pairs number are possible. In this section, the example of NSPP=0.75 is treated. With this NSPP, there are 9 teeth for 4 magnets, so 2.25 teeth per magnet. The distribution factor is maximized if 9 windings coils are wound around 2 teeth. The phase shift between

two neighbors coils is $\frac{2 \cdot 360}{9} = 80^\circ$. It results in the complex phase diagram shown in figure 3.9.

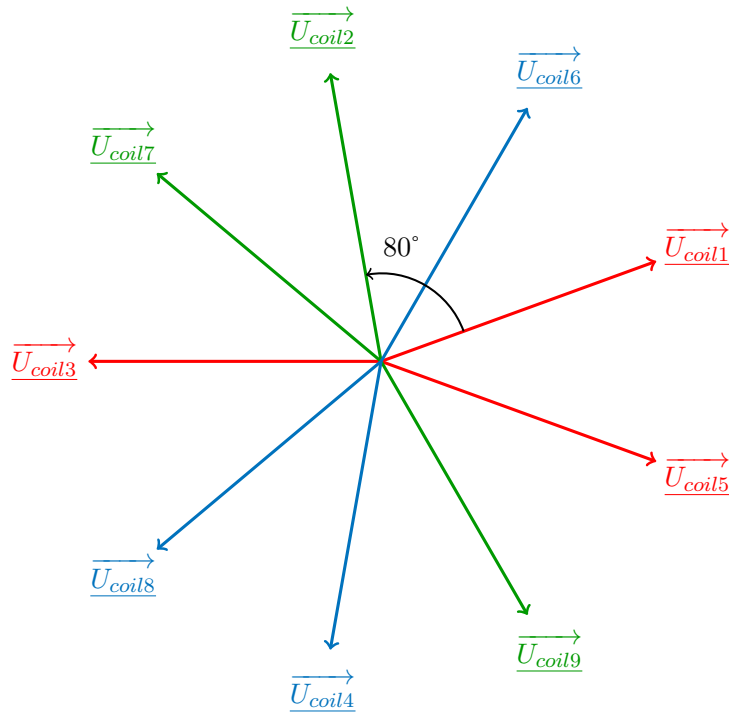


FIGURE 3.9: Complex phase diagram (NSPP=0.75)

The winding is maximized with the following connection of the coils:

- Phase U: Coils 1 and 5 in series with reversed coil 3
- Phase V: Coils 4 and 8 in series with reversed coil 6
- Phase W: Coils 7 and 2 in series with reversed coil 9

The corresponding circuit diagram is shown in figure 3.10.

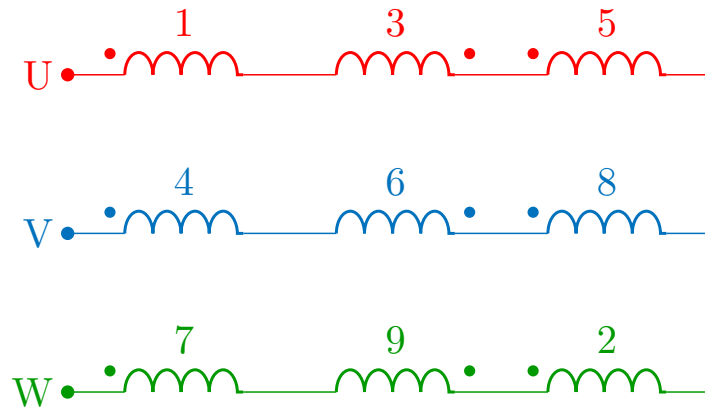


FIGURE 3.10: Electric circuit diagram (NSPP=0.75)

The winding factor k_w of this machine is:

$$\begin{aligned}
 k_w &= k_p \cdot k_d \\
 &= \frac{1 + 2 * \cos(20^\circ)}{3} \cdot \sin\left(\frac{2 * 80^\circ}{2}\right) \\
 &= 0.945
 \end{aligned}
 \tag{3.14}$$

The winding sheet of this machine is displayed in figure 3.11. This winding sheet shows approximately 2 pole pairs. 9 coils are wound around 2 teeth. In conformity with the electric circuit drawn in figure 3.10 the phase U is built with the serial connection of coils 1, 3 and 5. This winding sheet shows the difficulty to build fractional windings. At the upper coil end, the step is irregular. The coil end need to jump over 2 or 3 teeth. This irregular step makes the construction of the winding particularly difficult, especially for hairpin winding because it require different winding geometry. Furthermore it increases the size of the coil end.

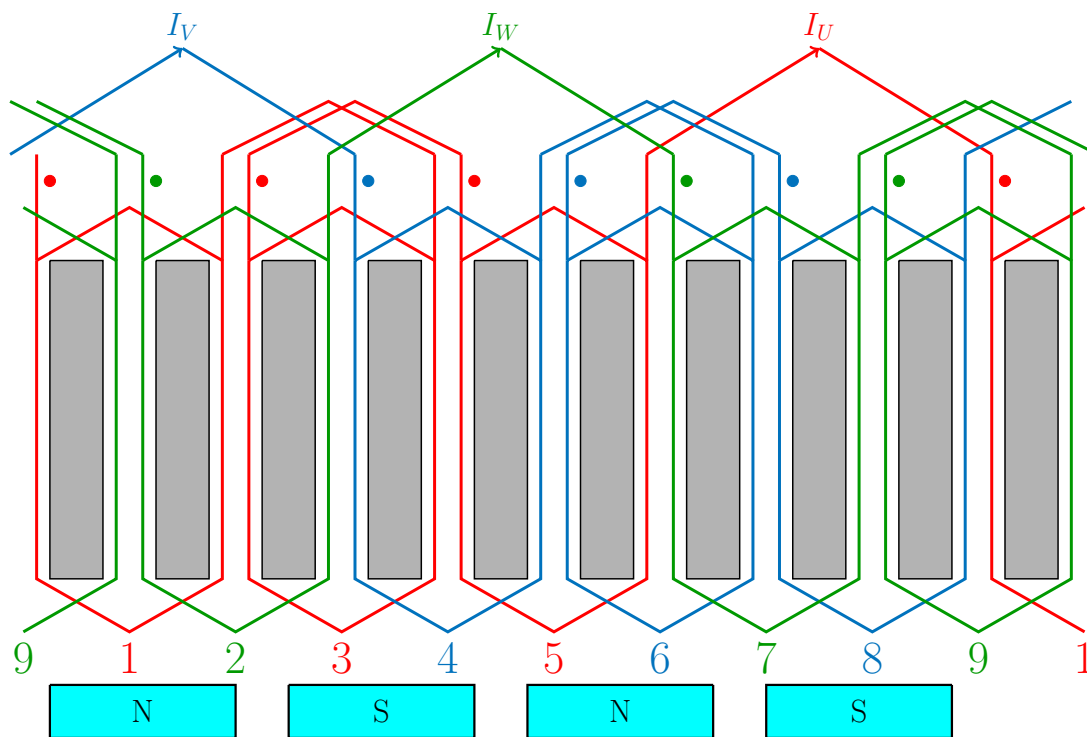


FIGURE 3.11: Winding sheet of one stator (NSPP=0.75)

The winding distribution with NSPP=0.75 is displayed in figure 3.12.

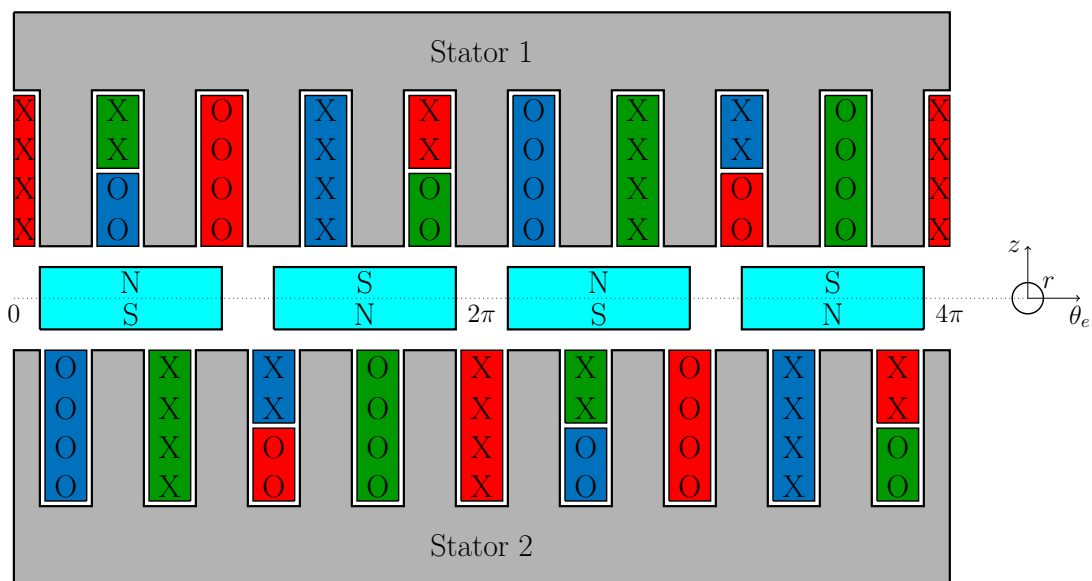


FIGURE 3.12: Winding distribution (NSPP=0.75)

3.4.3 Fractional distributed winding with NSPP=1.5

The winding distribution for NSPP=1.5 is presented in figure 3.13. This NSPP is particularly interesting thanks to following advantages:

- The period of the winding is one pole pair, so the electric connections are regular and every pole pair number is possible
- Such as NSPP=0.5, there is no resulting axial force on the rotor, as the forces on 2 neighbor magnets are opposed
- The width of the slots is smaller than with NSPP=0.5, so the magnetic coupling is increased

The main disadvantage of NSPP=1.5 is the size of the large coil ends which increases the copper losses and reduces the efficiency.

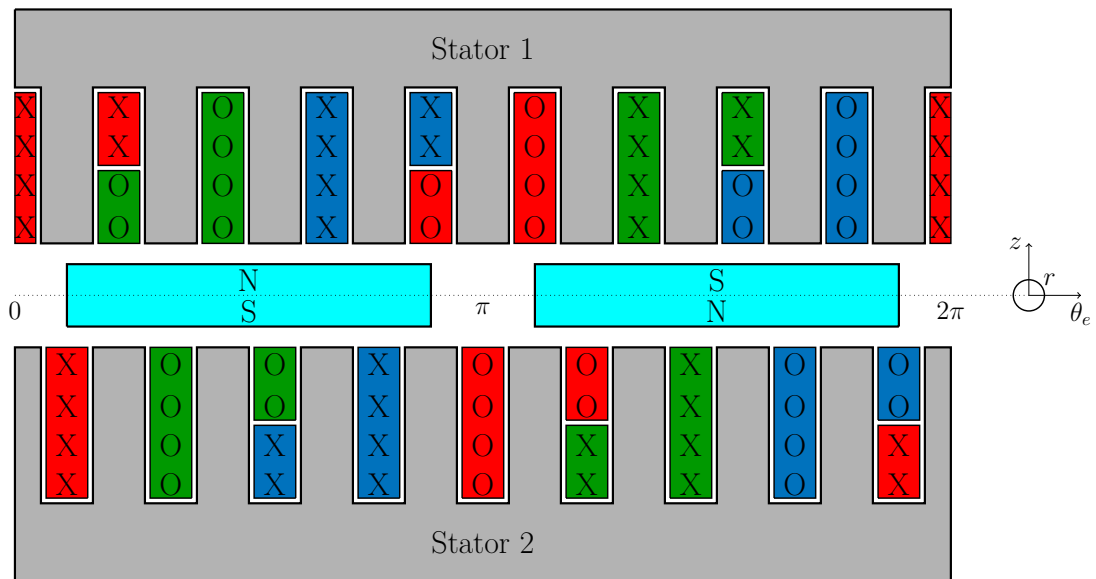


FIGURE 3.13: Winding distribution (NSPP=1.5)

The winding factor k_w of this machine is:

$$\begin{aligned}
 k_w &= k_p \cdot k_d \\
 &= \frac{1 + 2 * \cos(20^\circ)}{3} \cdot \sin\left(\frac{160^\circ}{2}\right) \\
 &= 0.945
 \end{aligned}
 \tag{3.15}$$

3.5 Comparison between the numbers of slots per pole per phase

In this section a comparison is performed between four different NSPP: NSPP=0.5, NSPP=0.75, NSPP=1 with short-pitch and NSPP=1.5. At first the spectrum of Magneto-Motive Force (MMF) is analyzed. Then, FEM simulations are performed to compare the performances of these machines and choose the best suited NSPP.

3.5.1 Magneto-motive force

The analysis of the MMF and its harmonics is particularly important to compare different NSPP. The fundamental component of the MMF needs to be as high as possible to maximize the torque generated by the machine. On the contrary, harmonics need to be minimized to avoid the generation of losses in the rotor induced by harmonics of the air gap magnetic field. Furthermore high harmonics content increases the inductance of the winding and reduces the maximum peak power of the machine (see 2.2.2). The number of turns of the machine with NSPP=0.5 is assumed to be $N=1$. For other machines, the number of turns have been scaled to maintain the same electric loading and enables a fair comparison.

The MMF of the global machine (both stators) are plotted in figure 3.14. The fundamental is plotted with dashed lines. Machines with NSPP=0.75 and NSPP=1.5 have the highest fundamental in their MMF and should generated the highest torque. The machine with NSPP=0.5 has the smallest fundamental.

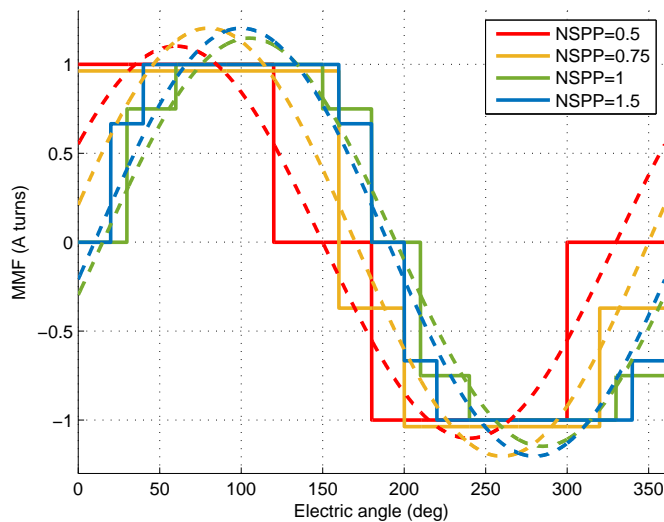


FIGURE 3.14: Magneto-motive forces and fundamental for NSPP=0.5, NSPP=0.75, NSPP=1 and NSPP=1.5

The spectrum of the MMF up to the 20th harmonic are displayed in figure 3.15. Following observations can be made:

- NSPP=0.5 has only uneven component in its mmf. It is the only winding without $3 \cdot n^{th}$ harmonics. But this winding has high 5th, 7th, 11th and 13th harmonics which are responsible of an important torque ripple and high rotor losses. The Total Harmonic Distortion (THD) is 8.5%.
- NSPP=0.75 is the only machine with even orders in the mmf. Theses harmonics do not generate torque ripple but generate rotor losses. Uneven harmonics, especially the 5th, 7th, 11th and 13th harmonics are small. The winding has the worst THD (9.4%).
- NSPP=1 has small 3th, 5th and 7th harmonics but the 11th and 13th are higher. This winding has the best THD(4.1%). This machine appears as a good concept to minimize the rotor losses and the torque ripple.
- NSPP=1.5 has the same spectrum as NSPP=0.75 without even components. Only the 17th and 19th could generate a torque ripple or rotor losses, but the amplitude of theses critical harmonics are much smaller than for other NSPP. This machine has the second best THD (5.2%) and appears like NSPP=1 as good solution to minimize rotor losses and the torque ripple.

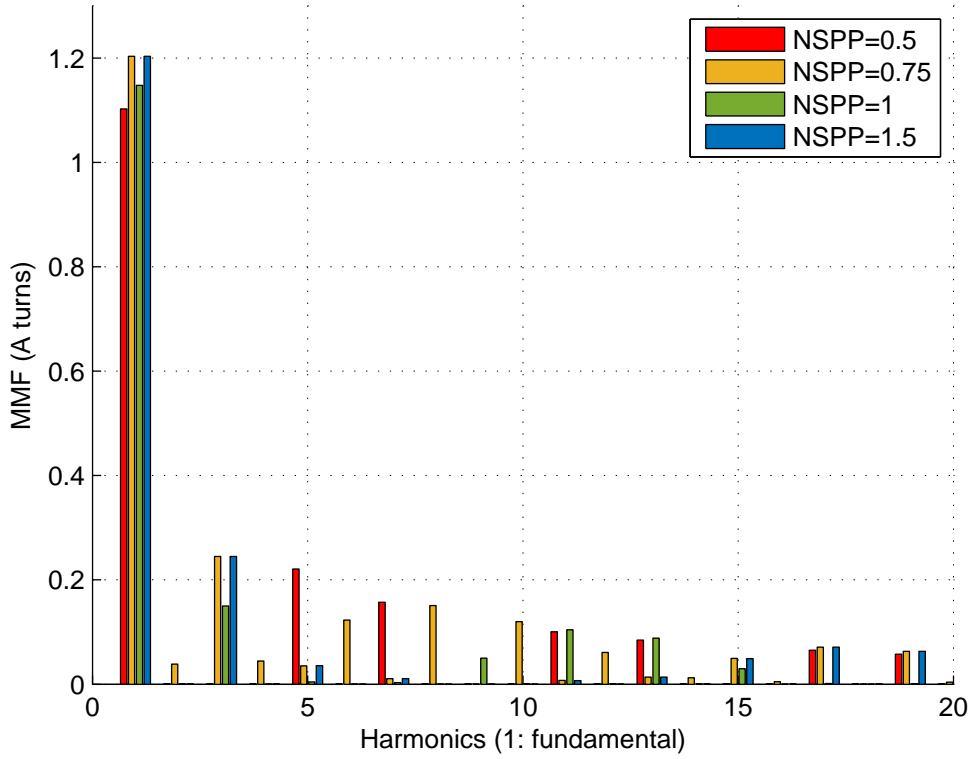


FIGURE 3.15: Fourier spectrum of the magneto-motive forces

3.5.2 FEM simulations

This comparison is based on an example of AFM . With an inside diameter of 185 mm, an outside diameter of 280 mm, an axial length of 80 mm and a peak torque of approximately 300 Nm this machine fits roughly the specification (see table 2.1). This reference machine has 54 teeth. This number is compatible with the 4 selected NSPP. The geometry of the stator is unchanged. The rotor geometry is adapted to modify the number of pole pairs and so the NSPP. In this comparison, an additional machine with NSPP=1.5 and 8 pole pairs is simulated to show the potential of this winding which suffers from too high magnetic saturation with lower pole pair numbers. To make a fair comparison the magnet mass as well as the current density are the same for each design. All designs have been simulated in the three extreme operating points defined in the appendix A.4.

- OP1: no load ($I = 0$, α undefined, $n = n_{max}=7000$ rpm)
- OP2: full load ($I = I_{max} = I_q$, $\alpha = 90^\circ$, $n=2000$ rpm)
- OP3: short circuit ($I = I_{sc}$, $\alpha = 180^\circ$, $n = n_{max}=7000$ rpm)

	Parameter	NSPP				
		0.5	0.75	1	1.5	
	Pole pairs number	18	12	9	6	8
	Number of slots	54	54	54	54	72
OP1	Induced voltage	233 Vrms	265 Vrms	254 Vrms	263 Vrms	272 Vrms
	Cogging torque (peak)	34 Nm	1 Nm	24 Nm	7 Nm	5 Nm
	Magnet losses	1175 W	1192 W	1180 W	1083 W	902 W
	Axial force (per magnet)	7 N	10 N	18 N	16 N	12 N
	Axial force (rotor)	0 N	0 N	288 N	0 N	0 N
OP2	Maximum torque	294 Nm	324 Nm	323 Nm	284 Nm	321 Nm
	Saturation	23 %	25 %	22 %	34 %	28 %
	Torque ripple (peak)	39 Nm	6 Nm	25 Nm	34 Nm	16 Nm
	Magnet losses	205 W	199 W	207 W	162 W	132 W
	Axial force (per magnet)	20 N	39 N	21 N	18 N	14 N
	Axial force (rotor)	0 N	0 N	216 N	0 N	0 N
	Efficiency	86 %	87 %	85 %	82 %	85 %
OP3	Isc	200 Arms	212 Arms	181 Arms	177 Arms	205 Arms
	Magnet losses	443 W	508 W	416 W	344 W	310 W
	Axial force (per magnet)	21 N	20 N	19 N	6 N	5 N
	Axial force (rotor)	0 N	0 N	314 N	0 N	0 N
	Phase resistance (100 °C)	15 mΩ	18 mΩ	21 mΩ	23 mΩ	20 mΩ
	Inductance	88 μH	137 μH	181 μH	337 μH	226 μH

TABLE 3.1: Comparison between main NSPP

These results enable following observations:

- NSPP=0.5: the concentrated winding has the smallest torque and is far away from achieving the specification. Furthermore the torque ripple and the magnet losses are bad with this design. Optimizing these parameters by increasing the air gap or adapting the teeth geometry would probably decrease the peak torque. The main advantage of this winding is the small electric resistance thanks to smaller coil end windings which reduce the copper losses and increase the efficiency. This machine have been simulated with 18 pole pairs. In this case, the electric frequency at the maximum rotational speed is 2100 Hz. This frequency is very high and could lead to difficulties to be driven properly by the inverter. A reduction of the number of pole pairs appears necessary.
- NSPP=0.75: this winding has the best torque density and the best torque ripple. At no load, magnet losses are mainly depending on the number of teeth (and the

space between two neighbor teeth). Magnet losses at load are smaller than with concentrated winding. Under load, this machine has the worst axial force on the magnets but no resulting axial force on the rotor. Thanks to small coil ends and a high torque density this machine has the best efficiency.

- NSPP=1: This winding has a similar torque density than the machine with NSPP=0.75 but a much worse torque ripple mainly due to the cogging torque and the 11th and 13th harmonics in the MMF. The main disadvantages of this winding are the axial force on the rotor and a poor efficiency due to the coil end windings.
- NSPP=1.5: This winding has the best magnet losses thanks to its MMF with the second best THD. With the same stator design than the other NSPP, the torque density is poor. With only 6 pole pairs, this machine has much higher magnetic saturation than the other machines. This is mainly due to the reduction of the number of pole pair which increases the length of the magnetic flux lines and saturates the stator yoke. This is not a characteristic of NSPP=1.5. The machine have been scaled to 8 pole pairs (same current density, same magnet mass) by increasing the number of teeth to 72 and reducing the space between two neighbor teeth by a quarter. This modification increases the peak torque to a similar value as with NSPP=0.75 and NSPP=1 and strongly reduces the magnet losses and the torque ripple.

3.5.3 Selection of the optimum NSPP

The main advantages and disadvantages of the several NSPP are displayed in the following spider plot:

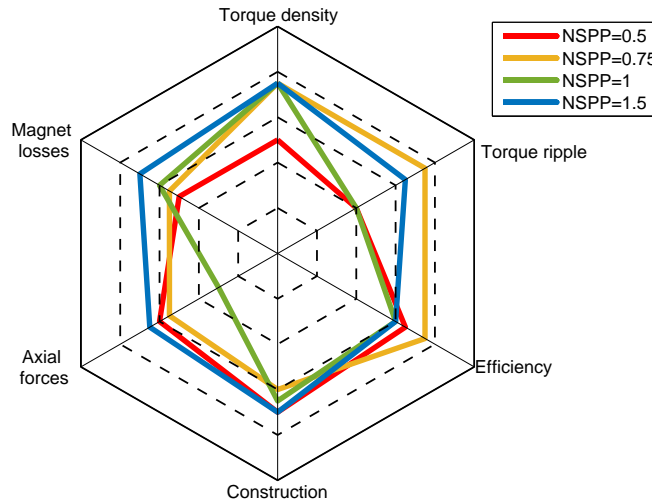


FIGURE 3.16: Spider plot comparison of the selected NSPP

In this spider plot, NSPP=0.75 and NSPP=1.5 appear as the best suited NSPP. NSPP=0.5 suffers from a poor torque density, high magnet losses and a high torque ripple. NSPP=1 is beaten by NSPP=1.5 for every parameter. NSPP=0.75 appears as the best NSPP for machines requiring high torque density, high efficiency and a small torque ripple. Main disadvantages are higher magnet losses (even if a proper design could reduce them) and a harder construction of the winding due the irregular winding step. NSPP=1.5 offers a good torque density and low magnet losses but suffers from a bad efficiency due to larger coil end windings. **Optimizing the efficiency is a major priority in the designing of an electric machine for hybrid and electric vehicles, for this reason NSPP=0.75 is selected. The machine with NSP=0.75 simulated in 3.5.2 will be noted AFM₁.**

Conclusion

In this chapter, the number of slots per pole per phase is studied. The relation between the number of stator slots and the number of poles influences strongly the performances of the machine. Following NSPP have been studied:

- NSPP=0.5: this NSPP is often used for integrated motor-generators. It has a simple topology and offers small coil end windings. However the torque density is poor and the magnet losses are high.
- Integer NSPP: this NSPP show interesting performances but suffers from the unbalanced induced voltage making the parallel connection of the stator harder and the high axial force on the rotor.
- Fractional concentrated windings: these NSPP offer a high torque density. However, the rotor losses are high and the high inductance reduces the peak power.
- Fractional distributed windings: these NSPP, especially NSPP=0.75 offer good performances. The construction of the windings is harder and needs to be taken into account.
- NSPP=1.5: this NSPP offers a good torque density and reduced magnets losses but suffers from the large coil ends worsening the efficiency.

After a comparison of these NSPP, NSPP=0.75 has been selected for the dimensioning of the machine.

Chapter 4

Analytic model for losses in axial-flux machines

Contents

Introduction	80
4.1 Joule losses in the electric conductors	80
4.1.1 Generalities over conductor losses	80
4.1.2 Alternating current losses	81
4.1.2.1 Skin effect in electrical machines	81
4.1.2.2 Analytic model	82
4.1.3 Optimized hairpin winding for axial-flux machines	87
4.1.3.1 Concept and FEM calculations	87
4.1.3.2 Analytic model	90
4.2 Iron losses in the stator soft magnetic material	93
4.2.1 Hysteresis losses	93
4.2.2 Eddy current losses	94
4.2.3 Excess losses and global expression	94
4.3 Eddy current losses in the rotor permanent-magnets	96
4.3.1 Generalities over magnet eddy current losses	96
4.3.2 Analytic model for magnet losses	98
4.3.2.1 Influence of the coil current on magnet losses	98
4.3.2.2 Influence of the temperature	102
Conclusion	105

Introduction

The minimization of losses in an electric machine is a priority of its dimensioning. High losses reduce the efficiency of the machine and limits their continuous power. In this chapter, following losses sources generated in the magnetic circuit are investigated and modeled with an analytic model:

- Joule losses in the electric conductors
- Iron losses in the stator soft magnetic material
- Induced eddy current losses in the rotor permanent-magnets

Other losses like friction or bearing losses are not investigated in this work.

4.1 Joule losses in the electric conductors

4.1.1 Generalities over conductor losses

The conductor losses P_{cu} can be calculated thanks to the well known equation 4.1.

$$P_{cu} = n_{phase}RI^2 \quad (4.1)$$

Where R is the phase resistance and I is the RMS value of the phase current. For a continuous current, the phase resistance R_{dc} is obtained thanks to formula 4.2 [5].

$$R_{dc} = \frac{Nl_{wdg}}{\sigma p_{wdg}s_{wdg}} \quad (4.2)$$

Where N is the number of turns, l_{wdg} is the total length of the conductor, p_{wdg} is the number of parallel conductors, s_{wdg} is the surface of the conductor and σ is the electric conductivity of the conductor. σ depends on the material and increases with the temperature (see table C.2). For automotive applications and especially hybrid motors, the temperature of the winding is much higher than 20 °C and typically oscillates between 100 °C and 180 °C.

4.1.2 Alternating current losses

4.1.2.1 Skin effect in electrical machines

Additional conductor losses are generated by alternating current due to the skin effect and the proximity effect in the conductor. The alternative current flowing in the conductor generates a pulsating magnetic field in the conductor and its neighborhood. This magnetic field induces eddy current in the conductor (skin effect) and eventually in the neighbors conductors (proximity effect). This additional eddy current generates additional Joule losses in the conductor and increases its resistance with the frequency of the current flowing in it. These additional losses are AC (Alternative Current) losses. Figure 4.1 shows the skin effect in a bar conductor sandwiched by magnetic material like in the slot of an electric motor.

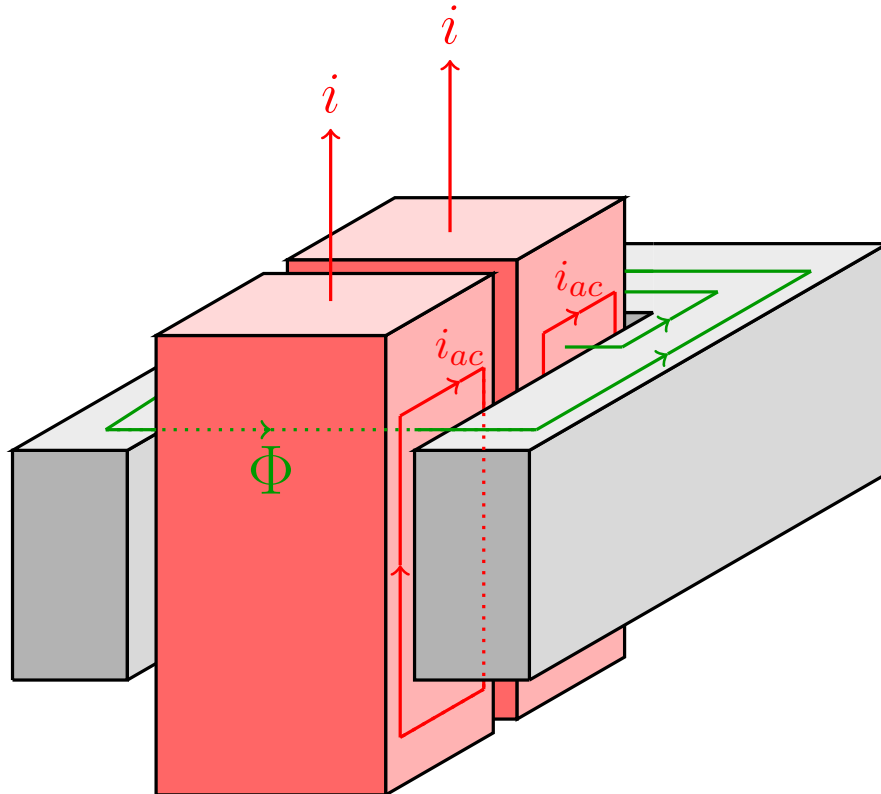


FIGURE 4.1: Skin effect in bar conductors in electric machines ($N_h = 2$)

In figure 4.1 the electric current i circulates in the conductor from the bottom to the top. It generates a magnetic field Φ flowing counter clockwise (see from the top) and from the left to the right in the conductor. This magnetic field induces an eddy current i_{ac} flowing in the conductor from the bottom to the top in the front and from the top to the bottom at the back. So the induced eddy current increases the current density in

the front of the conductor (nearby the air gap) and reduces it nearby the back iron. The reduction of the area where electric current is flowing increases the electric resistance of the conductor and the losses according to equation 4.2.

In electric machines, the presence of magnetic material around the conductor increases significantly the generated magnetic field and the consequences of skin effect. For this reason the increase of the resistance with the electric frequency is mainly localized in the magnetic circuit and is negligible in the end connections [5].

4.1.2.2 Analytic model

The skin effect coefficient $k_r(f)$ is defined as the relation between the electric resistance of a winding at a related frequency f and its resistance at 0 Hz:

$$k_r(f) = \frac{R(f)}{R_{dc}} \quad (4.3)$$

4.1.2.2.1 Hairpin winding

A calculation of this coefficient has been done in [113]. In the case of N_h rectangular conductors disposed above each other in a rectangular slot and carrying the same electric current (see figure 4.2), the skin effect coefficient can be estimated with equation 4.4.

$$k_r(f) = \varphi(\varepsilon(f)) + \frac{N_h^2 - 1}{3} \psi(\varepsilon(f)) \quad (4.4)$$

In the case of two layers of conductors belonging to two different electric phases (see figure 4.2), k_r can be calculated thanks to following equation [5]:

$$k_r(f) = \varphi(\varepsilon(f)) + \left(\frac{N_h^2 - 1}{3} - \left(\frac{N_h}{2} \sin \frac{\gamma}{2} \right)^2 \right) \psi(\varepsilon(f)) \quad (4.5)$$

Where N_h is the number of electric conductors per slot arranged above each other and γ is the phase difference between the electric current circulating in the 2 layers. For three phase winding, $\gamma = 60^\circ$.

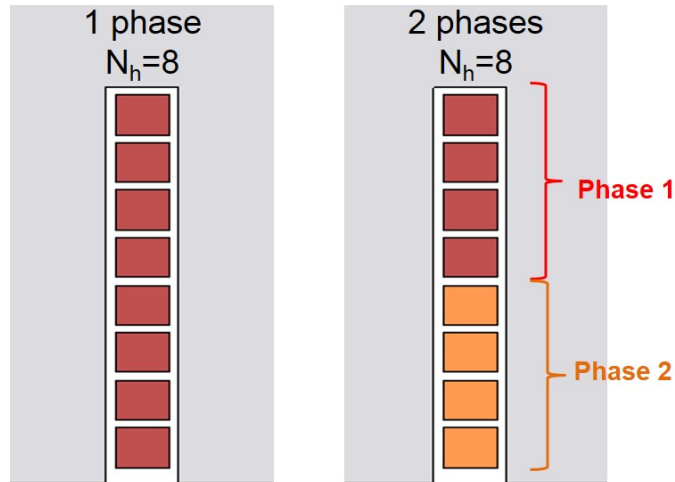


FIGURE 4.2: One-phase and two-phases conductors in a rectangular slot

$\varphi(\varepsilon(f))$ and $\psi(\varepsilon(f))$ are defined in following formulas:

$$\varphi(\varepsilon(f)) = \varepsilon(f) \frac{\sinh 2\varepsilon(f) + \sin 2\varepsilon(f)}{\cosh 2\varepsilon(f) - \cos 2\varepsilon(f)} \quad (4.6)$$

$$\psi(\varepsilon(f)) = 2\varepsilon(f) \frac{\sinh \varepsilon(f) - \sin \varepsilon(f)}{\cosh \varepsilon(f) + \cos \varepsilon(f)} \quad (4.7)$$

For rectangular conductors arranged above each other (hairpin winding), $\varepsilon(f)$ is defined by following formula:

$$\varepsilon(f) = h_c \sqrt{\pi f \mu_0 \sigma \frac{w_c}{w_s}} \quad (4.8)$$

Where h_c is the height of each electric conductor, w_c its width, f is the frequency of the electric current, μ_0 is the vacuum permeability, σ is the electric conductivity and w_s is the width of the slot.

To check the precision of the FEM calculations, a simple winding comprising 8 rectangular conductors (similar to figure 4.2) in a slot has been simulated with FEM between 0 Hz and 1000 Hz. The copper losses and k_r are obtained from the FEM calculations. Two cases have been calculated:

- 1 phase: only one electric phase in the slot, so the same current flows in the 8 conductors ($\gamma = 0$)
- 2 phases: double layer winding with $\gamma = 60^\circ$

The model presented in equation 4.5 is compared with the FEM calculations in figure 4.3. In both cases, the model and the FEM calculations give the same results. The error is smaller than 1%, so FEM calculations can be trusted:

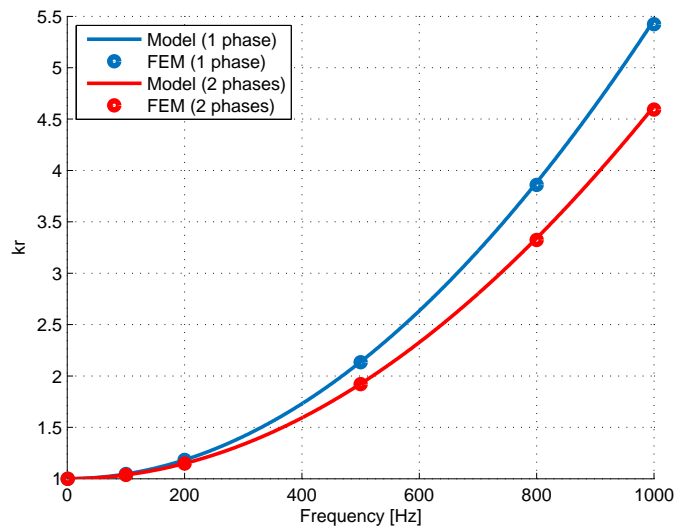


FIGURE 4.3: Skin effect coefficient k_r depending on the electric frequency

4.1.2.2.2 Pull in winding

For pull in winding (round small conductors), equation 4.8 has to be modified. Each conductor is approximated as a square equivalent conductor with the same section:

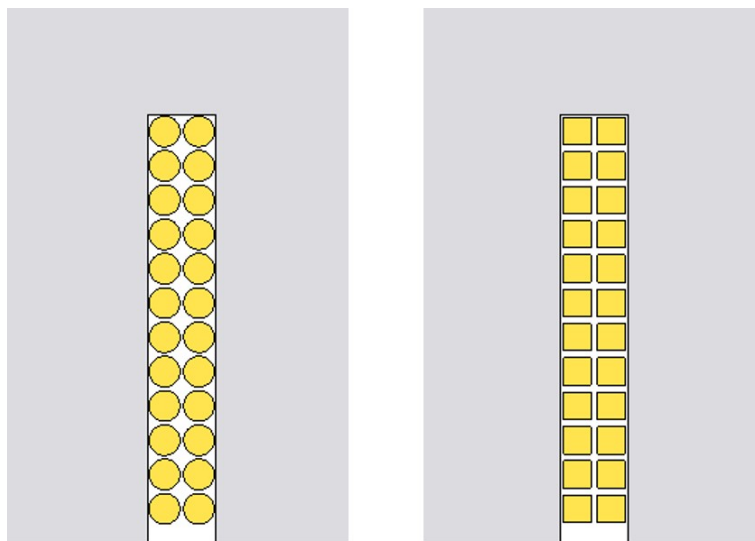


FIGURE 4.4: Round and equivalent square conductors in a rectangular slot

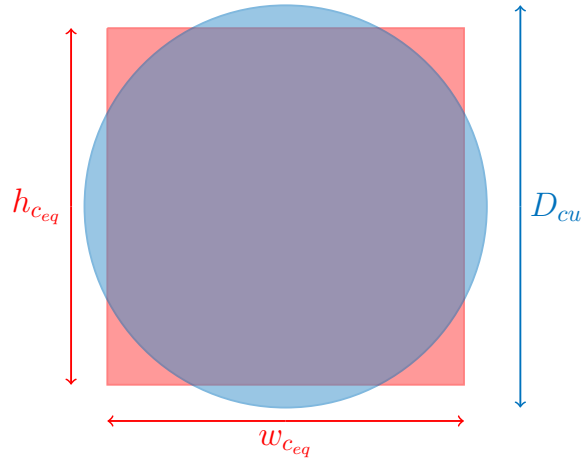


FIGURE 4.5: Equivalent square conductor

$$h_{c_{eq}} = w_{c_{eq}} = D_{cu} \sqrt{\frac{\pi}{4}} \quad (4.9)$$

Where D_{cu} is the diameter of the conductor. The copper fill factor k_{cu} is the relation between the copper surface and the slot surface and can be calculated with following formula:

$$k_{cu} = \frac{N_w N_h \frac{\pi}{4} D_{cu}^2}{w_s h_s} \quad (4.10)$$

Where h_s is the height of the slot, N_h is the number of conductors arranged above each other and N_w is the number of conductors arranged side by side in the slot ($N_h = 12$ and $N_w = 2$ in figure 4.4). Furthermore the copper fill factors in the width and the height directions are the same, so:

$$\frac{N_w}{w_s} = \frac{N_h}{h_s} \quad (4.11)$$

$$k_{cu} = \left(\frac{N_w D_{cu} \sqrt{\pi}}{2w_s} \right)^2 \quad (4.12)$$

So $\varepsilon(f)$ can be calculated as:

$$\begin{aligned}
 \varepsilon(f) &= h_{ceq} \sqrt{\pi f \mu_0 \sigma \frac{N_w w_{ceq}}{w_s}} \\
 &= D_{cu} \frac{\pi}{2} \sqrt{f \mu_0 \sigma \frac{N_w D_{cu} \sqrt{\pi}}{2 w_s}} \\
 &= D_{cu} \frac{\pi}{2} \sqrt{f \mu_0 \sigma \sqrt{k_{cu}}}
 \end{aligned} \tag{4.13}$$

Round wires and the equivalent rectangular wires have been calculated with FEM. The results are presented in figure 4.6. Approximating the round wire with an equivalent square conductor leads to a small overestimation of the skin effect coefficient (4% in this case). The model proposed in equation 4.13 fits very well the rectangular equivalent conductor and gives a good approximation of the round wire.

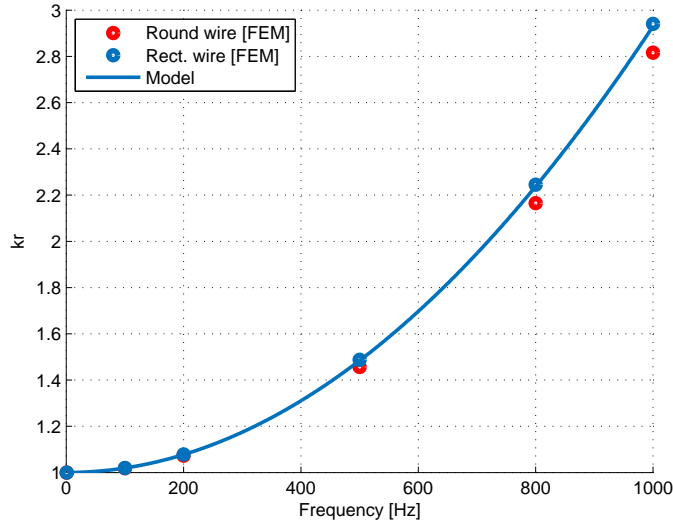


FIGURE 4.6: Skin effect coefficient k_r depending on the electric frequency

Contrary to the hairpin winding, the positioning of the conductors with pull in winding is often disordered. This influences the skin effect coefficient and the precision of the proposed model is worsen.

4.1.2.2.3 End windings

As explained in 4.1.2.1, skin effect in electric machines only appears in the magnetic circuit, so the resistance of the coil end winding remains constant. The variation of the electric resistance with the frequency f is:

$$R(f) = R_{dc} \frac{2k_r(f)l_{fe} + l_{co_{out}} + l_{co_{in}}}{2l_{fe} + l_{co_{out}} + l_{co_{in}}} \quad (4.14)$$

Where R_{dc} is the phase resistance at 0 Hz, $k_r(f)$ is the skin effect coefficient, l_{fe} is the radial length of the magnetic circuit and $l_{co_{out}}$ and $l_{co_{in}}$ are respectively the length of the outside and inside coil ends per turn.

4.1.3 Optimized hairpin winding for axial-flux machines

4.1.3.1 Concept and FEM calculations

The construction of the stator of an AFM by pressing of SMC adds some geometry constraints (see 2.4.5.1.2). One of them, is that the slot needs a trapezoidal profile (wider on the air gap as on the teeth ground) and can not be built rectangular like in common radial-flux machines. The slot width w_s depends on the axial position in the slot. The winding's dispositions (state of the art and optimized) in one stator slot are displayed in figure 4.7.

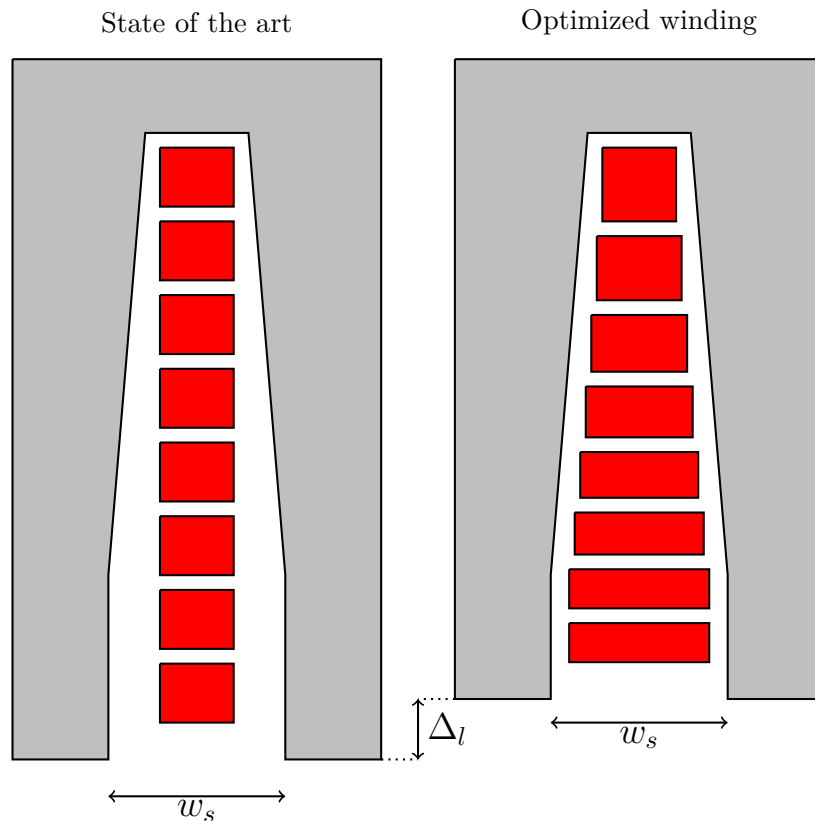


FIGURE 4.7: State of the art and optimized hairpin winding for AFM

The state of the art construction has the disadvantage that the copper fill factor is poor. On the top of the slot, there is a large loss of space at each side of the conductor. With the optimized construction, following advantages can be obtained compared to the state of the art solution:

- The copper fill factor is better. It enables a smaller current density in the conductor and lower Joule losses. Furthermore, the winding needs a shorter axial length, so the teeth length can be reduced (Δl). It leads to a reduction of the axial length of the machine, its weight, a reduction of the iron losses and an increased torque by reducing the effects of magnetic saturation in the stator.
- The AC losses in the copper can be reduced. Conductors placed on the top of the slot are more sensitive to skin effect. By reducing their height and making them wider, the skin effect coefficient calculated with equations 4.5 and 4.8 is reduced.

To estimate the benefit of this construction on the copper losses, the skin effect coefficient has been calculated with FEM (Finite Element Method) calculations with the software JMAG. For this study, 9 slots containing 8 conductors are modeled. This configuration enables the simulation of a three phase winding with slots containing one or two phases. The section of the conductors is fixed to 7.5 mm^2 . The isolation between the conductors each other and between them and the teeth is fixed to 0.5 mm. Solutions with 1, 2, 4 and 8 different conductor sizes are evaluated.

Figure 4.8 shows the model with 2 different sizes of winding:

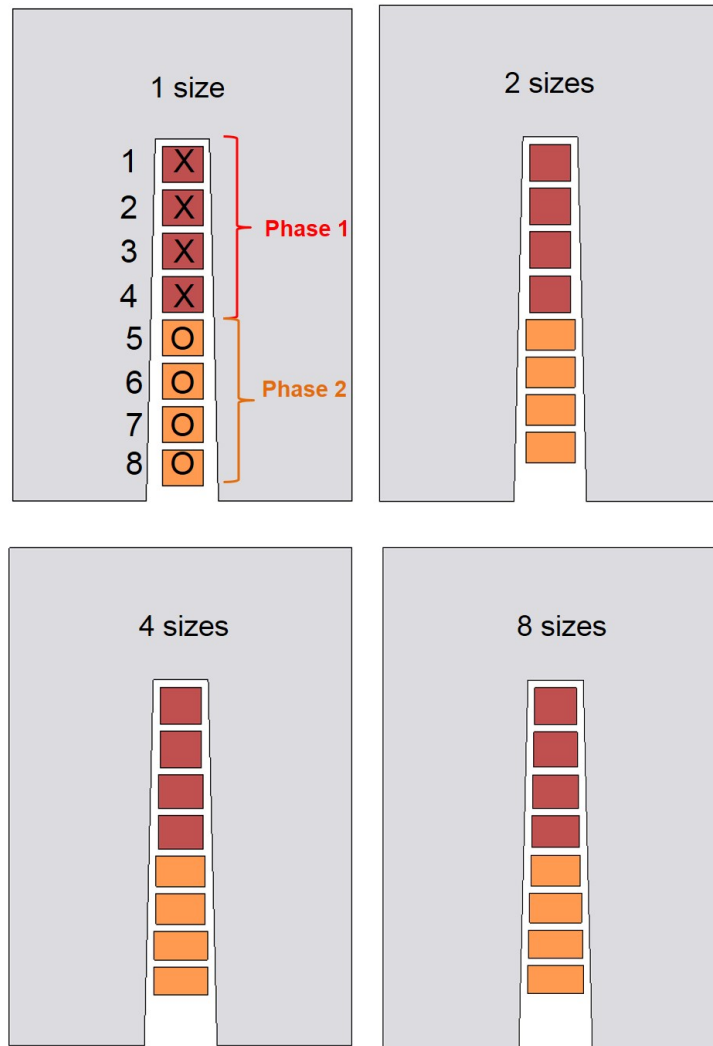


FIGURE 4.8: FEM Model with 1,2,4 and 8 different conductor sizes

The frequency of the electric current is varied between 0 Hz and 1000 Hz. The resistivity of the copper is fixed to $\rho = 2.30 \cdot 10^{-8} \Omega.m$ which corresponds to a temperature of 100 °C (see table C.2). The evolution of the skin effect coefficient k_r is presented in figure 4.9.

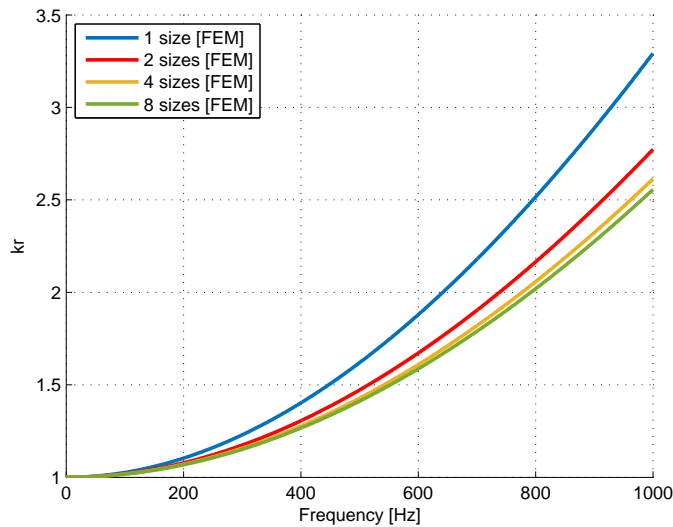


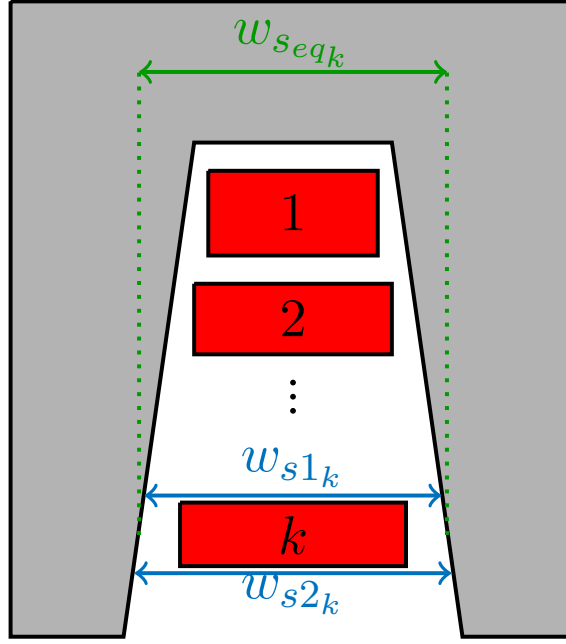
FIGURE 4.9: Skin effect coefficient k_r depending on the electric frequency

This figure shows the effect of skin effect on the electric resistance and the influence of the conductor geometry. With only 2 different conductor sizes, the skin effect coefficient is reduced by 17% ($k_r = 3.55$ to $k_r = 2.97$). With 4 and 8 different conductor sizes, this reduction reaches 22% ($k_r = 2.77$) and 24% ($k_r = 2.7$). The construction of the winding according to the proposed geometry is harder and leads to additional construction difficulties and cost. So, for each design, the technical advantages have to be evaluated and compared to the additional cost in order to find the optimum between performances and cost.

4.1.3.2 Analytic model

The model proposed in 4.1.2.2 is well suited for rectangular slots and identical conductors sizes. In the case of the optimized winding this model has to be adapted. An example of calculation of the skin effect for arbitrary cross section is presented in [113].

The goal of this analytic model is to calculate the skin effect coefficient of each conductor (noted $k_{rk}(f)$ for the k^{th} conductor) and obtain from these values the skin effect coefficient of the complete winding: $k_r(f)$. In [113], $k_{rk}(f)$ is calculated for a rectangular section. In this expression, $k_{rk}(f)$ depends only on k , the geometry of the conductor and the width of the slot alongside the conductor. For this analytic model, the slot width is assumed to stay constant alongside the k^{th} conductor. The equivalent slot width is noted ws_{eqk} . This assumption stays right as long as the chamfer angle is small.


 FIGURE 4.10: Calculation of the equivalent slot width (k^{th} conductor)

$$w_{seq_k} = \frac{w_{s1_k} + w_{s2_k}}{2} \quad (4.15)$$

Coefficient $\varepsilon_k(f)$ and functions $\varphi(\varepsilon_k(f))$ and $\psi(\varepsilon_k(f))$ can be defined analog to the analytic calculation presented in 4.1.2.2. The only difference, is that $\varepsilon_k(f)$ has a different value for each conductor, as the width and the height of the conductor (w_{c_k} and h_{c_k}) and the slot width are different for every conductor:

$$\varepsilon_k(f) = h_{c_k} \sqrt{\pi f \mu_0 \sigma \frac{w_{c_k}}{w_{seq_k}}} \quad (4.16)$$

$$\varphi(\varepsilon_k(f)) = \varepsilon_k(f) \frac{\sinh 2\varepsilon_k(f) + \sin 2\varepsilon_k(f)}{\cosh 2\varepsilon_k(f) - \cos 2\varepsilon_k(f)} \quad (4.17)$$

$$\psi(\varepsilon_k(f)) = 2\varepsilon_k(f) \frac{\sinh \varepsilon_k(f) - \sin \varepsilon_k(f)}{\cosh \varepsilon_k(f) + \cos \varepsilon_k(f)} \quad (4.18)$$

In the case of a two layer winding (see figure 4.11), the skin effect coefficient of the k^{th} conductor $k_{r_k}(f)$ is different if the conductor is located in the first layer ($1 \leq k \leq \frac{N_h}{2}$) or in the second layer ($\frac{N_h}{2} + 1 \leq k \leq N_h$). In the first layer [113]:

$$k_{r_k}(f) = \varphi(\varepsilon_k(f)) + (k^2 - k)\psi(\varepsilon_k(f)) \quad (4.19)$$

For the conductors in the second layer:

$$k_{r_k}(f) = \varphi(\varepsilon_k(f)) + \left(k^2 - k + \frac{1}{2}(N_h^2 + N_h - 2kN_h)(1 - \cos\gamma) \right) \psi(\varepsilon_k(f)) \quad (4.20)$$

The skin effect coefficient of the global winding depending on the frequency of the electric current $k_r(f)$ can be calculated with:

$$k_r(f) = \frac{1}{N_h} \sum_{k=1}^{N_h} k_{r_k}(f) \quad (4.21)$$

This model has been applied to the winding calculated in 4.1.3.1 and compared with the results of the FEM calculation in figure 4.11.

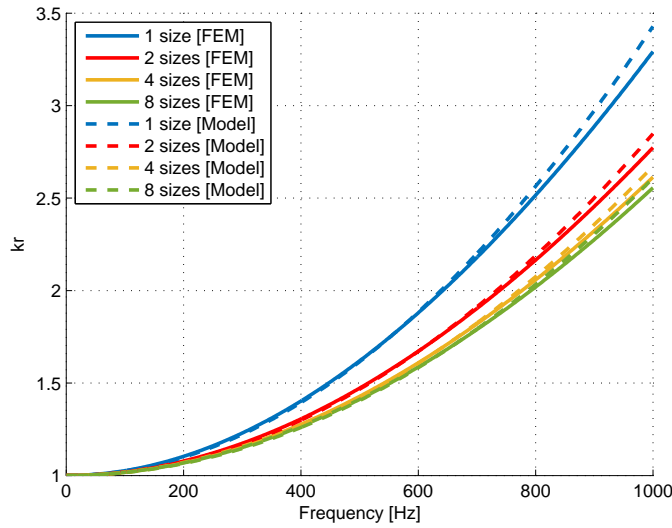


FIGURE 4.11: Skin effect coefficient comparison between FEM and the model

The model gives a satisfying estimation of the skin effect coefficient. Depending on the geometry, the error varies between 2% and 4%. The model lightly overestimates the losses. This overestimation is mainly due to the underestimation of the length on the magnetic flux line (see figure 4.10) which underestimates the equivalent slot width w_{seq_k} . The precision and the light over estimation make this model satisfying for a fast estimation of the skin effect coefficient by saving long FEM calculations.

4.2 Iron losses in the stator soft magnetic material

Iron losses in the stator magnetic material can be divided in three main losses sources:

- Hysteresis losses
- Eddy current losses
- Excess losses

4.2.1 Hysteresis losses

Hysteresis losses are caused by the energy needed to change the direction of the magnetic flux in the material [97]. The hysteresis cycle of a magnetic material (inclusive SMC) is presented in figure 4.12.

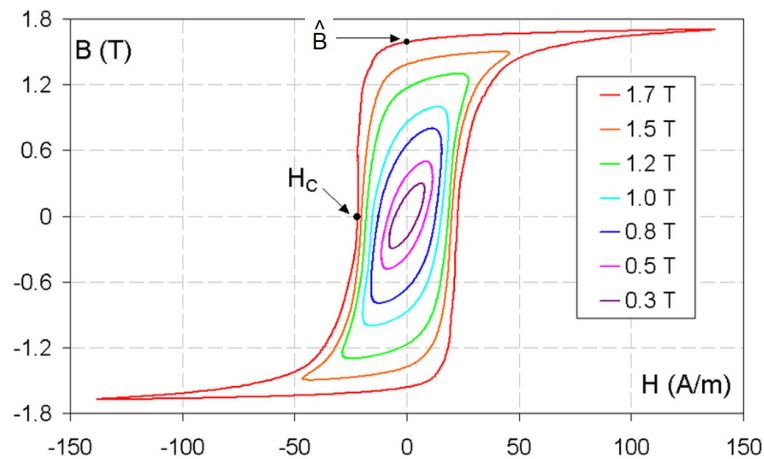


FIGURE 4.12: Hysteresis cycle of a magnetic material [114]

In this figure, the hysteresis loop for several amplitudes of the magnetic flux density \hat{B} are plotted. H_c is the coercivity of the magnetic material and increases with \hat{B} . The area of the hysteresis cycle is the energy lost per cycle and per m^3 . It depends on the coercivity. Materials with low coercivity have a small hysteresis loop and reduced hysteresis losses. Hysteresis losses P_{fe_h} can be obtained by multiplying the energy lost per cycle with the frequency of the magnetic field. They increase linearly with the frequency, so with the rotational speed. The hysteresis losses depending on the amplitude of the magnetic field and the frequency can be modeled with following formula:

$$P_{fe_h}(\hat{B}, f) = K_h \hat{B}^{\gamma_h} f \quad (4.22)$$

Where K_h is a constant depending on the material and the volume. The influence of the amplitude of the magnetic field over the hysteresis losses (γ_h) has been studied in the literature. [5, 97, 115] propose a quadratic dependency of the losses with the amplitude of the magnetic field, so $\gamma_h = 2$. [116] proposes $\gamma_h = 1.548$ for SMC.

4.2.2 Eddy current losses

After hysteresis losses, the second main iron loss source are eddy current losses. Their cause is the pulsating magnetic flux inducing eddy current in the steel lamination or in the iron particles of the SMC causing additional Joule losses.

In steel lamination, eddy current losses can be reduced by increasing the electric resistivity of the material. It can be done by increasing the percentage of silicium in the material making the magnetic properties worse. Another way is to reduce the thickness of the steel lamination, but it reduces the lamination factor and increases material and production costs. For axial-flux machines, steel lamination has to be stacked up radially to reduce the eddy current losses (see 2.4.5.2). So the axial and tangential component of the magnetic flux can not generate high eddy current. But, if there is a radial component, even if it is small, eddy current losses can increase dramatically [33]. Soft magnetic composite is well suited to reduce eddy current losses. This material is composed of microscopic iron particles electrically isolated each other. Furthermore, SMC is an isotropic material, so the direction of the magnetic field, especially an eventually radial component, does not influence the eddy current losses.

Eddy current losses can be expressed with formula 4.23. These losses increase quadratically with the frequency and with the magnetic flux [5, 115, 117]. Compared to hysteresis losses, eddy current losses are particularly relevant at high frequencies but often negligible at low frequency. The coefficient K_j is dependent on the material, especially its electric resistivity, and the thickness of the steel lamination or the size of the iron particle in SMC.

$$P_{fe_j}(\hat{B}, f) = K_j \hat{B}^2 f^2 \quad (4.23)$$

4.2.3 Excess losses and global expression

The comparison between losses calculated with equations 4.22 and 4.23 and measured values is often poor [5]. Calculated losses underestimate the real iron losses. For this reason, excess losses (or additional losses) has to be integrated in the losses equations. In [97] the existence of these losses is justified by the dynamic dependency of the hysteresis

losses. The coercivity and the area of hysteresis loop can increase with the frequency of the magnetic field. Metallurgical, manufacturing processes and mechanical stress can modify the losses of the magnetic material and increase them [5]. Excess losses can be modeled with following formula [115, 117] :

$$P_{fe}(\hat{B}, f) = K_e \hat{B}^{1.5} f^{1.5} \quad (4.24)$$

The global iron losses can be expressed as the sum of hysteresis losses, eddy current losses and excess losses (see equations 4.22, 4.23 and 4.24) :

$$P_{fe}(\hat{B}, f) = K_h \hat{B}^{\gamma_h} f + K_j \hat{B}^2 f^2 + K_e \hat{B}^{1.5} f^{1.5} \quad (4.25)$$

This expression does not take into account the harmonics of the magnetic flux density. In real operating conditions, the magnetic flux is not sinusoidal due to harmonics of the flux generated by the permanent-magnets and the coil. By taking these harmonics into account, the iron losses can be expressed as:

$$P_{fe}(\hat{B}, f) = \sum_{k=1}^{\infty} K_h \hat{B}_k^{\gamma_h} k f + K_j \hat{B}_k^2 (k f)^2 + K_e \hat{B}_k^{1.5} (k f)^{1.5} \quad (4.26)$$

Where f is the frequency of the fundamental of the magnetic flux and \hat{B}_k is the amplitude of the magnetic flux density of the fundamental or the harmonic (fundamental: $k=1$, harmonics: $k>1$).

4.3 Eddy current losses in the rotor permanent-magnets

4.3.1 Generalities over magnet eddy current losses

In application of the Maxwell-Faraday equation and the Ohm's law (see equations 4.27 and 4.28) the variation of the magnetic flux density in the magnets is responsible of the induction of eddy current in them:

$$\text{rot } \vec{E} = -\frac{\partial \vec{B}}{\partial t} \quad (4.27)$$

$$\vec{j} = \frac{1}{\rho} \vec{E} \quad (4.28)$$

Where \vec{E} is the electric field, \vec{B} is the magnetic field density, \vec{j} is the current density and ρ is the resistivity of the material. The losses (P_{mag}) overall the whole magnet (Volume V) can be calculated with following equation:

$$P_{mag} = \iiint_V \frac{dP_{mag}}{d\tau} d\tau = \iiint_V \vec{j} \cdot \vec{E} d\tau \quad (4.29)$$

Magnet losses are in most cases negligible compared to copper and iron losses and do not worsen the efficiency. But, due to the difficulties to cool the rotor of an AFM and the high sensitivity of NdFeB (Neodym Iron Bore) magnets to high temperatures, theses losses have to be minimized to avoid any risk of demagnetization of the magnets, otherwise the continuous power of the machine has to be limited, especially at high rotations speed. In an AFM, the magnetic field flows axially through the magnets, so the induced eddy current flows circularly in the magnet like in figure 4.13.

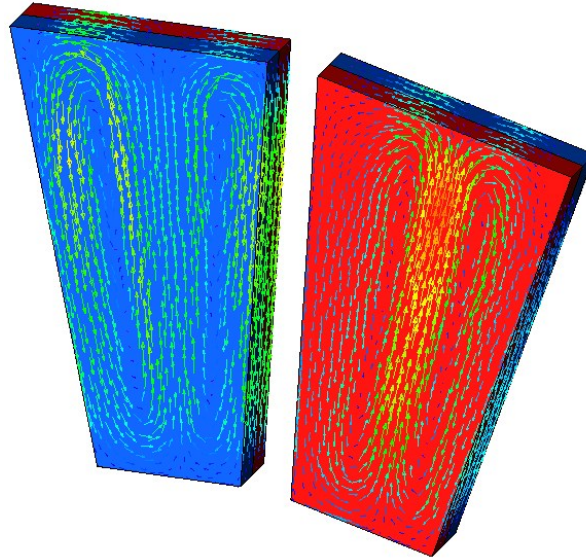


FIGURE 4.13: Induced eddy current in axially-magnetized permanent-magnets

The variation of the magnetic flux density in the permanent-magnets can be explained by three causes [112, 118]:

- No load losses: the stator slots provoke a variation of the reluctance seen by the magnets. For this reason, the magnetic flux density is higher under the teeth and weaker under the slots. These losses are particularly relevant for AFM and are often negligible in RFM with buried magnets.
- On-load eddy current induced by the winding mmf (MagnetoMotive Force) harmonics. Depending on the winding topology, the magnetic field generated by the winding is not perfectly sinusoidal. Harmonics of the field are responsible for magnetic flux density variations in the air gaps and in the magnets.
- On-load eddy current induced by the current time harmonics. The current flowing in the winding is not perfectly sinusoidal and additional losses occur in the magnets due to the additional harmonics of the magnetic field.

4.3.2 Analytic model for magnet losses

Magnet losses strongly depend on the operating point of the machine. The coil current, the rotational speed and the temperature have a huge influence on them. In this section, an analytic model is proposed to estimate these losses in every operating point with a limited number of FEM calculations. This model has been published at the INTERMAG 2014 conference [119]. Magnet losses have been calculated with FEM calculations at the maximum rotational speed n_{max} , where these losses peak. The quadratic evolution of the losses with the speed can be modeled with:

$$P_{mag}(n) = P_{mag}(n = n_{max}) \cdot \left(\frac{n}{n_{max}} \right)^2 \quad (4.30)$$

In this section, a three-phase AFM with a concentrated winding has been designed. This machine is similar to the machine presented 2.4. The magnet material used for the calculation is the Vacodym 881 TP [120]. A linear magnetic material has been used to avoid the effects of saturation of the stator material. The coil current varies up to $I_{max}=400$ Arms and is supposed to be perfectly sinusoidal.

4.3.2.1 Influence of the coil current on magnet losses

To get the influence of the coil current on magnet losses, its RMS value I has been varied from 0A to 400 Arms in the whole dq plane (see figure 4.14). The temperature is fixed to 20 °C (magnet remanence $B_r=1.20$ T and a resistivity $\rho=1.4 \cdot 10^{-6}\Omega.m$) [120].

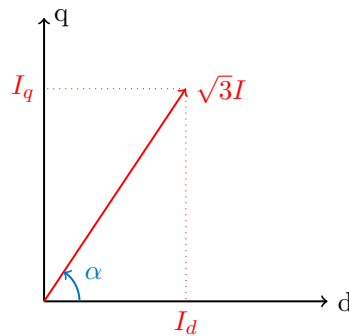


FIGURE 4.14: Definition of I and α

The results of the FEM calculations are presented in figure 4.15. Operating points OP1, OP2 and OP3 are marked. These operating points correspond to extreme load conditions at maximum rotational speed (see appendix A.4):

- OP1: no load ($I = 0$, α undefined, $n = n_{max}=7000$ rpm)
- OP2: full load ($I = I_{max}$, $\alpha = 90^\circ$, $n=7000$ rpm)
- OP3: short circuit ($I = I_{sc}$, $\alpha = 180^\circ$, $n = n_{max}=7000$ rpm)

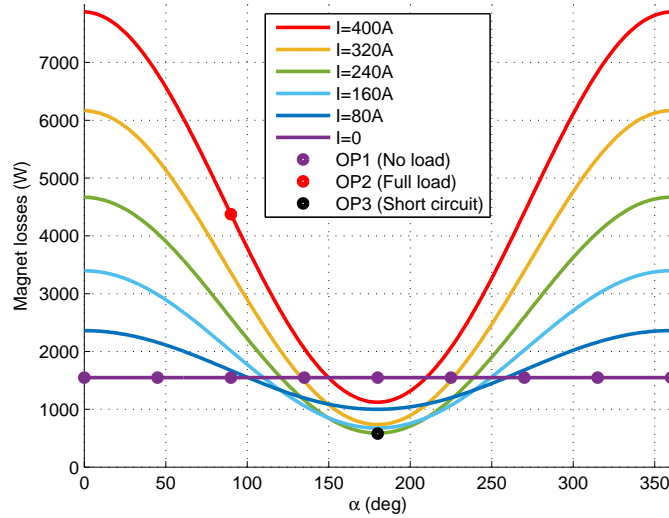


FIGURE 4.15: Magnet losses as function of the coil current at 20 °C

Figure 4.15 shows that magnet losses are not only depending on the coil current amplitude but its orientation too. Field weakening ($I_d \leq 0$, $90^\circ \leq \alpha \leq 270^\circ$) reduces the losses. Magnet losses are symmetrical between motor ($I_q \geq 0$, $0^\circ \leq \alpha \leq 180^\circ$) and generator ($I_q \leq 0$, $180^\circ \leq \alpha \leq 360^\circ$) operating points. Magnet losses depending on α are periodic with a period 2π , so their expression depending on I and α can be expressed as a series of Fourier:

$$P_{mag}(I, \alpha) = a_0(I) + \sum_{k=1}^{\infty} a_k(I) \cos(k\alpha + \varphi_k(I)) \quad (4.31)$$

To get a model for the magnet losses depending on I and α , the Fourier coefficients $a_k(I)$ and $\varphi_k(I)$ must be interpolated. The evolution of the six first Fourier coefficients is shown in figure 4.16.

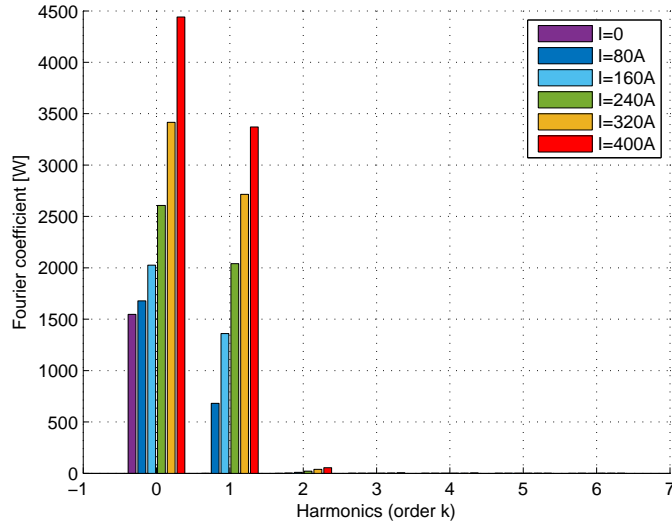


FIGURE 4.16: Fourier coefficients of the magnet losses for the simulated coil currents

The spectrum is mainly dominated by the mean value ($k = 0$) and the fundamental ($k = 1$). The Total Harmonic Distorsion (THD) is below 5%. The Fourier series of equation 4.31 can be reduced and becomes:

$$P_{mag}(I, \alpha) = a_0(I) + a_1(I)\cos(\alpha + \varphi_1(I)) \quad (4.32)$$

Magnet losses peak for $\alpha = 0$, so $\varphi_1(I) = 0$. Figure 4.16 suggests that the Fourier coefficients a_0 and a_1 vary respectively quadratic and linearly with the current I . This observation enables to propose following model:

$$\begin{aligned} a_0(I) &= P_0 + aI^2 \\ a_1(I) &= bI \end{aligned} \quad (4.33)$$

Thanks to equations 4.32 and 4.33, following model for the magnet losses at maximum rotational speed and 20 °C is proposed:

$$P_{mag}(I, \alpha) = aI^2 + bI \cos \alpha + P_0 \quad (4.34)$$

Coefficients a , b and P_0 can be evaluated with 3 FEM calculations at operating points OP1, OP2 and OP3:

- OP1: P_0 are no load losses
- OP2: a can be calculated with full load calculation and following equation:

$$P_{mag}(I_{max}, 90^\circ) = aI_{max}^2 + P_0$$

$$a = \frac{P_{mag}(I_{max}, 90^\circ) - P_0}{I_{max}^2} \quad (4.35)$$

- OP3: b can be calculated with short circuit calculation and following equation:

$$P_{mag}(I_{sc}, 180^\circ) = aI_{sc}^2 - bI_{sc} + P_0$$

$$b = \frac{aI_{sc}^2 + P_0 - P_{mag}(I_{sc}, 180^\circ)}{I_{sc}} \quad (4.36)$$

In figure 4.17 the interpolation of the Fourier coefficients $a_0(I)$ and $a_1(I)$ is displayed. Both coefficients are well estimated, so the model proposed in equation 4.33 is validated.

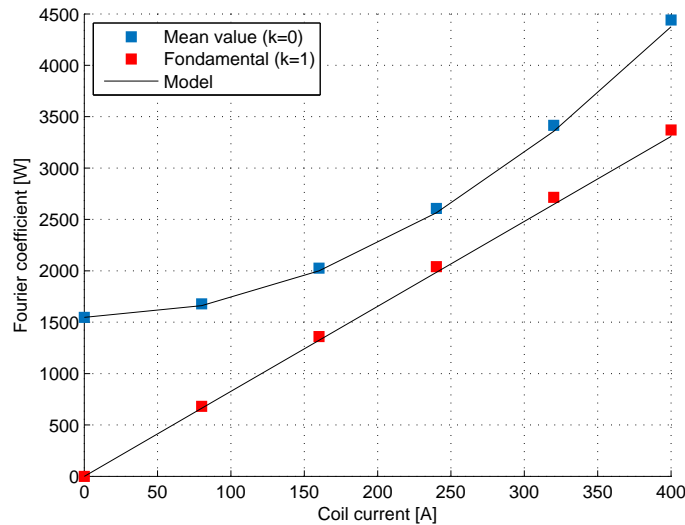


FIGURE 4.17: Interpolation of the Fourier coefficients of the magnet losses for the simulated coil currents

The model for the magnet losses proposed in equation 4.34 has been applied to the proposed design. The coefficient a , b and P_0 are presented in equation 4.37. In figure 4.18 the model is compared with the losses obtained from the FEM calculations. The error in every operating point is smaller than 5%.

$$P_{mag}(I, \alpha) = 0.0177 \cdot I^2 + 8.27 \cdot I \cos \alpha + 1547 \quad (4.37)$$

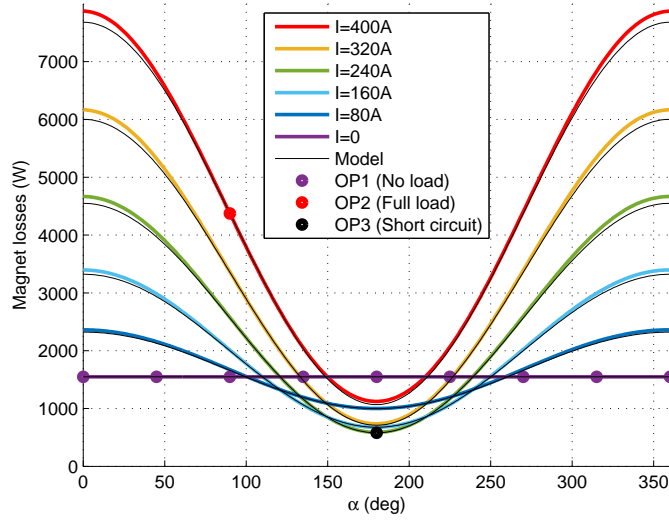


FIGURE 4.18: Magnet losses and model as function of the coil current at 20 °C

With only three FEM calculations (instead of 61 if each operating point is calculated) it is possible to get an accurate estimation of the magnets losses for each operating point. Thanks to equation 4.30, the model proposed in equation 4.34 can be extended for every rotational speed n at 20 °C:

$$P_{mag}(I, \alpha, n, T = 20^\circ C) = (aI^2 + bI \cos \alpha + P_0) \left(\frac{n}{n_{max}} \right)^2 \quad (4.38)$$

4.3.2.2 Influence of the temperature

The temperature of the magnet has an influence on its remanence and its resistivity, so on its losses. In this section, the effects of the variation of the magnet temperature on the model obtained in 4.3.2.1 will be studied. To obtain the influence of the magnet remanence on the losses, the resistivity is assumed to stay constant ($\rho=1.4 \cdot 10^{-6} \Omega.m$). The magnet temperature varies between -30 °C (remanence 1.25 T) and 180 °C (remanence 1 T) [120]. The magnet losses have been calculated with FEM calculations for several remanences, especially singular operating points studied in 4.3.2.1: OP1, OP2 and OP3. The calculated losses in these operating points ($P_{mag_{noLoad}}$, $P_{mag_{fullLoad}}$ and $P_{mag_{shortCircuit}}$) are presented in table 4.1. It has to be noted, that the short circuit current I_{sc} increases linearly with the remanence.

B_r [T]	OP1 [W]	OP2 [W]	I_{sc} [Arms]	OP3 [W]
1.00	1075	3880	191	405
1.05	1185	3995	200	446
1.10	1300	4116	210	489
1.15	1421	4242	220	534
1.20	1547	4375	229	580
1.25	1679	4511	239	629

TABLE 4.1: Magnet losses in OP1, OP2 and OP3 for B_r between 1 T and 1.25 T

From these results, it is possible to calculate the coefficients a , b and P_0 from the losses model obtained in 4.3.2.1 thanks to equations 4.35 and 4.36. Following interpolation is proposed:

- P_0 increases with the square of the remanence
- a is not dependent on the remanence
- b varies linearly with the remanence

In figure 4.19 this interpolation is evaluated. The calculated coefficients are displayed depending on the remanence. To get a readable figure, the coefficients have been scaled to their value at 1.20 T obtained in 4.3.2.1.

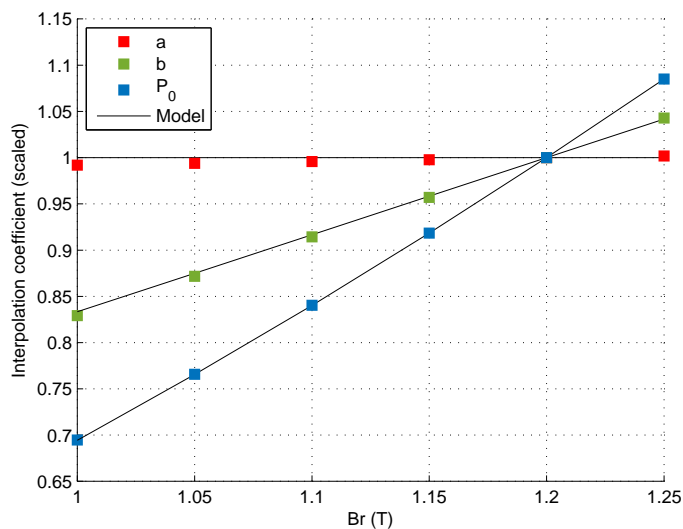


FIGURE 4.19: Comparison between the calculated coefficients obtained with FEM calculations and the proposed interpolation as function of the magnet remanence

The proposed interpolation fits well (error smaller than 1%) and can be validated. It enables an extension of the model to other remanences. The precision of this interpolation has been evaluated for a remanence of 1T by comparing it to FEM calculations (figure 4.20). The maximal error is smaller than 5% and corresponds to the precision obtained at 20 °C.

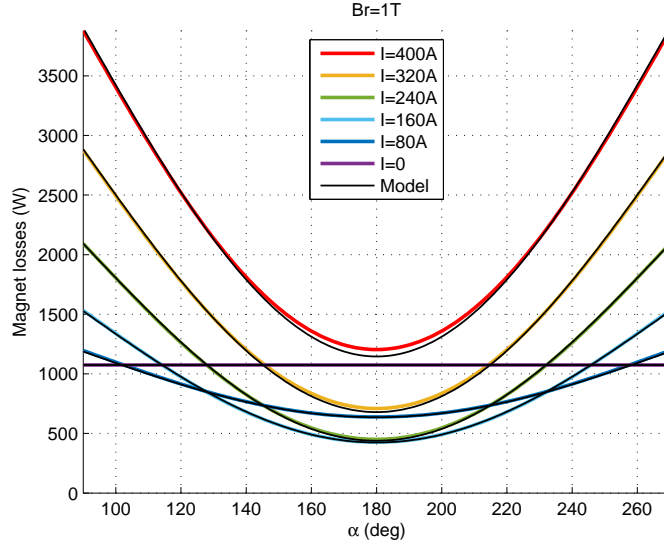


FIGURE 4.20: Comparison between the calculated magnet losses with FEM calculations and the analytic model at maximum rotational speed as function of the coil current ($B_r=1.00$ T)

Eddy current losses increase linearly with the electric conductivity of the material, so with the inverse of the resistivity. The evolution of the resistivity of NdFeB permanent-magnets with the temperature has been studied in [121]. The model obtained with equation 4.38 can be extended to every operating temperature of the magnet:

$$P_{mag}(I, \alpha, n, T) = \frac{\rho(T_{ref})}{\rho(T)} \left(aI^2 + b \frac{B_r(T)}{B_r(T_{ref})} I \cos \alpha + P_0 \left(\frac{B_r(T)}{B_r(T_{ref})} \right)^2 \right) \left(\frac{n}{n_{max}} \right)^2 \quad (4.39)$$

Coefficients a , b and no load losses P_0 are obtained from FEM calculations at an arbitrary defined temperature T_{ref} and at maximum rotational speed n_{max} .

Conclusion

In this chapter the losses in axial-flux machines have been studied. A good knowledge of the losses is necessary to make a proper dimensioning of an electric machine and improve its efficiency. To fasten the dimensioning, analytic models interpolating the losses are useful to minimize the number of FEM calculations. Two analytic models are proposed to estimate the copper and the magnet losses:

- The copper losses model extends the model proposed in the literature for trapezoidal slots and different conductor geometries.
- The magnet losses model interpolates the losses for every operating point of the machine (rotational speed, current and temperature) with only 3 FEM calculations. This model has been published at the INTERMAG 2014 conference [119].

With a maximum error smaller than 5% the precision of these models are satisfying. Furthermore, iron losses in soft magnetic materials are presented.

Chapter 5

Dimensioning

Contents

Introduction	108
5.1 Manual dimensioning	109
5.1.1 Design	109
5.1.1.1 Publications	109
5.1.1.2 Designing of the machine	110
5.1.1.3 Final design (AFM ₆₀)	112
5.1.2 Validation of the design definition	116
5.1.2.1 Teeth alignment	117
5.1.2.2 Winding construction	118
5.1.2.3 Electric connection	119
5.1.2.4 Number of slots per pole per phase	121
5.2 Multi-objective optimization	124
5.2.1 Presentation	124
5.2.1.1 Software toolchain	124
5.2.1.2 Parameters and objectives	128
5.2.2 Sensitivity analysis	129
5.2.2.1 Presentation and motivation	129
5.2.2.2 Results	130
5.2.2.3 Conclusion	134
5.2.3 Optimization	135
5.2.3.1 Selection of optimized design	135
5.2.3.2 Torque and power characteristics	138
5.2.3.3 Comparison with the manually designed machine	140
Conclusion	143

Introduction

In this chapter, the dimensioning of the machine is presented. This chapter is divided in 3 parts:

- At first the machine has been manually designed. This dimensioning is based on the concept defined in the chapters 2 and 3:
 - Topology: internal rotor axial-flux machine
 - Hairpin winding
 - Permanent-magnets: NdFeB rectangular permanent-magnets
 - Soft magnetic material: soft magnetic composite Somaloy 5P700HR with a compressible geometry
 - Design: shifted teeth and parallel star electric connection
 - NSPP=0.75

This dimensioning method is based on try and error. The geometry of the machine is successively modified to improve the design and meet the requirements.

- The concept defined in chapters 2 and 3 is confirmed by checking that this concept stays advantageous for the designed machine.
- Secondly a multi-objective optimization is performed. With this process, the dimensioning of the machine is partially automatized. New designs are automatically generated with an optimization algorithm. This algorithm searches the best design by calculating a huge number of designs.

5.1 Manual dimensioning

5.1.1 Design

5.1.1.1 Publications

During this PhD, alternative internal rotor AFM designs have been proposed and published:

- Hybrid rotor construction: in this concept, the rotor is built with several materials to improve the cooling of the magnets and increase the continuous power. A metal can be used to conduct the heat from the magnets to the shaft. To avoid the generation of additional eddy current losses, a non electric conductive material like reinforced plastic is used in the magnetic circuit [122–124].
- Stator with waved windings: in this concepts, the windings are built in the shape of waves and stacked up one phase over the other. The advantage, is that the coil ends are reduced thanks to the absence of electric connections but the copper fill factor is reduced [125, 126].
- A direct cooling concept with a cooling channel between the windings and the stator yoke [127]
- A segmented stator where the stator is built in several parts to make its construction easier [128, 129]

5.1.1.2 Designing of the machine

During the designing phase, 60 designs have been successively calculated. The maximum phase current and the battery voltage are fixed according to the specification ($I_{max}=420$ Arms and $U_{bat}=300$ Vdc). The first design is the machine with NSPP=0.75 (AFM₁) used for the definition of the NSPP (see 3.5.2). This machine has 12 pole pairs and achieved 324 Nm and 65 kW. **The design 60 is the selected machine. It will be named (AFM₆₀). It achieves 325 Nm and 84 kW.**

The objectives of the optimization are:

- Achieving the required peak torque and peak power
- Minimization of the magnet mass and the magnet losses
- Maximization of the efficiency at full load

Following parameters are modified during the dimensioning process:

- Pole pairs numbers:
 - 8: between design 2 and 5
 - 10: between designs 6 and 42
 - 12: design 1 and between 43 and 60
- Magnets: thickness, inside and outside diameter and space between 2 magnets
- Stator: slot width, slot height, inside and outside diameter and yoke thickness
- Winding: section and number of turns

The evolution of the peak torque and the peak power scaled to the selected design (AFM₆₀) is showed in figure 5.1.

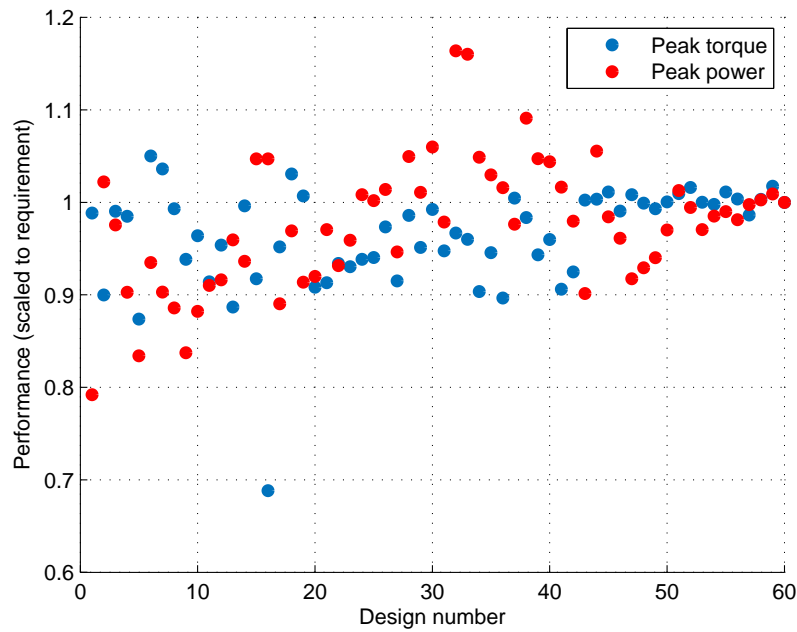


FIGURE 5.1: Evolution of the peak torque and the peak power

The evolution of the magnet mass, the magnet losses and the efficiency at full load is showed in figure 5.2. Values are scaled to the performances of AFM_{60} . It is a good compromise between the fulfillment of the requirements, the minimization of the magnet mass and losses and a good efficiency. These results show that the manual dimensioning based on try and error is a method to obtain a design filling the requirement.

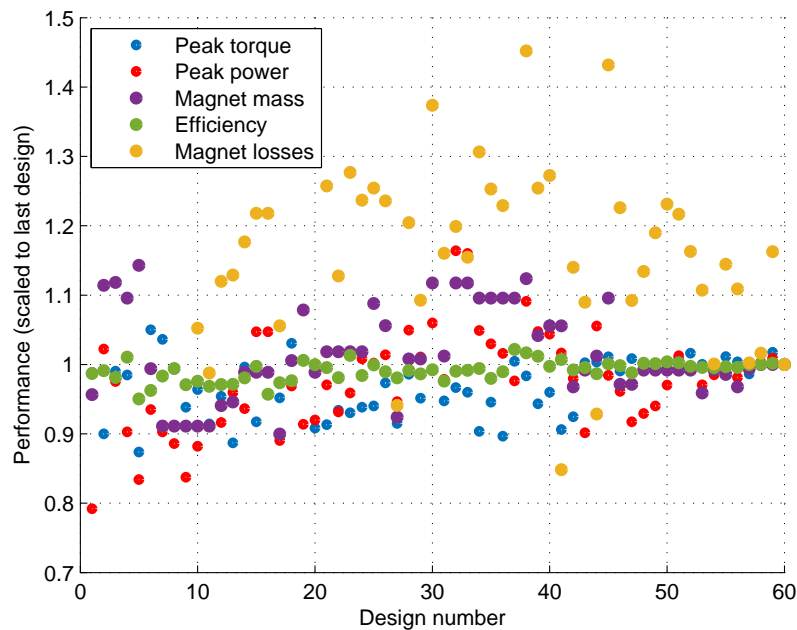


FIGURE 5.2: Evolution of the other optimization parameters

5.1.1.3 Final design (AFM₆₀)

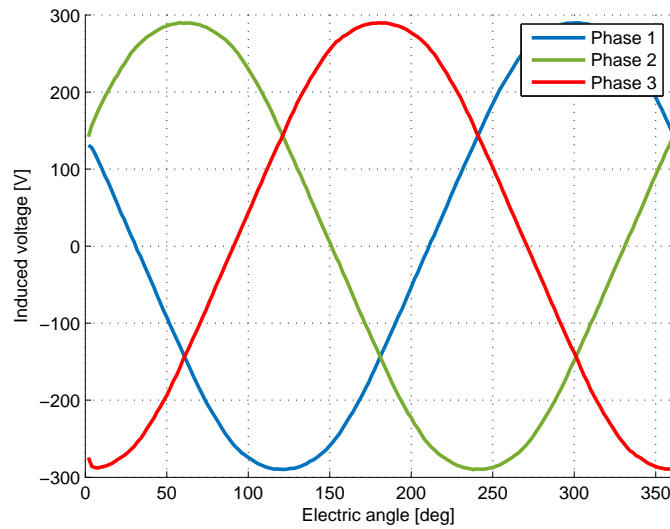
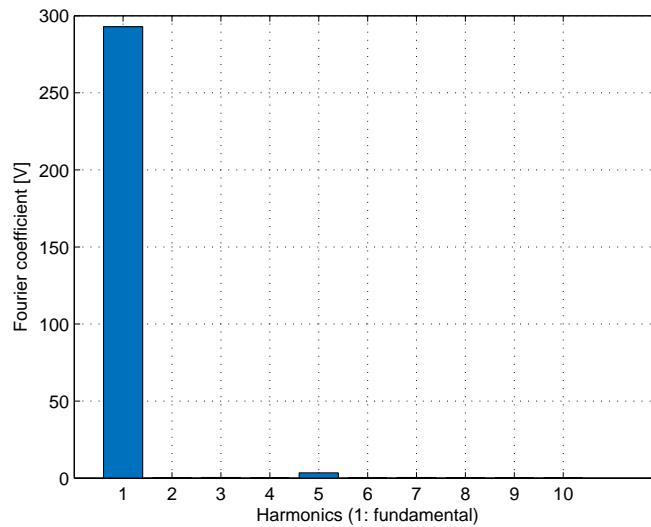
The main parameters of the machine are displayed in table 5.1.

Description	Value	Specification
Pole pairs number	12	
Number of magnets	24	
NSPP	0.75	
Number of slots	54	
Number of winding turns	4	
Total length	73.2 mm	≤ 80 mm
Inside diameter (end windings)	180 mm	≥ 182 mm
Outside diameter (end windings)	285 mm	≤ 282 mm
Volume	2.8 L	min
Total magnets mass	817 g	min
Magnet grade	UH ¹	min
Dysprosium mass	61.3 g	min
Peak torque	325 Nm	≥ 330 Nm
Torque density	116 Nm.L ⁻¹	max
Peak power	84 kW	≥ 80 kW
Power density	30 kW.L ⁻¹	max

TABLE 5.1: Parameters of the designed machine (AFM₆₀)

The induced voltage at 7000 rpm is presented in figure 5.3. Its RMS value is 206 V_{rms}. The induced voltage is sinusoidal. The Fourier coefficients are displayed in figure 5.4. The machine has an excellent THD (2%). A small component of the 5th harmonic can be observed.

¹The demagnetization safety is checked in appendix E.5.

FIGURE 5.3: Induced voltage of AFM₆₀ at 7000 rpm [FEM]FIGURE 5.4: Fourier decomposition of the induced voltage of AFM₆₀

The cogging torque is presented in figure 5.5. The main frequency of the cogging torque is the least common multiple of the number of slots and the number of magnets [130]. The designed machine has 24 magnets and 108 teeth (both stator), so the frequency of the cogging torque is 216 times the mechanical frequency, or 18 times the electric frequency ($n_p = 12$). The torque at full load is displayed in figure 5.6. The designed machine achieves a peak torque of 325 Nm with a small torque ripple (7 Nm).

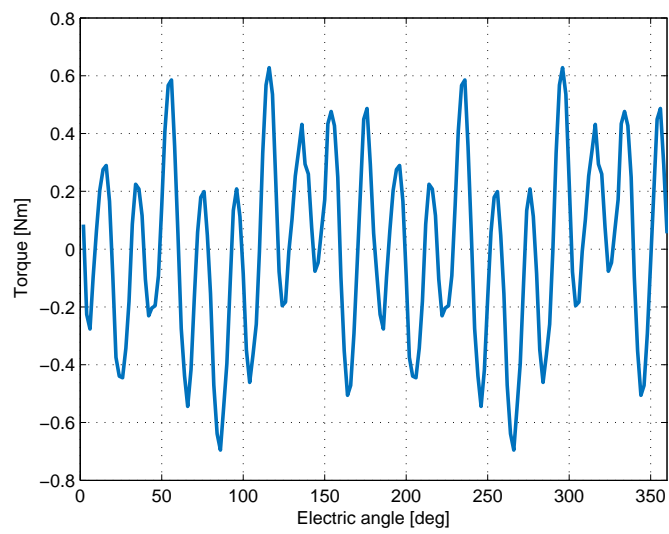


FIGURE 5.5: Cogging torque of AFM₆₀ [FEM]

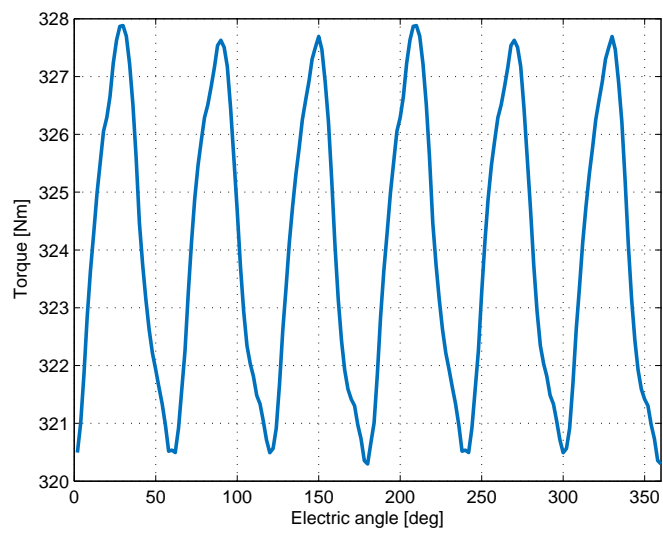


FIGURE 5.6: Peak torque of AFM₆₀ [FEM]

The peak torque and power characteristics are displayed in figures 5.7 and 5.8.

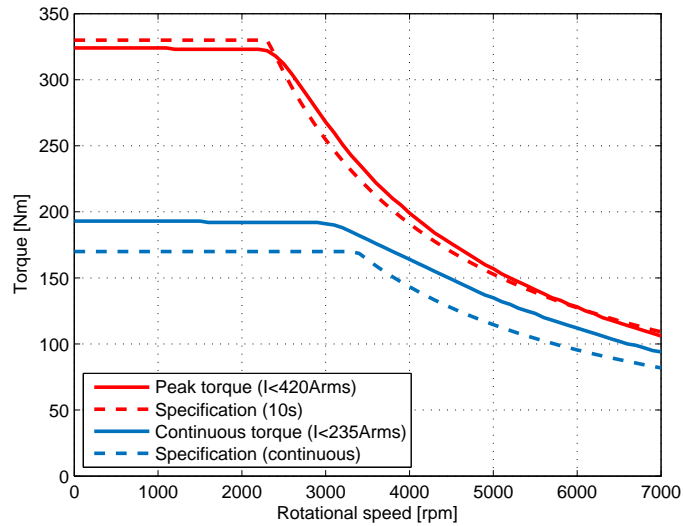


FIGURE 5.7: Torque characteristic of AFM_{60}

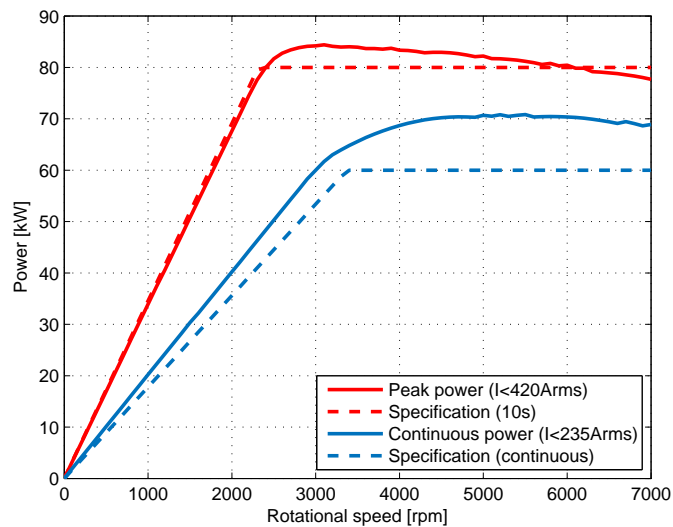


FIGURE 5.8: Power characteristic of AFM_{60}

The designed machine does not fit exactly the required specification. The maximum torque is 325 Nm. The peak power of 84 kW is achieved nearby 3000 rpm but is reduced to 78 kW at 7000 rpm. This power and torque reduction is due to the increase of the phase resistance with the speed which was precisely modeled after the design freeze and to small changes in the geometry of the stator to make its construction easier. The required continuous torque (170 Nm) and power (60 kW) are achievable with a maximum phase current of 235 Arms. The MTPA (Maximum Torque Per Ampere) characteristic is displayed in figure 5.9. The effects of saturation in the magnetic material

are recognizable. For high currents, the curve leaves the characteristic obtained with a linear interpolation. At 420 Arms, the torque is reduced about 9%.

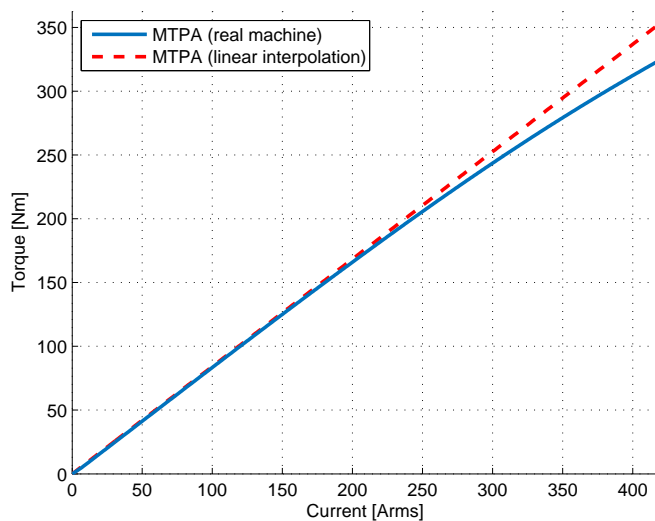


FIGURE 5.9: MTPA characteristic

This machine is characterized in appendix E.

5.1.2 Validation of the design definition

In this section, the design definition performed in chapters 2 and 3 is checked. Following parameters of the machine are independently modified:

- Teeth alignment
- Winding technology
- Electric connection
- Number of slots per pole per phase

For this comparison the geometry of the original machine is adapted to the alternative concepts. Every adaptation has been performed with following assumptions:

- Rotor: the magnet mass stays unchanged
- Stator: the teeth length and the back iron length are not modified. If the number of slots is modified, the slot width is proportionally reduced or increased
- Winding: the electric loading and the current density are not modified

Like in the design definition, the designs are evaluated in following operating points (see appendix A):

- OP1: no load ($I = 0$, α undefined, $n = n_{max}=7000$ rpm)
- OP2: full load ($I = I_{max}$, $\alpha = 90^\circ$, $n=2000$ rpm)
- OP3: short circuit ($I = I_{sc}$, $\alpha = 180^\circ$, $n = n_{max}=7000$ rpm)

5.1.2.1 Teeth alignment

To validate the teeth alignment, the machine has been simulated with aligned teeth. Other parameters like the rotor geometry or the windings stay unchanged. Results of the FEM calculations are presented in table 5.2.

Operating point	Parameter	Teeth alignment	
		shifted	aligned
OP1	Induced voltage	206 Vrms	208 Vrms
	Cogging torque (peak-peak)	1 Nm	1 Nm
	Magnet losses	455 W	827 W
	Axial force (per magnet)	8 N	0 N
OP2	Maximum torque	325 Nm	323 Nm
	Saturation	9 %	10 %
	Torque ripple (peak-peak)	8 Nm	4 Nm
	Magnet losses	103 W	254 W
	Axial force (per magnet)	13 N	0 N
OP3	Short circuit current	270 Arms	269 Arms
	Magnet losses	154 W	519 W
	Axial force (per magnet)	5 N	0 N
Pole pairs number		12	12
Phase resistance (100 °C)		13 mΩ	13 mΩ
Inductance		87 μH	88 μH

TABLE 5.2: Comparison between shifted and aligned teeth

The performances, the electric parameters and the short circuit current of both machine are only lightly modified. The machine with shifted teeth has a higher torque ripple, but stays in an acceptable range. The two main differences are the magnet losses which are much smaller with shifted teeth and the axial force on the magnet if the teeth are shifted. This study confirms the results of the design definition and validates the choice of shifted teeth which strongly reduces magnet losses.

5.1.2.2 Winding construction

Hairpin and pull in windings have been presented in 2.4.1. In this section, hairpin and pull in winding are compared. For the pull in winding, a copper fill factor of $k_{cu_{pullin}} = 50\%$ is assumed. The machine with NSPP=0.75 has a period of 2 pole pairs. The machine has 12 pole pairs, so the phase current is split into 6 windings connected in parallel. To maintain the same electric load, the number of turns has to be multiplied by 6: $N_{pullin} = \frac{n_p}{2} \cdot N_{hairpin} = \frac{12}{2} \cdot 8 = 48$ conductors are disposed in each slot. The diameter D_{pullin} of the conductor can be calculated with following equation:

$$N_{pullin} \pi \frac{D_{pullin}^2}{4} = k_{cu_{pullin}} A_{slot} \quad (5.1)$$

$$D_{pullin} = \sqrt{\frac{4k_{cu_{pullin}} A_{slot}}{\pi N_{pullin}}}$$

By applying the model for the skin effect for both winding constructions presented in 4.1.3.2 the resistance of one conductor phase from 0 rpm to 7000 rpm has been calculated for a copper temperature of 100 °C (resistivity : $2.30 \cdot 10^{-8} \Omega.m$) and is displayed in figure 5.10.

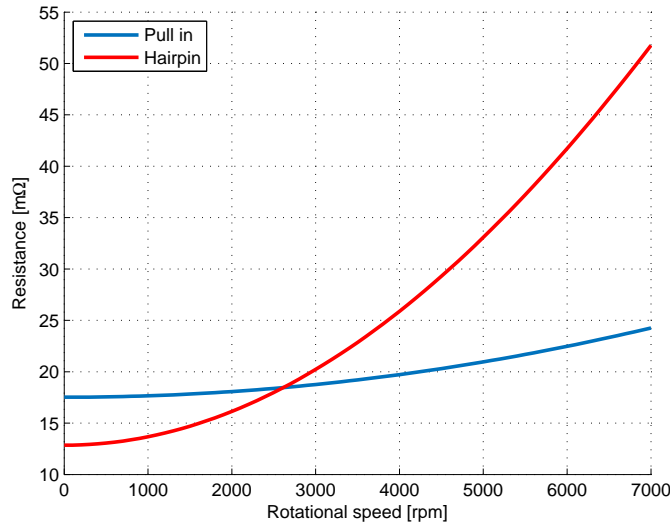


FIGURE 5.10: Comparison between hairpin and pull in windings (AFM₆₀) [model]

Thanks to a better copper fill factor, the hairpin winding is much better at small rotational speeds, but the skin effect dramatically increases the phase resistance with the rotational speed. For a rotational speed over 2500 rpm, the pull in winding is better. The machine is mainly driven at small rotational speeds (see figure 2.3). To maximize

the efficiency of the machine over its life cycle, the hairpin winding is selected. In figure 5.11, the phase resistance for temperatures between $-20\text{ }^{\circ}\text{C}$ and $180\text{ }^{\circ}\text{C}$ is displayed. At high rotational speed, the resistance is smaller for hot conductors. This result is surprising as the resistivity of the copper increases with the temperature. By increasing the temperature, the resistivity, so the DC resistance of the copper winding increases. But, the induced eddy current due to the skin effect is reduced.

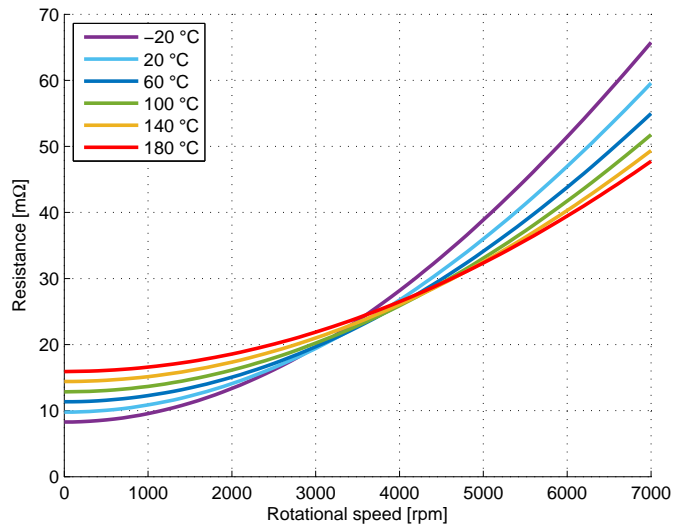


FIGURE 5.11: Phase resistance depending on the copper temperature (AFM₆₀) [model]

5.1.2.3 Electric connection

By moving from a parallel connection to a serial connection, the current delivered by the inverter is not separated anymore but flows in the winding of both stators. To maintain the same current density and the same electric loading, the number of turns has to be divided by 2 and the section of the windings needs to be doubled. As long as the electric loading is not modified, the connection has no influence on the magnetic circuit. The torque, forces or magnetic losses are not modified. Furthermore the armature constant and the inductance stay unchanged. The only modified parameter is the phase resistance because the construction of the winding has been modified. The evolution of the winding is shown in figure 5.12.

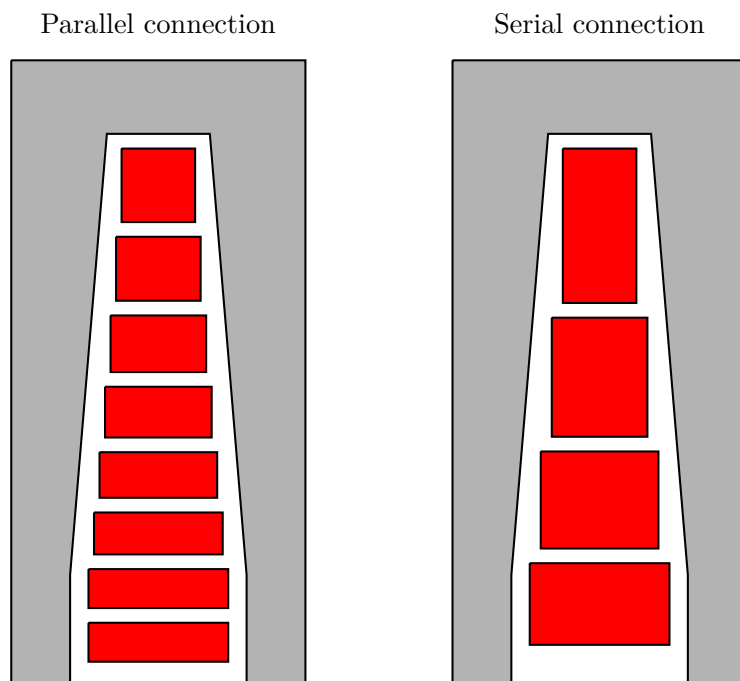
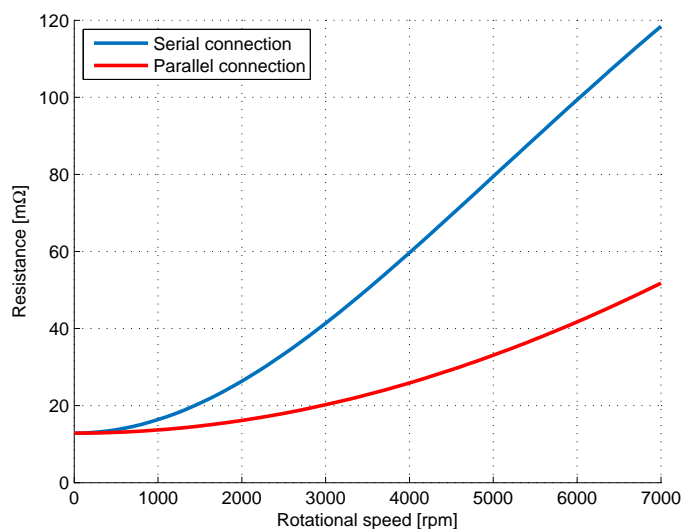


FIGURE 5.12: Evolution of the winding's geometry for serial and parallel connection

Doubling the section of the conductors in the same slot geometry involves the doubling of the height of the conductor. The increase of the phase resistance due to skin effect depends on the geometry of the winding (see 4.1.2.2). The evolution of the phase resistance with the rotational speed of the machine has been simulated for a serial connection and is compared with the parallel connection in figure 5.13.

FIGURE 5.13: Comparison of the phase resistance depending on the electric connection (AFM₆₀) [model]

As expected, the serial connection is much more sensitive to the skin effect than the parallel connection. At maximum rotational speed, the resistance is 2.3 times higher than a serial connection. That would lead to much higher copper losses and a worsen efficiency. For this reason, the choice of the parallel connection is validated.

5.1.2.4 Number of slots per pole per phase

In the design definition (see 3.5) NSPP=0.75 has been selected. The concentrated winding with NSPP=0.5 has been rejected due to too low torque density and too high magnet losses. NSPP=1 has already been rejected due to the axial force acting on the rotor. NSPP=1.5 appears as the second best concept. With a low pole pairs number ($n_p = 6$) the high saturation in the stator back iron reduced the torque density, but a higher number of pole pairs ($n_p = 8$) has revealed the potential of this winding topology. In this section, the original designed machine (NSPP=0.75) is compared with two machines with NSPP=1.5. The first one has the same stator than the original machine and 6 pole pairs, the second one has been scaled to 8 pole pairs. The results of the FEM calculations are shown in table 5.3.

Operating point	Parameter	NSPP		
		0.75	1.5	
Pole pairs number		12	6	8
Number of slots		54	54	72
OP1	Induced voltage	206 Vrms	210 Vrms	215 Vrms
	Cogging torque (peak-peak)	1 Nm	4 Nm	3 Nm
	Magnet losses	455 W	496 W	338 W
	Axial force (per magnet)	8 N	2 N	2 N
OP2	Maximum torque	325 Nm	291 Nm	325 Nm
	Saturation	9 %	19 %	12 %
	Torque ripple (peak-peak)	8 Nm	12 Nm	13 Nm
	Magnet losses	103 W	83 W	55 W
	Axial force (per magnet)	13 N	25 N	19 N
	Efficiency	88 %	85 %	87 %
OP3	Short circuit current	270 Arms	241 Arms	283 Arms
	Magnet losses	154 W	136 W	93 W
	Axial force (per magnet)	5 N	14 N	8 N
Coil end windings		17 mm	26 mm	21 mm
Phase resistance (100 °C)		13 mΩ	16 mΩ	15 mΩ
Inductance		87 μH	198 μH	129 μH

TABLE 5.3: Comparison between NSPP=0.75 and NSPP=1.5

Both NSPP have advantages and disadvantages:

- NSPP=0.75: the main advantage of this winding are the reduced copper losses at low rotational speed (smaller DC resistance and coil ends)
- NSPP=1.5: this winding offers smaller magnet losses. The smaller pole pair number reduces the iron losses and improve the efficiency at high rotational speed. The outside and inside coil end windings are larger, so the magnetic circuit needs to be reduced in the radial direction.

This second comparison has confirmed the results of the design definition. NSPP=0.75 enables a good efficiency in the most common operating points of the machine (see figure 2.3). NSPP=1.5 has a better continuous power thanks to smaller losses at high rotational speed especially in the magnets. The best concept depends on the application. **For a application as IMG for PHEV vehicles, the efficiency is very important to minimize the battery cost. For this reason, the choice of NSPP=0.75 is confirmed.**

In this section the design definition has been verified. The concept defined in chapters 2 and 3 is confirmed:

- Shifted teeth
- Hairpin winding
- Star-parallel electric connection NSPP=0.75

5.2 Multi-objective optimization

5.2.1 Presentation

The dimensioning of an electric machine needs to optimize several objectives. The ideal machine meets the requirements, is cheap, small, easy to build and has a good efficiency. Unfortunately in the high majority of optimization problems the objectives are contradictory, that means that the optimum design satisfying one objective is not the best regarding another objective: there is no solution optimizing every objective simultaneously. In this situation it is not possible to define the optimum solution, it is only possible to find a compromise between the objectives and obtain a design satisfying every objective. The selection of this "optimum" design is of course dependent on the relative weight between the objectives. Generalities on MOO including a simple example and information on the algorithms are presented in the appendix D.

5.2.1.1 Software toolchain

The software toolchain designed to resolve the MOO problem is shown in figure 5.14.

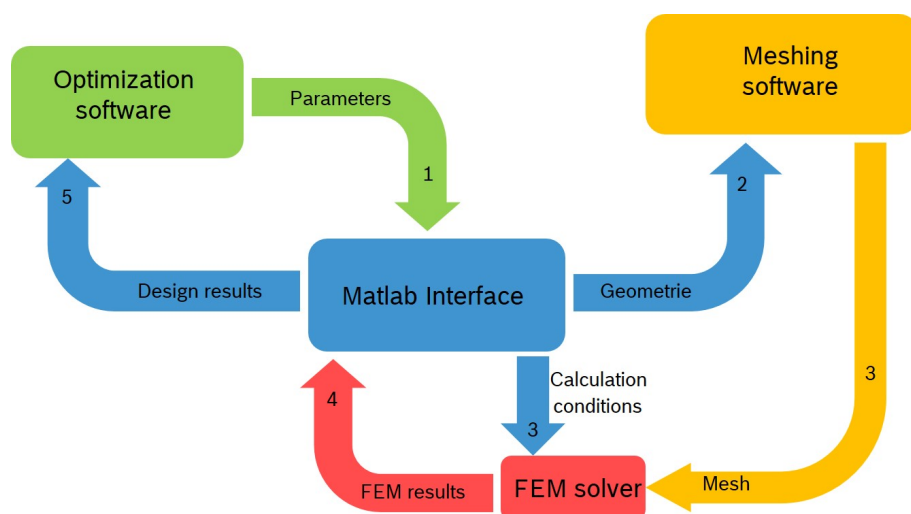


FIGURE 5.14: Software toolchain for the multi-objective optimization

The optimization software generates new designs thanks to the results of previous designs and the integrated genetic algorithm. The Matlab interface is the main component of the toolchain. Its work is to estimate every result which does not need a FEM calculation. Furthermore the Matlab interface sends the geometry parameters to the meshing software and the calculation conditions to the FEM solver. It collects the results when the calculation is finished and forwards them to the optimization software.

The different steps in the evaluation of one design are displayed in figure 5.16. At first, the Matlab interface calculates the sizes of all the conductors depending on the slot width, the number of turn and the winding section. Then, the size of the inside and outside coil end windings are estimated. The ratio between the height of the teeth and its width is evaluated. If it is greater than 4, the stator is assumed to be not compressible (see 2.4.5.1.2). In that case, the winding section is reduced from 0.1 mm^2 and the previous calculation is performed once again until the SMC geometry is satisfying. To avoid the calculation of designs with too high current density (over 35 A/mm^2), designs with winding sections smaller than 6 mm^2 are rejected.

In a second step, the mesh is generated thanks to the meshing software. If the mesh is not successful, a second generation with a reduced mesh size is tried. If this generation is not successful, the design is rejected. Then the demagnetization safety is checked. At first a cheaper UH magnet is tested, if it is not safe against demagnetization, the same test is performed with a EH magnet. If no magnet is safe, the design is rejected.

In a third step three operating points are evaluated via FEM:

- OP1: no load calculation at maximum rotational speed to calculate the armature constant and the losses at no load.
- OP2: full load calculation to calculate the maximum torque, the maximum torque ripple, the efficiency for high torque operating points and the maximum axial force acting on the magnets and on the stators. The rotational speed is fixed to 2000 rpm.
- OP4: the third calculation is performed at maximum rotational speed (7000 rpm) with a phase current of 200 Arms and a field weakening angle of 60° . This operating point corresponds approximately to the maximum required continuous power (60 kW - 82 Nm) at maximum rotational speed and is a worst case for the thermal. In this operating point, the efficiency for high rotational speeds, the maximum magnet losses and the inductance are evaluated.

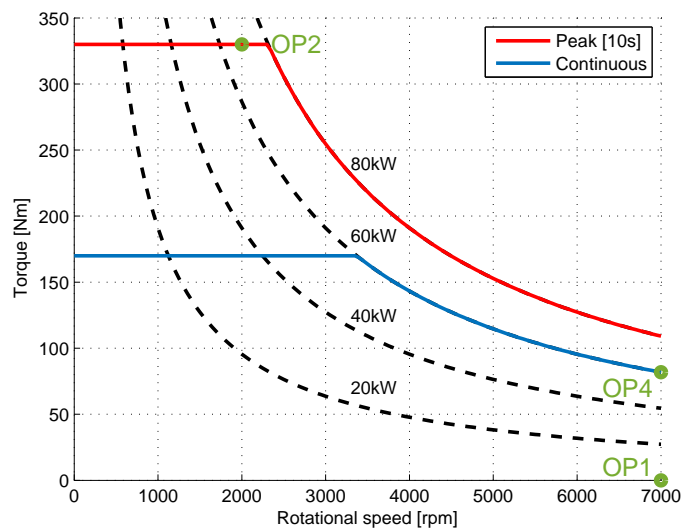


FIGURE 5.15: Operating points for the MOO

In a fourth step, the torque and power characteristic are calculated. For example it is possible to check if the machine achieves the required maximum power, especially at high rotational speed.

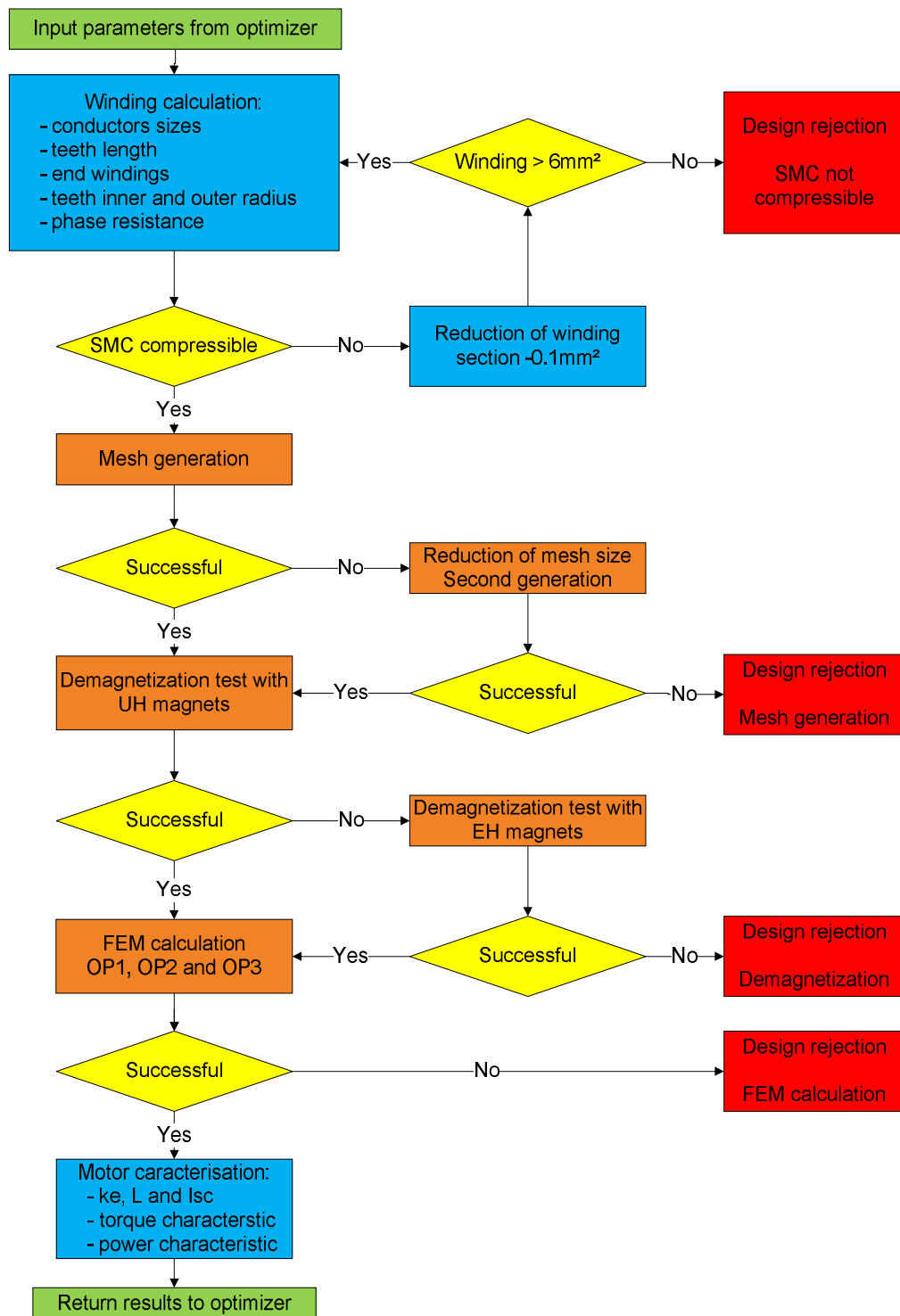


FIGURE 5.16: Calculations steps of a design in the MOO software toolchain

5.2.1.2 Parameters and objectives

A design definition have been performed in 2.4 to select the best suitable concept for this application:

- Hairpin winding
- Shifted teeth between both stators
- Rectangular magnets
- Electric connection: parallel star connection
- SMC geometry:
 - Height to width ratio smaller than 4
 - Trapezoidal slot
 - Straight part on the top of the teeth
- **NSPP: the construction of the second prototype of the AFM has shown that hairpin winding with NSPP=0.75 is hard to construct. The irregular step of one coil end (see figure 3.11) increases its size. Furthermore, the prototype based on this design could not have been built with the optimized winding presented in figure 4.7 (see 7.2). It increases the losses at high rotational speed and limits the continuous and peak power. To improve the continuous and peak power at high rotational speed and achieve the specification, the second best NSPP is selected for the MOO: NSPP=1.5**

For this optimization, following geometry parameters are used:

- General parameters:
 - pole pairs number (between 6 and 10)
 - air gap (between 1.2 mm and 2 mm)
 - number of winding turns (between 2 and 4)
- Magnets: thickness, inside and outside diameter and space between 2 magnets
- Stator: slot width, slot height, inside and outside diameter, yoke thickness and winding section

The objective of the optimization have been chosen in order to fit to the objectives defined at the begin of the work.

- Achieving the required peak torque and peak power
- Minimization of the magnet cost
- Minimization of the magnet losses
- Maximization of the efficiency
- Minimization of the axial length

5.2.2 Sensitivity analysis

5.2.2.1 Presentation and motivation

The sensitivity analysis is a study where a large amount of designs are randomly selected and evaluated. The main goal of the sensitivity analysis is to find correlations between inputs and outputs or between outputs themselves. Furthermore, the sensitivity analysis can reveal the possibilities like for example an approximation of the maximum achievable torque. In the case of a MOO the sensitivity analysis is performed for three reasons:

- Identify contradictory objectives which have to be set as objectives for the optimization. If two objectives are not contradictory, it is possible to optimize only one of them to reduce the number of objectives and fasten the convergence of the optimization algorithm
- Define the concept by reducing the number of input parameters if some of them do not influence the results or reduce the variation of one or several input parameters to concentrate the optimization in a meaningful area
- The results of the sensitivity analysis is used as start population for the optimization algorithm

500 designs have been calculated for this sensitivity analysis. The calculation took one week. The sampling of the designs have been performed with a Latin hypercube sampling. This algorithm is recommended to scan the design space [131].

5.2.2.2 Results

In this section, interesting results from the sensitivity analysis are displayed. On some figure it is possible to recognize an approximation of the Pareto front between two objectives.

In figure 5.17 the peak torque of each design is displayed depending on the peak power at maximum rotational speed. The color of each design is the number of turns varying from 2 to 4. The number of turns has a huge influence on the peak torque and power. Designs with 4 turns have an higher peak torque but a lower peak power, but no of them achieves the requires peak torque (330 Nm) and the required peak power (80 kW). Designs with $N=2$ have the lower peak torque but the higher peak power. All designs achieves 80 kW but no design achieves the required peak torque. Only a few designs with $N=3$ are achieving the required peak torque and the required peak power.

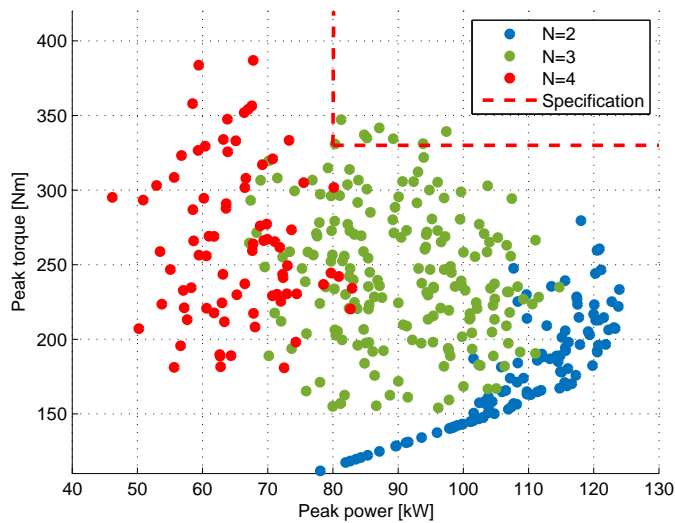


FIGURE 5.17: Peak torque and power depending on the number of turns

In figure 5.18 the peak torque is once again displayed depending on the peak power, but in this figure the color displays the number of pole pairs varying between $n_p = 6$ and $n_p = 10$. Every designs with $n_p = 6$ do not achieve a higher torque than 270 Nm which is very insufficient. Designs with $n_p = 7$, $n_p = 8$ or $n_p = 9$ appear more suitable for the application. Some of them achieve the required torque and power. Designs with $n_p = 10$ are rejected. These designs necessitate 90 teeth on each stator. For these designs the SMC is only compressible with $N=2$.

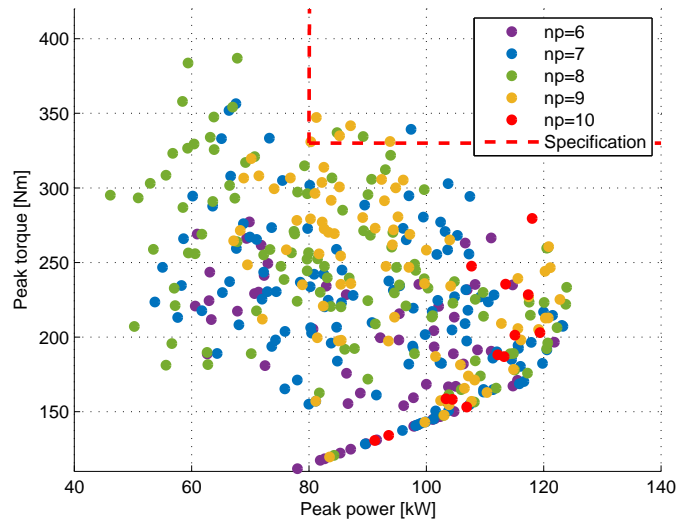


FIGURE 5.18: Peak torque and power depending on the pole-pair number

In figure 5.19 the peak torque is displayed depending on the maximum demagnetizing field applied to the magnet during the demagnetization calculation. If this field is higher to the h_{k95} of the magnet (-709 kA/m for UH grade, -899 kA/m for EH grade, see table C.1) the magnet is assumed to be demagnetized. Only a few designs with $N=2$ are safe with UH magnets. Furthermore the high majority of designs with $N=4$ are not safe against the demagnetization. The majority of designs with $N=3$ are safe with EH magnets. In this first comparison $N=3$ appears as the only suitable solution for the designs. Other number of turns either generate not enough torque or power nor are not safe against demagnetization.

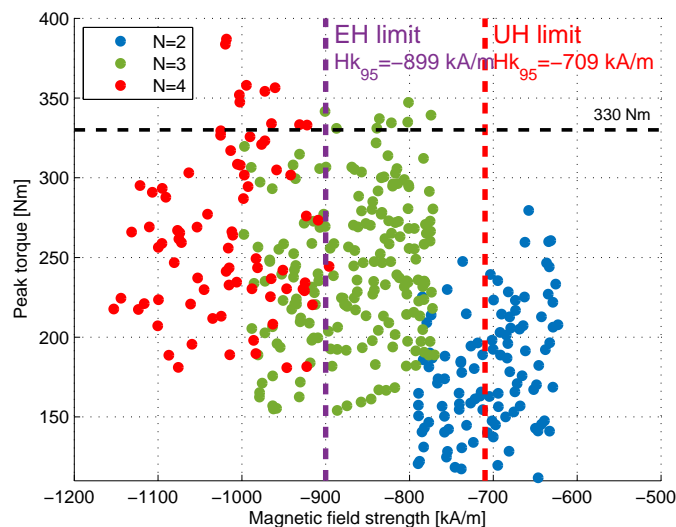


FIGURE 5.19: Peak torque and demagnetizing field depending on the number of turns

Figure 5.20 displays the magnet losses at OP4 (≈ 60 kW at maximum rotational speed) depending on these losses at OP1 (no load at maximum rotational speed). These losses are coupled, so the minimization of the magnet losses in one operating point minimizes the losses in the other one, so to fasten the convergence of the optimization algorithm the magnet losses are only minimized at OP4.

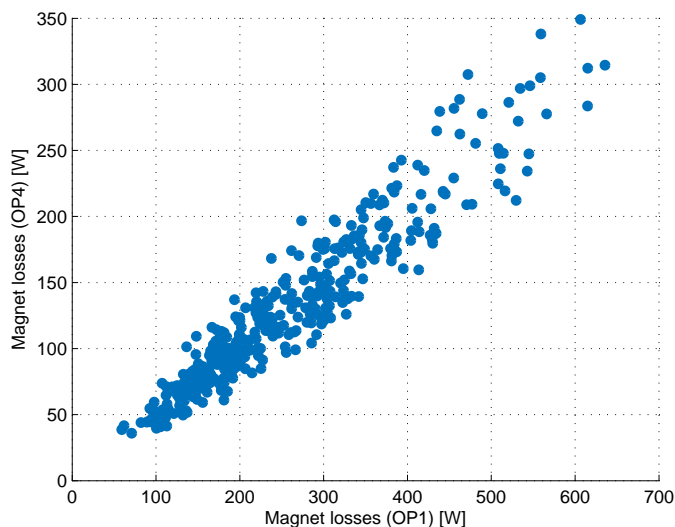


FIGURE 5.20: Relation between magnet losses at no load (OP1) and in field weakening operation (OP4)

Figure 5.21 displays the magnet losses at OP4 depending on the air gap. This figure is very interesting as it shows the high influence of the air gap on magnet losses. A larger air gap strongly reduces the magnet losses.

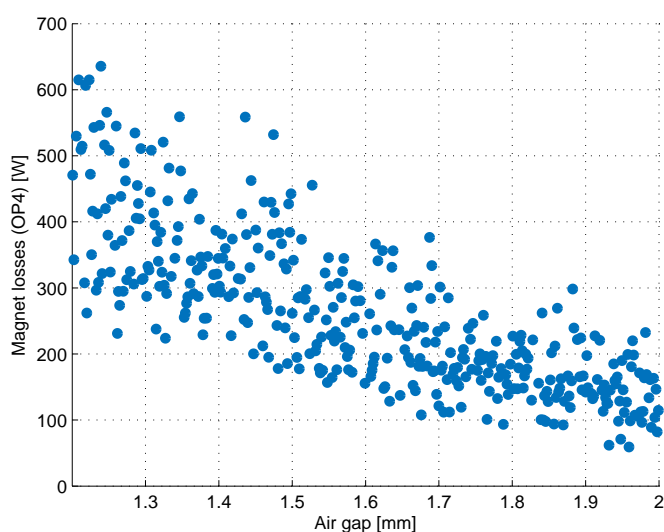


FIGURE 5.21: Relation between magnet losses and air gap

Figure 5.22 displays the peak power depending on the short circuit current. The color of each design is the number of turns varying from 2 to 4. This figure helps to verify that the peak power increases linearly with the short circuit current (see 2.2.2). Designs with $N=2$ have a short circuit current greater than 350 Arms which is the maximum allowed short circuit current. Over this limit the peak power appears as not linear with I_{sc} . These designs have a small torque, so a small induced voltage. Furthermore the inductance with $N=2$ is very low, so the field weakening area starts at a very high rotational speed. At 7000 rpm, these machines are not in the field weakening area and do not achieve their peak power at this rotational speed.

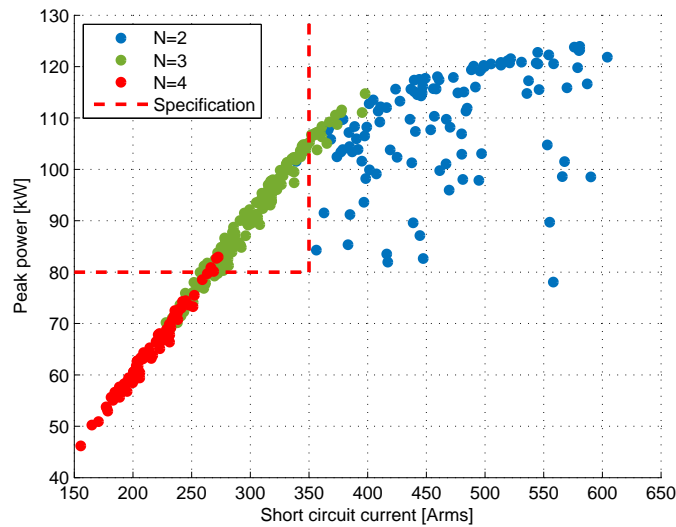


FIGURE 5.22: Peak power depending on the short circuit current and the number of turns

Figure 5.23 displays the peak torque depending on the total axial length of the machine and the number of turns. Higher number of turns increases the length of the teeth, so the axial length of the machine. Every design achieve the required axial length of 80 mm. The reduction of the axial length is a main objective of this work, but this study shows that the high majority of designs offers a very satisfying axial length. To fasten the convergence of the optimization algorithm the total length has been excluded from the objectives of the optimization. To avoid too long designs, any design longer than 75 mm is rejected.

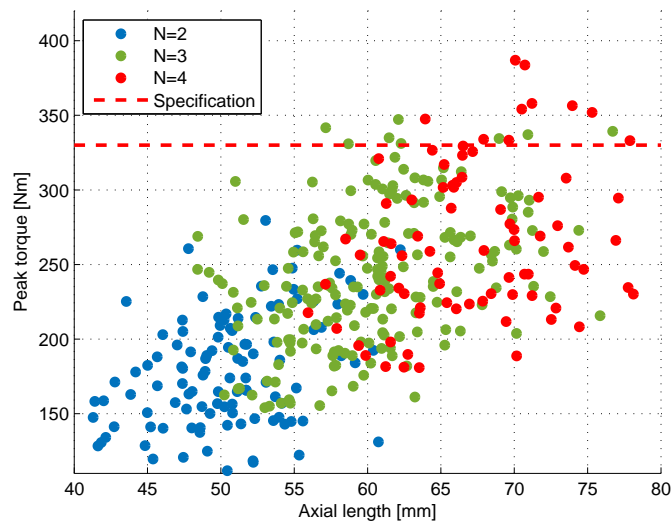


FIGURE 5.23: Peak torque depending on axial length and the number of turns

5.2.2.3 Conclusion

The sensitivity analysis has enabled a better definition of the machine design. The number of turns N is fixed to 3 and the variation of the pole pairs number is limited between $n_p = 7$ and $n_p = 9$.

Four objectives are defined for the optimization:

- Minimization of the magnet mass
- Maximization of the efficiency at full load (OP2)
- Maximization of the efficiency at maximum rotational speed (OP4)
- Minimization of the magnet losses at maximum rotational speed (OP4)

5.2.3 Optimization

5.2.3.1 Selection of optimized design

The multi-objective optimization has been performed and a total of 11000 designs have been evaluated. This high number of designs give a very good estimation of the physically possible performances. In figure 5.24, the peak torque of each design is displayed as function of the peak power. The required performances (330 Nm and 80 kW) are displayed in red. It can be observed that a large number of designs achieves the requirements. The peak performances vary in a very large range between 150 Nm and 450 Nm for the torque and between 65 kW and 120 kW for the power.

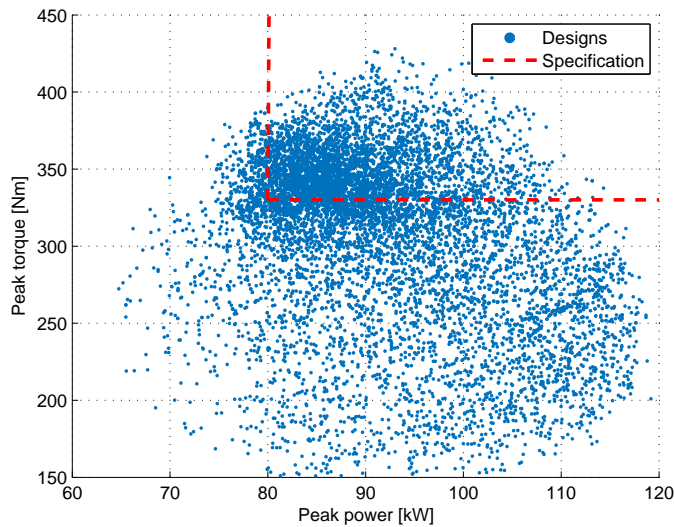


FIGURE 5.24: Peak torque and peak power of the calculated designs

Figure 5.25 displays the results of the multi-objective optimization. The Pareto front between the four objectives are plotted.

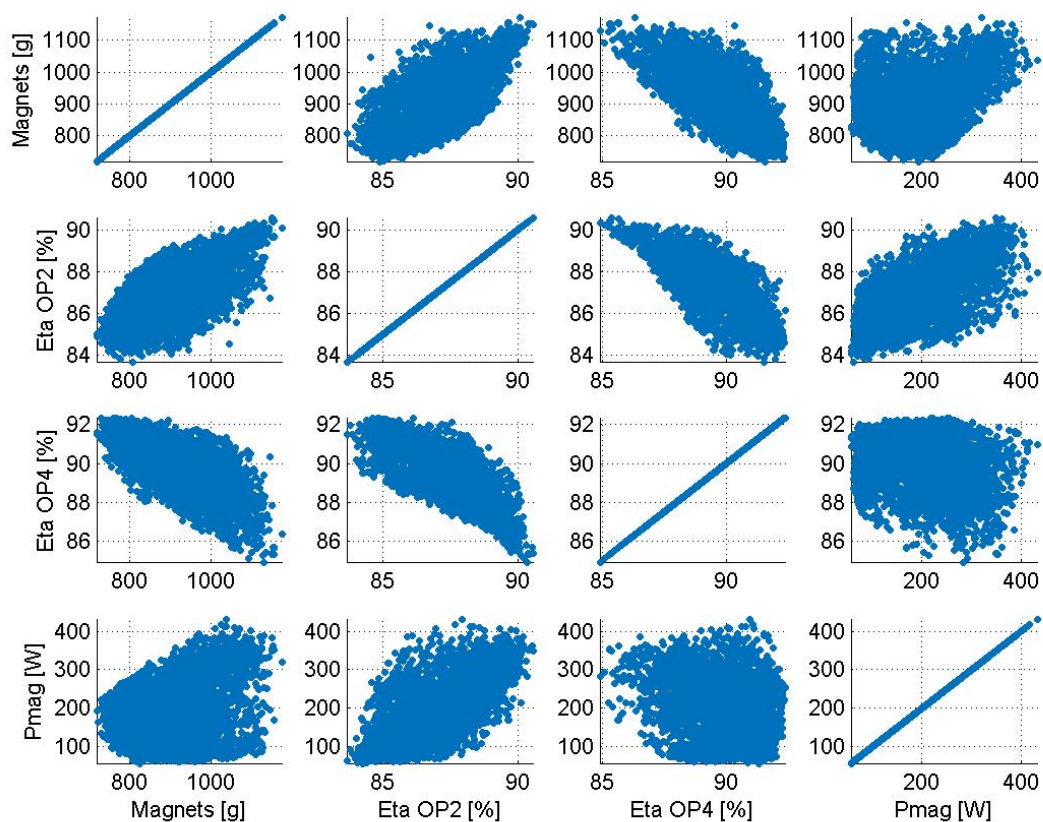


FIGURE 5.25: Pareto fronts of the multi-objectives optimization

To select the design, a first filtering is performed between the designs:

- Step 1: Selection of designs needing less than 800 g magnets to get an improvement compared to the manually designed machine
- Step 2: Selection of designs with less than 200 W magnet losses
- Step 3: To maximize the efficiency of the machine at the low speed operating points (which are the most important for the lifetime efficiency, see figure 2.3), only designs with an efficiency greater than 86 % in the operating point OP2 are selected.

This filtering has reduced the number of designs to 950 designs. These designs are displayed in figure 5.26 (selected design in red).

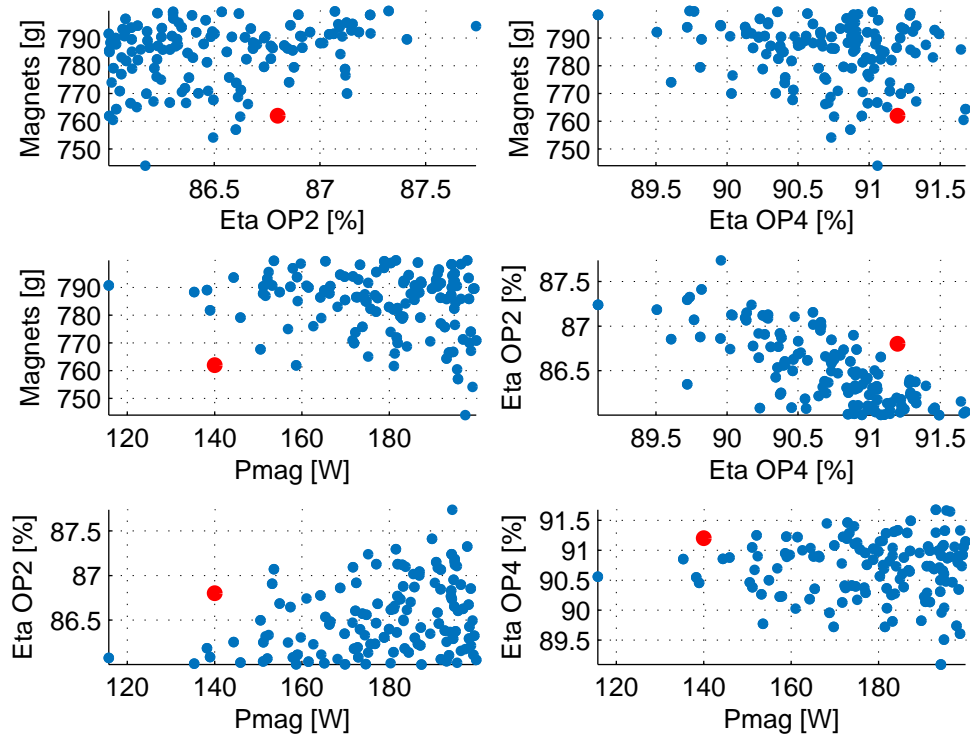


FIGURE 5.26: Pareto fronts of the filtered designs

The selected design is one of the designs with the smallest magnet mass and the smallest magnet losses. Its efficiency at full load (OP2) is satisfying. At high rotational speed (OP4) this design is in the first quarter of the selected designs. This good efficiency and reduced magnet losses should ensure a high continuous power. The main parameters of the selected design are displayed in table 5.4.

Description	Value	Specification
Pole pairs number	9	
Number of magnets	18	
NSPP	1.5	
Number of slots	81	
Number of winding turns	3	
Total length	65 mm	≤ 80 mm
Inside diameter (end windings)	185 mm	≥ 182 mm
Outside diameter (end windings)	282 mm	≤ 282 mm
Volume	2.3 L	min
Total magnets mass	762 g	min
Magnet grade	EH	min
Dysprosium mass	68.6 g	min
Peak torque	344 Nm	≥ 330 Nm
Torque density	150 Nm.L^{-1}	max
Peak power	85 kW	≥ 80 kW
Power density	37 kW.L^{-1}	max

TABLE 5.4: Parameters of the optimized design (AFM_{MOO})

5.2.3.2 Torque and power characteristics

The torque and power characteristics are displayed in figures 5.27 and 5.28. The designed machine achieves a maximum torque of 344 Nm and a maximum power of 85 kW at 3000 rpm. At 7000 rpm, the peak power is 81 kW. The required continuous torque (170 Nm) and power (60 kW) are achievable with a maximum phase current of 235 Arms. The designed machine achieves the specification.

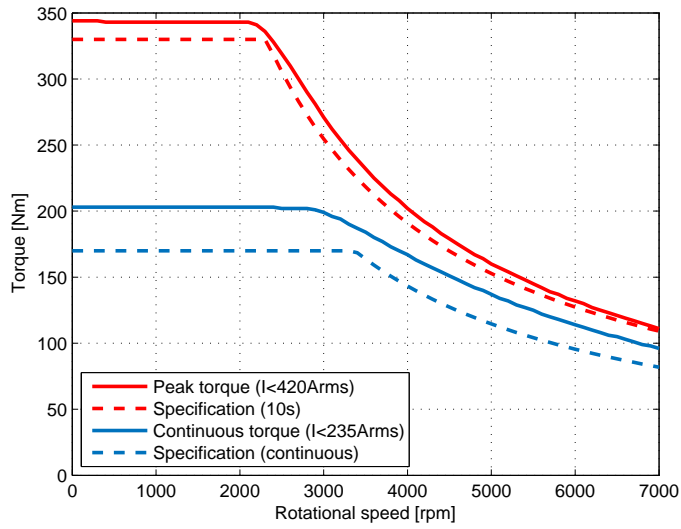


FIGURE 5.27: Torque characteristic

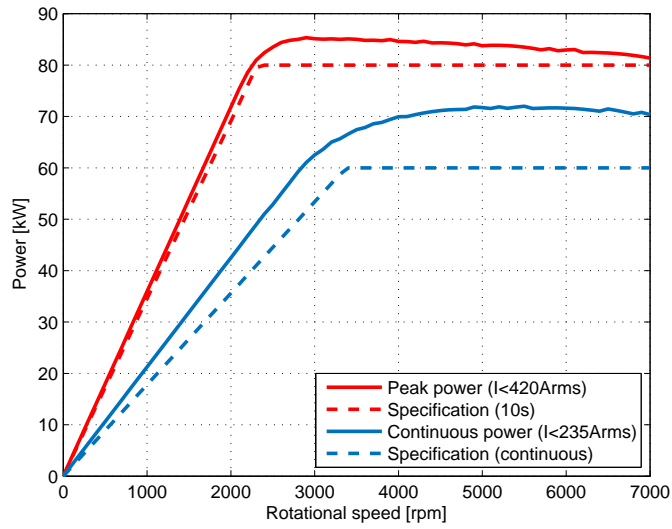


FIGURE 5.28: Power characteristic

The MTPA (Maximum Torque Per Ampere) characteristic is displayed in figure 5.29. The reduction of the torque due to saturation of the magnetic material can be observed over 200 Arms. At the maximum phase current, the torque is reduced by 7%.

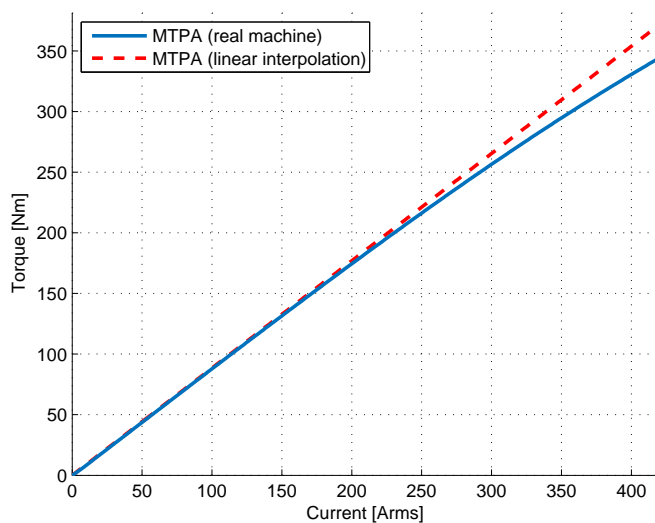


FIGURE 5.29: MTPA characteristic

This machine is characterized in appendix F.

5.2.3.3 Comparison with the manually designed machine

The main machine parameters of the manually designed machine and the design obtain with the multi-objective optimization are compared in table 5.5. This first comparison shows the improvement in the design thanks to the MOO. The peak performance of the machine (torque and power) are increased by a few percent. Thanks to the reduction of the axial length by 11 % the torque density is increased by 29 %. A reduction of the magnet mass has been achieved but a more expensive magnet needs to be used, so the mass of dysprosium is increased.

Parameter	Manual design (AFM ₆₀)	MOO (AFM _{MOO})	Evolution
Axial length	73.2 mm	65 mm	-11 %
Outside diameter	285 mm	282 mm	-1 %
Inside diameter	180 mm	185 mm	+3 %
Volume	2.8 L	2.3 L	-18 %
Peak torque	325 Nm	344 Nm	+6 %
Torque density	116 Nm.L ⁻¹	150 Nm.L ⁻¹	+29 %
Peak power	84 kW	85 kW	+1 %
Power density	30 kW.L ⁻¹	37 kW.L ⁻¹	+23 %
Magnet mass	817 g	762 g	-7 %
Magnet grade	UH	EH	-
Dysprosium mass	61.3 g	68.6 g	+ 12 %

TABLE 5.5: Comparison between the manually designed and the MOO machine

To compare both machines, their torque and power characteristics are displayed in figures 5.30 and 5.31. The machine designed with MOO achieves a greater torque and a greater peak power. Thanks to a reduced electric resistance at high rotational speeds compared to the manually designed machine, the peak power decreases less at high rotational speeds.

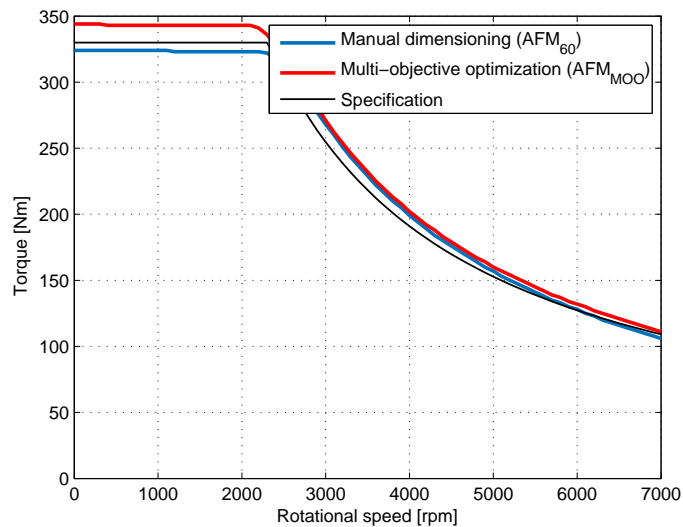


FIGURE 5.30: Torque characteristic of both designed machines

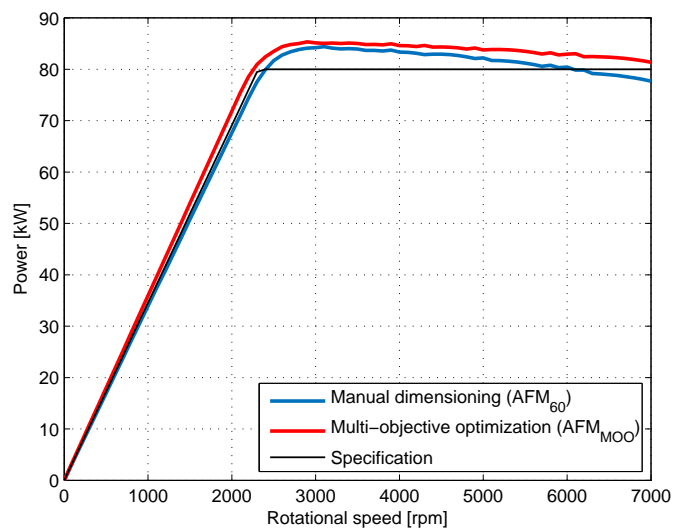


FIGURE 5.31: Power characteristic of both designed machines

A comparison between both machine is made in appendix F.

Conclusion

In this chapter the dimensioning of the axial-flux machine is presented. Two machines have been designed:

- The first machine has been manually designed. 60 designs have been successively evaluated based on the try and error method. This manual dimensioning is a good way to obtain a satisfying design in a short time but is not adapted to get the optimum. The selection of the concept defined in the chapter 2 and 3 is confirmed. With a peak torque of 325 Nm and a peak power of 84 kW, the machine does not completely achieve the requirements.
- The second machine has been designed with a multi-objective optimization. This method is based on a software toolchain which automatically generates new designs and evaluates them. Thanks to this automation a huge number of designs are calculated and the optimum can be found. Compared to the manually designed machine, the torque density has been increased by 29%, the axial length reduced by 11% and the magnet losses reduced by 40%.

Chapter 6

Comparison with a radial-flux machine

Contents

Introduction	146
6.1 Comparison with same specification	147
6.1.1 RFM design RFM ₃₀₀	147
6.1.2 Design comparison	149
6.1.3 Torque and power characteristics	149
6.1.4 Losses and efficiency	150
6.1.5 Torque ripple	153
6.2 Comparison with same dimensions	154
6.2.1 RFM design RFM ₂₈₂	154
6.2.2 Design comparison	156
6.2.3 Torque and power characteristics	156
6.2.4 Losses and efficiency	157
6.2.5 Torque ripple	160
Conclusion	161

Introduction

In this chapter, the designed axial-flux machine is compared with a Radial-Flux Machine (RFM) designed for a similar hybrid application. The reference RFM is the IMG300 developed by Bosch and built for example in the Volkswagen Touareg hybrid [107, 108]. The main characteristics and performances of this machine are shown in table 6.1. The comparison is performed in two steps:

- At first, the magnetic circuit of the RFM stays unchanged. The axial length and the number of turns of the windings are modified to fit the required specification (330 Nm and 80 kW). The main goal of this study is to compare the dimensions and the performances of two machines delivering similar power data.
- In a second step, the magnetic circuit of the RFM is lightly modified to fit to the inside and outside diameters of the AFM. The axial length is fixed, so both machines have the same dimensions. In this study, the power data and the performances of two machines having the same dimensions are compared.

In this chapter, the performances of both machines are compared with difference performance maps. In each of them, positive values mean that the axial-flux machine is better than the radial-flux machine. For example, a positive efficiency difference means that the AFM has a higher efficiency than the RFM. On the contrary a positive losses difference means that the losses in the AFM are lower than in the RFM for this operating point.

Iron length	55 mm
Axial length (with coil ends)	70 mm
Outside diameter	300 mm
Inside diameter	195 mm
Volume	2.9 L
Copper fill factor	55 %
Pole pairs	12
Number of turns	104
Peak torque ($I_{max}=420$ Arms)	393 Nm
Torque density	138 Nm.L ⁻¹
Peak power ($U_{bat}=300$ Vdc)	63 kW
Power density	22 kW.L ⁻¹

TABLE 6.1: Characteristics and performances of IMG300

6.1 Comparison with same specification

6.1.1 RFM design RFM₃₀₀

The magnetic design of the IMG300 is presented in figure 6.1. This machine has a concentrated winding with a NSPP=0.5. In this figure, only one pole pair (30 mechanical degrees) is displayed.

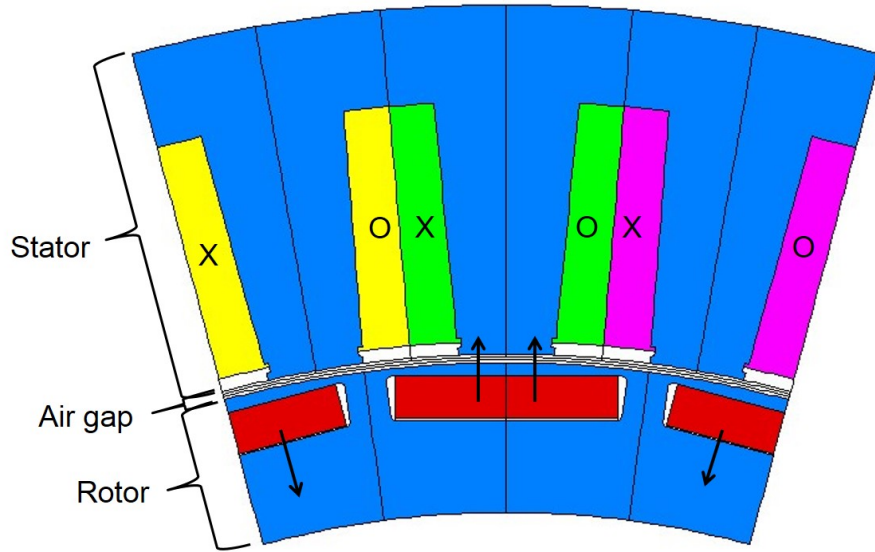


FIGURE 6.1: Magnetic design of the reference radial-flux machine (IMG300)

The torque characteristic is compared with the specification in figure 6.2. The reference machine delivers a too high torque but not enough power.

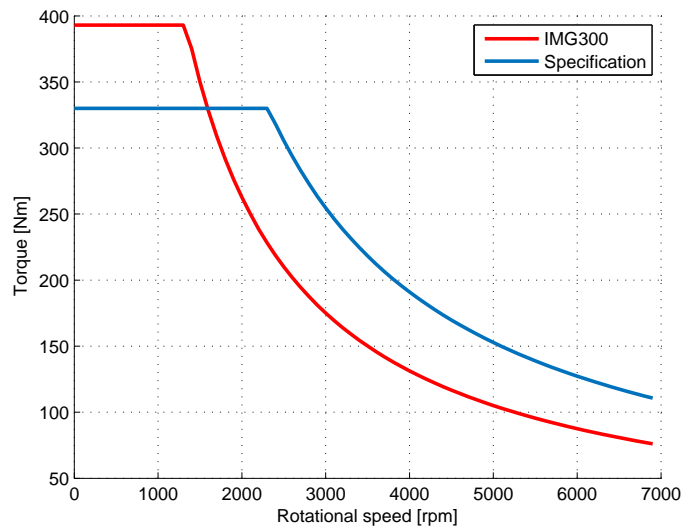


FIGURE 6.2: Torque characteristic of the reference radial-flux machine (IMG300)

To fit this machine to the requirements, the iron length l_{fe} and the number of turns N are modified. The peak power at maximum rotational speed depending on l_{fe} and N is displayed in figure 6.3.

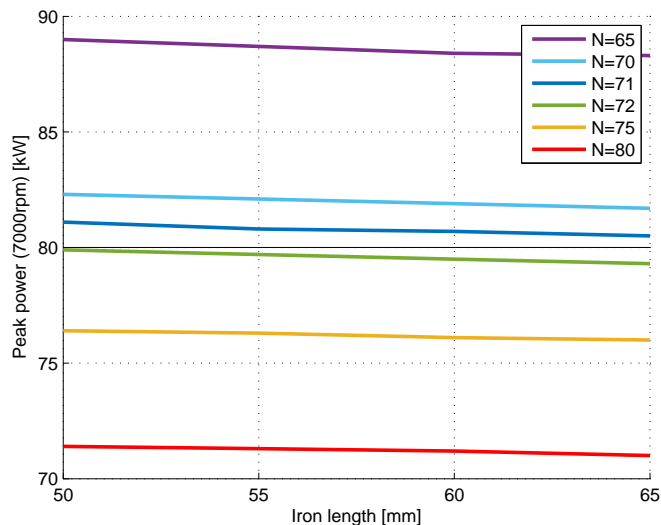


FIGURE 6.3: Peak power at maximum rotational speed depending on the iron length and the number of turns

In this figure, the peak power depends mainly on the number of turns and varies only lightly with the iron length. To achieve the required power of 80 kW, $N=71$ is selected. The peak torque depending on the number of turns and the iron length is displayed in figure 6.4. It increases linearly with the iron length.

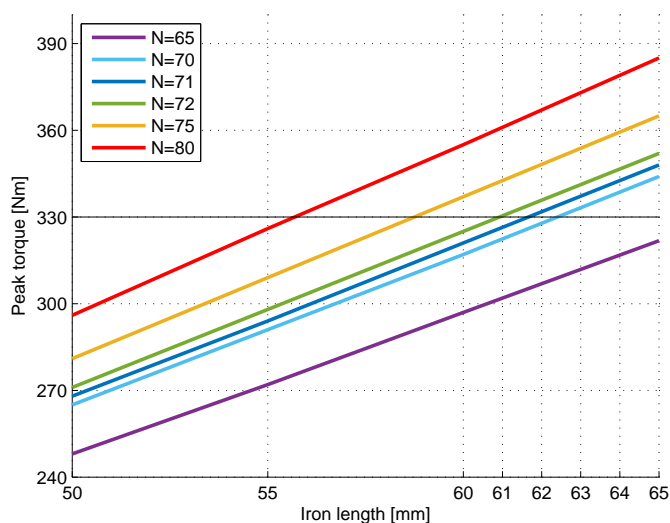


FIGURE 6.4: Peak torque depending on the iron length and the number of turns

The scaled IMG300 with $N=71$ and $l_{fe}=62$ mm is selected for this first comparison. This machine will be noted RFM₃₀₀ and will be compared with the design obtained from the multi-objective optimization: AFM_{MOO}.

6.1.2 Design comparison

The main characteristics the both machines are displayed in table 6.2.

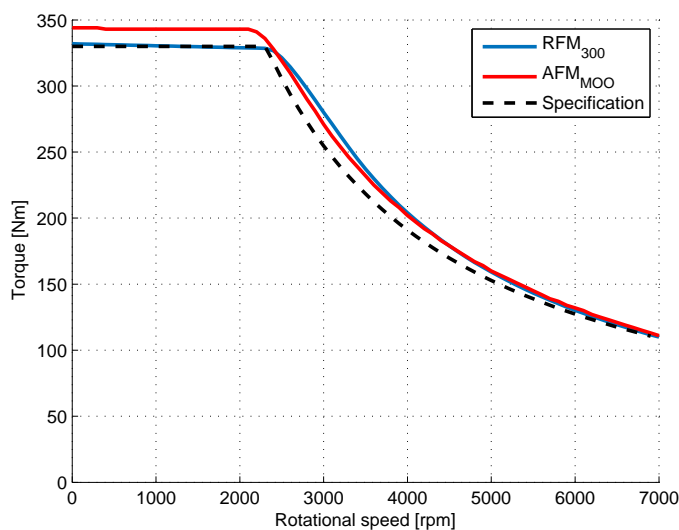
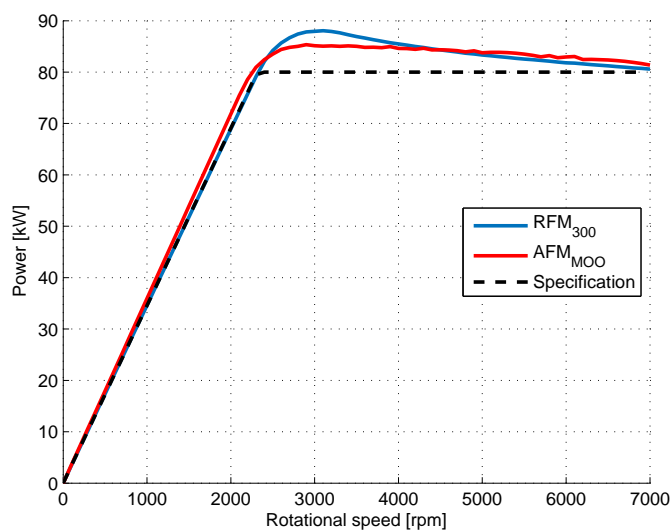
Parameter	RFM ₃₀₀	AFM _{MOO}	Evolution
Axial length	77 mm	65 mm	-16%
Outside diameter	300 mm	282 mm	-6%
Inside diameter	195 mm	185 mm	-5%
Volume	3.1 L	2.3 L	-18%
Peak torque	332 Nm	344 Nm	+4%
Torque density	106 Nm.L ⁻¹	149 Nm.L ⁻¹	+41%
Peak power	88 kW	85 kW	-3%
Power density	28 kW.L ⁻¹	37 kW.L ⁻¹	+31%
Magnet mass	1129 g	762 g	-33%
Magnet grade	EH	EH	0%
Dysprosium mass	102 g	69 g	-33%

TABLE 6.2: Comparison between RFM₃₀₀ and AFM_{MOO}

Thanks to a smaller volume and a higher torque the torque density of the AFM is more than 40 % higher than the RFM. The same observation can be done for the power density which has been increased by more than 30%. In this comparison, the AFM needs one third less magnet than the RFM. This improvement is mainly due to the necessity to increase the length of the RFM to achieve the peak torque and the peak power.

6.1.3 Torque and power characteristics

The torque and power characteristics of both machines are displayed in figures 6.5 and 6.6. The RFM achieves a lightly higher peak power than the RFM thanks to the reluctance torque. In this machine, $L_d \neq L_q$, so a reluctance torque is generated in case of field weakening. This reluctance torque increases lightly the power in the field weakening operating points but tends to zero at high rotational speed (I_q tends to zero, see appendix A). For this reason, the peak power of the RFM drops off at high rotational speed.

FIGURE 6.5: Peak torque characteristics of RFM₃₀₀ and AFM_{MOO}FIGURE 6.6: Peak power characteristics of RFM₃₀₀ and AFM_{MOO}

6.1.4 Losses and efficiency

The phase resistance of both machines are plotted in figure 6.7. Thanks to a reduced current density and smaller coil ends (concentrated winding), the resistance of the RFM is lower than the AFM. Furthermore, at high rotational speed the RFM is less sensitive to skin effect thanks to the pull-in winding. The copper losses difference between both machines is plotted in figure 6.8. Positive values means that the losses in the AFM are lower than in the RFM. Except in the low speed and low torque operating points, the RFM has smaller copper losses.

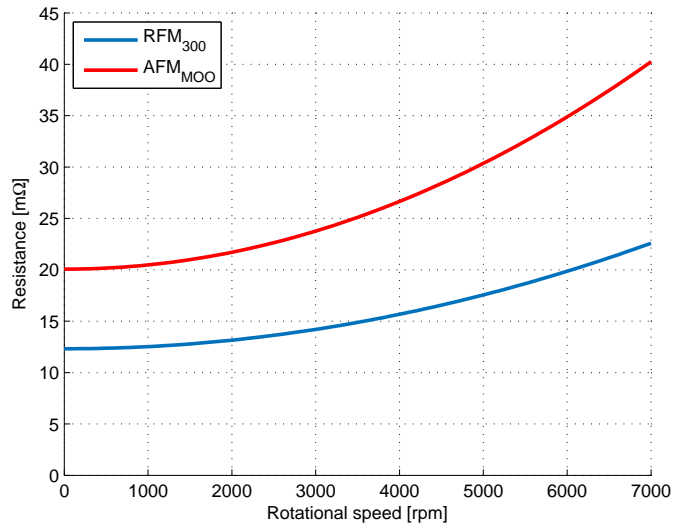


FIGURE 6.7: Phase resistance of RFM₃₀₀ and AFM_{MOO} [model]

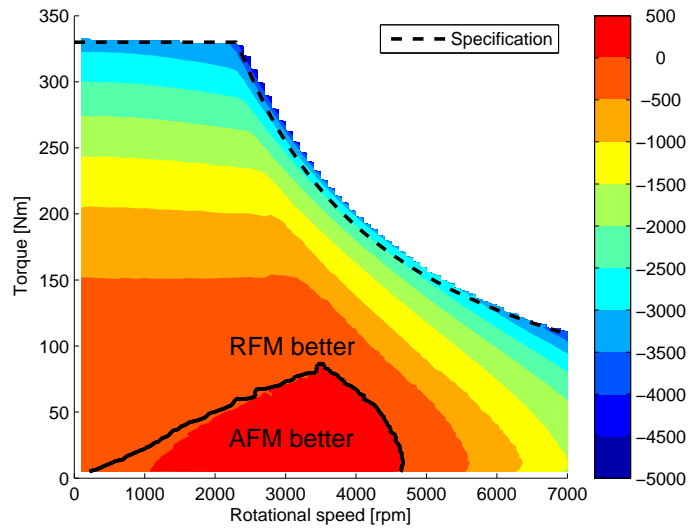


FIGURE 6.8: Copper losses difference between RFM₃₀₀ and AFM_{MOO} [W]

Iron and rotor losses differences are respectively plotted in figures 6.9 and 6.10. The AFM has smaller iron losses in every operating point. This is mainly due to the short axial length which reduces the quantity of iron, the lower electric frequency and the distributed winding which generates less harmonics in the magnetic field and less eddy current in the rotor.

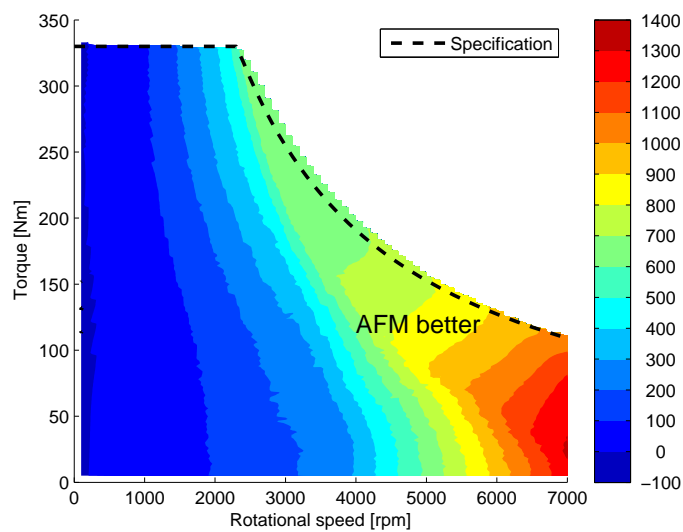


FIGURE 6.9: Stator iron losses difference between RFM_{300} and AFM_{MOO} [W]

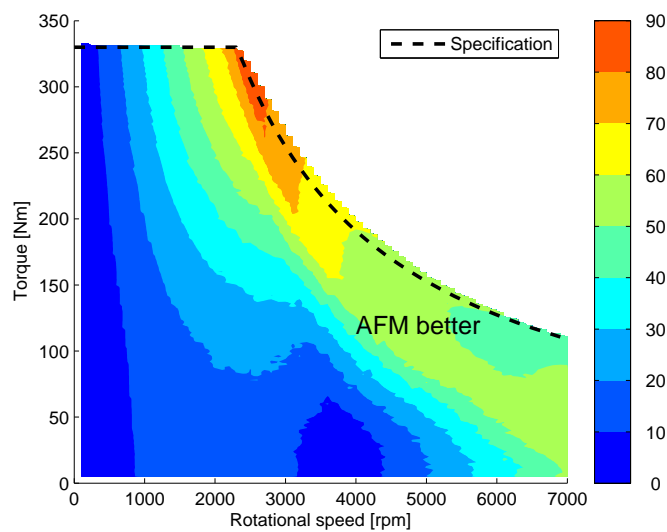


FIGURE 6.10: Rotor losses difference between RFM_{300} and AFM_{MOO} [W]

The efficiency difference is plotted in figure 6.11. Positive values are operating points where the AFM has a better efficiency. The AFM is better for low torque and low speed operating points. In these operating points the AFM needs less current than the RFM and so generates less copper losses. At high rotational speeds, the AFM has a higher induced voltage and needs more field weakening which worsens its efficiency.

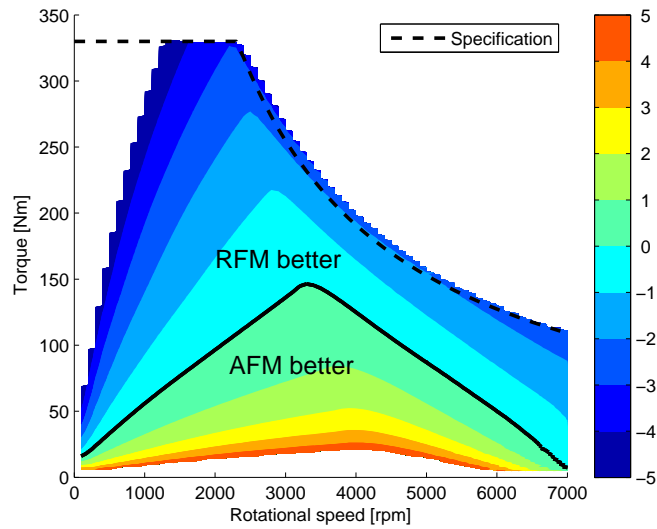


FIGURE 6.11: Efficiency difference between AFM_{MOO} and RFM_{300} [%]

The RFM has been simulated in the driving cycle presented in 2.2. In this cycle, the average power consumption is 2.96 kW compared to 2.19 kW for a perfect machine. The additional consumption due to the losses is 8% higher for the RFM than for the AFM.

6.1.5 Torque ripple

The torque ripple difference is displayed in figure 6.12. Positive values are operating points where the torque ripple of the AFM is smaller than of the RFM. The AFM has a lower torque ripple in high torque operating points.

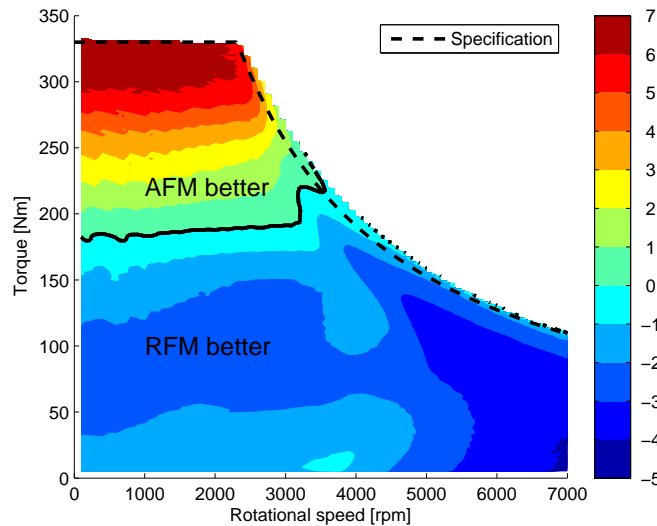


FIGURE 6.12: Torque ripple difference between RFM_{300} and AFM_{MOO} [Nm]

6.2 Comparison with same dimensions

6.2.1 RFM design RFM₂₈₂

In this section, the magnetic design of the reference radial-flux machine is scaled to fit to the inside and outside diameter of the AFM:

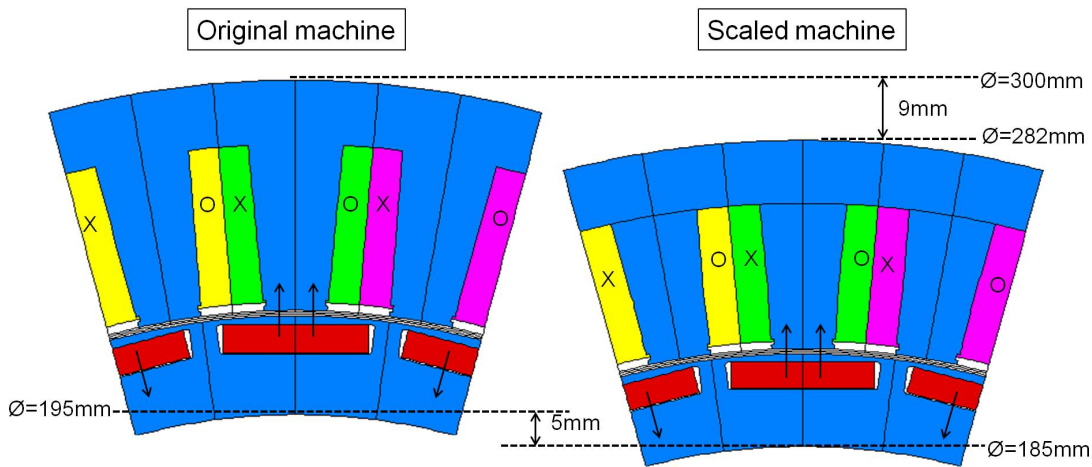


FIGURE 6.13: Radial scaling of the reference radial-flux machine

Following design rules have been applied to scale the machine:

- The rotor have been homothetically reduced with a ratio $\lambda = \frac{185}{195} \approx 0.949$. This transformation ensures similar mechanical properties and high speed stability.
- The air gap is not modified.
- The back iron is maintained constant.
- The height of the stator teeth is determined from the previous assumptions. The slot width is unchanged.

For this comparison the axial length of the machine is the same as in the axial-flux machine: $l_{tot}=65$ mm. As the slot width remains unchanged, the coil end winding remains unchanged and is 15 mm (both sides). So, the iron length of the scaled radial-flux machine is fixed to $l_{fe}=50$ mm. For this machine, only the number of turns N can be modified.

The torque and power characteristics of the scaled machine with several number of turns are displayed in figures 6.14 and 6.15. Machines with higher number of turns achieve more torque but less peak power. No machine can deliver the required torque and power (330 Nm and 80 kW at maximum rotational speed), so the scaled radial-flux machine

can not achieve the specification in the available space. A longer axial length would be necessary to fit the specification.

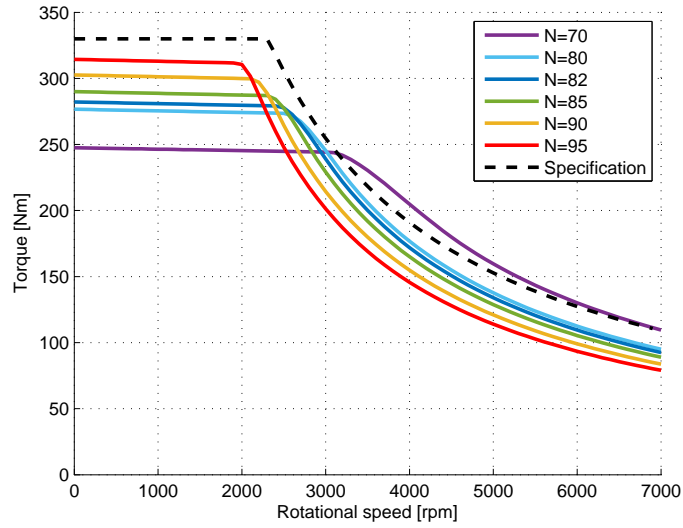


FIGURE 6.14: Torque characteristic depending on the number of turns

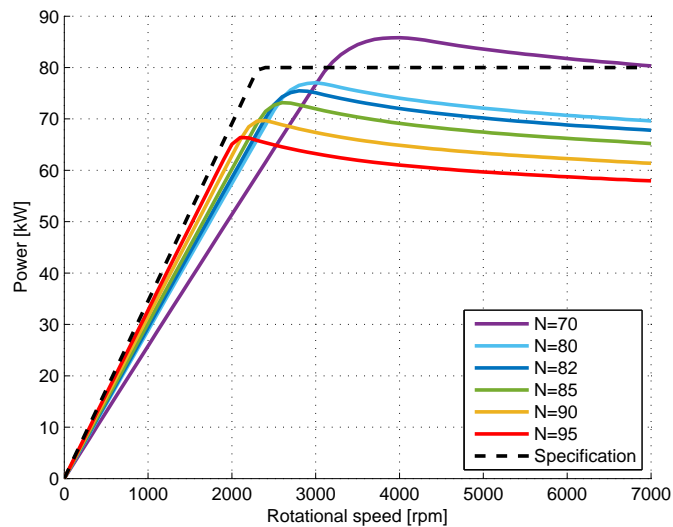


FIGURE 6.15: Power characteristic depending on the number of turns

The machine with $N=82$ achieves 282 Nm and 67.8 kW at maximum rotational speed. These both values correspond to 85 % of the specification, so this winding number is the best compromise between the peak torque and the peak power and is selected for the comparison. The scaled machine with $N=82$ is named RFM_{282} .

6.2.2 Design comparison

The main characteristic of both machines are displayed in table 6.3.

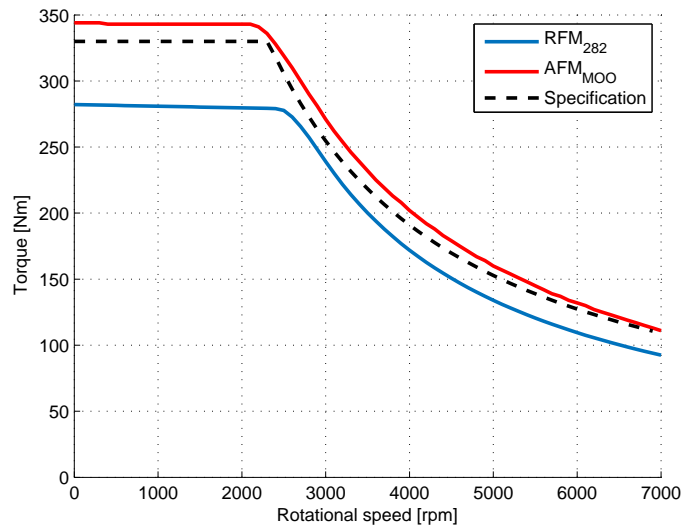
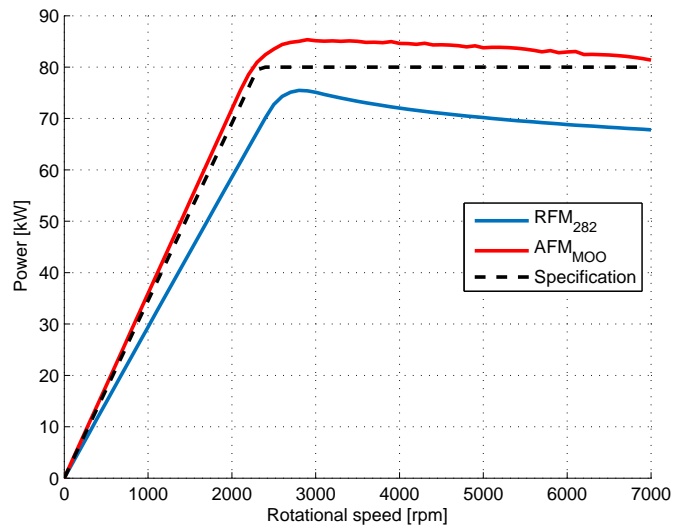
Parameter	RFM ₂₈₂	AFM _{MOO}	Evolution
Axial length	65 mm	65 mm	0%
Outside diameter	282 mm	282 mm	0%
Inside diameter	185 mm	185 mm	0%
Volume	2.3 L	2.3 L	0%
Peak torque	282 Nm	344 Nm	+22%
Torque density	122 Nm.L ⁻¹	149 Nm.L ⁻¹	+22%
Peak power	76 kW	85 kW	+12%
Power density	33 kW.L ⁻¹	37 kW.L ⁻¹	+12%
Magnet mass	819 g	762 g	-7%
Magnet grade	EH	EH	0%
Dysprosium mass	74 g	69 g	-7%

TABLE 6.3: Comparison between RFM₂₈₂ and AFM_{MOO}

In the same volume, the AFM generates more torque and achieves a higher peak power. The torque and power density are respectively increased by 22% and 12%. The magnet mass is reduced by 7%. In this first comparison, the AFM is better than the RFM, but the difference is smaller than between the AFM and the unscaled machine (see 6.1.2). The unscaled RFM suffers from longer stator teeth which increase the magnetic saturation and the inductance reducing the peak torque and the peak power. Thanks to smaller teeth, the torque density of the RFM is improved in the scaled machine, but the higher current density could lead to higher copper losses and a reduced efficiency.

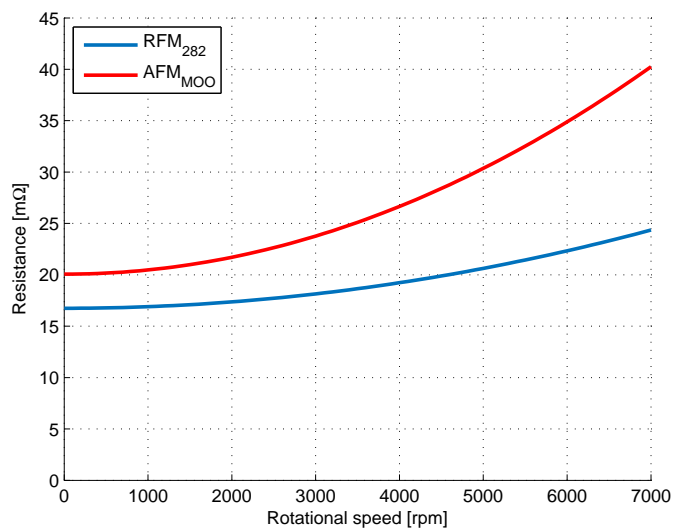
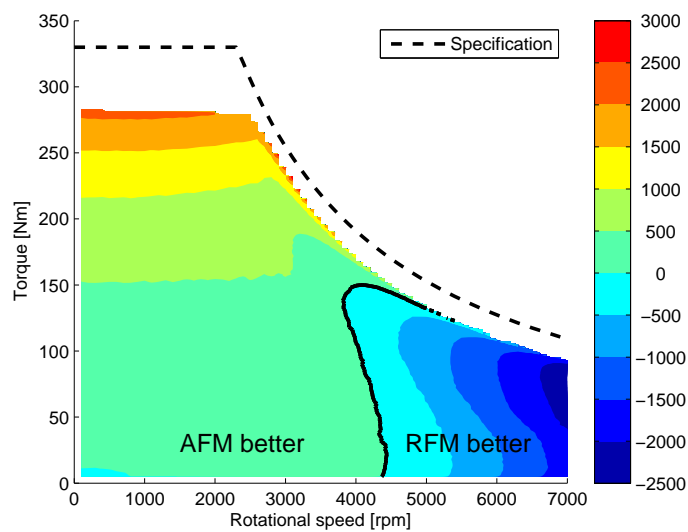
6.2.3 Torque and power characteristics

The torque and power characteristics of both machines are displayed in figures 6.16 and 6.17. The RFM can not achieve the required torque and power due to the too short axial length. Similar observation as in the previous comparison (see 6.1.3) can be made, especially the peak power of the RFM which drops off due to the reluctance torque.

FIGURE 6.16: Peak torque characteristics of RFM₂₈₂ and AFM_{MOO}FIGURE 6.17: Peak power characteristics of RFM₂₈₂ and AFM_{MOO}

6.2.4 Losses and efficiency

The phase resistance of both machines are plotted in figure 6.18. Like in the first comparison, the RFM has a better phase resistance. The copper losses difference between both machines is plotted in figure 6.19. Positive values means that the losses in the AFM are lower than in the RFM. On the contrary to the first comparison, the AFM has lower copper losses in a much wider area (rotational speed under 4500 rpm). At higher rotational speeds, the AFM suffers from its higher induced voltage and the necessary field weakening.

FIGURE 6.18: Phase resistances of RFM₂₈₂ and AFM_{MOO} [model]FIGURE 6.19: Copper losses difference between RFM₂₈₂ and AFM_{MOO} [W]

Iron and rotor losses differences are respectively plotted in figures 6.20 and 6.21. Like in the first comparison, the AFM has smaller iron losses in the high majority of the operating points. The RFM has a lightly smaller stator iron losses for very low rotational speed and lower rotor losses for low torque operating points over 3000 rpm.

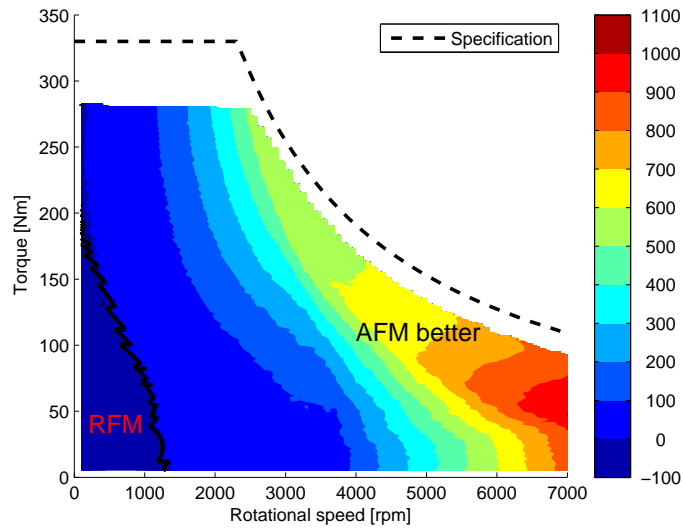


FIGURE 6.20: Stator iron losses difference between RFM₂₈₂ and AFM_{MOO} [W]

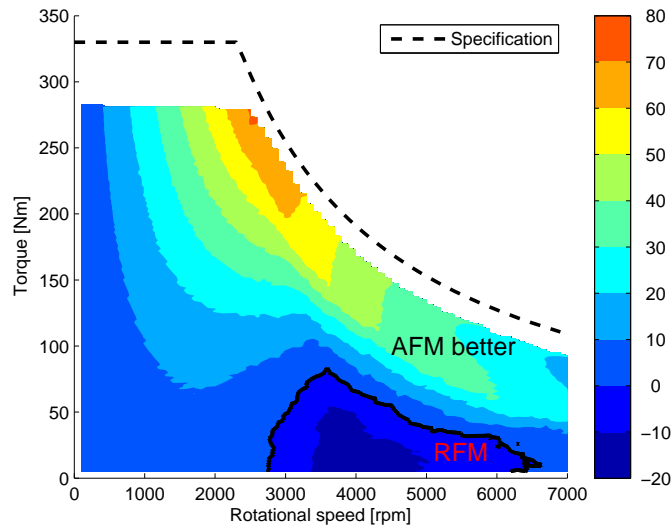
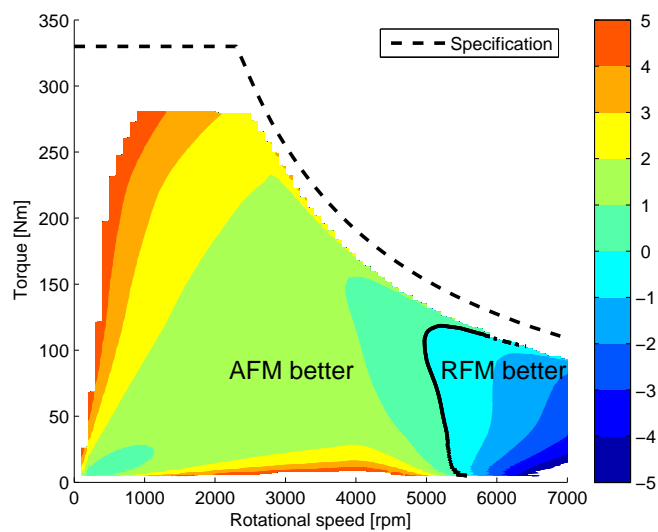


FIGURE 6.21: Rotor losses difference between RFM₂₈₂ and AFM_{MOO} [W]

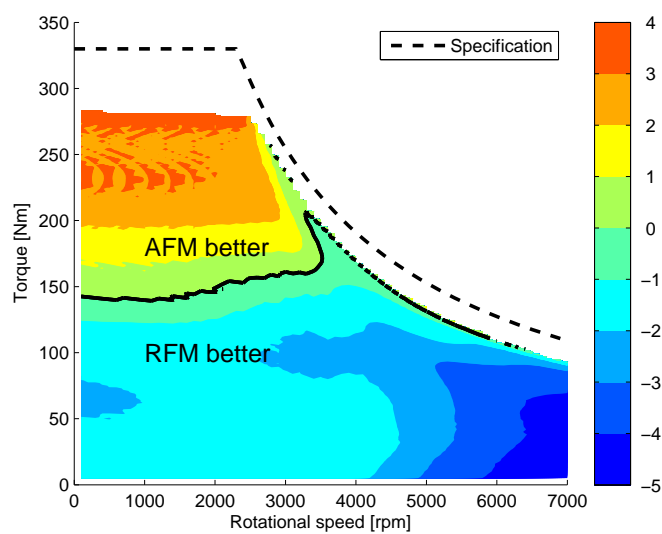
The efficiency difference is plotted in figure 6.22. Positive values are operating points where the AFM has a better efficiency. On the contrary to the first comparison, the AFM has a better efficiency than the RFM in the majority of the operating points. The RFM is only better for rotational speeds over 5000 rpm.

FIGURE 6.22: Efficiency difference between AFM_{MOO} and RFM_{282} [%]

The RFM has been simulated in the driving cycle presented in 2.2. In this cycle, the average power consumption is 3.06 kW compared to 2.19 kW for a perfect machine. The additional consumption due to the losses is 22% higher for the RFM than for the AFM.

6.2.5 Torque ripple

The torque ripple difference is plotted in figure 6.23. Like in the first comparison, the AFM has a lower torque ripple for high torque operating points.

FIGURE 6.23: Torque ripple difference between RFM_{282} and AFM_{MOO} [Nm]

Conclusion

In this chapter, the designed axial-flux machine has been compared with a state of the art radial-flux machine. The reference radial-flux machine is the integrated motor-generator built in the Volkswagen Touareg hybrid. Two comparisons are performed:

- At first, the RFM is scaled to fulfill the performances requirements (peak torque and power). This comparison shows that the AFM needs 18% less volume to obtain the same performances. The efficiency of the RFM is better in the high majority of the operating points.
- In a second step, the RFM is scaled to the same dimensions than the AFM. In that case, it does not fulfill the requirements anymore and the AFM delivers 22% more torque and 12% more power. Contrary to the first comparison, the AFM has in that case a better efficiency in the high majority of the operating points.

These comparisons show the potential of the AFM for integrated motor-generators, especially when the axial length is short. In that case, the RFM suffers from a reduced iron length, higher losses and can not fulfill the requirements.

Chapter 7

Prototypes and tests

Contents

Introduction	164
7.1 First prototype: AFM_{P1}	164
7.1.1 Description	164
7.1.2 Measurements	165
7.1.2.1 Induced voltage and short circuit current	165
7.1.2.2 Torque current characteristic	167
7.1.2.3 Torque speed characteristic	169
7.2 Second prototype: AFM_{P2}	171
7.2.1 Description	171
7.2.2 Measurements	172
7.2.2.1 Induced voltage and no load losses	172
7.2.2.2 Short circuit current and short circuit losses	175
7.2.2.3 Torque current characteristic	177
7.2.2.4 Losses performance map	178
Conclusion	179

Introduction

During this PhD two prototypes of internal rotor AFM have been built:

- A first prototype with concentrated windings built in 2014: AFM_{P1}
- A second prototype with NSPP=0.75 based in the manually designs machine (AFM₆₀) presented in 5.1.1.3: AFM_{P2}

This chapter presents these prototypes and their measurement. This work is of course a team work. My contribution is limited to the designing of the magnetic circuit and some measurements. I'd like to thanks all my colleagues who worked on these prototypes and enabled the completion of this chapter.

7.1 First prototype: AFM_{P1}

7.1.1 Description

In the early phase of the project and this work (2013-2014), a first prototype of axial-flux machine has been built. The main parameters of this machine are indicated in table 7.1.

Description	Value	Specification
Pole pairs number	12	
Number of magnets	24	
NSPP	0.5	
Number of slots	36	
Number of winding turns	4	
Total length	80 mm	≤ 80 mm
Inside diameter (end windings)	180 mm	≥ 182 mm
Outside diameter (end windings)	280 mm	≤ 282 mm
Volume	2.9 L	min
Total magnets mass	910 g	min
Magnet grade	EH	min
Dysprosium mass	81.9 g	min

TABLE 7.1: Parameters of the first prototype (AFM_{P1})

The magnetic circuit of this machine, is similar to the basis AFM presented in 4.3.2. A concentrated winding with NSPP=0.5 and a pull in winding has been used. The 12

coils composing each electric phase are connected in parallel. The magnetic number of turn is 4, but due to this parallelization, 48 turns are necessary for each coil. Figure 7.1 displays the machine on the test bench.

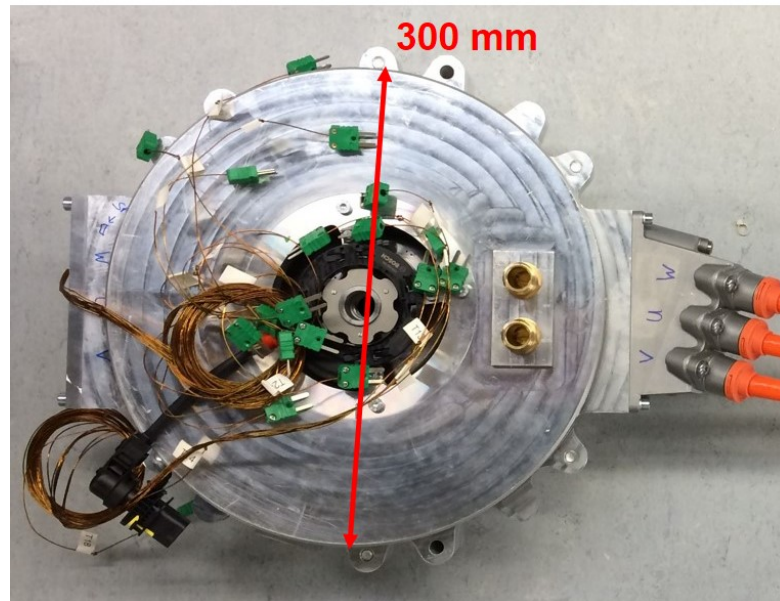
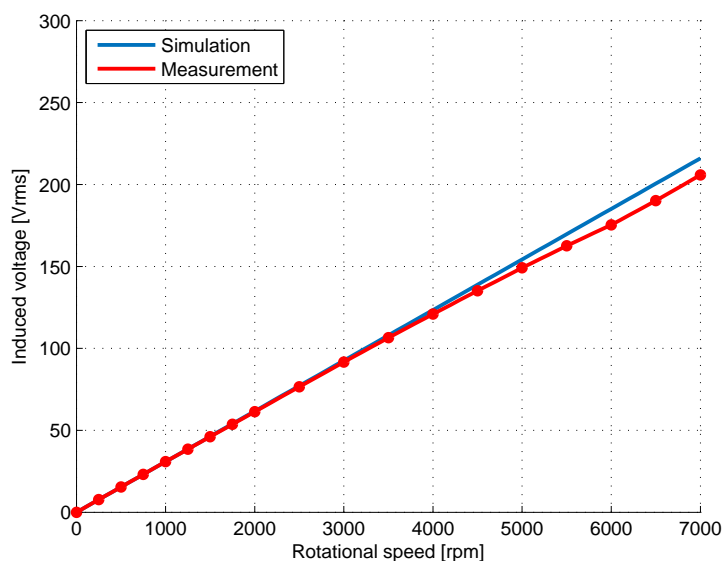
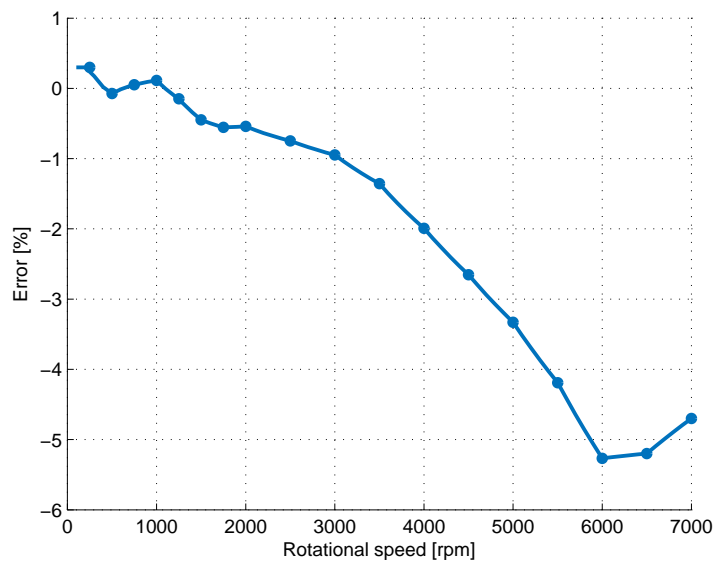


FIGURE 7.1: First prototype of AFM (AFM_{P1})

7.1.2 Measurements

7.1.2.1 Induced voltage and short circuit current

At first, the electric parameters of the machine are verified. The induced voltage has been measured at no load between 0 rpm and 7000 rpm. The cooling temperature of the machine has been fixed to 20 °C. The simulations and the measurements are compared in figure 7.2. The error between the measured induced voltage and the simulation is displayed in figure 7.3.

FIGURE 7.2: Induced voltage characteristic (AFM_{P1})FIGURE 7.3: Induced voltage error (AFM_{P1})

At low rotational speed, the measurement fits very well the simulation. Under 4000 rpm (which corresponds to more than 90% of the operating points of the machine (see figure 2.3)) the error remains smaller than 2%. At higher rotational speed, the error stays under 5%. As the induced voltage should be linear with the rotational speed an fits very well the simulation at very small rotational speed, the error can not only be due to an error in the simulation. During the speeding up, the temperature of the magnet increases due to high eddy current losses. This reduces their remanence and explains why the induced voltage is not linear with the rotational speed.

Figure 7.4 displays the measured and the simulated short circuit current. The error is displayed in figure 7.5. Except at very low rotational speeds, the error is smaller than 3%.

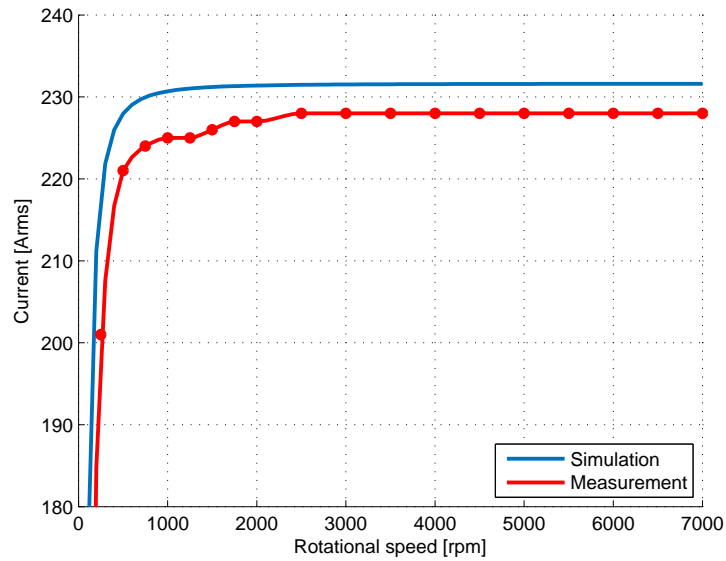


FIGURE 7.4: Short circuit current characteristic (AFM_{P1})

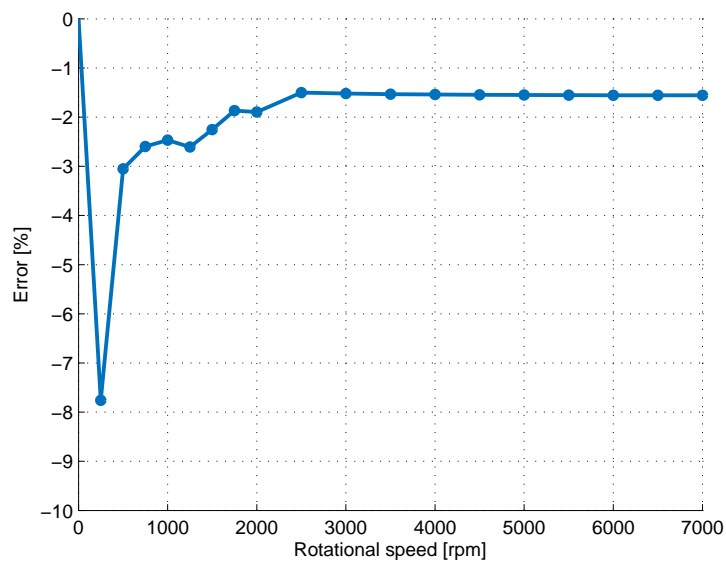
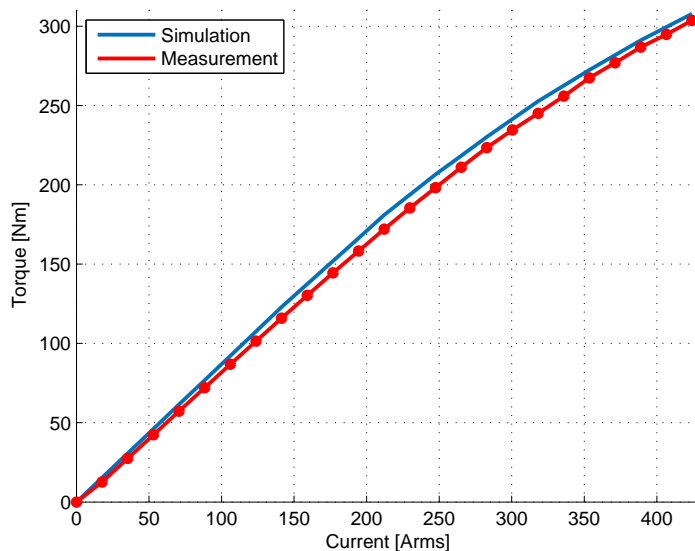
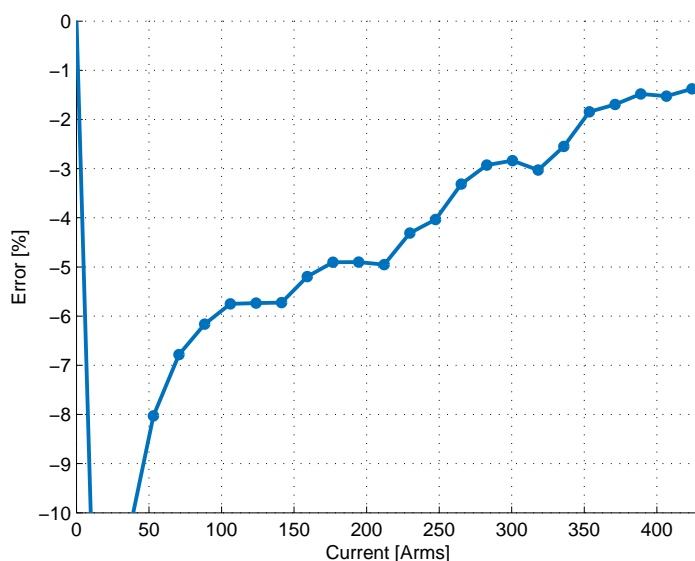


FIGURE 7.5: Short circuit current error (AFM_{P1})

7.1.2.2 Torque current characteristic

In a third step the evolution of the torque with the current has been measured at a constant rotational speed of 1000 rpm. The results and the error are displayed in figures

7.6 and 7.7.

FIGURE 7.6: Torque current characteristic (AFM_{P1})FIGURE 7.7: Torque current characteristic error (AFM_{P1})

The simulations lightly overestimate the torque. At small current ($I < 200Arms$) there is no saturation in the magnetic material and the torque increases linearly with the current. For these small currents, the error is higher than 5% (between 3 Nm and 8 Nm). This could be explained by non-simulated effects like the friction losses which brake the machine. The error decreases with the current, especially over 200 Arms where the effects of the magnetic saturation are observable. The saturation is well modeled in the FEM simulations.

7.1.2.3 Torque speed characteristic

The torque speed characteristic has unfortunately only been measured under up to 3500 rpm. Over this rotational speed, the software control was unstable. The measurements are compared with the simulations in 7.8 and 7.9.

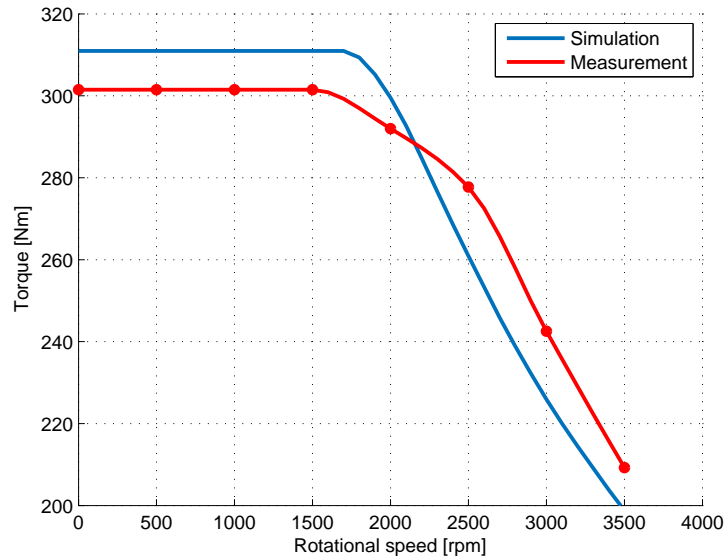


FIGURE 7.8: Torque speed characteristic (AFM_{P1})

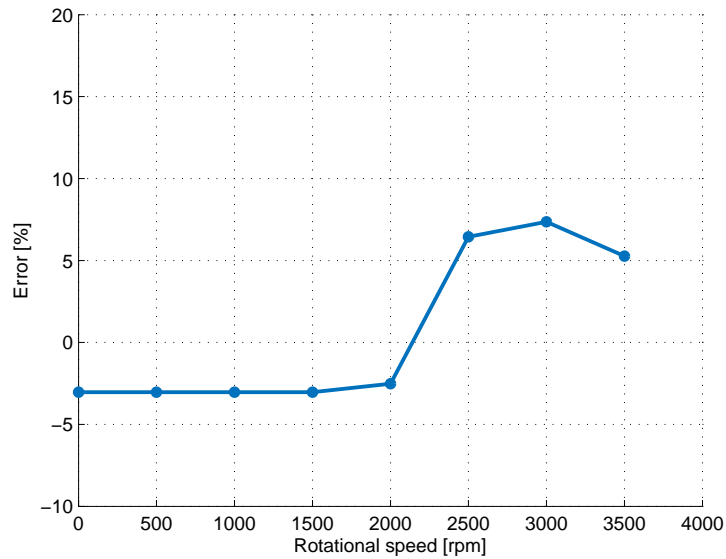


FIGURE 7.9: Torque speed characteristic error (AFM_{P1})

Before the knee point of the characteristic, the torque is underestimated (like in the previous measurements). The knee point of the prototype is between 1500 rpm and 2000 rpm

which corresponds to the simulations (approximately 1700 rpm). Over 2500 rpm the measured torque is higher than in the simulations. The error is smaller than 8% and tends to decrease with the rotational speed.

7.2 Second prototype: AFM_{P2}

7.2.1 Description

A second prototype has been built as part of the project. The magnetic design is the same than the machine designed in 5.1.1.2 and characterized in 5.1.1.3 and in appendix E. The main parameters of this machine have been given in table 5.1 and are reminded in table 7.2:

Description	Value	Specification
Pole pairs number	12	
Number of magnets	24	
NSPP	0.75	
Number of slots	54	
Number of winding turns	4	
Total length	73.2 mm	≤ 80 mm
Inside diameter (end windings)	180 mm	≥ 182 mm
Outside diameter (end windings)	285 mm	≤ 282 mm
Volume	2.8 L	min
Total magnets mass	817 g	min
Magnet grade	UH	min
Dysprosium mass	61.3 g	min
Peak torque	325 Nm	≥ 330 Nm
Torque density	116 Nm.L ⁻¹	max
Peak power	84 kW	≥ 80 kW
Power density	30 kW.L ⁻¹	max

TABLE 7.2: Parameters of the second prototype (AFM_{P2})

The winding of this prototype is built with hairpin winding. Due to the high complexity of the construction, the optimized construction presented in 4.1.3.1 has not been built. In the prototype, all conductors have the same geometry. This different construction increases the skin effect in the conductors and the phase resistance at high rotational speed is worsened. The phase resistance have been calculated at 100 °C with the analytic model presented in 4.1.3.2 and is compared in figure 7.10 with the resistance calculated in 5.1.2.2.

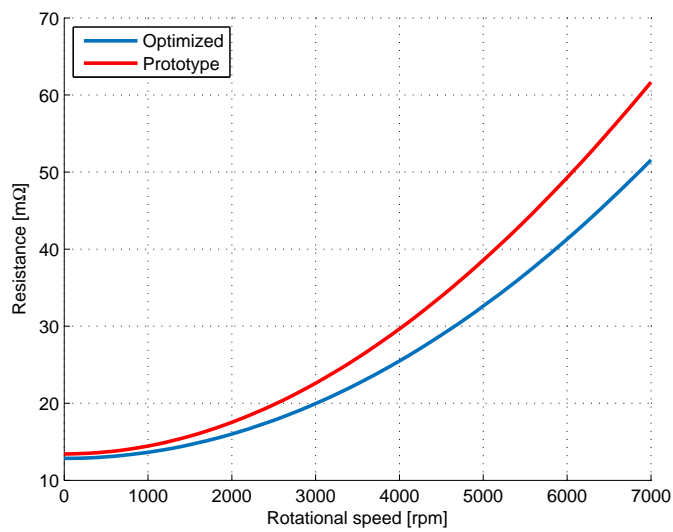


FIGURE 7.10: Phase resistance depending on the rotational speed (AFM_{P2}) [model]

7.2.2 Measurements

Figure 7.11 shows the machine on the test bench.

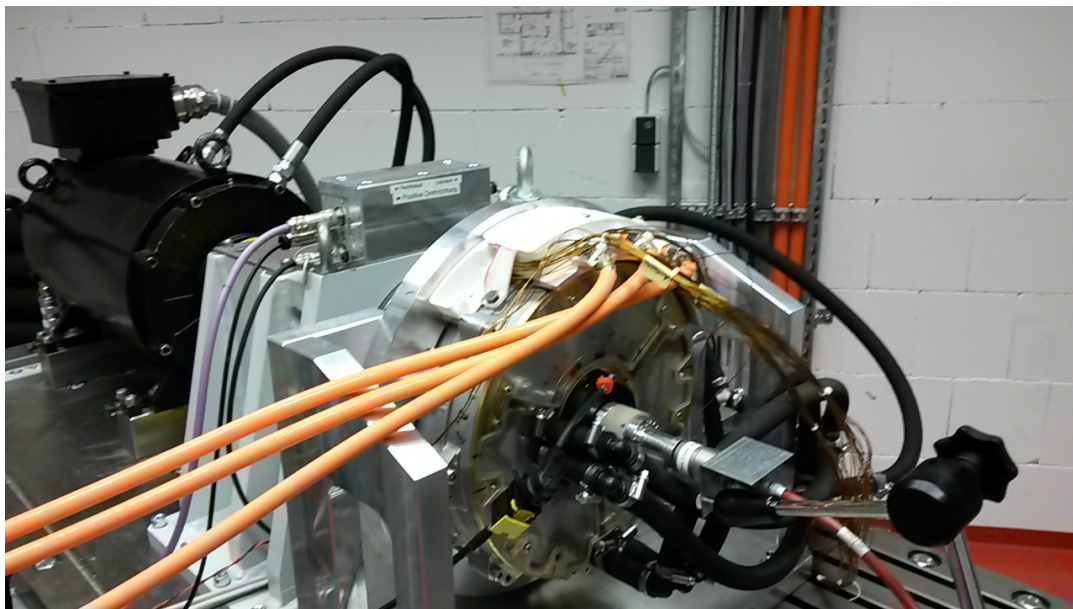


FIGURE 7.11: AFM_{P2} on the test bench

7.2.2.1 Induced voltage and no load losses

As for the first prototype, the induced voltage depending on the rotational speed has been measured. For the measurement of the second prototype, the cooling temperature

of the machine has been fixed to 90 °C. The simulations and the measurements are compared in figure 7.12. The error between the measured induced voltage and the simulation is displayed in figure 7.13.

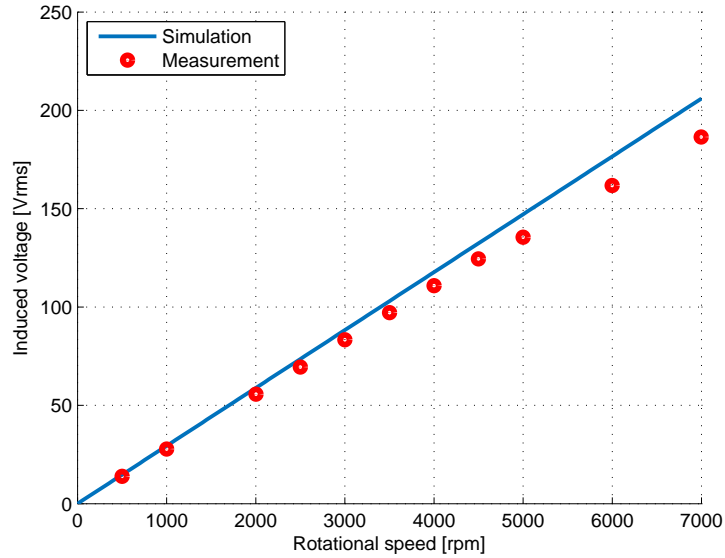


FIGURE 7.12: Induced voltage characteristic (AFM_{P2})

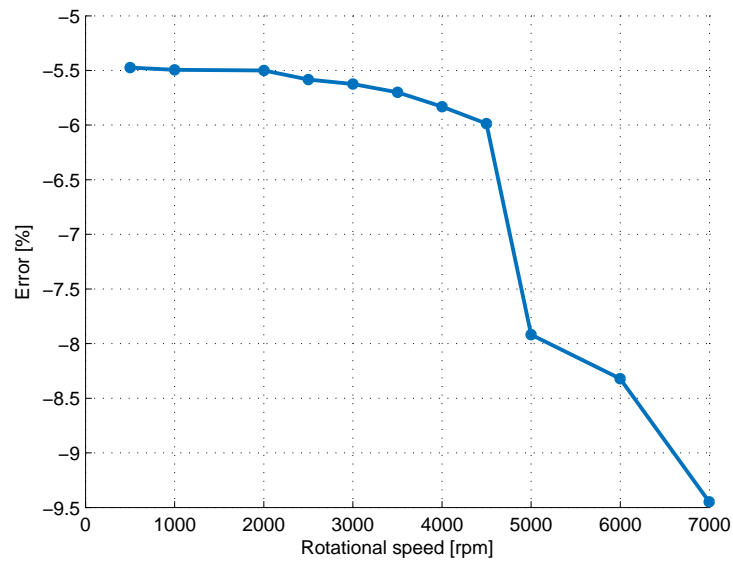


FIGURE 7.13: Induced voltage error (AFM_{P2})

As for the first machine the induced voltage has been overestimated. Under 5000 rpm the error is approximately 5%. This error can be explained by the mechanical tolerances (especially the air gap), a smaller magnet remanence or a non-perfect magnetization.

At higher rotational speed, the error increases due to the heating of the magnet during the measurement.

Figures 7.14 and 7.15 show the measured no load losses and the error depending on the rotational speed. The measured losses fit quite well the simulation. The error peaks at 6% at 4500 rpm and drops off at higher rotational speed.

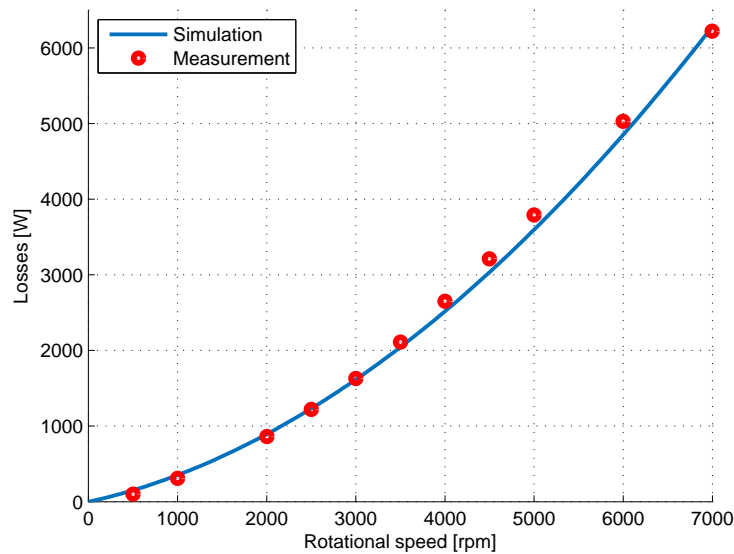


FIGURE 7.14: No load losses characteristic (AFM_{P2})

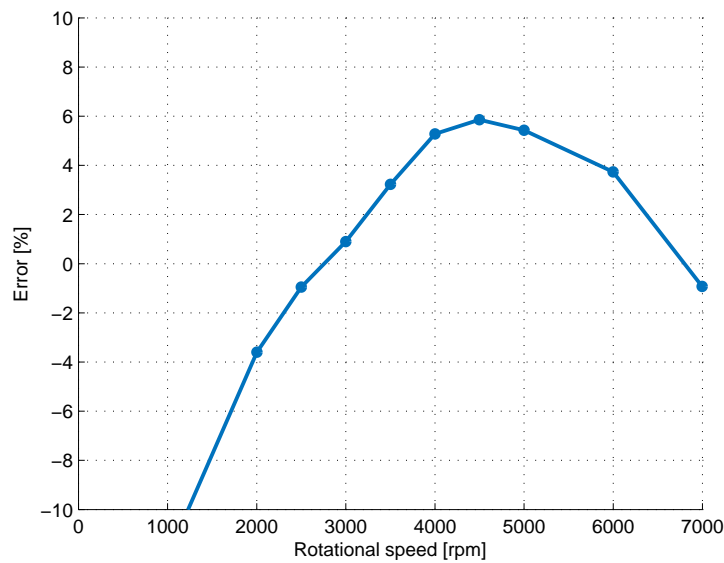


FIGURE 7.15: No load losses error (AFM_{P2})

7.2.2.2 Short circuit current and short circuit losses

The short circuit current has been measured under the same conditions than the induced voltage. Figures 7.16 and 7.17 show the results of these measurements. As for the first prototype, the short circuit current is good calculated. The error between the simulations and the measurements is smaller than 2%. Over 5000 rpm, the short circuit current lightly decreases due to the heating of the magnet during the measurement.

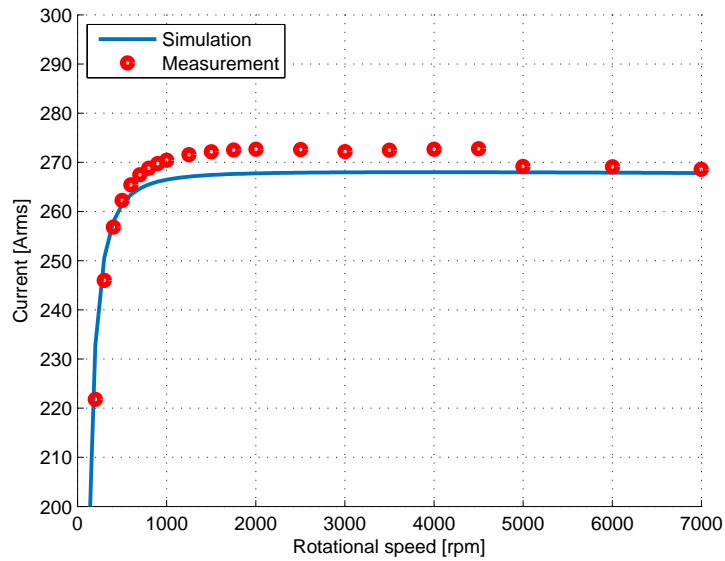


FIGURE 7.16: Short circuit current characteristic (AFM_{P2})

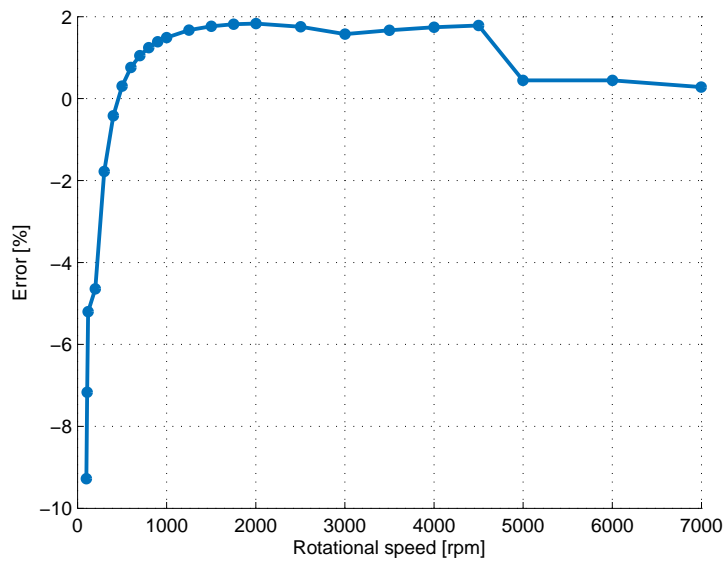


FIGURE 7.17: Short circuit current error (AFM_{P2})

Figures 7.18 and 7.19 show the measured short circuit losses and the error depending on the rotational speed. The short circuit losses increase significantly with the rotational speed due to the skin effect in the conductors. The error is important at small rotational speed (over 15% under 2500 rpm) but drops off at higher rotational speed.

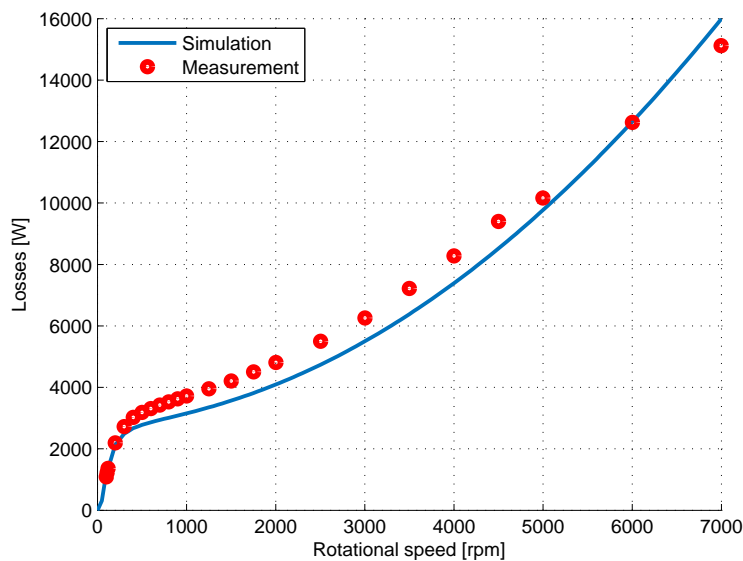


FIGURE 7.18: Short circuit losses characteristic (AFM_{P2})

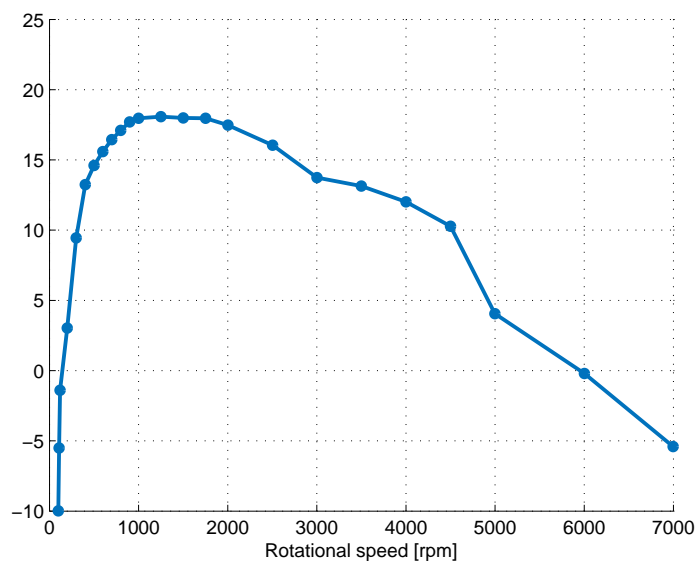


FIGURE 7.19: Short circuit losses error (AFM_{P2})

7.2.2.3 Torque current characteristic

In a third step the evolution of the torque with the current has been measured at a constant rotational speed of 500 rpm. The measurements and the error are displayed in figures 7.20 and 7.21.

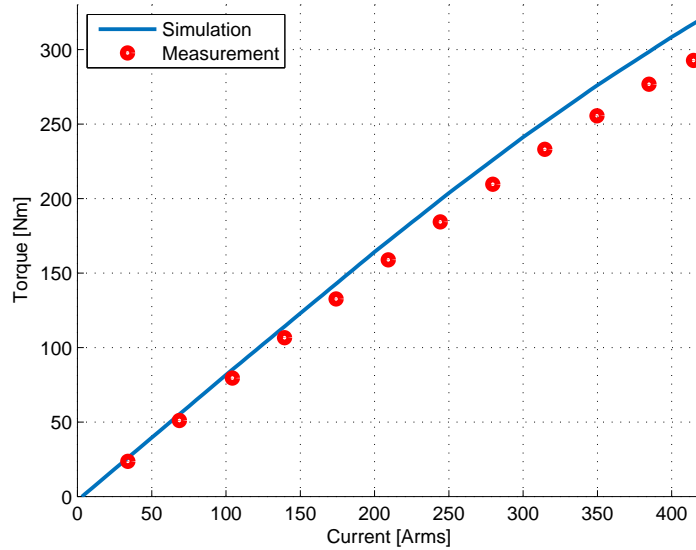


FIGURE 7.20: Torque current characteristic (AFM_{P2})

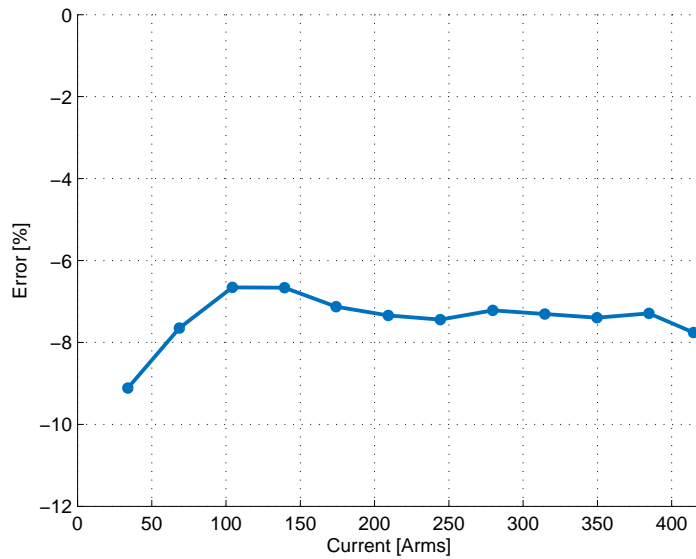


FIGURE 7.21: Torque current characteristic error (AFM_{P2})

The torque has been overestimated in the simulations by approximately 7%. This error is mainly due to the induced voltage (overestimation by more than 5%). The error is

constant with the current so, as for the first prototype, the magnetic saturation of the SMC is well simulated.

7.2.2.4 Losses performance map

In a fourth step, the machine has been measured in its complete operating map between 0 rpm and 7000 rpm. The difference between the measured losses and the simulated losses is plotted in the figure 7.22.

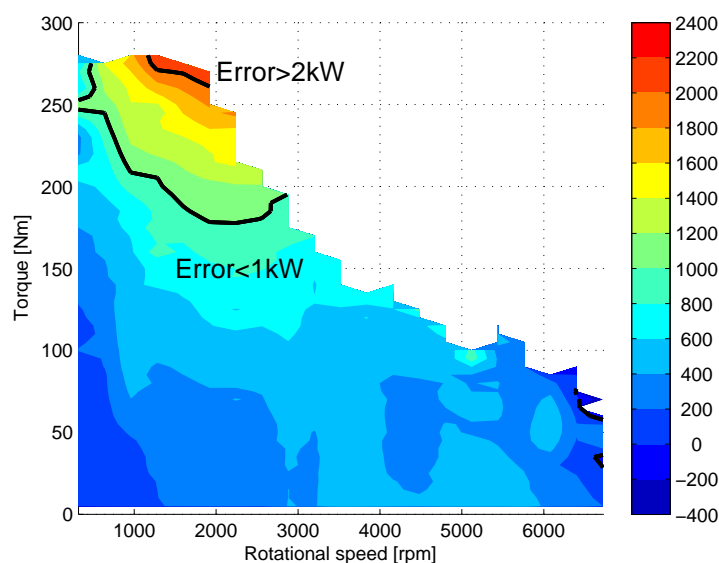


FIGURE 7.22: Difference between the measured and the simulated losses (AFM_{P2}) [W]

The difference is positive in the high majority of the operating points, so the losses have been underestimated in the FEM calculation:

- Under 4000 rpm: the error increases with the torque and peaks at 2 kW. The measured torque is smaller than the simulated torque, so the machine needs more current to achieve a specified value of the torque increasing the copper losses. This explains why the error increases with the torque.
- Over 4000 rpm: at high rotational speed the error remains under 600 W.

Conclusion

In this chapter, the two prototypes built during the PhD are presented. The first prototype has been built in 2014 to validate the electromagnetic calculations and acquire experience in the construction on an AFM. This prototype has a concentrated winding. The induced voltage, the short circuit current, the torque-current and the torque-speed characteristics between 0 rpm and 3500 rpm have been measured. The precision of the FEM calculations is satisfying, as the error between the measurement and the simulation is smaller than 5%. The second prototype is based on the design presented in 5.1.1.2. Due to mechanical tolerances, the measured induced voltage is smaller by 5% than the simulated value. It results an error in the measured torque which is smaller than in the FEM calculations. The short circuit current is good estimated. Contrary to the first prototype, the losses have been measured and compared to the simulations. At no load, the precision is very satisfying as the error is smaller than 6% over 2000 rpm. Finally, this prototype has been measured in its complete operating map showing an underestimation of the losses in the FEM calculations.

Conclusion

Disc rotor electric machines, especially axial-flux machines, could be a good alternative to radial-flux machines for hybrid traction. Axial-flux machines are well adapted to an available space requiring a short axial length and a large diameter. It fits exactly to the available space designed for integrated motor-generators.

In this PhD, the suitability of disc rotor electric machines to an integrated motor-generator application is studied. At first, the state of the art shows that the internal rotor axial-flux machine is the best topology to minimize the axial length and the magnets cost. In a second step, the electromagnetic design is defined. For example, shifted teeth strongly reduce the rotor losses and maximize the continuous power of the machine. In a third step the losses in an axial-flux machines are studied. Two analytic models to estimate the copper and the magnets losses are proposed. The precision of these models is satisfying. They enable a good evaluation of these losses for every operating point with a reduced number of FEM calculations. In a fourth step, two axial-flux machines are designed. The first machine is manually designed and the second one thanks to a multi-objective optimization which enables an improvement of the performances. The axial length is reduced by 11% and the torque density is improved by 29%. In a fifth step, the axial-flux machine designed with multi-objective optimization is compared with the integrated motor-generator built in the Volkswagen Touareg representing the state of the art. This comparison shows that the axial-flux machine is better suited to short axial length. Compared to the radial-flux machines, the magnet mass is reduced by approximately 20% and the axial length by approximately 16%. Finally, two prototypes have been built. Their measurement validate partially the simulations. Further investigation should be performed to explain the error in the calculations of induced voltage and the losses.

This PhD shows the potential of axial-flux machines for an integrated motor-generator application. The reduction of the axial length makes the integration of the machine in the drive shaft easier. Furthermore, the axial-flux machine needs less magnets than the radial-flux machine, so the material cost are reduced. To confirm the potential of the axial-flux machine for an automotive application, following topics need to be analyzed:

- Thermal management: the cooling capability of an electric machine determines its continuous power. Integrated motor-generators are water or oil cooled. The suitability of an AFM for these cooling concepts and the thermal performance needs to be studied.
- Noise: electric machines for hybrid applications need to be as silent as possible. The noise generated by the electromagnetic forces has to be evaluated and optimized.
- Industrialization: the construction process of an axial-flux machine are different than the ones of a radial-flux machines. The influence of these new processes on the reliability of the machine and its cost is decisive.

Appendices

Contents

A	Permanent-Magnet Synchronous Machines (PMSM)	184
A.1	Equivalent circuit	184
A.2	dq transformation	185
A.3	Torque expression	186
A.4	Characteristic and evolution of the current	187
A.5	Effects of a phase shift in the induced voltages	191
B	Torque generation in axial-flux machines	194
B.1	Analytic calculation	194
B.2	Determination of the optimum diameter ratio	197
C	Material database	200
C.1	Permanent-magnets	200
C.2	Soft magnetic composite	202
C.3	Electric properties of copper	203
D	Multi-objective optimization	204
D.1	Example of multi-objective optimization	204
D.2	Multi-objective optimization algorithms	205
E	Manually designed machine (AFM₆₀)	207
E.1	Losses and efficiency	207
E.2	Axial forces	209
E.3	Torque ripple	211
E.4	Short circuit current	212
E.5	Demagnetization safety	213
F	Multi-objective optimized machine (AFM_{MOO})	216
F.1	Winding technology	216
F.2	Losses and efficiency	218
F.3	Axial forces and torque ripple	222
F.4	Short circuit current	225
F.5	Demagnetization safety	226

A Permanent-Magnet Synchronous Machines (PMSM)

A.1 Equivalent circuit

The equivalent circuit of a Permanent-Magnet Synchronous Machine (PMSM) in motor operating condition is:

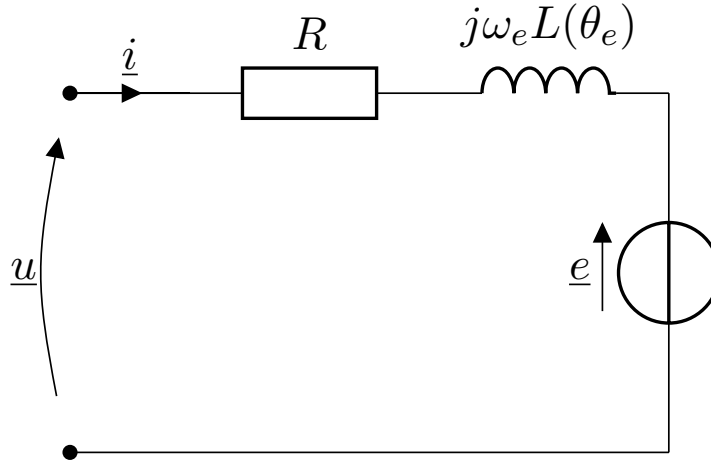


FIGURE A.1: Equivalent circuit of a Permanent-Magnet Synchronous Machine

In the case of a machine with saliency, the inductance L is not constant and depends on the position of the rotor (θ_e). Contrary to the radial-flux machine, the internal rotor of an AFM does not require a magnetic material in the rotor. The rotor disc has no magnetic functionality and could be built in a non magnetic material ($\mu_r = 1$) like reinforced plastic to avoid eddy current losses. The magnetic permeability of the magnet ($\mu_{r_{magnet}} \approx 1.05$) is approximately the same as this from the rotor, so the inductance is not depending on the position of the rotor.

The phase voltage is defined by:

$$u(t) = Ri(t) + L \frac{di(t)}{dt} + e(t) \quad (\text{A.1})$$

The voltage drop along the resistance is often much smaller than along the inductance or the induced voltage. For this reason it is neglected in this appendix. The induced voltage $e(t)$ is defined by following equation (Maxwell-Faraday):

$$e(t) = - \frac{d\Phi}{dt} \quad (\text{A.2})$$

where Φ is the magnetic flux generated by the magnets flowing in the coils. This flux is periodic for each pole pair (periodicity $\frac{2\pi}{n_p}$) and can be decomposed as a series of Fourier. In the case of a sinusoidal phase current only the fundamental of the induced voltage generates torque. The fundamental of the flux is defined by:

$$\begin{aligned}\Phi_1(\theta_e) &= \Psi_{PM}\cos(\theta_e) \\ &= \Psi_{PM}\cos(\omega_e t)\end{aligned}\tag{A.3}$$

where θ_e is the electric angle and ω_e is the electric pulsation in rad.s^{-1} . The RMS value of the fundamental is:

$$\begin{aligned}e_1(t) &= \Psi_{PM}\omega_e\sin(\omega_e t) \\ E_{1rms} &= \frac{\Psi_{PM}}{\sqrt{2}}\omega_e \\ &= k_E\omega_e\end{aligned}\tag{A.4}$$

where $k_E = \frac{\Psi_{PM}}{\sqrt{2}}$ is the armature constant of the machine in V.s.

A.2 dq transformation

The dq transformation has been introduced by Park in the 1920s [132]. Thank a reference frame rotation it transforms the three phases system into a two variables system. AC variables like currents, voltages or flux become constants. The dq reference frame is fixed to the rotor. The d axis corresponds to the direction of magnetic excitation generated by the rotor. The rotor position θ_e is defined as the electric angle between the first electric phase (U) and the d axis. The power-invariant dq transformation is defined by following equations:

$$\begin{pmatrix} i_\alpha \\ i_\beta \end{pmatrix} = \sqrt{\frac{2}{3}} \begin{pmatrix} 1 & -\frac{1}{2} & -\frac{1}{2} \\ 0 & \frac{\sqrt{3}}{2} & -\frac{\sqrt{3}}{2} \end{pmatrix} \begin{pmatrix} i_u \\ i_v \\ i_w \end{pmatrix}\tag{A.5}$$

$$\begin{pmatrix} I_d \\ I_q \end{pmatrix} = \begin{pmatrix} \cos(\theta_e) & \sin(\theta_e) \\ -\sin(\theta_e) & \cos(\theta_e) \end{pmatrix} \begin{pmatrix} i_\alpha \\ i_\beta \end{pmatrix}\tag{A.6}$$

In the case of balanced three-phase currents:

$$\begin{aligned}
 i_u(t) &= \sqrt{2}I \cos(\theta_e + \varphi) \\
 i_v(t) &= \sqrt{2}I \cos(\theta_e + \varphi - \frac{2\pi}{3}) \\
 i_w(t) &= \sqrt{2}I \cos(\theta_e + \varphi + \frac{2\pi}{3})
 \end{aligned} \tag{A.7}$$

$$\begin{aligned}
 i_\alpha(t) &= \sqrt{3}I \cos(\theta_e + \varphi) \\
 i_\beta(t) &= \sqrt{3}I \sin(\theta_e + \varphi) \\
 I_d &= \sqrt{3}I \cos(\varphi) \\
 I_q &= \sqrt{3}I \sin(\varphi)
 \end{aligned} \tag{A.8}$$

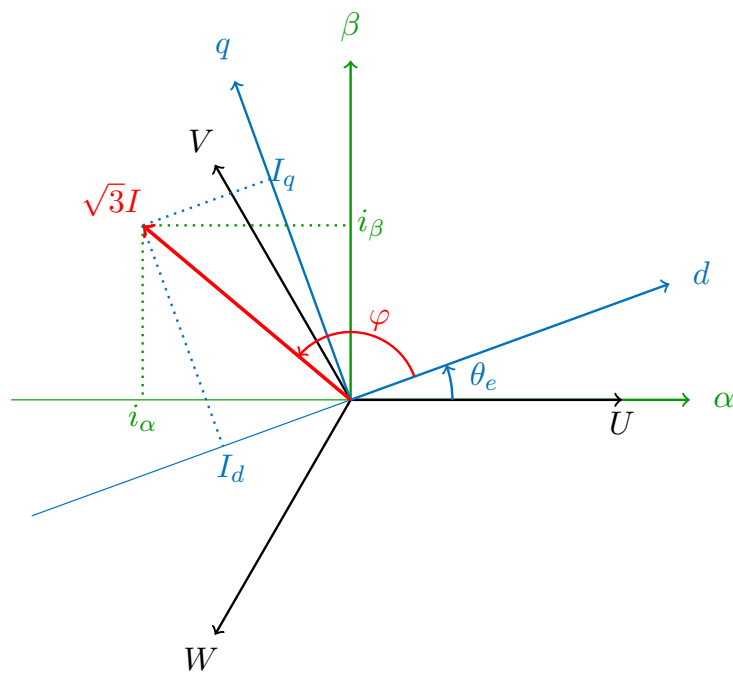


FIGURE A.2: dq transformation

A.3 Torque expression

The electromagnetic torque generated by a permanent-magnet synchronous machine is defined by the following expression [133]:

$$\begin{aligned}
 T_{em} &= n_p(\Psi_d I_q - \Psi_q I_d) \\
 &= n_p \left(\left(\sqrt{\frac{3}{2}} \Psi_{PM} + L_d I_d \right) I_q - L_q I_q I_d \right) \\
 &= n_p \sqrt{\frac{3}{2}} \Psi_{PM} I_q + n_p (L_d - L_q) I_q I_d
 \end{aligned} \tag{A.9}$$

In this equation, the torque is decomposed in two components:

- The synchronous torque obtained by the interaction between the magnetic field generated by the permanent-magnet and the quadratic field generated by the winding.
- The reluctance torque obtained by the saliency of the rotor which modifies the inductance of the rotor depending on the rotor position ($L_q \neq L_d$). In the case of a single rotor axial-flux machine, there is not saliency in the rotor ($L = L_d = L_q$), so there is no reluctance torque.

A.4 Characteristic and evolution of the current

The power and torque characteristic of a permanent-magnet synchronous machine depending on the rotational speed n are plotted in figure A.3. The voltages phasor diagrams depending on the rotational speed are displayed in figure A.4.

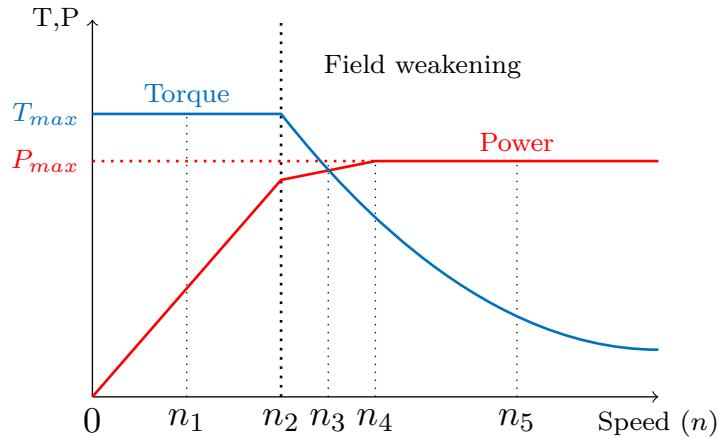


FIGURE A.3: Peak torque and power characteristic depending on the rotational speed

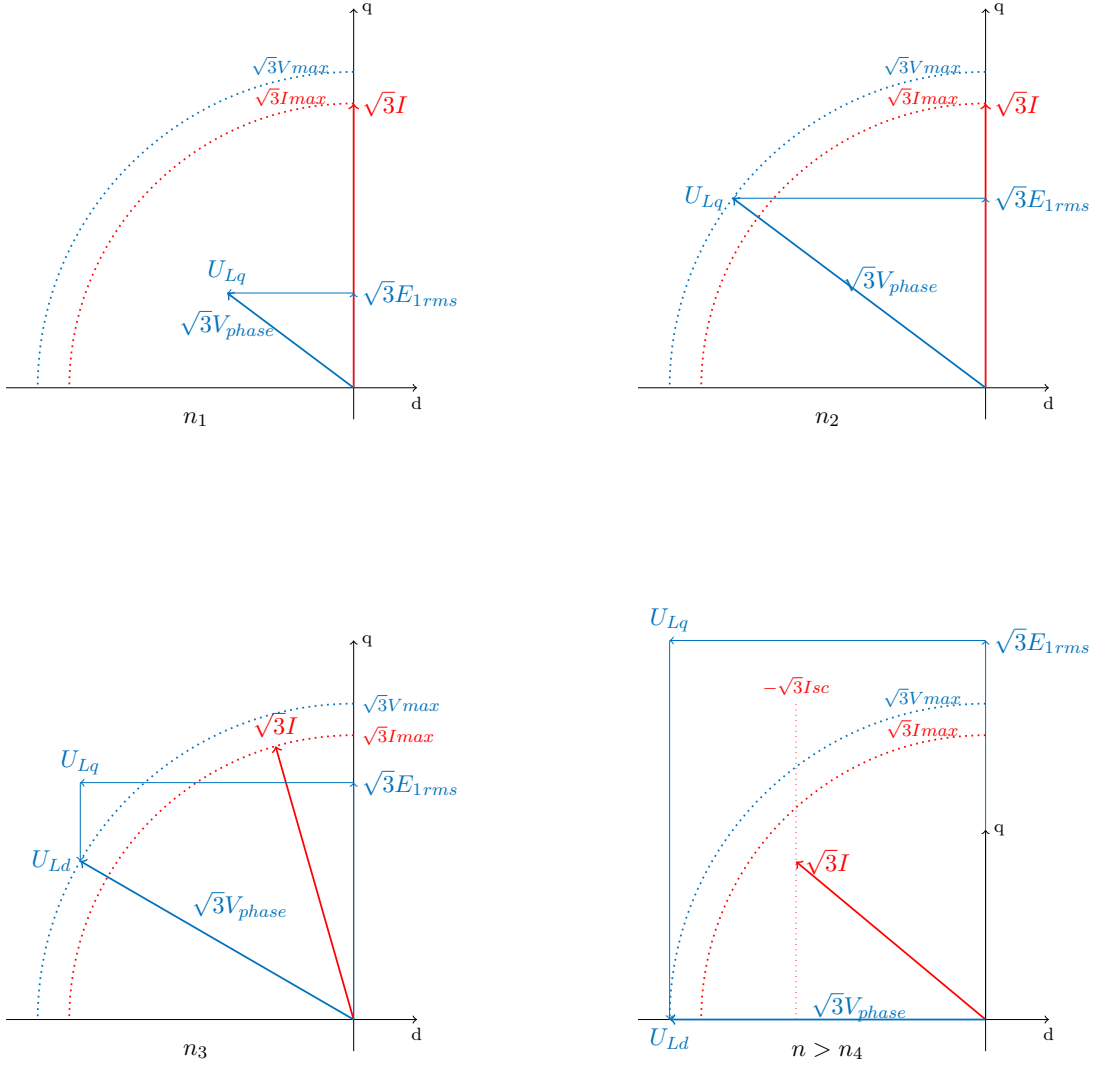


FIGURE A.4: Voltage diagrams depending on the rotational speed

There are three operating areas:

- $0 \leq n \leq n_2$: in the basic speed area the phase voltage is smaller than the maximum voltage so there is no necessity to do field weakening and the torque is maximized ($I_q = \sqrt{3}I_{max}$). The power increases linearly with the rotational speed (constant torque).
- $n_2 \leq n \leq n_4$: in the field weakening 1 area, the phase voltage reaches its maximum allowed value. The field weakening current $-I_d$ increase with the rotational speed, I_q and the torque need to be reduced to maintain the phase current under its maximum value. Even if the torque is reduced, the power lightly increase.
- $n \geq n_4$: in the field weakening 2 area, the induced voltage is completely compensated by the field weakening, so the field weakening current is equal to the short

circuit current ($I_d = -\sqrt{3}I_{sc}$) and has not to be increased anymore. I_q continues to drop off to maintain the phase voltage under its maximum value.

The evolution of the phase current along the characteristic is plotted in figure A.5.

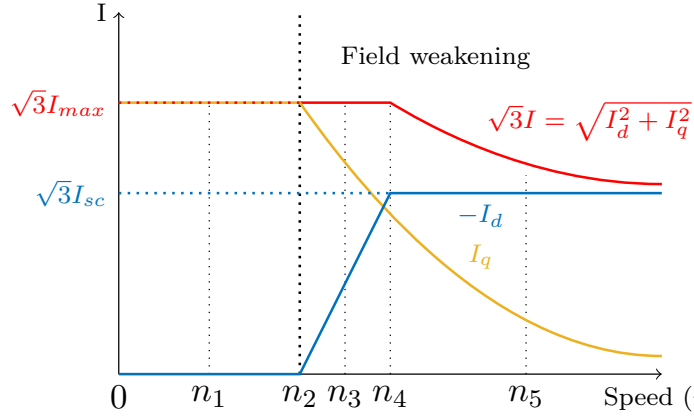


FIGURE A.5: Currents I_d , I_q and I depending on the rotational speed

In figure A.5 the currents I_q and I_d vary in following range:

$$\begin{aligned} 0 &\leq I_q \leq \sqrt{3}I_{max} \\ -\sqrt{3}I_{sc} &\leq I_d \leq 0 \end{aligned} \tag{A.10}$$

The evolution of the current along the peak performance characteristic and in every operating point in the dq plane are displayed in figure A.6. The blue line corresponds to the evolution of the current along the limit characteristic. Following operating points are marked:

- OP1: no load ($I = 0$, α undefined, $n = n_{max}=7000$ rpm)
- OP2: full load ($I = I_{max}$, $\alpha = 90^\circ$, $n=2000$ rpm)
- OP3: short circuit ($I = I_{sc}$, $\alpha = 180^\circ$, $n = n_{max}=7000$ rpm)

Theses remarkable operating points correspond to extreme load conditions. In other operating points, the current is mainly driven inside the triangle built by theses operating points.

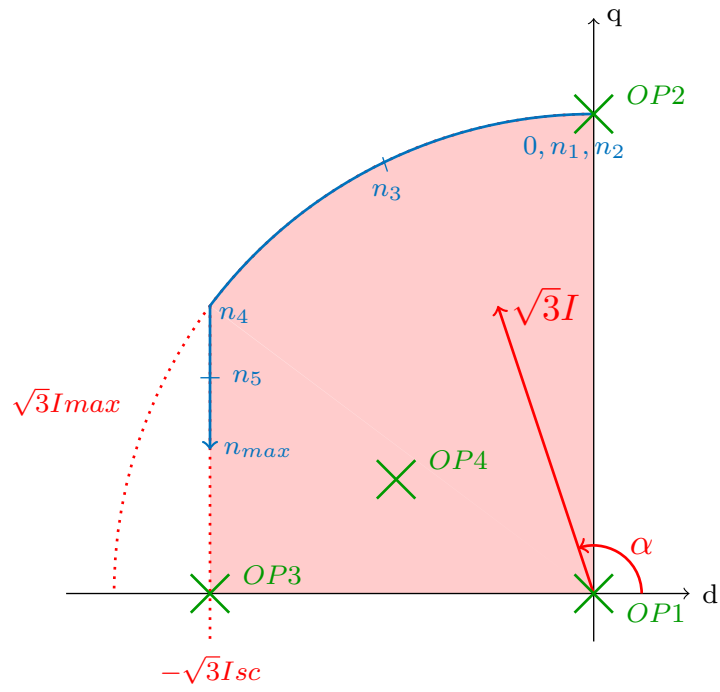


FIGURE A.6: Evolution of the current in the dq plane

A.5 Effects of a phase shift in the induced voltages

The equivalent circuit a 3 phases PMSM with parallel-star connection is displayed in figure A.7.

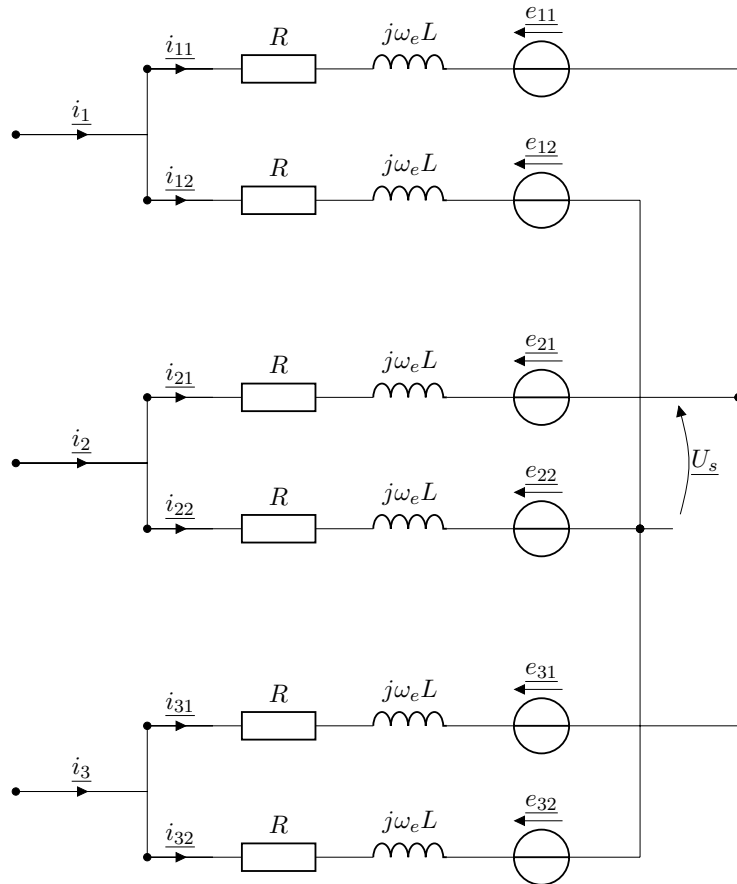


FIGURE A.7: Equivalent circuit of a 3-phase PMSM with parallel-star connection

If the induced voltages of both stators are phase shifted by an angle β , the phase diagram becomes:

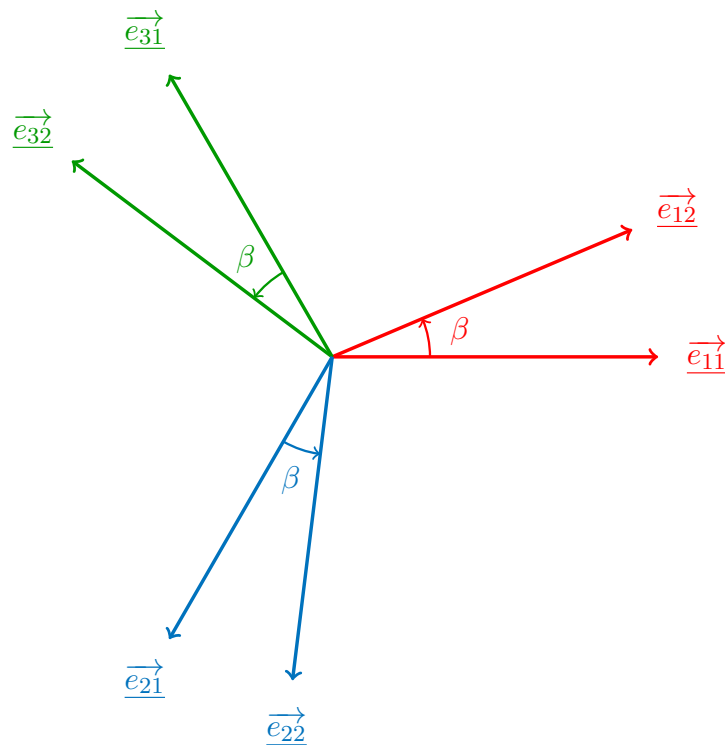


FIGURE A.8: Complex phase diagram with phase shift

The current flowing in the electric phases of each stator can be decomposed as the sum of the phase current and a circular current i_c :

$$\begin{aligned}
 i_{11} &= \frac{i_1}{2} + i_{c1} \\
 i_{12} &= \frac{i_1}{2} - i_{c1} \\
 i_{21} &= \frac{i_2}{2} + i_{c2} \\
 i_{22} &= \frac{i_2}{2} - i_{c2} \\
 i_{31} &= \frac{i_3}{2} + i_{c3} \\
 i_{32} &= \frac{i_3}{2} - i_{c3}
 \end{aligned}
 \tag{A.11}$$

The voltage between both star points (\underline{U}_s) can be expressed as:

$$\begin{aligned}
 \underline{U}_s &= \underline{e}_{12} + (R + j\omega_e L)\underline{i}_{12} - (R + j\omega_e L)\underline{i}_{11} - \underline{e}_{11} \\
 &= \underline{e}_{12} - \underline{e}_{11} - 2(R + j\omega_e L)\underline{i}_{c1} \\
 &= \underline{e}_{22} - \underline{e}_{21} - 2(R + j\omega_e L)\underline{i}_{c2} \\
 &= \underline{e}_{32} - \underline{e}_{31} - 2(R + j\omega_e L)\underline{i}_{c3}
 \end{aligned} \tag{A.12}$$

As $i_{c1} + i_{c2} + i_{c3} = 0$ (star connection), $U_s = 0$. The circular current can be expressed as:

$$\begin{aligned}
 \underline{i}_{c1} &= \frac{\underline{e}_{12} - \underline{e}_{11}}{2(R + j\omega_e L)} \\
 \underline{i}_{c2} &= \frac{\underline{e}_{22} - \underline{e}_{21}}{2(R + j\omega_e L)} \\
 \underline{i}_{c3} &= \frac{\underline{e}_{32} - \underline{e}_{31}}{2(R + j\omega_e L)}
 \end{aligned} \tag{A.13}$$

The electromagnetic torque \underline{T}_1 generated by the first phase is:

$$\begin{aligned}
 \underline{T}_1 &= \frac{\underline{e}_{11}\underline{i}_{11} + \underline{e}_{12}\underline{i}_{12}}{\omega_m} \\
 &= \frac{\underline{i}_1}{2} \frac{\underline{e}_{11} + \underline{e}_{12}}{\omega_m} + \frac{\underline{i}_{c1}}{2} \frac{\underline{e}_{11} - \underline{e}_{12}}{\omega_m} \\
 &= \frac{\underline{i}_1}{2} \frac{\underline{e}_{11} + \underline{e}_{12}}{\omega_m} - \frac{(\underline{e}_{12} - \underline{e}_{11})^2}{4(R + j\omega_e L)\omega_m}
 \end{aligned} \tag{A.14}$$

where ω_m is the mechanical pulsation. I is the RMS value of the phase current and E is the RMS value of the induced voltage. The electromagnetic torque T_{em} generated by the machine is:

$$T_{em} = \frac{3EI \cos\left(\frac{\beta}{2}\right)}{2\omega_m} - \frac{3E^2 \sin^2\left(\frac{\beta}{2}\right)}{4\omega_m \sqrt{R^2 + (L\omega_e)^2}} \tag{A.15}$$

The electromagnetic torque generated by the machine is the difference between the electromagnetic torque generated by the machine if the connection would have be a serial connection and the breaking torque due to the induced circular current.

B Torque generation in axial-flux machines

The objective of this study is to determine an expression of the torque generated by an axial-flux machine depending on its dimensions. In the literature, analog theoretical calculations have been performed for example in [5, 14], but show different results. For example, in [14] the torque increases with the square of the diameter, but in [12] it increases with its cube.

B.1 Analytic calculation

In this calculation, following assumptions are made:

- The machine is a single rotor double stator machine. The rotor is assumed to be perfectly centered, so the same torque is generated in both air gaps.
- The machine has n_p pole pairs and is supposed to be perfectly identical for each pole pair, so the magnetic flux generated by the magnets $B(r, \theta, t)$ is periodic with a period angle $\frac{2\pi}{n_p}$.
- The magnetic flux generated by the rotor magnets is assumed to be independent of the radius.
- The magnetic materials are assumed to be linear and perfect, so there is no saturation in the stator, the magnets can not be demagnetized and the magnetic permeability of the material is assumed to be infinite.

The general Fourier decomposition of the axial component of the magnet field generated by the magnets depending on the radius r , the angular position θ_e and the time t is:

$$B_z(r, \theta_e, t) = \sum_{k=1}^{\infty} B_{z_k}(r, t) \cos(k(\omega_e t + \theta_e) + \varphi_{B_k}) \quad (\text{B.1})$$

The magnetic field is assumed to be independent of the radius r and the time t , so $B_{z_k}(r, t) = B_{z_k}$. The magnetic flux flowing in one coil of the first electric phase can be expressed with following expression:

$$\begin{aligned}
 \Phi_1(t) &= N \iint_S B_z(\theta_e, t) dS \\
 &= N \int_{r_i}^{r_o} \int_{\alpha_1}^{\alpha_2} \sum_{k=1}^{\infty} B_{z_k} \cos(k(\omega_e t + \theta_e) + \varphi_{B_k}) \frac{r}{n_p} dr d\theta_e \\
 &= \frac{N(r_o^2 - r_i^2)}{2n_p} \sum_{k=1}^{\infty} \int_{\alpha_1}^{\alpha_2} B_{z_k} \cos(k(\omega_e t + \theta_e) + \varphi_{B_k}) d\theta_e \\
 &= \frac{N(r_o^2 - r_i^2)}{2n_p} \sum_{k=1}^{\infty} B_{z_k} (\sin(k(\omega_e t + \alpha_2) + \varphi_{B_k}) - \sin(k(\omega_e t + \alpha_1) + \varphi_{B_k}))
 \end{aligned} \tag{B.2}$$

where N is the number of turns of the coil, $\omega_e = n_p \omega_m$ is the electric pulsation, n_p is the number of pole pairs, r_i and r_o are respectively the inside and outside radius of the magnetic circuit and α_1 and α_2 are the position of the begin and the end of the coil. Considering a serial connection of both stators, the induced voltage of the first phase is:

$$\begin{aligned}
 e_1(t) &= -2n_p \frac{d\Phi_1(t)}{dt} \\
 &= -N(r_o^2 - r_i^2) \omega_e \sum_{k=1}^{\infty} B_{z_k} (\cos(k(\omega_e t + \alpha_2) + \varphi_{B_k}) - \cos(k(\omega_e t + \alpha_1) + \varphi_{B_k})) \\
 &= 2N(r_o^2 - r_i^2) \omega_e \sum_{k=1}^{\infty} B_{z_k} \sin\left(k \frac{\alpha_2 - \alpha_1}{2}\right) \sin\left(k\omega_e t + \varphi_{B_k} + k \frac{\alpha_1 + \alpha_2}{2}\right)
 \end{aligned} \tag{B.3}$$

The induced voltages of the two other electric phases can be expressed as:

$$\begin{aligned}
 e_2(t) &= 2N(r_o^2 - r_i^2) \omega_e \sum_{k=1}^{\infty} B_{z_k} \sin\left(k \frac{\alpha_2 - \alpha_1}{2}\right) \sin\left(k\omega_e t + \varphi_{B_k} + k \frac{\alpha_1 + \alpha_2}{2} - k \frac{2\pi}{3}\right) \\
 e_3(t) &= 2N(r_o^2 - r_i^2) \omega_e \sum_{k=1}^{\infty} B_{z_k} \sin\left(k \frac{\alpha_2 - \alpha_1}{2}\right) \sin\left(k\omega_e t + \varphi_{B_k} + k \frac{\alpha_1 + \alpha_2}{2} + k \frac{2\pi}{3}\right)
 \end{aligned} \tag{B.4}$$

The phase currents are assumed to be perfectly sinusoidal:

$$\begin{aligned}
 i_1(t) &= I\sqrt{2} \cos(\omega_e t + \varphi_I) \\
 i_2(t) &= I\sqrt{2} \cos(\omega_e t + \varphi_I - \frac{2\pi}{3}) \\
 i_3(t) &= I\sqrt{2} \cos(\omega_e t + \varphi_I + \frac{2\pi}{3})
 \end{aligned} \tag{B.5}$$

The torque $T_1(t)$ generated by the first electric phase is:

$$\begin{aligned}
 T_1(t) &= \frac{e_1(t) \cdot i_1(t)}{\omega_m} \\
 &= 2\sqrt{2}NIn_p(r_o^2 - r_i^2) \sum_{k=1}^{\infty} B_{z_k} \sin\left(k \frac{\alpha_2 - \alpha_1}{2}\right) \sin\left(k\omega_e t + \varphi_{B_k} + k \frac{\alpha_1 + \alpha_2}{2}\right) \cos(\omega_e t + \varphi_I) \\
 &= \sqrt{2}NIn_p(r_o^2 - r_i^2) \sum_{k=1}^{\infty} B_{z_k} \sin\left(k \frac{\alpha_2 - \alpha_1}{2}\right) \\
 &\quad \left(\sin\left((k+1)\omega_e t + \varphi_{B_k} + k \frac{\alpha_1 + \alpha_2}{2} + \varphi_I\right) + \sin\left((k-1)\omega_e t + \varphi_{B_k} + k \frac{\alpha_1 + \alpha_2}{2} - \varphi_I\right) \right)
 \end{aligned} \tag{B.6}$$

The torques $T_2(t)$, $T_3(t)$ and the global torque $T(t)$ can be expressed as:

$$\begin{aligned}
 T_2(t) &= \frac{e_2(t) \cdot i_2(t)}{\omega_m} \\
 T_3(t) &= \frac{e_3(t) \cdot i_3(t)}{\omega_m} \\
 T(t) &= T_1(t) + T_2(t) + T_3(t)
 \end{aligned} \tag{B.7}$$

The average value T_m of the torque generated by the machine is:

$$\begin{aligned}
 T_m &= 3 \langle T_1(t) \rangle \\
 &= 3\sqrt{2}NIn_p B_{z_1} (r_o^2 - r_i^2) \sin\left(\varphi_{B_1} + k \frac{\alpha_1 + \alpha_2}{2} - \varphi_I\right) \sin\left(k \frac{\alpha_2 - \alpha_1}{2}\right)
 \end{aligned} \tag{B.8}$$

The torque is maximized when $\varphi_{B_1} + k \frac{\alpha_1 + \alpha_2}{2} - \varphi_I = \frac{\pi}{2}$. That means that the magnetic flux generated by the magnets and the phase current are shifted by $\frac{\pi}{2}$, so a positive current on the q axis ($I_q = \sqrt{3}I$, $I_d = 0$). $k_{\omega_1} = k_{d_1} = \sin\left(k \frac{\alpha_2 - \alpha_1}{2}\right)$ is the distribution factor of the winding. It is equal to the winding factor, as the magnetic flux flowing is assumed to be the same in each coils of one electric phase. The expression of the torque under an optimized phase current becomes:

$$T_m = 3\sqrt{2}B_{z_1}NIn_pk_{\omega_1}(r_o^2 - r_i^2) \tag{B.9}$$

This expression is similar to the results obtained in [5, 14]. Under theses assumptions, the torque increases with the square of the diameter.

This expression has been compared to the results of FEM calculations. To perform this comparison a specific axial-flux machine has been designs:

- The magnets are trapezoidal to ensure the independence of the magnetic flux regarding the radius
- The stator slots are minimized
- The coil ends are deliberately increased to ensure that the magnetic flux generated by the coil ends does not flow in the stator
- The magnetic material is perfect

The torques calculated with B.8 and with FEM are compared in figure B.1. The average values are plotted in dotted lines. This result is satisfying, as the average value of the torque is estimated with an error smaller than 2%.

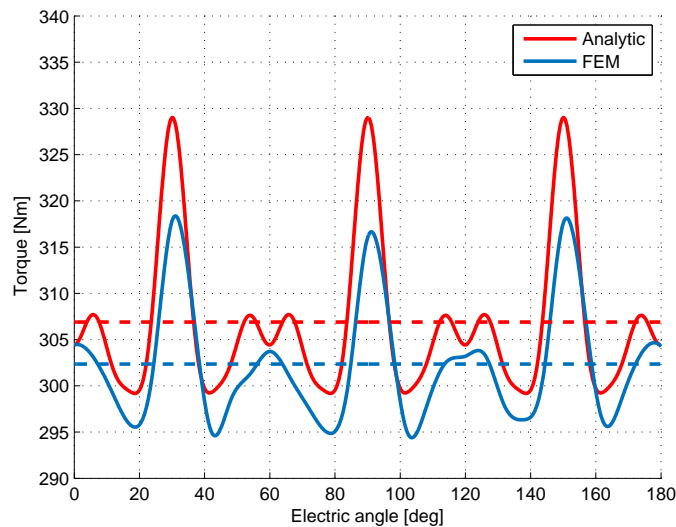


FIGURE B.1: Comparison between the analytic and FEM calculations

B.2 Determination of the optimum diameter ratio

By defining the diameter ratio of the machine $\lambda = \frac{r_i}{r_o}$, the expression of the torque obtained in equation B.9 becomes:

$$T_m = 3\sqrt{2}B_{z_1}NI n_p k_{\omega_1} r_o^2 (1 - \lambda^2) \quad (\text{B.10})$$

Under these assumptions the optimum diameter ratio would be $\lambda = 1$. That means that the machine delivers its maximum torque with $r_i = 0$. Examples in the literature show that the optimum diameter ratio varies between 0.46 [18] and 0.63 [66]. Furthermore machines with $r_i = 0$ can not be built due to coil end windings.

To correct this error and improve the model, it must be considered that the electric loading $n_p NI$ at the inside radius increases linearly with it. This assumption is true by considering that either the number of pole pairs n_p or the number of turns N increases linearly with the inner radius (like in [12]). It is proposed to introduce the coefficient k_{ri} defined as:

$$k_{ri} = \frac{Nn_p}{r_i} \quad (\text{B.11})$$

The expression of the torque calculated in equation B.10 becomes:

$$\begin{aligned} T_m &= 3\sqrt{2}B_{z_1}Ik_{\omega_1}k_{ri}r_i r_o^2(1 - \lambda^2) \\ &= 3\sqrt{2}B_{z_1}Ik_{\omega_1}k_{ri}r_o^3(\lambda - \lambda^3) \end{aligned} \quad (\text{B.12})$$

With this last assumption, the torque increases with the cube of the outside diameter which corresponds to the evolution calculated by [5, 12]. Furthermore if $r_i = 0$ or $r_i = r_o$ the machine does not generate torque, which is a realistic model. The torque is maximized for following diameter ratio:

$$\lambda_{opt} = \frac{1}{\sqrt{3}} \approx 0.58 \quad (\text{B.13})$$

The evolution of the torque with the diameter ratio has been checked with FEM calculations. This comparison is shown in figure B.2. This comparison confirms the precision of the model and the optimum torque ratio.

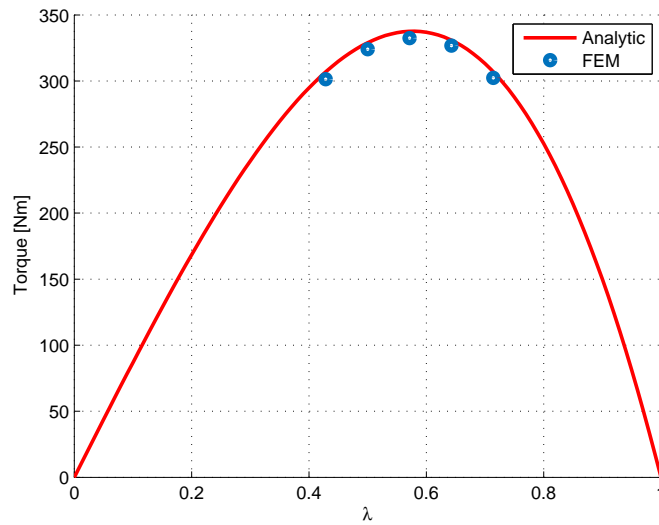


FIGURE B.2: Torque depending on the diameter ratio

The optimum diameter ratio is consistent with the values obtained in [18, 66] where λ_{opt} varies between 0.46 and 0.63. The error with these values can be explained by the saturation of the magnetic material or some approximations induced by the assumption, especially the independence of the magnetic field generated by the magnet with the radius which strongly depends on the shape of the magnet and the stator design. Furthermore the diameter ratio has a huge influence on the efficiency of the machine. Small diameter ratios offer better efficiency [118] thanks to smaller coil end windings. To optimize the efficiency, the maximum available space should be used.

C Material database

C.1 Permanent-magnets

Permanent-magnet are divided in 4 main categories [5]:

- Ferrite magnets
- Aluminum Nickel Cobalt magnets
- Samarium Cobalt magnets
- Neodymium iron Boron (NdFeB) magnets

Rare earth NdFeB magnets are commercialized since the 1990s and have better magnetic properties than other magnets. The main disadvantage of these magnets, is their sensitivity to the temperature. At high temperatures (over 100 °C) these magnets are easy to demagnetize. To ensure operating temperatures required for automotive applications (above 150 °C) special magnets with high dysprosium content are necessary. Dysprosium lightly reduces the remanence of the magnet and dramatically increases their cost. The magnetic characteristic of a NdFeB magnet is plotted in figure C.1.

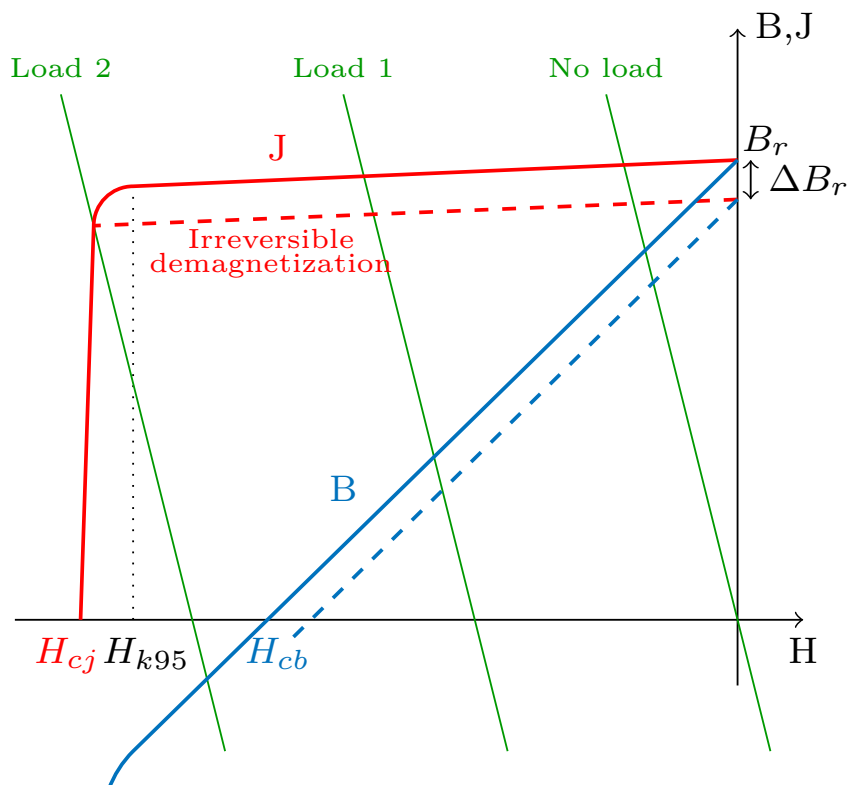


FIGURE C.1: Magnetic characteristic a NdFeB permanent-magnet

The remanence (B_r) of the magnet corresponds to the maximum magnetic field density generated by the magnet. In the real case, even without opposed magnetic field, the magnet generates a smaller flux density due to the reluctance of the field lines. When the magnet is submitted to an opposed flux (Load 1), it's operating point is shifted to the left and its magnetic polarization (J) is lightly reduced. The magnetic flux density is calculated with following formula:

$$B = J + \mu_0\mu_r H \quad (\text{C.1})$$

where $\mu_0 = 4\pi \cdot 10^{-7} \text{ H.m}^{-1}$ is the vacuum permeability and μ_r is the relative permeability of the magnet (typically $\mu_r=1.05$ for NdFeB magnets). Under this load condition, the opposed field is not strong enough to demagnetize the magnet.

Load 2 represents a stronger opposed magnetic field. In this case, the magnetic polarization is pushed over the knee point of the characteristic (H_{k95}) and the magnet is partially demagnetized. Even if the opposed magnetic field is removed, the magnet has irreversibly lost a part of its remanence (ΔB_r).

NdFeB magnets are arranged in grades depending on their magnetic properties. SH, UH and EH are the main grades for automotive applications. Their magnetic properties depending on the temperature are displayed in table C.1. The SH grade has the highest remanence thanks to a lower dysprosium content, it is already the less expensive magnets. But this magnet has a reduced coercivity and is easy to demagnetize at high temperature. On the contrary the EH magnet has a reduced remanence, a higher coercivity and is more expensive.

Temperature [°C]	Br [T]			Hcj [kA.m ⁻¹]			Hk95 [kA.m ⁻¹]		
	SH	UH	EH	SH	UH	EH	SH	UH	EH
-20	1.36	1.29	1.23	-1900	-2413	-2993	-1805	-2293	-2843
20	1.31	1.25	1.20	-1594	-1995	-2377	-1515	-1895	-2258
90	1.22	1.18	1.14	-954	-1280	-1509	-906	-1216	-1433
150	1.11	1.08	1.05	-475	-747	-946	-451	-709	-899

TABLE C.1: Magnetic properties of different magnet grades

C.2 Soft magnetic composite

In this PhD, the Somaloy 5P700HR magnetic material is used. This SMC is built with large magnetic particles enabling good magnetic properties and a high insulation composite to minimize the losses [134]. The BH curve and the losses curves are respectively plotted in figure C.2 and C.3 ¹.

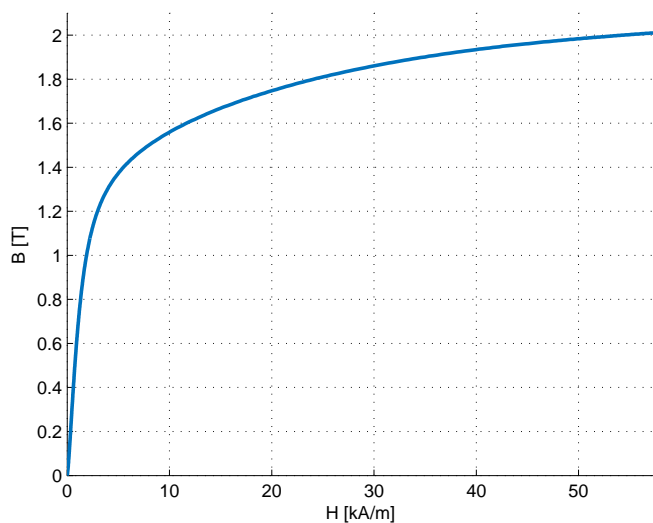


FIGURE C.2: BH curve of soft magnetic material [SMC 5P700HR]

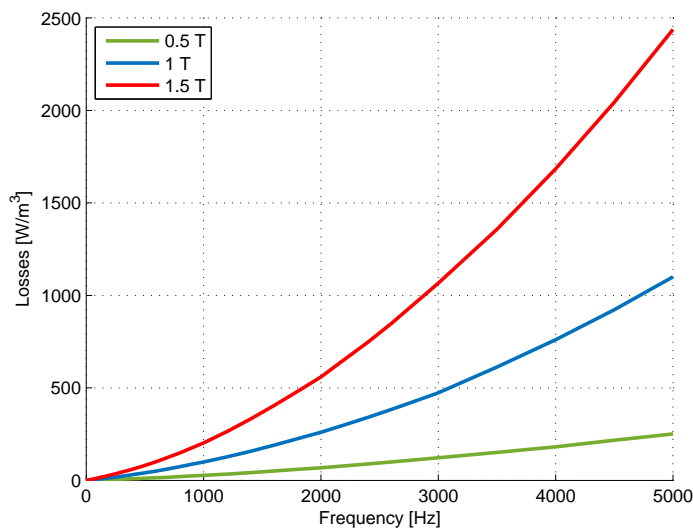


FIGURE C.3: Losses curves of soft magnetic material [SMC 5P700HR]

¹I would like to thank my colleague who measured the BH curves and the losses of the SMC material.

C.3 Electric properties of copper

The electric properties of copper depends on the temperature. In the case of electric machines, this dependency is particularly relevant due to the influence of copper losses on the efficiency of the machine. In this PhD, the electric conductivity and resistivity defined in table C.2 are used [5]:

Temperature °C	Resistivity $\Omega\cdot\text{m}$	Conductivity $\Omega^{-1}\cdot\text{m}^{-1}$
-50	$1.28 \cdot 10^{-8}$	$7.84 \cdot 10^7$
-40	$1.34 \cdot 10^{-8}$	$7.44 \cdot 10^7$
-30	$1.41 \cdot 10^{-8}$	$7.08 \cdot 10^7$
-20	$1.48 \cdot 10^{-8}$	$6.75 \cdot 10^7$
-10	$1.55 \cdot 10^{-8}$	$6.46 \cdot 10^7$
0	$1.62 \cdot 10^{-8}$	$6.18 \cdot 10^7$
10	$1.69 \cdot 10^{-8}$	$5.93 \cdot 10^7$
20	$1.75 \cdot 10^{-8}$	$5.70 \cdot 10^7$
30	$1.82 \cdot 10^{-8}$	$5.49 \cdot 10^7$
40	$1.89 \cdot 10^{-8}$	$5.29 \cdot 10^7$
50	$1.96 \cdot 10^{-8}$	$5.10 \cdot 10^7$
60	$2.03 \cdot 10^{-8}$	$4.93 \cdot 10^7$
70	$2.10 \cdot 10^{-8}$	$4.77 \cdot 10^7$
80	$2.16 \cdot 10^{-8}$	$4.62 \cdot 10^7$
90	$2.23 \cdot 10^{-8}$	$4.48 \cdot 10^7$
100	$2.30 \cdot 10^{-8}$	$4.34 \cdot 10^7$
110	$2.37 \cdot 10^{-8}$	$4.22 \cdot 10^7$
120	$2.44 \cdot 10^{-8}$	$4.10 \cdot 10^7$
130	$2.51 \cdot 10^{-8}$	$3.99 \cdot 10^7$
140	$2.58 \cdot 10^{-8}$	$3.88 \cdot 10^7$
150	$2.64 \cdot 10^{-8}$	$3.78 \cdot 10^7$
160	$2.71 \cdot 10^{-8}$	$3.69 \cdot 10^7$
170	$2.78 \cdot 10^{-8}$	$3.60 \cdot 10^7$
180	$2.85 \cdot 10^{-8}$	$3.51 \cdot 10^7$
190	$2.92 \cdot 10^{-8}$	$3.43 \cdot 10^7$
200	$2.99 \cdot 10^{-8}$	$3.35 \cdot 10^7$

TABLE C.2: Electric properties of copper depending on the temperature

D Multi-objective optimization

D.1 Example of multi-objective optimization

In this part, a simple Multi-Objective Optimization (MOO) problem is treated. This problem deals with the minimization of the surfaces of two areas of a parallelepiped guaranteeing a minimum volume:

- Minimization of surface s_1
- Minimization of surface s_2
- Constraint on volume: $V > 500 \text{ cm}^3$
- The height of the parallelepiped is fixed: $h = 20 \text{ cm}$

a and b are input parameters and vary between $0 \text{ cm} \leq a \leq 10 \text{ cm}$ and $0 \text{ cm} \leq b \leq 20 \text{ cm}$.

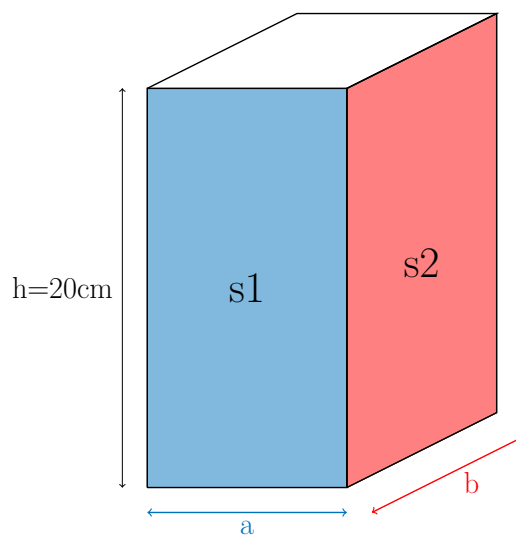


FIGURE D.1: Definition of the optimization problem

To perform the optimization, 3000 designs have been randomly selected and evaluated. The designs respecting the volume constraints are plotted in blue in figure D.2. The red line corresponds to the Pareto front of the optimization. Each design on the Pareto front is called a Pareto optimum and has to be considered as an optimum because it is not possible to find another design improving both objectives compared to it. The main goal of a MOO is to obtain the Pareto front(s) corresponding to the physical possibilities and be sure to select an optimum design.

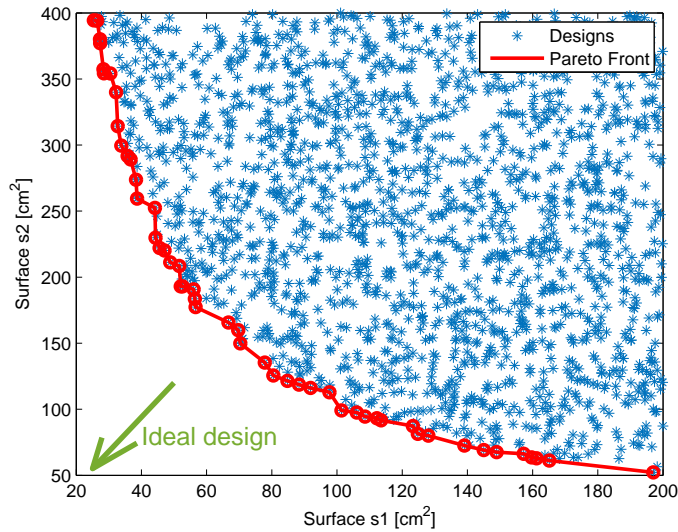


FIGURE D.2: Results of the MOO example

In this example it is very easy to calculate randomly a huge number of designs and obtain the Pareto front in a short time. For more complex problems with more than 2 input parameters or objectives necessitating FEM calculations to evaluate a design, this method takes too much time.

D.2 Multi-objective optimization algorithms

A MOO software uses special well adapted algorithms to find the Pareto fronts and enable the choice of an optimum design. Several algorithms can be found in the literature and can be classified in two categories [131, 135]:

- deterministic approach: these algorithms are repeatable, generate always the same results with the same initial conditions and do not leave things to the chance. To search the minimum of an objective, these algorithms use the variation of the objectives depending on the variation of the inputs parameters (gradient). Depending on the problem, these methods can converge in a short time but often converge in the nearest optimum and not in the global optimum.
- stochastic approach: these algorithms are based on probabilistic and random transitions to select new designs. Thanks to this approach, these algorithms are well suited to find the global optimum but can need a huge number of iterations to find it. Evolutionary algorithms, especially genetic algorithms are the most famous stochastic algorithms and are often used for MOO problems. In this work, a genetic algorithm has been used.

Genetic algorithms are iterative algorithms. Their functioning is explained in figure D.3. At first, a start population is initialized. A large amount of designs are randomly selected and evaluated. After this evaluation, the Pareto optima of this first generation are selected. Thanks to a crossover algorithm, a new generation of designs is created by combining the parameters of the Pareto optima. Furthermore random mutations occur. This new generation is then evaluated and added to the global designs population. Then the Pareto optima are selected and used to determine the next generation. By iterating this process, the genetic algorithm always uses the best designs to evaluate the next generation of designs and ensures a convergence after several iterations. The number of necessary iterations depends on the number of parameters, the number of objectives and the number of designs per generation. To ensure a fast convergence, the number of objectives has to be minimized.

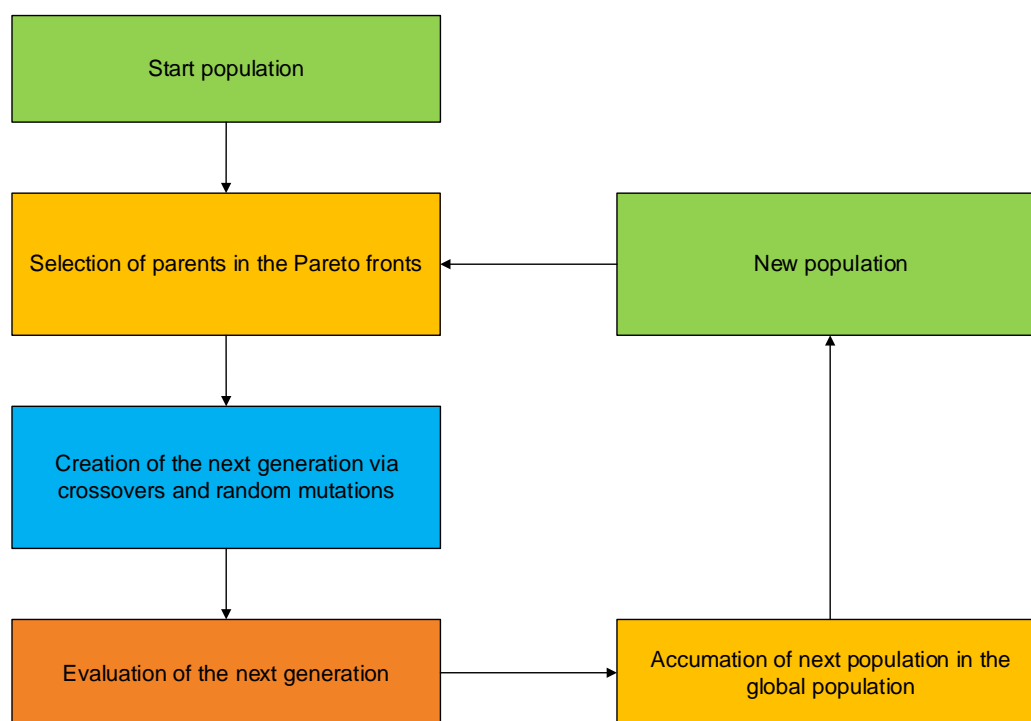


FIGURE D.3: Functioning of a genetic algorithm

E Manually designed machine (AFM₆₀)

E.1 Losses and efficiency

Losses studied in the chapter 4 have been calculated for every operating point of the machine. SMC (hysteresis, Joule and excess losses) and magnet losses have been calculated with FEM at the maximum rotational speed and have been interpolated for every rotational speed with equations 4.25 and 4.30. Copper losses are obtained with equation 4.1 by taking into account the evolution of the resistance with the rotational speed (see figure 5.11).

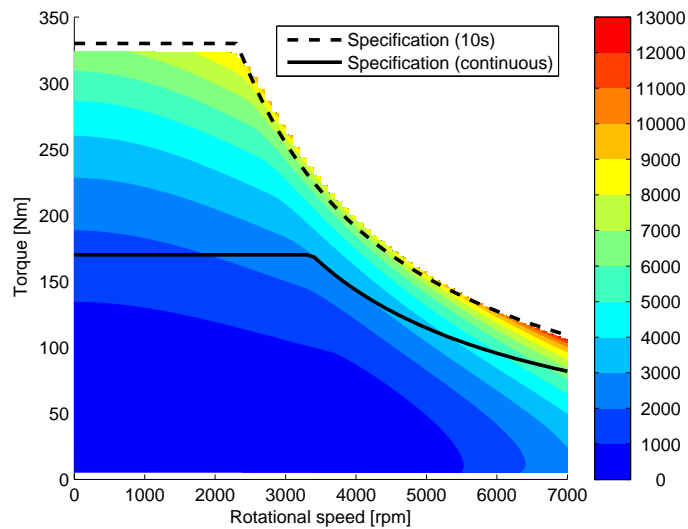


FIGURE E.1: Copper losses performance map of AFM₆₀ [W]

At high rotational speed, even if the maximum current decreases, copper losses increase due to the skin effect in the conductors. At high rotational speed, the effects of the field weakening on magnet and SMC losses is recognizable. SMC losses peak at 4000 rpm. Over this speed the increase of magnet losses is braked:

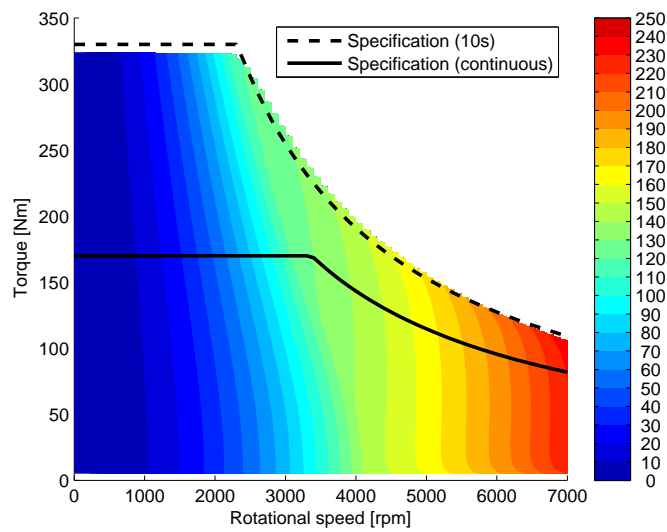


FIGURE E.2: Magnet losses performance map of AFM₆₀ [W]

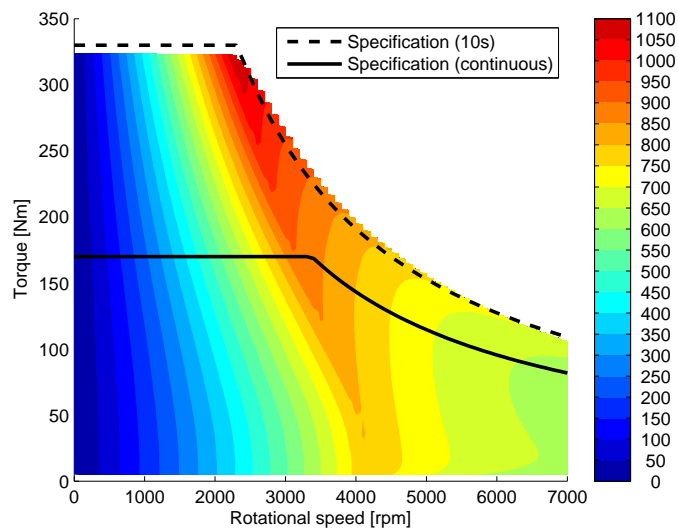


FIGURE E.3: SMC losses performance map of AFM₆₀ [W]

The total losses and the efficiency of the machine are plotted in following performance maps:

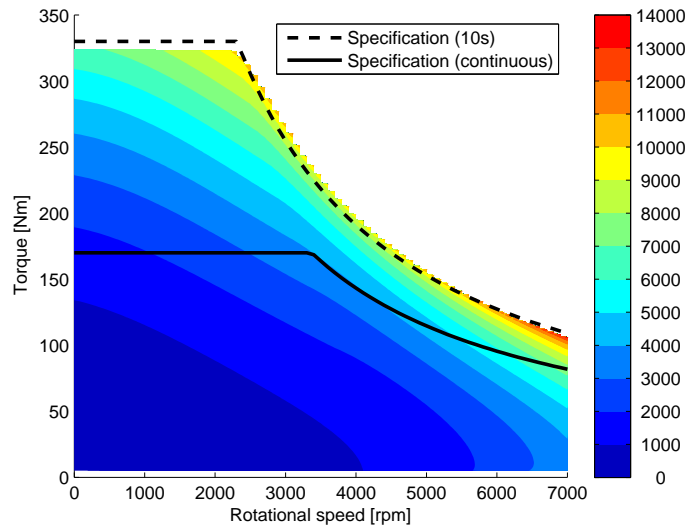


FIGURE E.4: Total losses performance map of AFM₆₀ [W]

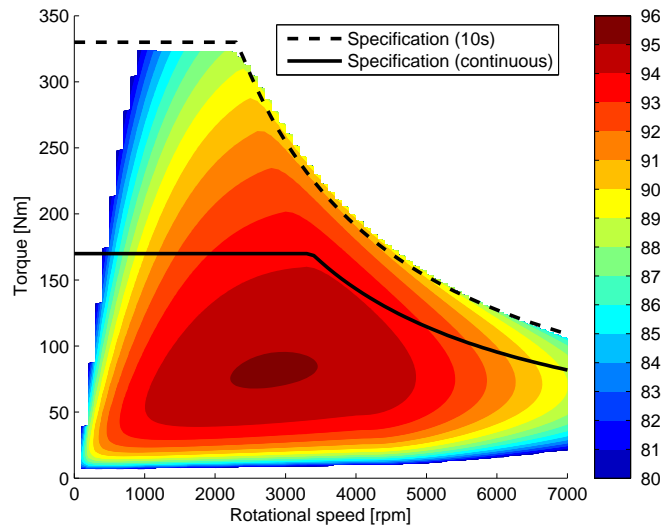


FIGURE E.5: Efficiency performance map of AFM₆₀ [%]

The optimum efficiency is obtained around 100 Nm and 3000 rpm. This machine has been simulated in the driving cycle presented in 2.2. In this cycle, the average power consumption is 2.93 kW compared to 2.19 kW for a perfect machine.

E.2 Axial forces

Axial forces on each stator and on the rotor permanent-magnets are plotted in following performance maps. At small rotational speeds, both of these forces increase with the

torque and are lightly depending on the rotational speed. In field weakening operation, the reduction of the magnetic flux in the machine reduces both of these forces.

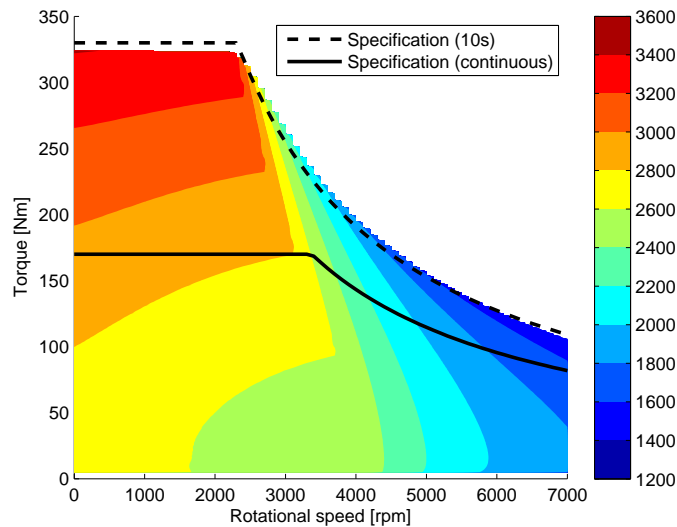


FIGURE E.6: Per stator axial force performance map of AFM₆₀ [N]

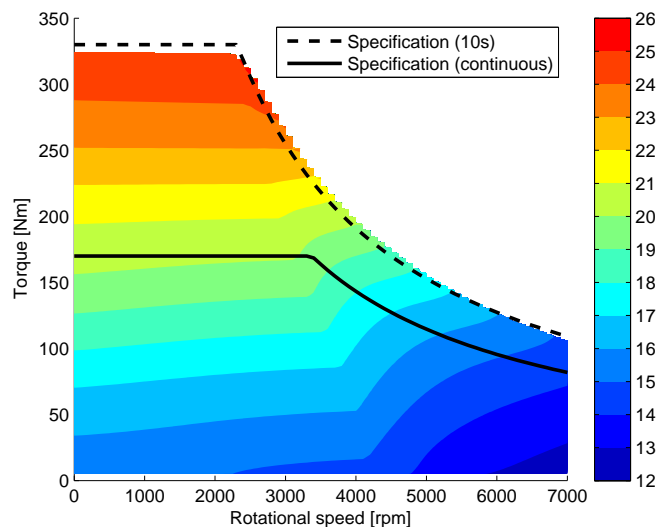
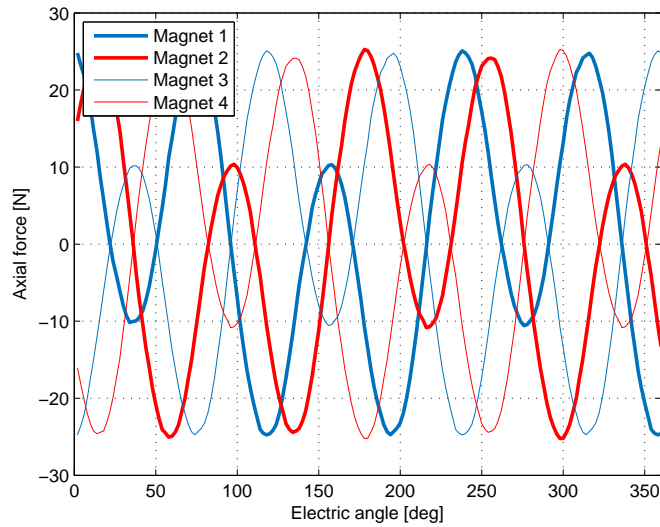


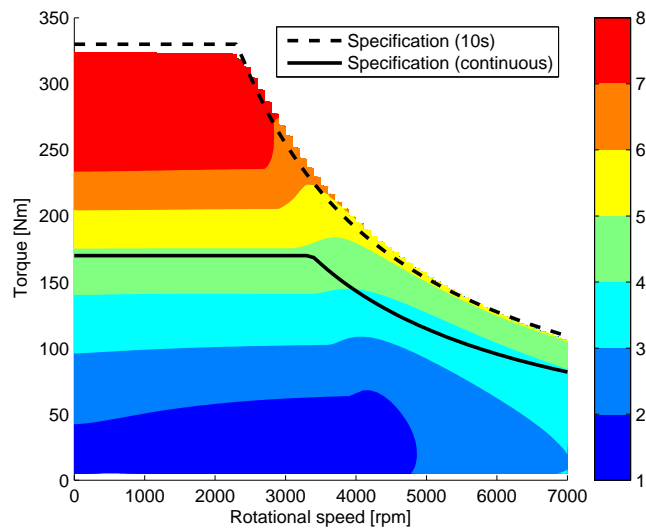
FIGURE E.7: Per magnet axial force performance map of AFM₆₀ [N]

Figure E.8 shows the axial force on 4 successive magnets over one electric period at full load. It can be observed that the forces acting on magnet 1 and 3 and on magnet 2 and 4 are opposed and compensate themselves. The force can be decomposed as the sum of the no load force due to the teeth (frequency: 4.5 the electric frequency) and the force generated by the electric current.


 FIGURE E.8: Per magnet axial force at full load of AFM₆₀ [FEM]

E.3 Torque ripple

The cogging torque and the torque ripple at full load have been displayed in 5.1.1.3. In these operating points, the machine offers very good performances with a maximum torque ripple of 7 Nm. The performance map of the torque ripple is shown in figure E.9 and confirms that the torque ripple stays under this value for every operating points. This good result is obtained thanks to the low harmonics contents of the induced voltage 5.4.


 FIGURE E.9: Torque ripple performance map of AFM₆₀ [Nm]

E.4 Short circuit current

The short circuit current I_{sc} depending on the temperature T and the rotational speed n of a permanent-magnet synchronous machine without saliency is defined by:

$$I_{sc}(T, n) = \frac{E_{rms}(T, n)}{Z_{phase}(T, n)} \quad (E.1)$$

$$I_{sc}(T, n) = \frac{k_E(T) \frac{\pi}{30} n n_p}{\sqrt{(L \frac{\pi}{30} n n_p)^2 + (R(T, n))^2}}$$

where $E_{rms}(T, n)$ is the RMS value of the induced voltage, $k_E(T)$ is the armature constant of the machine, n the rotational speed in rpm, L_d the inductance on the d axis and $R(T, n)$ the phase resistance depending on the temperature and the rotational speed. The inductance of the machine depends on the phase current and decreases when the magnetic material saturates. The evolution of the inductance with the phase current is shown in figure E.10. At no load and for high field weakening angle, the inductance can be considered as constant $L=86 \mu\text{H}$. For high phase current and no field weakening, the saturation of the magnetic material reduces the inductance by 9%.

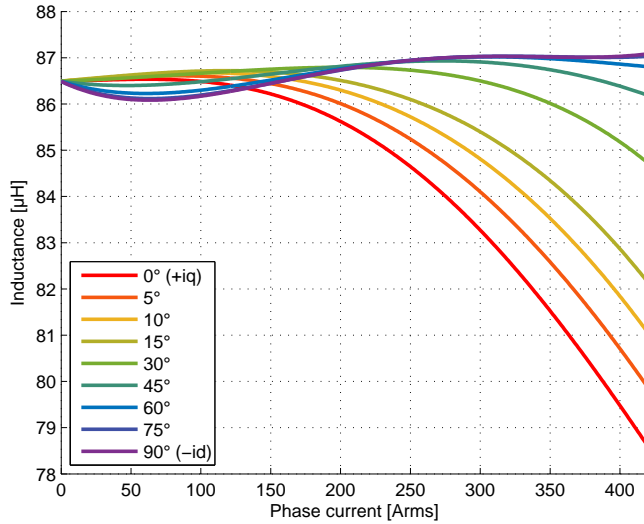


FIGURE E.10: Inductance depending on the current of AFM₆₀

The induced voltage increases linearly with the magnet remanence and depends on the temperature. At 90 °C ($B_r=1.18 \text{ T}$) and 7000 rpm, an induced voltage of 205.6 Vrms has been calculated. The armature constant is :

$$\begin{aligned}
 k_E(T) &= \frac{E_{rms}(T, n)}{\frac{\pi}{30} n n_p} \\
 k_E(90^\circ C) &= \frac{205.6}{\frac{\pi}{30} \cdot 7000 \cdot 12} \\
 k_E(90^\circ C) &= 23mV.s
 \end{aligned} \tag{E.2}$$

By taking into account the evolution of the resistance with the temperature and the rotational speed (figure 5.11), the short circuit current at -20 °C, 20 °C, 90 °C and 150 °C can be plotted:

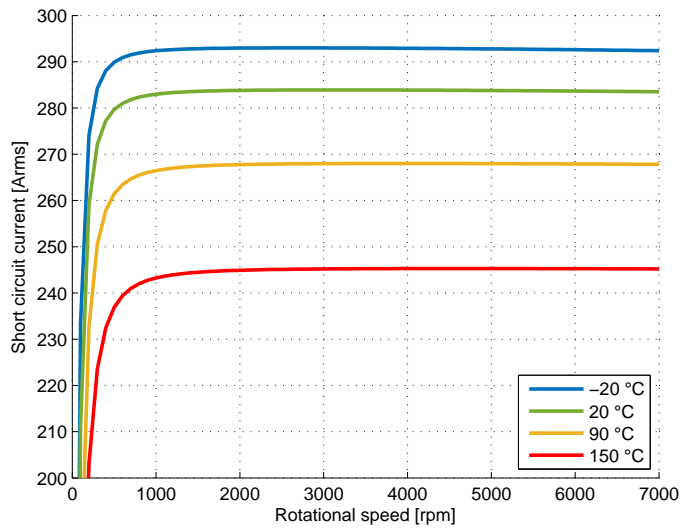


FIGURE E.11: Short circuit current depending on the rotational speed and the temperature (AFM₆₀)

E.5 Demagnetization safety

The specification requires the safety against the demagnetization at 150 °C for following current:

$$\begin{aligned}
 I_{demag} &= 2\sqrt{2}I_{scmax}(150^\circ C) \\
 I_{sc}(n) &= 2\sqrt{2} \cdot 247 \\
 I_{sc}(n) &= 698A
 \end{aligned} \tag{E.3}$$

To ensure the demagnetization safety, the machine has been simulated with a phase current of 700 A in the first phase and -350 A in both other phases. This current is

assumed to be constant and the rotor is turned over one electric period to test every current combination (including worst case). To ensure the demagnetization safety, it has to be checked, that the magnetic field strength in the magnet does not exceed the maximum allowed demagnetization field ($h_{k95} = -709kA.m^{-1}$ at 150 °C for a UH Magnet). The magnetic field strength for the worst case position is showed in figure E.12.

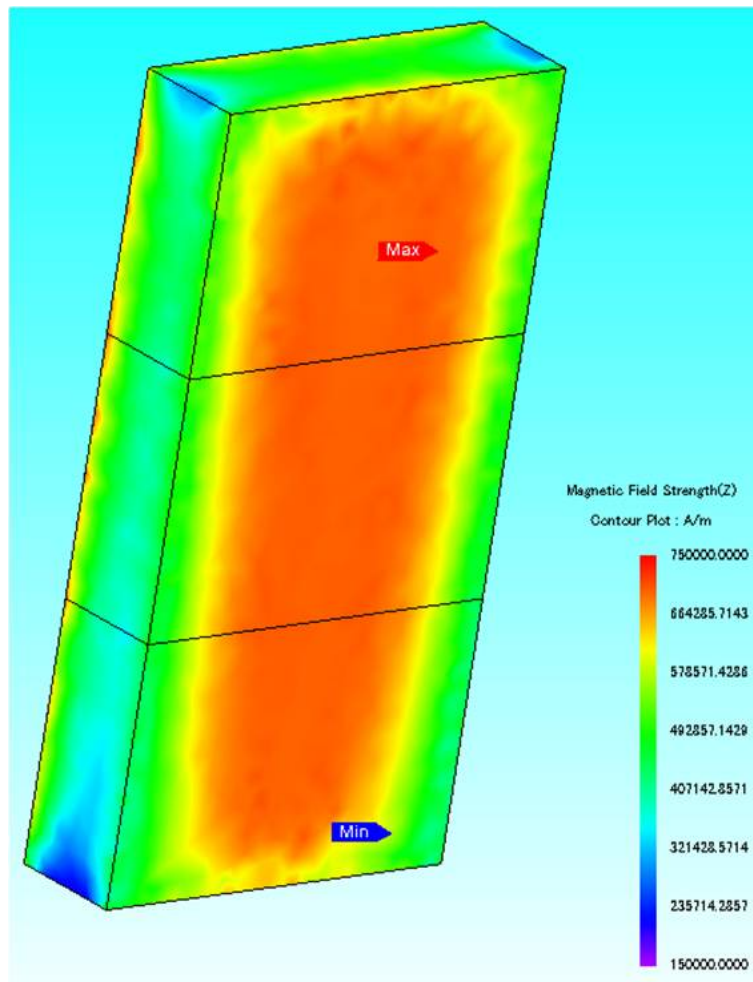


FIGURE E.12: Magnetic field strength in the magnet (worst case demagnetization current-AFM₆₀)

The highest magnetic field strength is localized on the front and back face of the magnet. The results on the front face is detailed in figure E.13. The magnetic field strength does not exceed $h_{k95} = -709kA.m^{-1}$ (see table C.1). The magnet can be considered as safe at 150 °C. The safety margin is very small in this case. To avoid any risk of demagnetization on the test bench, a more expensive magnet with the same remanence that a UH magnet but a higher coercivity has been used for the prototype (see 7.2).

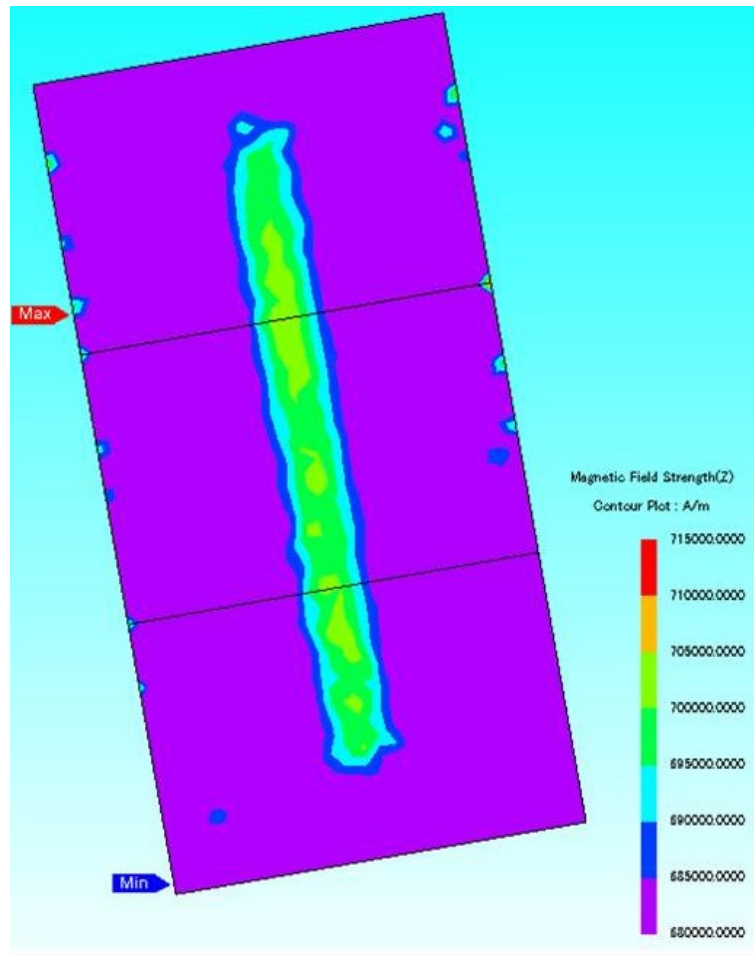


FIGURE E.13: Magnetic field strength on the front face (worst case demagnetization current-AFM₆₀)

F Multi-objective optimized machine (AFM_{MOO})

F.1 Winding technology

A comparison between the phase resistances at 100 °C with hairpin and pull in winding is displayed in figure F.1. Like the previous machine, the hairpin winding is better for small rotational speeds (under 3700 rpm) and worse for high rotational speeds. The machine is mainly driven under this rotational speed (see figure 2.3), so the hairpin winding is selected. The evolution of the phase resistance with the temperature is shown in figure F.2.

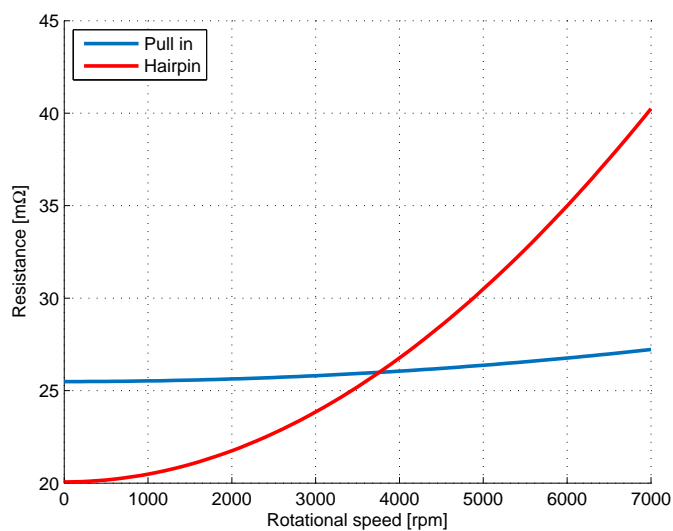


FIGURE F.1: Comparison between hairpin and pull in windings (AFM_{MOO})

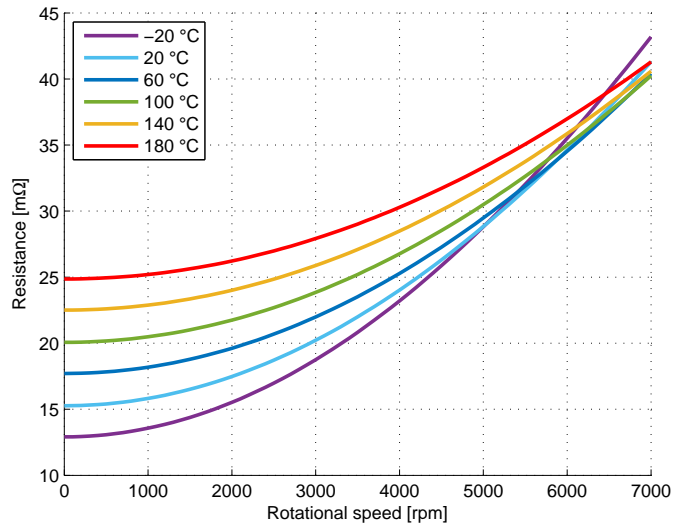


FIGURE F.2: Phase resistance depending on the copper temperature (AFM_{MOO}) [model]

The phase resistances of both designed machines are displayed in figure F.3 for a temperature of 100 °C. Thanks to smaller coil ends and current density, the resistance of the manually designed (AFM₆₀) machine is better at small rotational speeds. At high rotational speeds, the machine designed with multi-objective optimization (AFM_{MOO}) has a better phase resistance. It can be explained by the smaller section of the winding (which reduces the induced eddy current) and the smaller electric frequency.

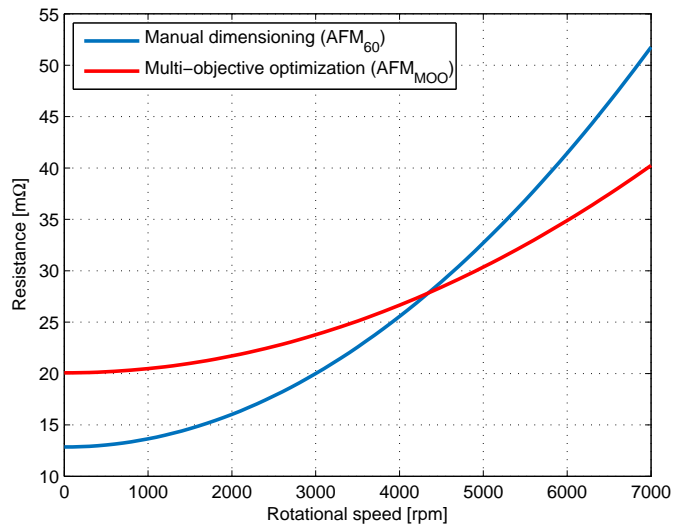


FIGURE F.3: Phase resistances of AFM₆₀ and AFM_{MOO} [model]

F.2 Losses and efficiency

Copper, SMC and magnet losses are respectively displayed in figures F.4, F.5 and F.6.

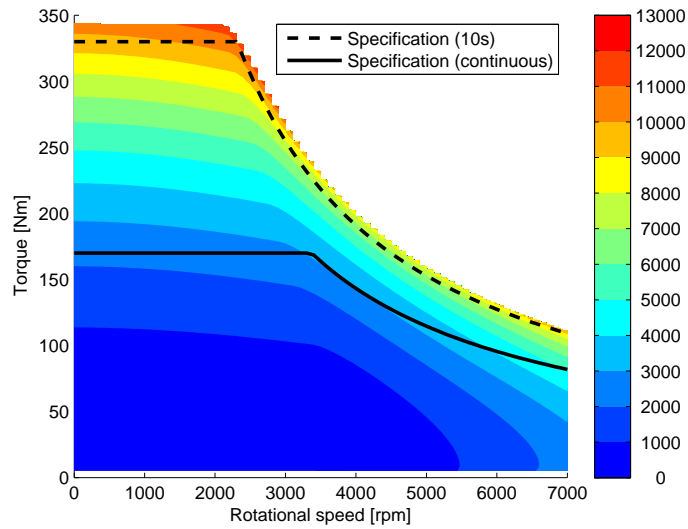


FIGURE F.4: Copper losses performance map of AFM_{MOO} [W]

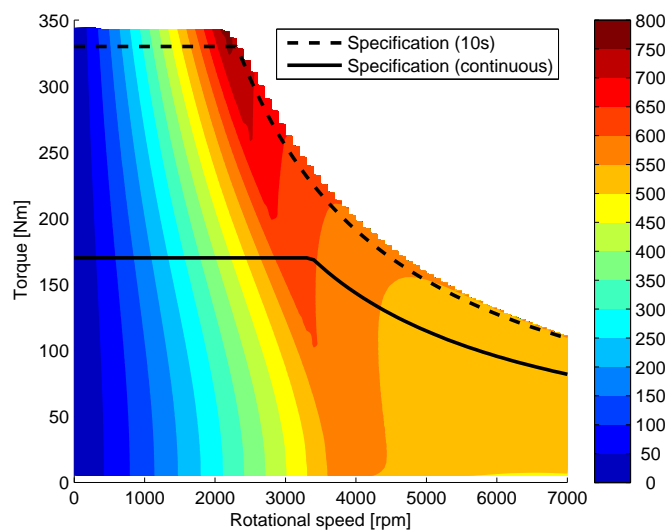
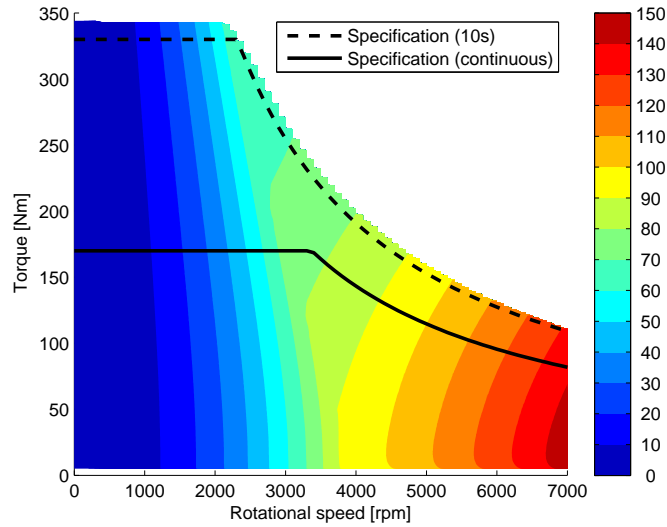
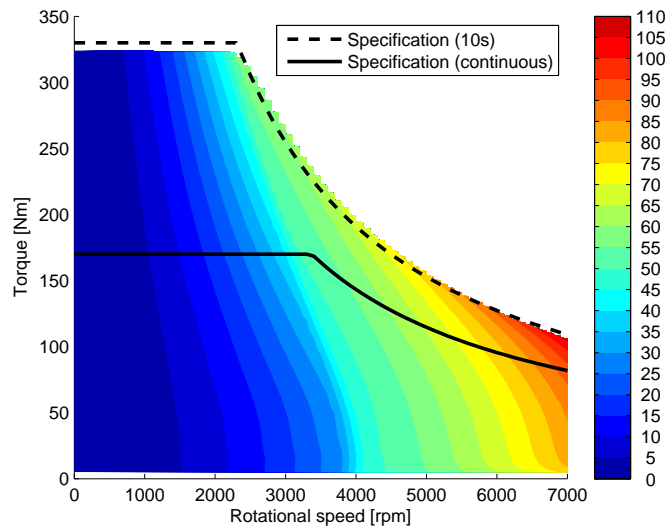


FIGURE F.5: SMC losses performance map of AFM_{MOO} [W]


 FIGURE F.6: Magnet losses performance map of AFM_{MOO} [W]

Magnet losses are much smaller in the machine designed with MOO than in the machine designed manually. Their maximum value is 150 W compared to 240 W, which corresponds to a reduction of approximately 40 %. In figure F.7, the difference between magnet losses in the MOO and in the manually designed machine are displayed. Positive values means that the losses in the MOO design are smaller. Magnet losses in the MOO designed machine are better in every operating point. At no load, the reduced slot width reduces the variation of the magnetic flux, so the magnet losses. Under load, the low harmonic content of the winding with a NSPP=1.5 is another advantage. Furthermore, the reduced magnet mass and the lower electric frequency helps to minimize these losses.


 FIGURE F.7: Difference magnet losses performance map between AFM₆₀ and AFM_{MOO} [W]

The total losses and the efficiency of the machine are displayed in figures F.8 and F.9.

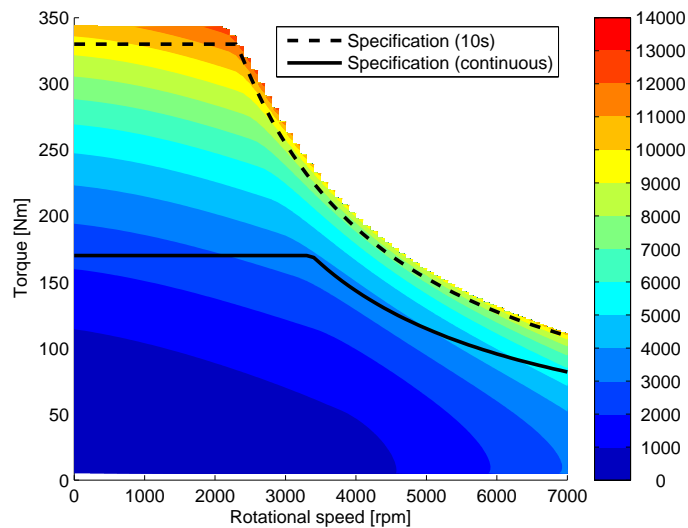


FIGURE F.8: Total losses performance map of AFM_{MOO} [W]

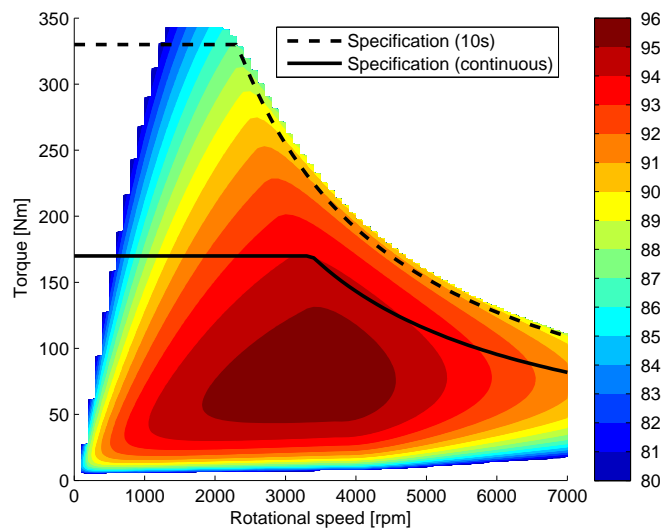


FIGURE F.9: Efficiency performance map of AFM_{MOO} [%]

The difference efficiency map between both machines is displayed in figure F.10. The efficiency of the manually designed machine has been subtracted to the efficiency of the MOO design, so positive values mean that the MOO design is better. It happens for rotational speeds over 3000 rpm and is particularly important for the continuous power of the machine which should be increased thanks to lower magnet and total losses. At small rotational speeds, the MOO design stays better for low torque operating points. These operating points are particularly important for driving cycles like the NEDC which does not require strong accelerations and stay in the low torque operating points. At

high torque operating points the manually designed machine is better thanks to lower copper losses.

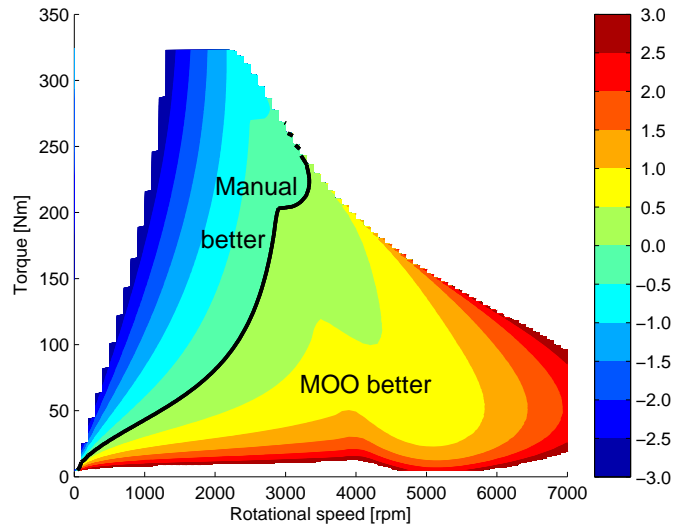


FIGURE F.10: Difference efficiency performance map between between AFM_{MOO} and AFM₆₀ [%]

The optimum efficiency is obtained around 100 Nm and 3500 rpm. This machine has been simulated in the driving cycle presented in 2.2. In this cycle, the average power consumption is 2.91 kW compared to 2.19 kW for a perfect machine. Compared to the manually designed machine the additional consumption due to the losses in the cycle are reduced by 3%.

F.3 Axial forces and torque ripple

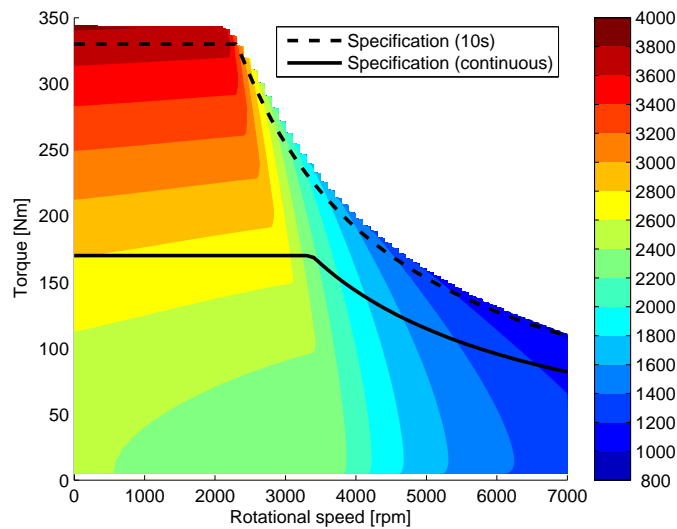


FIGURE F.11: Per stator axial force performance map of AFM_{MOO} [N]

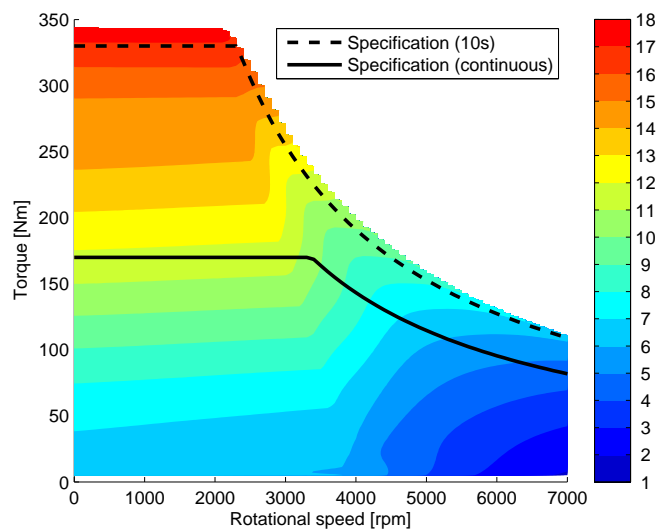


FIGURE F.12: Per magnet axial force performance map of AFM_{MOO} [N]

The performance map of the stator axial force (figure F.11) is quite similar to the manually designed machine. The force is greater (up to 3800 N at high torque compared to 3400 N). At high rotational speeds the reduction of the axial force thanks to field weakening observed for the manually designed machine (see figure E.6) is accentuated. The axial force on magnet (figure F.12) is reduced compared to the first design (see figure E.7). At high torque this force peaks at 18 N compared to 26 N for the previous designs. Furthermore, at high rotational speeds, this force is negligible.

The performance map of the torque ripple is displayed in figure F.13. The torque ripple peaks at 15 Nm for high torque operating points. This value is higher than the manually designed machine but amounts only 4% of the peak torque which remains a satisfying result. The torque at full load is displayed in figure F.14.

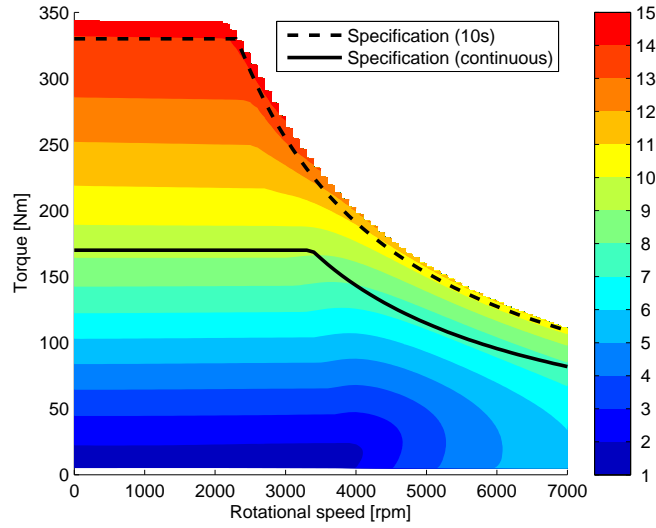


FIGURE F.13: Torque ripple performance map of AFM_{MOO} [Nm]

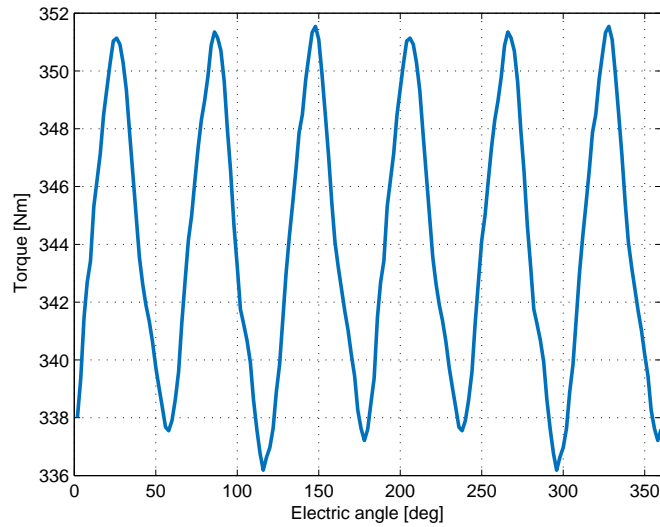
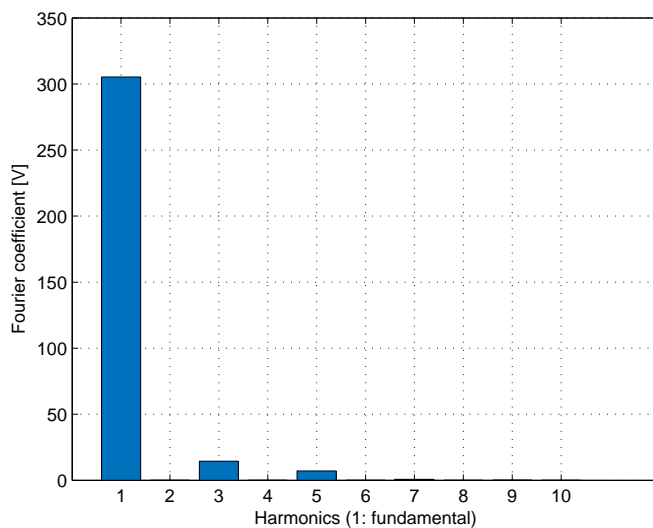
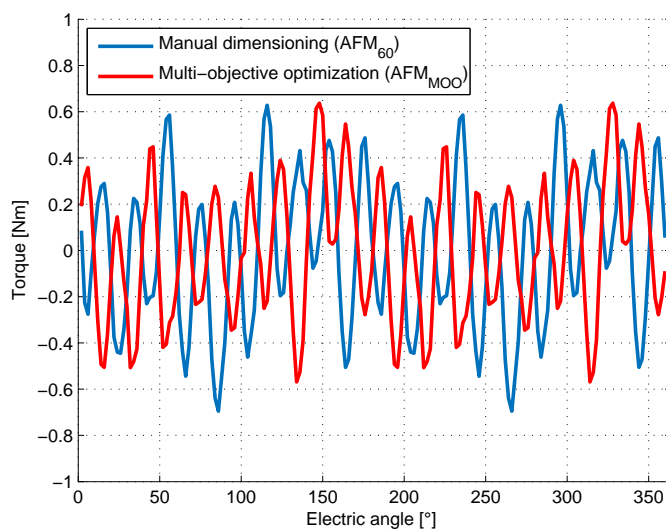


FIGURE F.14: Peak torque of AFM_{MOO} [FEM]

This higher torque ripple can be explained by the spectrum of the induced voltage (see figure F.15). The 5th and 7th harmonics are much higher than for the first machine (respectively 14.4 V and 7.1 V compared to 3.4 V and 0.4 V).


 FIGURE F.15: Fourier decomposition of the induced voltage of AFM_{MOO}

The cogging torque of both designs is displayed in figure F.16. It is similar and small. The main frequency of the cogging torque is the least common multiple of the number of slots and the number of magnets [130]. The designed machine has 18 magnets and 162 teeth (both stator), so the frequency of the cogging torque is 162 times the mechanical frequency, or 18 times the electric frequency ($n_p = 9$):


 FIGURE F.16: Cogging torque of AFM₆₀ and AFM_{MOO} [FEM]

F.4 Short circuit current

The evolution of the inductance with the operating point of the machine is similar to the manually designed machine. At high current, the saturation in the magnetic material reduces the inductance.

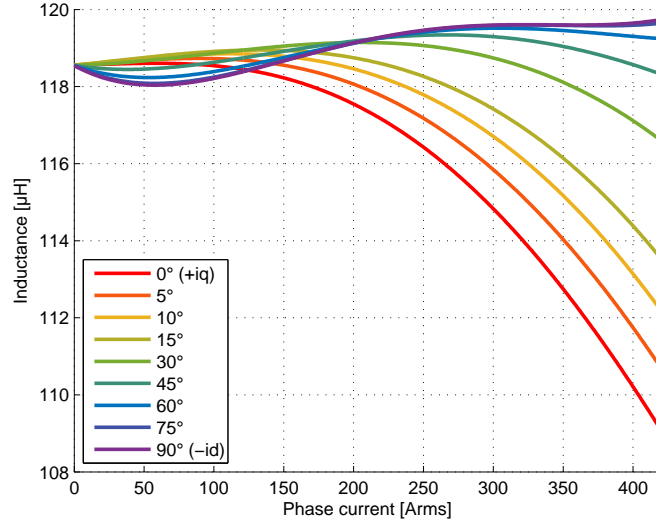


FIGURE F.17: Inductance depending on the current of AFM_{MOO}

In combination with the evolution of the phase resistance displayed in figure F.2, the impedance of one phase can be determined in every operating condition. The armature constant at 90 °C is calculated in equation F.1. Its evolution with the temperature is assumed to be linear with the remanence of the magnet (see EH grade in table C.1). The short circuit current for several temperatures (-20 °C, 20 °C, 90 °C and 150 °C) depending on the rotational speed is displayed in figure F.18.

$$\begin{aligned}
 k_E(T) &= \frac{E_{rms}(T, n)}{\frac{\pi}{30} n n_p} \\
 k_E(90^\circ C) &= \frac{216.2}{\frac{\pi}{30} \cdot 7000 \cdot 9} \\
 k_E(90^\circ C) &= 33mV.s
 \end{aligned} \tag{F.1}$$

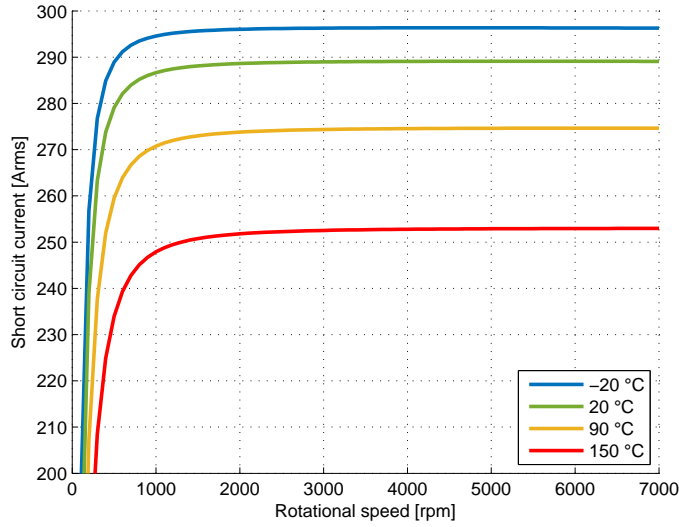


FIGURE F.18: Short circuit current depending on the rotational speed and the temperature (AFM_{MOO})

F.5 Demagnetization safety

The short circuit current at 150 °C peaks at 253 Arms at 7000 rpm, so the specification requires a demagnetization safety against following current:

$$\begin{aligned}
 I_{demag} &= 2\sqrt{2}I_{scmax}(150^{\circ}C) \\
 I_{sc}(n) &= 2\sqrt{2} \cdot 253 \\
 I_{sc}(n) &= 716A
 \end{aligned} \tag{F.2}$$

The same study as for the manually designed machine has been made. A simulation with a current of 720 A in one phase and -360 A in the both other phases have been performed. The rotor is turning to ensure that every rotor position, especially the worst case is simulated. It has to be checked, that the magnetic field does not exceed the maximum allowed demagnetization field of a EH magnet at 150 °C : $h_{k95} = -899kA.m^{-1}$. The magnetic field in the magnet is displayed in figure F.19 for the worst case position. The magnetic field strength peaks at 895 kA.m⁻¹, so the magnet can be considered as safe up to 150 °C. Like for the first machine, the safety margin is small.

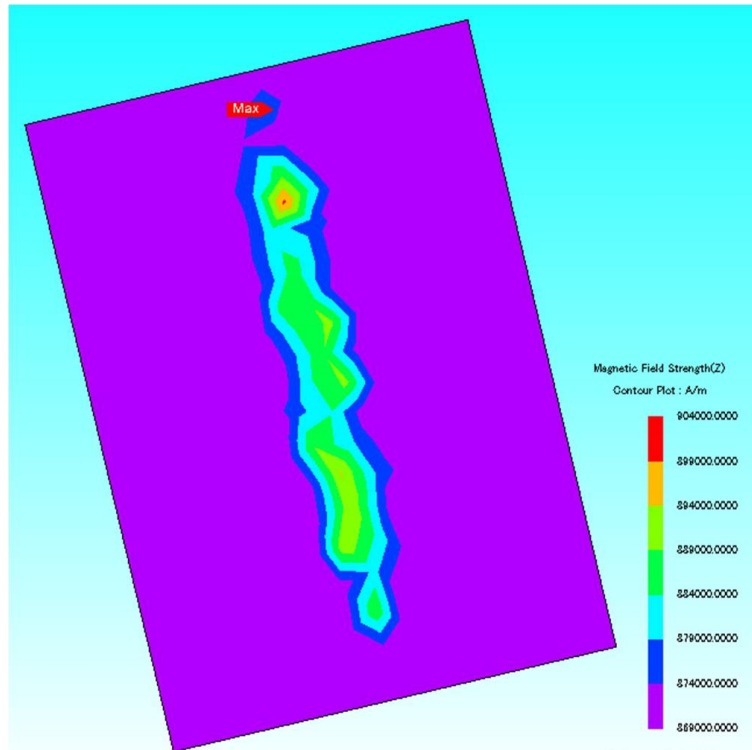


FIGURE F.19: Magnetic field strength on the front face (worst case demagnetization current-AFM_{MOO})

List of Figures

1	Hybrid and electric vehicles categories	2
2	Chronology of the PhD	4
1.1	Classification of disc rotor electric machines	8
1.2	Cylindrical coordinates frame	9
1.3	Magnetic circuit a single air gap AFM ($I = 0$)	10
1.4	Magnetic circuit a double air gap internal stator AFM ($I = 0$)	12
1.5	TORUS axial-flux machine	13
1.6	Magnetic circuit an AFIS machine without back iron ($I = 0$)	14
1.7	YASA axial-flux machine	15
1.8	Ironless AFIS machine	16
1.9	Magnetic circuit a double air gap internal rotor AFM ($I = 0$)	18
1.10	Magnetic circuit a double air gap internal rotor AFM (shifted teeth, $I = 0$)	19
1.11	Stator for disc rotor transverse-flux machine	24
2.1	Peak and continuous performances specifications	29
2.2	Distribution of the operating points an electrical machine for PHEV application [%]	30
2.3	Distribution of the rotational speed an electrical machine for PHEV application [%]	31
2.4	Three-phases concentric transverse-flux machine (1 stator)	35
2.5	Three-phase concentric transverse-flux machine (1 pole pair at no load)	36
2.6	Alternative TFM designs	36
2.7	Magnetic saturation in the transverse-flux machine	37
2.8	TFM performances compared to the specification	37
2.9	Spider plot comparison of the selected topologies	41
2.10	Single rotor double stator AFM with a concentrated winding	43
2.11	Star and delta electric connections a double stator AFM	45
2.12	Winding distribution with aligned teeth	47
2.13	Winding distribution with unaligned teeth	47
2.14	Schematic representation of a SMC powder	50
2.15	Detailed geometry of a SMC tooth	51
3.1	Advantageous numbers of slots per pole per phase	57
3.2	Winding distribution with unaligned teeth (NSPP=0.5)	59
3.3	Winding distribution (NSPP=1)	61
3.4	Complex phase diagram (NSPP=1)	62
3.5	Winding distribution with short-pitch (NSPP=1)	63

3.6	Phase diagram with short-pitch (NSPP=1)	63
3.7	Pitch angle and winding factor reduction depending on $\frac{N_2}{N}$	65
3.8	Winding distribution with short-pitch (NSPP=1)	65
3.9	Complex phase diagram (NSPP=0.75)	68
3.10	Electric circuit diagram (NSPP=0.75)	69
3.11	Winding sheet of one stator (NSPP=0.75)	70
3.12	Winding distribution (NSPP=0.75)	70
3.13	Winding distribution (NSPP=1.5)	71
3.14	Magneto-motive forces and fundamental for NSPP=0.5, NSPP=0.75, NSPP=1 and NSPP=1.5	72
3.15	Fourier spectrum of the magneto-motive forces	74
3.16	Spider plot comparison of the selected NSPP	77
4.1	Skin effect in bar conductors in electric machines ($N_h = 2$)	81
4.2	One-phase and two-phases conductors in a rectangular slot	83
4.3	Skin effect coefficient k_r depending on the electric frequency	84
4.4	Round and equivalent square conductors in a rectangular slot	84
4.5	Equivalent square conductor	85
4.6	Skin effect coefficient k_r depending on the electric frequency	86
4.7	State of the art and optimized hairpin winding for AFM	87
4.8	FEM Model with 1,2,4 and 8 different conductor sizes	89
4.9	Skin effect coefficient k_r depending on the electric frequency	90
4.10	Calculation of the equivalent slot width (k^{th} conductor)	91
4.11	Skin effect coefficient comparison between FEM and the model	92
4.12	Hysteresis cycle of a magnetic material [114]	93
4.13	Induced eddy current in axially-magnetized permanent-magnets	97
4.14	Definition of I and α	98
4.15	Magnet losses as function of the coil current at 20 °C	99
4.16	Fourier coefficients of the magnet losses for the simulated coil currents	100
4.17	Interpolation of the Fourier coefficients of the magnet losses for the simulated coil currents	101
4.18	Magnet losses and model as function of the coil current at 20 °C	102
4.19	Comparison between the calculated coefficients obtained with FEM calculations and the proposed interpolation as function of the magnet remanence	103
4.20	Comparison between the calculated magnet losses with FEM calculations and the analytic model at maximum rotational speed as function of the coil current (Br=1.00 T)	104
5.1	Evolution of the peak torque and the peak power	111
5.2	Evolution of the other optimization parameters	111
5.3	Induced voltage of AFM ₆₀ at 7000 rpm [FEM]	113
5.4	Fourier decomposition of the induced voltage of AFM ₆₀	113
5.5	Cogging torque of AFM ₆₀ [FEM]	114
5.6	Peak torque of AFM ₆₀ [FEM]	114
5.7	Torque characteristic of AFM ₆₀	115
5.8	Power characteristic of AFM ₆₀	115
5.9	MTPA characteristic	116
5.10	Comparison between hairpin and pull in windings (AFM ₆₀) [model]	118

5.11	Phase resistance depending on the copper temperature (AFM ₆₀) [model]	119
5.12	Evolution of the winding's geometry for serial and parallel connection	120
5.13	Comparison of the phase resistance depending on the electric connection (AFM ₆₀) [model]	120
5.14	Software toolchain for the multi-objective optimization	124
5.15	Operating points for the MOO	126
5.16	Calculations steps of a design in the MOO software toolchain	127
5.17	Peak torque and power depending on the number of turns	130
5.18	Peak torque and power depending on the pole-pair number	131
5.19	Peak torque and demagnetizing field depending on the number of turns	131
5.20	Relation between magnet losses at no load (OP1) and in field weakening operation (OP4)	132
5.21	Relation between magnet losses and air gap	132
5.22	Peak power depending on the short circuit current and the number of turns	133
5.23	Peak torque depending on axial length and the number of turns	134
5.24	Peak torque and peak power of the calculated designs	135
5.25	Pareto fronts of the multi-objectives optimization	136
5.26	Pareto fronts of the filtered designs	137
5.27	Torque characteristic	139
5.28	Power characteristic	139
5.29	MTPA characteristic	140
5.30	Torque characteristic of both designed machines	141
5.31	Power characteristic of both designed machines	142
6.1	Magnetic design of the reference radial-flux machine (IMG300)	147
6.2	Torque characteristic of the reference radial-flux machine (IMG300)	147
6.3	Peak power at maximum rotational speed depending on the iron length and the number of turns	148
6.4	Peak torque depending on the iron length and the number of turns	148
6.5	Peak torque characteristics of RFM ₃₀₀ and AFM _{MOO}	150
6.6	Peak power characteristics of RFM ₃₀₀ and AFM _{MOO}	150
6.7	Phase resistance of RFM ₃₀₀ and AFM _{MOO} [model]	151
6.8	Copper losses difference between RFM ₃₀₀ and AFM _{MOO} [W]	151
6.9	Stator iron losses difference between RFM ₃₀₀ and AFM _{MOO} [W]	152
6.10	Rotor losses difference between RFM ₃₀₀ and AFM _{MOO} [W]	152
6.11	Efficiency difference between AFM _{MOO} and RFM ₃₀₀ [%]	153
6.12	Torque ripple difference between RFM ₃₀₀ and AFM _{MOO} [Nm]	153
6.13	Radial scaling of the reference radial-flux machine	154
6.14	Torque characteristic depending on the number of turns	155
6.15	Power characteristic depending on the number of turns	155
6.16	Peak torque characteristics of RFM ₂₈₂ and AFM _{MOO}	157
6.17	Peak power characteristics of RFM ₂₈₂ and AFM _{MOO}	157
6.18	Phase resistances of RFM ₂₈₂ and AFM _{MOO} [model]	158
6.19	Copper losses difference between RFM ₂₈₂ and AFM _{MOO} [W]	158
6.20	Stator iron losses difference between RFM ₂₈₂ and AFM _{MOO} [W]	159
6.21	Rotor losses difference between RFM ₂₈₂ and AFM _{MOO} [W]	159
6.22	Efficiency difference between AFM _{MOO} and RFM ₂₈₂ [%]	160

6.23	Torque ripple difference between RFM ₂₈₂ and AFM _{MOO} [Nm]	160
7.1	First prototype of AFM (AFM _{P1})	165
7.2	Induced voltage characteristic (AFM _{P1})	166
7.3	Induced voltage error (AFM _{P1})	166
7.4	Short circuit current characteristic (AFM _{P1})	167
7.5	Short circuit current error (AFM _{P1})	167
7.6	Torque current characteristic (AFM _{P1})	168
7.7	Torque current characteristic error (AFM _{P1})	168
7.8	Torque speed characteristic (AFM _{P1})	169
7.9	Torque speed characteristic error (AFM _{P1})	169
7.10	Phase resistance depending on the rotational speed (AFM _{P2}) [model]	172
7.11	AFM _{P2} on the test bench	172
7.12	Induced voltage characteristic (AFM _{P2})	173
7.13	Induced voltage error (AFM _{P2})	173
7.14	No load losses characteristic (AFM _{P2})	174
7.15	No load losses error (AFM _{P2})	174
7.16	Short circuit current characteristic (AFM _{P2})	175
7.17	Short circuit current error (AFM _{P2})	175
7.18	Short circuit losses characteristic (AFM _{P2})	176
7.19	Short circuit losses error (AFM _{P2})	176
7.20	Torque current characteristic (AFM _{P2})	177
7.21	Torque current characteristic error (AFM _{P2})	177
7.22	Difference between the measured and the simulated losses (AFM _{P2}) [W]	178
A.1	Equivalent circuit of a Permanent-Magnet Synchronous Machine	184
A.2	dq transformation	186
A.3	Peak torque and power characteristic depending on the rotational speed	187
A.4	Voltage diagrams depending on the rotational speed	188
A.5	Currents Id, Iq and I depending on the rotational speed	189
A.6	Evolution of the current in the dq plane	190
A.7	Equivalent circuit of a 3-phase PMSM with parallel-star connection	191
A.8	Complex phase diagram with phase shift	192
B.1	Comparison between the analytic and FEM calculations	197
B.2	Torque depending on the diameter ratio	199
C.1	Magnetic characteristic a NdFeB permanent-magnet	200
C.2	BH curve of soft magnetic material [SMC 5P700HR]	202
C.3	Losses curves of soft magnetic material [SMC 5P700HR]	202
D.1	Definition of the optimization problem	204
D.2	Results of the MOO example	205
D.3	Functioning of a genetic algorithm	206
E.1	Copper losses performance map of AFM ₆₀ [W]	207
E.2	Magnet losses performance map of AFM ₆₀ [W]	208
E.3	SMC losses performance map of AFM ₆₀ [W]	208
E.4	Total losses performance map of AFM ₆₀ [W]	209
E.5	Efficiency performance map of AFM ₆₀ [%]	209
E.6	Per stator axial force performance map of AFM ₆₀ [N]	210

E.7	Per magnet axial force performance map of AFM ₆₀ [N]	210
E.8	Per magnet axial force at full load of AFM ₆₀ [FEM]	211
E.9	Torque ripple performance map of AFM ₆₀ [Nm]	211
E.10	Inductance depending on the current of AFM ₆₀	212
E.11	Short circuit current depending on the rotational speed and the temperature (AFM ₆₀)	213
E.12	Magnetic field strength in the magnet (worst case demagnetization current-AFM ₆₀)	214
E.13	Magnetic field strength on the front face (worst case demagnetization current-AFM ₆₀)	215
F.1	Comparison between hairpin and pull in windings (AFM _{MOO})	216
F.2	Phase resistance depending on the copper temperature (AFM _{MOO}) [model]	217
F.3	Phase resistances of AFM ₆₀ and AFM _{MOO} [model]	217
F.4	Copper losses performance map of AFM _{MOO} [W]	218
F.5	SMC losses performance map of AFM _{MOO} [W]	218
F.6	Magnet losses performance map of AFM _{MOO} [W]	219
F.7	Difference magnet losses performance map between AFM ₆₀ and AFM _{MOO} [W]	219
F.8	Total losses performance map of AFM _{MOO} [W]	220
F.9	Efficiency performance map of AFM _{MOO} [%]	220
F.10	Difference efficiency performance map between between AFM _{MOO} and AFM ₆₀ [%]	221
F.11	Per stator axial force performance map of AFM _{MOO} [N]	222
F.12	Per magnet axial force performance map of AFM _{MOO} [N]	222
F.13	Torque ripple performance map of AFM _{MOO} [Nm]	223
F.14	Peak torque of AFM _{MOO} [FEM]	223
F.15	Fourier decomposition of the induced voltage of AFM _{MOO}	224
F.16	Cogging torque of AFM ₆₀ and AFM _{MOO} [FEM]	224
F.17	Inductance depending on the current of AFM _{MOO}	225
F.18	Short circuit current depending on the rotational speed and the temperature (AFM _{MOO})	226
F.19	Magnetic field strength on the front face (worst case demagnetization current-AFM _{MOO})	227

List of Tables

2.1	Specifications	28
2.2	Evaluation table of selected topologies	40
2.3	Comparison between aligned and shifted teeth	48
2.4	Magnetic properties of different magnet grades	49
3.1	Comparison between main NSPP	75
4.1	Magnet losses in OP1, OP2 and OP3 for B_r between 1 T and 1.25 T	103
5.1	Parameters of the designed machine (AFM ₆₀)	112
5.2	Comparison between shifted and aligned teeth	117
5.3	Comparison between NSPP=0.75 and NSPP=1.5	122
5.4	Parameters of the optimized design (AFM _{MOO})	138
5.5	Comparison between the manually designed and the MOO machine	141
6.1	Characteristics and performances of IMG300	146
6.2	Comparison between RFM ₃₀₀ and AFM _{MOO}	149
6.3	Comparison between RFM ₂₈₂ and AFM _{MOO}	156
7.1	Parameters of the first prototype (AFM _{P1})	164
7.2	Parameters of the second prototype (AFM _{P2})	171
C.1	Magnetic properties of different magnet grades	201
C.2	Electric properties of copper depending on the temperature	203

Bibliography

- [1] K. Bradsher. Prices of rare earth metals declining sharply. *New-York Times*, 16.11.2011.
- [2] R. Marquardt. Trägheitsarmer Direktantrieb. Patent DE102006036707B3, 2006.
- [3] R. Marquardt. Trägheitsarmer Direktantrieb hoher Leistungsdichte. Patent DE102007013732A1, 2007.
- [4] U. Deuke, L. Krell, M. Levin, H. Nolte, A. Petrich, H. Schilp, G. Steinhoff, J. Tachtler and J. Thannheuser ; BMW. Entwurf und Industrialisierung einer Transversalfluss-E-Maschine und einer angepassten Leistungselektronik. iFlux research report, 2013.
- [5] J. F. Gieras, R.-J. Wang and M. J. Kamper. *Axial flux permanent magnet brushless machines*, volume 1. Springer, 2008.
- [6] M. Doppelbauer. A short history of electric motors, 2014. URL <http://www.eti.kit.edu/english/1376.php>.
- [7] K. Kondo, T. Maekawa and S. Kusase ; Denso Corp. A new multi air gap motor with trech shaped coil for HEV applications. SAE international, Detroit, USA, 2014.
- [8] E. Bommé, A. Foggia and T. Chevalier. Double air-gaps permanent magnets synchronous motors analysis. *IEEE Internationnal Conference on electrical machines*, 2008.
- [9] R. Qu and T. A. Lipo. Dual-rotor, radial-flux, toroidally wound, permanent-magnet machines. *IEEE Transactions on Industry Applications*, 2003.
- [10] M. Kowalczyk, A. Vezzini and L. Grzesiak. Cylindrical double air gap motor for aerial applications. *Przegląd Elektrotechniczny*, 2013.

- [11] P. Pisek, B. Stumberger, T. Marcic and P. Virtic. Performance comparison of double and single rotor permanent magnet machine. *Przeglad Elektrotechniczny*, 2011.
- [12] M. Jaensch ; Porsche Engineering. Axialflussmaschinen als hochperformante Antriebe für Hybrid und Elektrofahrzeuge. Oral presentation Institutskolloquium KIT, Karlsruhe, Germany, 2014.
- [13] A. Hult, A. Tenhunen and J. Österman ; Kone Corporation. Method and apparatus for the assembly of an axial-flux permanent-magnet synchronous machine. Patent WO002006005796A1, 2004.
- [14] C. Du-Bar. Design of an axial flux machine for an in-wheel motor application. Master's thesis, Chalmers University of technology, Göteborg, Sweden, 2011.
- [15] M. Aydin and M. K. Guven ; Caterpillar Inc. Axial-flux electric machine. Patent WO002008016425A2, 2006.
- [16] O. de la Barriere, H. Ben Ahmed and M. Gabsi. Axial flux machine design for hybrid traction applications. *IEEE Conference on power electronics, machines and drives*, 2008.
- [17] A. Metin, H. Surong and T. A. Lipo. Design and 3D electromagnetic field analysis of non-slotted and slotted TORUS type axial flux surface mounted permanent magnet disc machines. *IEEE Electric Machines and Drives Conference*, 2001.
- [18] H. Surong, A. Metin and T. A. Lipo. Torus concept machines: pre-prototyping design assessment for two major topologies. *IEEE Industry Applications Conference*, 2001.
- [19] M. Cirani, C. Sadarangani and P. Thelin. Analysis of an innovative design for an axial flux torus machine. *Stockholm, Sweden*, 2002.
- [20] Minebea Co. Ltd. Motor mit axialem Magnetfluss und ringförmiger Stator. Patent DE000020314652U1, 2003.
- [21] W. Fu and S. Ho ; Hong-Kong polytechnic university. Axial-flux electric machine. Patent US020120212085A1, 2011.
- [22] Z. S. Soghomonian and A. B. Maslov ; Wavecrest Laboratories LLC. Rotary electric motor having both radial and axial air gap flux paths between stator and rotor segments. Patent WO002003094328A1, 2002.
- [23] T.J. Woolmer and M.D. McCulloch. Analysis of the yokeless and segmented armature machine. *IEEE Electric Machines and Drives Conference*, 2007.

- [24] W. Fei, P. C. K. Luk and K. Jinupun. A new axial flux permanent magnet segmented-armature-torus machine for in-wheel direct drive applications. *IEEE Power Electronics Specialists Conference*, 2008.
- [25] S. Lomheim. Analysis of a novel coil design for axial flux machines. Master's thesis, Norwegian University of Science and Technology, Trondheim, Norway, 2013.
- [26] D. Libault. Moteur électrique à flux axial. Patent FR000002994038A1, 2012.
- [27] J. E. Brennvall ; Greenway energy As. Coil assembly for three phased transverse axial flux multi disk machines. Patent WO002012128646A1, 2011.
- [28] D. Tanaka, T. Kato, Y. Shibukawa, Y. Naruse, T. Hatsuda and T. Kojima ; Nissan Motor Co. and Fujitsu General Ltd. Study on a high torque density motor for an electric traction vehicle. *SAE International*, 2009.
- [29] A. Mebarki, G. Saini, G. T. Thiagarajan, M. Shanel, A. Bell, R. Gray and N. Brown ; Cummins generator technologies limited. Axial flux machine. Patent WO002010007385A2, 2008.
- [30] YASA Motors. Products, 2015. URL <http://www.yasamotors.com/products/>.
- [31] YASA Motors Ltd. YASA 750. Datasheet, 2015.
- [32] M. Aydin, S. Huang and T. A. Lipo. A new axial flux surface mounted permanent magnet machine capable of field control. *IEEE Industry Applications Conference*, 2002.
- [33] H. Vansompel, P. Sergeant, L. Dupré, and A. Van den Bossche. Axial-flux pm machines with variable air gap. *IEEE Transactions on industrial electronics*, 2014.
- [34] T. Daho ; Eta SA Fabriques d'Ebauches. Micromoteur électromagnétique à flux axial. Patent EP000000509379B1, 1992.
- [35] R. Qu and J. W. Bray ; General Electric company. Superconducting rotating machines with stationary field coils and axial airgap flux. Patent US000007049724B2, 2004.
- [36] J. J. Pyrhönen, M. N. Valtonen, V. J. Naumanen and K. T. Rauma ; Visedo Oy. A permanent magnet rotor for an axial flux electrical machine of a mobile working machine. Patent EP000002453549A1, 2010.
- [37] K. H. Knörzer and H. Von König ; Perm Motor Company AG. Electric axial flow machine. Patent WO002001011755A1, 1999.

- [38] M. U. Lamperth and M. Jaensch; Evo Electric Ltd. A permanent magnet rotor for an axial flux electrical machine. Patent GB000002456067A, 2008.
- [39] B. S. Mularcik ; The Timken Company. Virtual moving air gap for an axial flux permanent magnet motor with dual stators. Patent WO002007089529A2, 2006.
- [40] E. Richter ; General Electric Company. Magnet arrangement for axial flux focussing for two-pole permanent magnet AC machines. Patent US000004308479A, 1980.
- [41] M. Aydin, T. A. Lipo and S. Huang. Wisconsin Alumni Research Foundation. Patent US000007608965B2, 2005.
- [42] M. Rantapää ; Sähkörantek Oy. Electric machine of the axial flux type. Patent WO002005124967A1, 2004.
- [43] A. Schimann and J. Kiderle ; BMW AG. Scheibenläufermaschine und Verfahren zum Betreiben einer elektrischen Scheibenläufermaschine. Patent DE102010003891A1, 2010.
- [44] Y. Li and J. D. Lloyd ; Emerson Electric Co. Axial flux reluctance machine with two stators driving a rotor. Patent US000005925965A, 1996.
- [45] R. Madhavan and B. G. Fernandes. Axial flux segmented SRM with a higher number of rotor segments for electric vehicles. *IEEE Transactions on Energy Conversion*, 2013.
- [46] G. Secondo ; ABB Research Ltd. Achsialfluss-Elektromotor. Patent DE000019801275A1, 1998.
- [47] L. Haydock and N. L. Brown ; Newage International Limited. Stator/rotor arrangement and exciter for an axial flux AC machine. Patent GB000002408154A, 2003.
- [48] L. P. Tessier, J. P. Doyle and J. L. Weber. Axial flux switched reluctance motor and method of manufacture. Patent WO002007143827A1, 2006.
- [49] R. Madhavan and B.G. Fernandes. A novel technique for minimizing torque ripple in axial flux segmented rotor SRM. *IEEE Energy Conversion Congress and Exposition*, 2011.
- [50] J. Igelspacher and H.-G. Herzog. Analytical description of a single-stator axial-flux induction machine with squirrel cage. *IEEE International Conference on electrical machines*, 2010.

- [51] M. Valtonen, A. Parviainen and J. Pyrhönen. Influence of the air-gap length to the performance of an axial-flux induction motor. *IEEE International Conference on electrical machines*, 2008.
- [52] J. Pyrhönen and A. Piispanen. Axial flux induction electric machine. Patent WO002006021616A1, 2004.
- [53] R. J. Carl Jr. and C. M. Stephens ; General Electric company. Axial flux induction motor. Patent US020040119374A1, 2002.
- [54] P. Evans ; Evans Electric Pty Ltd. Vehicle drive system. Patent US000008393443B2, 2006.
- [55] Golem. Direktantrieb Elektromotoren in Autorädern zum fahren und bremsen, 2013. URL <http://www.golem.de/news/direktantrieb-elektromotoren-in-autoraedern-zum-fahren-und-bremsen-1308-100749.html>.
- [56] S. M. Abu Sharkh and M. T. N. Mohammad. Axial field permanent magnet DC motor with powder iron armature. *IEEE Transactions on Energy Conversion*, 2007.
- [57] Y. T. Seo, Y. C. Choi, H. G. Kim and J. S. Kong. Axial flux brushless DC motor for electric vehicle. Patent KR102002066674A, 2001.
- [58] Drayson Racing Technologies. Drayson racing technologies : Lola drayson b12/69 ev, 2013. URL http://www.draysonstracingtechnologies.com/projects/B12/project_article_B12.html.
- [59] Electric Vehicle news. Renault eolab axial flux powered 282mpg plug-in hybrid, 2014. URL <http://www.electric-vehiclenews.com/2014/09/renault-eolab-axial-flux-powered-282mpg.html>.
- [60] N. Fremau, A. Vignon, A. Ketfi-Cherif and M. Daneau ; Renault SAS. Transmission hybride pour véhicule automobile à arbres primaires concentriques et procédé de commande. Patent FR000003001187A3, 2013.
- [61] K. M. Rahmann, S. Hiti, N. R. Patel, T. G. Ward, J. M. Nagashima, F. Crescimbin and F. Caricchi ; General Motors Corp. Zahnradloses Motorantriebssystem für Räder. Patent DE102004038884A1, 2003.
- [62] YASA Motors Ltd. YASA Motors, hybridisation, 2014. URL <http://www.yasamotors.com/applications/hybridisation/>.
- [63] EV World. UK firms debuts new axial flux electric motor. *EV World*, 2013.

- [64] R. Strong. Axial flux single rotor motor. Datasheet Ashwoods Automotive Ltd., 2011.
- [65] Axiflux. Axiflux joins EV Engineering, 2013. URL <http://axiflux.com/news/axiflux-joins-ev-engineering/>.
- [66] F. Caricchi, F. Crescimbin, E. Fedeli and G. Noia. Design and construction of a wheel-directly-coupled axial-flux PM motor prototype for EVs. *IEEE Industry Applications Society Annual Meeting*, 1994.
- [67] M. U. Lamperth ; Evo Electric Ltd. Hybrid vehicle drivetrain with axial flux machines. Patent GB000002454592A, 2007.
- [68] X. Ai and N. J. Sertell ; The Timken Company. Compact axial flux motor drive. Patent WO002007030558A1, 2005.
- [69] F. Hashimoto, R. S. Zhou and M. Gradu ; The Timken Company. Axial flux motor assembly. Patent WO002004047255A2, 2002.
- [70] Baudatenbank, Kone. KONE Energiespar-Offensive: Aufzug als Mini-Kraftwerk, 2014. URL http://www.bdb.at/Detailansicht/ProduktNewsDetailansicht?newsId=126921_9.
- [71] B.J. Chalmers, W. Wu and E. Spooner. An axial-flux permanent-magnet generator for a gearless wind energy system. *IEEE Transactions on energy conversion*, 1999.
- [72] A. Parviainen, J. Pyrhönen and P. Kontkanen. Axial flux permanent magnet generator with concentrated winding for small wind power applications. *IEEE Conference on electric machines and drives*, 2005.
- [73] F. Locment. *Conception et modélisation d'une machine synchrone à 7 phases à aimants permanents et flux axial : commande vectorielle en modes normal et dégradé*. PhD thesis, Université des Sciences et Technologies, Lille, France, 2006.
- [74] F. Locment, E. Semail, X. Kestelyn and A. Bouscayrol. Control of a seven-phase axial flux machine designed for fault operation. *IEEE Transactions on industrial electronics*, 2006.
- [75] M. Cavaliere ; Enel Green Power S.p.A. Aerogenerator with axial flux permanent magnets and regulation thereof. Patent EP000001340910A1, 2002.
- [76] B. C. Lhenry and J. M. Canini ; Tecddis. Axial flow electric rotary machine. Patent WO002009071843A2, 2007.

- [77] Compact Dynamics. Transversalflussmaschinen, 2015. URL [http://www.compact-dynamics.de/entwicklung/technologien-und-entwicklungsbeispiele/transversalfluss-maschinen/9d85310d17784db826e93723e46ddf82/?tx_news_pi1\[controller\]=News&tx_news_pi1\[action\]=detail&tx_news_pi1\[news\]=15](http://www.compact-dynamics.de/entwicklung/technologien-und-entwicklungsbeispiele/transversalfluss-maschinen/9d85310d17784db826e93723e46ddf82/?tx_news_pi1[controller]=News&tx_news_pi1[action]=detail&tx_news_pi1[news]=15).
- [78] R. Marquardt. Low inertia direct drive having high power density. Patent WO002009115247A1, 2009.
- [79] M. Siatkowski and B. Orlik. Flux linkage in transverse flux machines with flux concentration. *IEEE Conference on optimization of electrical and electronic equipment*, 2008.
- [80] Z. Ping, Z. Jing, L. Ranran, T. Chengde, W. Qian and S. Wei. Comparison and evaluation of different compound-structure permanent-magnet synchronous machine used for HEVs. *IEEE Energy conversion congress and exposition*, 2010.
- [81] N. Eckhart ; Robert Bosch GmbH. Elektrische Maschine in Axialflussbauweise. Patent EP000001480317A2, 2004.
- [82] E. F. Ritz Jr., J. E. Bales, T. Long, J. L. Saunders, R. Nelke and M. Sabri ; Apex Drive Laboratories. Axial flux permanent magnet machines. Patent US000007863784B2, 2006.
- [83] J. K. Chiarenza. Improved axial flux motor with active flux shaping. Patent WO002004112218A2, 2003.
- [84] B. de Metz-Noblat, F. Dumas and C. Poulain. *Cahier technique no. 158 ; Calculation of short-circuit currents*. Schneider Electric, 2005.
- [85] B. K. Suda and J. David. A novel third harmonic injection method for closed loop control of PMSM motors. *e-driveonline*, 2015.
- [86] M. Braun and M. Kremer ; Robert Bosch GmbH. Transversalflussmaschine mit verringerten Drehmomentschwankungen. Patent DE102013217360A1, 2013.
- [87] M. Kremer, M. Braun, H. Hanssen and C. Prag ; Robert Bosch GmbH. Stator-einheit für eine Transversalflussmaschine sowie Transversalflussmaschine. Patent DE102013215423A1, 2013.
- [88] M. Braun and M. Kremer ; Robert Bosch GmbH. Statoreinheit für eine Transversalflussmaschine mit einem Scheibenrotor sowie Transversalflussmaschine. Patent DE102013218086A1, 2013.

- [89] A. Akimoto, N. Taniguchi, A. Ishizuka, S. Tachibana, M. Dobashi, M. Hayashi and T. Kurosawa ; Denso. Method and apparatus for rolling electric wire for stator coil of electric rotating machine. Patent US020110174038A1, 2010.
- [90] S.N. Vukosavic. *Electrical Machines*. Power Electronics and Power Systems. Springer New York, 2012.
- [91] S. Constantinides. The important role of dysprosium in modern permanent magnets. *Arnold Magnetic Technologies*, 2012.
- [92] K. Reis, M. Lehr and A. Binder ; TU Darmstadt, Institut für elektrische Energiewandlung. Comparison of axial-flux and radial-flux machines for use in wheel-hub-drives. Oral presentation Advanced E-Motor Technology, Frankfurt am Main, Germany, 2014.
- [93] G. B. Kliman, C. M. Stephens and P. L. Jansen ; General Electric. Axial flux machine and method of fabrication. Patent US000006445105B1, 1999.
- [94] T. Jung. Axial-flux type permanent magnet synchronous generator and motor. Patent WO002013032122A1, 2011.
- [95] M. Aydin, Z.Q. Zhu, T.A. Lipo and D. Howe. Minimization of cogging torque in axial-flux permanent-magnet machines: design concepts. *IEEE Transactions on magnetics*, 2007.
- [96] T.D. Nguyen, K.J. Tseng, C. Zhang and S. Zhang. Loss study of a novel axial flux permanent magnet machine. *IEEE Conference on electric machines and drives*, 2011.
- [97] O. De La Barriere. *Modèles analytiques électromagnétiques bi et tri dimensionnels en vue de l'optimisation des actionneurs disques: étude théorique et expérimentale des pertes magnétiques dans les matériaux granulaires*. PhD thesis, École normale supérieure de Cachan-ENS Cachan, France, 2010.
- [98] L. Hultman and Z. Ye ; Höganäs. Soft Magnetic Composites, properties and applications. Powder metallurgy and particulate materials, Orlando, USA, 2002.
- [99] L. Hultman and O. Andersson ; Höganäs. Advances in SMC technology - materials and applications. Euro PM, Copenhagen, Denmark, 2009.
- [100] P. Garrigues ; Seb SA. Stator for axial flux electric motor. Patent WO002004075376A2, 2003.
- [101] R. J. Carl ; General Electric company. Axial flux machine, stator and fabrication method. Patent US000006707221B2, 2002.

- [102] Högänas AB. *Högänäs handbook for sintered components ; Design and mechanical properties*. Högänas AB, 2013.
- [103] Y. D. Chun, D. H. Koo, Y. H. Cho and S. H. Lim ; Korea electro technology research institute. Flat type motor stator having a roll stacked structure and a method for manufacturing the same, especially for forming slots along the length direction of a steel plate at predetermined distance. Patent KR000100668116B1, 2005.
- [104] Electric and hybrid vehicle technology expo. Axial flux stators manufacturing breakthrough, 2014. URL [http://www.evtechexpo.com/media/news/2014/11/25/axial-flux-stators-manufacturing-breakthrough!/.](http://www.evtechexpo.com/media/news/2014/11/25/axial-flux-stators-manufacturing-breakthrough!/)
- [105] M. Bernard and A. Makki ; Ateliers Bernard et Bonnefond and Keep'Motion. Stator pour machine électrique discoïde à flux axial dont le disque est construit par une pluralité de secteurs. Patent FR000002965125A1, 2010.
- [106] P. Sergeant, H. Vansompel and L. Dupré. Performance and implementation issues considering the use of thin laminated steel sheets in segmented armature axial-flux PM machines. *IEEE Conference on electrical machines*, 2014.
- [107] A. Tutu. Bosch parallel full hybrid system explained. *Auto Evolution*, 2010.
- [108] Robert Bosch GmbH. Gasoline Systems, Integrierter Motor Generator, 2008. URL http://products.bosch-mobility-solutions.com/specials/de/elektrifizierung/pdf/Bosch_E-Maschine_integrierter_Motor.pdf.
- [109] I. Dirba and I. Kreicberga. Axial magnetic flux generator/motor with permanent magnets. Patent LV000000014007B, 2009.
- [110] F. Libert and J. Soulard. Investigation on pole-slot combinations for permanent-magnet machines with concentrated windings. *IEEE International Conference on electrical machines*, 2014.
- [111] G. De Donato, F. G. Capponi, A. Rivellini and F. Caricchi. Integer-slot vs. fractional-slot concentrated-winding axial-flux permanent magnet machines: Comparative design, FEA and experimental tests. *IEEE Energy conversion congress and exposition*, 2011.
- [112] L. Jian, C. Da-Woon, C. Chang-Hum, K. Dae-Hyun and C. Yun-Hyun . Eddy-current calculation of solid components in fractional slot axial flux permanent magnet synchronous machines. *IEEE Transactions on magnetics*, 2011.
- [113] J. Lammeraner and M. Staffl. *Eddy Currents*. Praha, 1964.

- [114] Wikipedia. Hystérésis, 2016. URL <https://fr.wikipedia.org/wiki/Hyst%C3%A9r%C3%A9sis>.
- [115] A. Parviainen. *Design of axial-flux permanent-magnet low-speed machines and performance comparison between radial-flux and axial-flux machines*. PhD thesis, Acta Universitatis Lappeenrantaensis, Finland, 2005.
- [116] Y. Guo, J. G. Zhu, J. J. Zhong and W. Wu. Core losses in claw pole permanent magnet machines with soft magnetic composite stators. *IEEE Transactions on magnetics*, 2003.
- [117] F. Deng. An improved iron loss estimation for permanent magnet brushless machines. *IEEE Transactions on energy conversion*, 1998.
- [118] F. Şahin. *Design and development of a high-speed axial-flux permanent-magnet machine*. PhD thesis, Technische Universiteit Eindhoven, Netherlands, 2001.
- [119] M. Kremer, D. Flieller, G. Sturtzer and J. Mercké. Investigation and fast analytical model of an axial flux machine regarding magnet losses. *IEEE Magnetics Conference (INTERMAG)*, 2014.
- [120] Vacuumschmelze. Vacodym 881 TP. Datasheet, 2015.
- [121] S. Ruoho, M. Haavisto, E. Takala, T. Santa-Nokki and M. Paju. Temperature dependence of resistivity of sintered rare-earth permanent-magnet materials. *IEEE Transactions on magnetics*, 2010.
- [122] M. Steinle, M. Braun and M. Kremer ; Robert Bosch GmbH. Läuferinheit für eine elektrische Maschine sowie elektrische Maschine. Patent DE102014203944A1, 2014.
- [123] M. Fickert, M. Steinle, M. Braun, P. Fruehauf, M. Kremer and A. Braeunig ; Robert Bosch GmbH. Scheibenläufer für eine elektrische Maschine. Patent DE102014213508A1, 2014.
- [124] P. Fruehauf, M. Kremer, M. Fickert, A. Braeunig, M. Steinle and M. Braun ; Robert Bosch GmbH. Scheibenläufer für eine elektrische Maschine. Patent EP000002975731A2, 2014.
- [125] D. Flieller and M. Kremer ; Robert Bosch GmbH. Statoreinheit für eine elektrische Maschine sowie elektrische Maschine. Patent DE102013226020A1, 2013.
- [126] D. Flieller and M. Kremer ; Robert Bosch GmbH. Statoreinheit für eine elektrische Maschine sowie elektrische Maschine. Patent EP000002884636A2, 2013.

- [127] M. Braun and M. Kremer ; Robert Bosch GmbH. Statoreinheit für eine elektrische Maschine sowie elektrische Maschine. Patent DE102014205034A1, 2013.
- [128] M. Steinle, M. Braun, J. Burghaus, J. Andrusch, M. Kremer and K. Foster ; Robert Bosch GmbH. Statorelement zum Aufbau einer Statoranordnung für eine elektrische Maschine, Statoranordnung und Verfahren zum Aufbau einer Statoranordnung. Patent DE102014203945A1, 2014.
- [129] M. Steinle, M. Braun, J. Burghaus, M. Kremer, K. Foster and J. Andrusch ; Robert Bosch GmbH. Stator element for constructing a stator arrangement for an electric machine, stator arrangement and method for constructing a stator arrangement. Patent WO002015132022A1, 2014.
- [130] D. Flieller, N. K. Nguyen, P. Wira, G. Sturtzer, D. O. Abdeslam and J. Mercklé. A self-learning solution for torque ripple reduction for nonsinusoidal permanent-magnet motor drives based on artificial neural networks. *IEEE Transactions on Industrial Electronics*, 2014.
- [131] Dynardo. *Optislang - the optimizing structural language ; software documentation*. Dynardo, 2011.
- [132] R. H. Park. Two-reaction theory of synchronous machines, generalized method of analysis-part I. *Transactions of the american institute of electrical engineers*, 1929.
- [133] D. Schröder. *Elektrische Antriebe - Grundlagen*. Springer Berlin, 2009.
- [134] SGTechnologies. S700 5P. Datasheet, 2014.
- [135] N. A. Karim. *Optimisation multi-critères et multi-physique d'aérogénérateurs à aimants permanents à flux axial*. PhD thesis, Université du Havre, France, 2008.